Monitoring, Prognosis and Decision-Making for Internet of Things Enabled Systems

Salman Jahani

A dissertation submitted in partial fulfillment of the requirements for the degree of

Doctor of Philosophy
(Industrial and Systems Engineering)

at the

UNIVERSITY OF WISCONSIN-MADISON

2021

Date of final oral examination: 03/26/2021
The dissertation is approved by the following members of the Final Oral Committee:

Prof. Shiyu Zhou (Committee Chair, Department of Industrial and Systems Engineering)

Prof. Dharmaraj Veeramani (Committee Co-chair, Department of Industrial and Systems Engineering)

Prof. Jeffrey Linderoth (Department of Industrial and Systems Engineering)

Prof. Kaibo Liu (Department of Industrial and Systems Engineering)

Prof. Zhengjun Zhang (Department of Statistics)

ACKNOWLEDGEMENTS

It would not have been possible to write this doctoral thesis without the support of the amazing people around me. It is a great pleasure to express my sincere gratitude to all of them.

I owe my deepest gratitude to my academic advisors, Professor Shiyu Zhou and Professor Dharmaraj Veeramani without whom this work would not have been possible. Their guidance brought a depth of knowledge to this thesis, and more importantly, their dedication and encouragement over the past five years inspired me to work hard and aim to achieve my full potential. It was a great honor to work under Professor Zhou's and Professor Veeramani's supervision and they have become, and will remain, my role models for a scientist, mentor and teacher.

I would like to express my special thanks to my other three committee members, Dr. Jeffrey Linderoth, Dr. Zhengjun Zhang, and Dr. Kiabo Liu for their time, support, and contribution to part of this research.

My thanks also go to my friends Raed, Chao, Akash, Jaesung, Congfang, Changyue, Behzad, Behzad, Yuhang, Abhijeet, and Jinwen who made my life very much enjoyable and memorable. Thank you for accompanying me in my PhD studies.

Above all, I thank my family without whom I could not have gone through this undertaking. Thank you mother and father, for your unconditional love and support for which my mere expression of thanks will never suffice. To my brothers Ehsan and Erfan, thank you for standing by me during these years. I specially thank Fatemeh who has been an inspiration to me during this last year. To my aunts Soheila, Rahele, Nasrin, and Zari, thank you for your love, your support made this possible.

I dedicate this dissertation to

My mother and father

Farah & Mousa

Thank you for being the reason I smile

ABSTRACT

The Internet of Things (IoT) refers to the interconnection of embedded computing devices within the Internet infrastructure. IoT has created a data-rich environment in which multiple sensors continuously monitor a unit's health status, and multiple units simultaneously transfer these data through the communication network to the processing center for analysis. This has provided an unprecedented opportunity for advanced data analytics and improving service decision making, which could lead to closer monitoring of a unit's health status, quicker fault diagnosis, more accurate forecasts of a unit's remaining lifetime, and proactive maintenance and control decisions that are better aligned to a unit's future conditions and performance. However, at the same time, it also creates new challenges for research in data analytics as to how this vast and complex data could be utilized to retrieve accurate diagnosis, meaningful prognosis, and real-time decision-making capability. Many existing techniques fall short of addressing this issue because most of them are developed when the data were collected in a well-controlled experimental setting. However, the monitoring data often involves many factors that are uncontrollable and, inevitably, has severe heterogeneity.

This research simultaneously addresses multiple challenges that arise from the monitoring data.

i. A primary focus of any diagnostic analytic technique is to discover the out-of-control condition as soon as possible. The characteristic of an engineering process under consideration can be represented by a functional relationship between a response variable and one or more explanatory variables. This functional relationship is typically referred to as profile. A non-parametric technique that capitalizes on the specific structure of multivariate profile data is essential for the effective diagnosis of any engineering system.

ii. One significant challenge in condition monitoring (CM) stems from the common industrial practice wherein an equipment is shut down (for maintenance or replacement) once its degradation signal reaches the failure threshold, and consequently no further condition monitoring data can be acquired beyond the failure threshold; this results in absence of information regarding the tail observations following truncation. Also, the CM signal observations in real-world applications are typically noisy as the sensors are subject to

environmental disturbances. Noisy CM signal observations can be inaccurate and may even contradict the underlying physics. For instance, CM signals should be monotonic over time when the underlying health is continually deteriorating. Thus, there is a need for an accurate yet flexible data-driven approach for modeling the evolution of degradation signals considering these two challenges.

iii. Individualizing the model is crucial for effective diagnosis and prognosis based on the monitoring data. The primary focus of collecting the monitoring data is to understand the specific in-service unit rather than studying the population behavior. Therefore, the predictions or diagnostic decisions based on the monitoring data needs to be highly individualized. This individualization is especially important in the current telemonitoring systems where environmental condition data are also available in large scale beside CM data. Thus, the model should be able to exploit both population level information and individual level CM data stream, as well as environmental condition data and update or adjust itself according to the newly collected data points from the specific individual.

iv. Many practical engineering systems only collect critical event occurrence data. Data analytics on such event data can provide meaningful prognostic and diagnostic information. A critical challenge in prognostic based on event data is individualizing the event prediction for a specific unit of interest rather than developing a population model. Such a framework should be able to map prognostic insights from similar performing unit to the special unit under study. The developed model should also be scalable and flexible enough to facilitate sharing of information and allows for analysis of flexible event patterns.

v. Prognostic models provide insights on the future evolution of health status of the engineering system under study. The next step for a prognostic model is to utilize the insights it provides and integrate it into a decision-making framework to optimize the performance of the system. Such an integrated analysis can consider individualized prognostic insight and develop individualized control policies.

To address those issues listed above, five tasks are investigated in this dissertation. (a) *To build a statistical monitoring framework for multivariate profile data which is able to account for correlation both within profiles and between profiles*. This technique greatly improves

diagnostics capability specifically for systems where multiple sensors monitor the underlying process. (b) *To propose a non-parametric Bayesian framework which is able to extrapolate the evolution of CM signal beyond its threshold level and to derive necessary and sufficient conditions which ensures monotonic evolution of such CM signals even with noisy observations.* This technique is non-parametric and scalable to large data sizes. (c) *To incorporate environmental factors in prognostics framework through a Brownian motion process with a drift dependent on the environmental conditions.* This technique allows incorporating multiple time-varying environmental factors into prognostic models through a semiparametric regression approach utilizing penalized splines to model the environmental covariate-drift relationship. (d) *To propose a non-parametric prognostic framework for individualized event prediction that is flexible and scalable to high dimensional settings.* This framework provides sharing of information between different units and allows for analysis of flexible event patterns. (e) *To integrate individualized prognostic model into a decision-making framework.* This framework leverages the prognostics insights and allows for more realistic decision making considering the uncertainty of units' health status.

TABLE OF CONTENTS

LIST OF FIGURES

LIST OF TABLES

Chapter 1

Introduction

1.1. Motivation

Major advances in IoT technology are transforming modern engineering systems into smart and connected systems. These systems embody three key characteristics: tangible physical components that comprise the engineering system, connectivity among components that enables data acquisition and sharing, and smart data analytics and decision-making capability. IoT enabled smart and connected systems have become increasingly available in practice. Examples include GM's OnStar® tele-service system, the InSite® tele-monitoring system from GE, and the KitchenConnect® system from Welbilt Inc.

Prognosis and diagnosis for the underlying health status of such systems are the keys for establishing a successful maintenance strategy and timely decision making. For those purposes, critical event data and condition monitoring (CM) data are often used. CM data is defined as a dataset that has been collected from individuals along the time, and it implicitly manifests the underlying unobservable system status. Also, in many cases, there are crucial events of interest and data analytics on such event data can provide meaningful prognostic and diagnostic information. For instance, many automotive companies try to establish an effective teleservice system. Teleservice systems monitor the in-field units and continuously generate data, which are transmitted through the communication network to the back office. The aggregated data are then processed and analyzed at the back-office to produce system prognosis. The prognosis results and the service alerts are passed individually to the in-field unit. The ultimate goal of a teleservice system is to improve the user experience, enhance the product safety, lower the ownership cost, and eventually gain competitive advantage for the manufacturer.

The unprecedented data availability in IoT enabled smart and connected systems provides significant opportunities for advanced data analytics and real-time decision-making; but, at the same time, it reveals critical challenges. *(i*) *Multivariate signal* data are becoming prevalent with the boom in sensor technology which offers significant opportunities for system *diagnostics* and *prognostics*. (*ii*) individual-level data including units' degradation and operating conditions as well as event stream data (like patient arrivals, failure events and etc.) has become available in large scale and consequently, there is a pressing need for *individualized* modeling and analysis. (*iii*) The large amount of data provides significant opportunities for realistic data-driven decision making. Since the hardware infrastructure of such monitoring system has not become mature until very recently, only limited work is available on developing statistical methods that are suitable for diagnosis, prognosis, and decision-making based on such data. Therefore, to truly fulfill the promise of smart and connected systems and facilitate the transformation from data-rich into decision-smart, new analytics and data-driven decision-making methods are urgently needed.

1.2. Research Objectives

Some of the challenges mentioned in the previous section make the existing statistical methods somewhat unsuitable for the real-time diagnosis, prognosis, and decision-making based on CM data. To fill this research gap, the objective of this dissertation is to establish a series of data-driven statistical methods that are tailored for both opportunities and the needs of prognosis, diagnosis, and decision-making based on the data collected from advanced monitoring systems. In details, the research tasks can be summarized as below.

i. A primary focus of any diagnostic analytic technique is to discover the out-of-control condition as soon as possible. The characteristic of an engineering process under consideration can be represented by a functional relationship between a response variable and one or more explanatory variables. This functional relationship is typically referred to as profile. A non-parametric technique that capitalizes on the specific structure of multivariate profile data is essential for the effective diagnosis of any engineering system.

ii. One significant challenge in condition monitoring stems from the common industrial practice wherein an equipment is shut down (for maintenance or replacement) once its

degradation signal reaches the failure threshold, and consequently no further condition monitoring data can be acquired beyond the failure threshold; this results in absence of information regarding the tail observations following truncation. Also, the CM signal observations in real-world applications are typically noisy as the sensors are subject to environmental disturbances. Thus, there is a need for an accurate yet flexible data-driven approach for modeling the evolution of degradation signals considering these two challenges.

iii. Individualizing the model is crucial for effective diagnosis and prognosis based on the monitoring data. The primary focus of collecting the monitoring data is to understand the specific in-service unit rather than studying the population behavior. Therefore, the predictions or diagnostic decisions based on the monitoring data needs to be highly individualized. This individualization is especially important in the current telemonitoring systems where environmental condition data are also available in large scale beside CM data. Thus, the model should be able to exploit both population level information and individual level CM data stream, as well as environmental condition data and update or adjust itself according to the newly collected data points from the specific individual.

iv. Occurrence of an event of interest across multiple similar units typically bears similarity and yet is distinct for each unit. A non-parametric framework that can handle multiple event stream data and account for heterogeneity is needed. Such a non-parametric framework can transfer knowledge acquired from similar units to enhance event prediction capability for a specific unit. The proposed framework should also be scalable to real-world high-dimensional data.

v. A data-driven decision-making framework for maintenance planning in smart and connected systems is needed. Specifically incorporating the individualized prognostics model into a decision-making framework to account for uncertainty in units' failure is essential for cost-effective maintenance plans. Such a maintenance plan is typically developed for multiple components in the system considering a finite planning horizon. Developed policy should also account for the effect of workload on degradation rates of different components in the system and considers the interactions between them.

Targeting the abovementioned research goals, five specific research tasks that correspond to each chapter of this dissertation are explained in the next section.

1.3. Outline of the Dissertation

The dissertation focuses on solving the aforementioned research problems for diagnosis, prognosis, and decision-making based on the data collected by various monitoring systems that have been established very recently. Figure 1.1 provides an overview of the research problems studied in each chapter of this dissertation and their relationship.

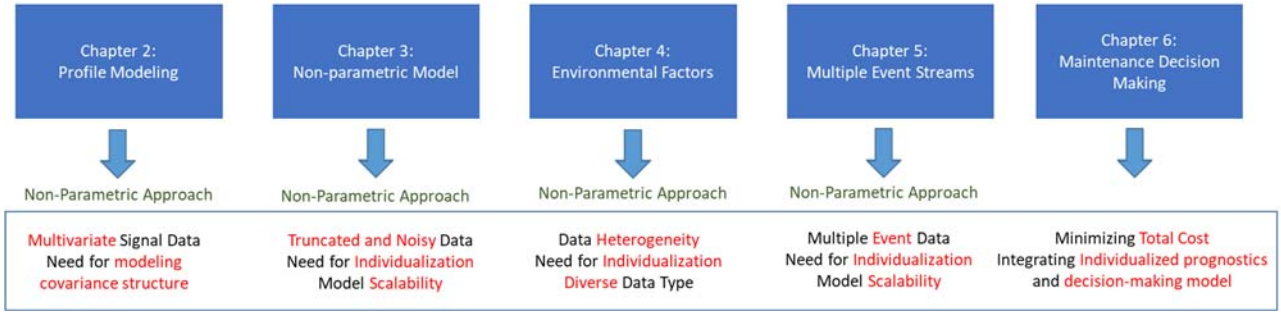

Figure 1.1. Overview of the research challenges studied in the dissertation

Chapter 2: *Statistical Monitoring of Multiple Profiles Simultaneously Using Gaussian Processes*

Multivariate signal data are becoming very common with the advances in sensor technology. In this task, an integrative diagnostic analytics method based on monitoring multivariate profile data from a manufacturing process is established. The proposed method utilizes the multivariate Gaussian process model based on non-separable covariance functions to establish an effective unified diagnostic analytics framework. The key advantage of the proposed technique is that it considers correlations both within profiles and between profiles and facilitates sharing of information. The proposed framework is highly flexible and can quickly detect different out-of-control states.

Chapter 3: *Remaining Useful Life Prediction Based on Degradation Signals Using Monotonic B-splines with Infinite Support*

One significant challenge in condition monitoring is the issue of truncated degradation signals. Moreover, based on the physics of degradation process, the CM signals should be inherently

monotonic. However, it is almost inevitable that most of the sensor-based degradation signals are subject to noise which can lead to misleading prediction results. In this task, a novel nonparametric approach to modeling and prognosis of CM signals using B-splines in a mixed effects setting is proposed. In order to deal with the issue of truncated historical CM signals, our approach is based on augmenting B-spline basis functions with functions of infinite support. Moreover, to model the degradation signal more accurately and robustly in a noisy setting, necessary and sufficient conditions to ensure monotonic evolution of the modeled signals are derived. Aside from being nonparametric, the flexible and individualistic approach in our model can scale for larger data sizes and automatically enforce the derived conditions for the in-service unit.

Chapter 4: *Stochastic Prognostics under Multiple Time-Varying Environmental Factors*

Many models assume that CM signals behave under similar environmental conditions or that environmental factors have no effect on the evolution of these signals. This assumption might not hold in real life applications. In this task we propose a nonparametric framework for modeling the evolution of CM signals under time-varying environmental factors. The unique feature of our model is that it does not assume any functional form for CM signals and is able to incorporate the effect of time-varying environmental factors through a semiparametric regression approach utilizing penalized splines.

Chapter 5: *Multi-output Gaussian Process Modulated Poisson Processes for Event Prediction*

This task aims to understand and model multiple event stream data of different units to make accurate individualized prediction for a specific unit of interest. To achieve this aim, a multitask Poisson point process model which leverages information from all units via multivariate Gaussian convolution processes is proposed. The unique advantage of this framework is that it models the temporal dependency of each event stream and takes advantage of the cross-correlation that exists among different event streams to give accurate learning and prediction. Moreover, a scalable inference scheme using variational approximation is developed which makes the framework appropriate for high dimensional big data.

Chapter 6: *Deep Reinforcement Learning for Maintenance and Operational Workload Planning*

The data-driven decision-making methods for maintenance and operational workload planning are investigated for smart and connected systems. This task proposes a novel stochastic control policy to plan for both maintenance and workload assignment actions in a system consisting of multiple similar units operating in a finite planning horizon. The problem is cast into a Markov decision process and a control policy that utilizes deep reinforcement learning is proposed. The proposed model aims to minimize maintenance and operational workload costs in a multi-component system considering components' degradation and economic dependency over a finite planning horizon. The proposed framework models the effect of workload on component degradation through a Brownian motion process and considers unit-to-unit variation using a Bayesian updating technique.

Finally, chapter 7 is the summary of the dissertation. It summarizes the contributions of the completed work and discusses the proposed future work.

Chapter 2

Statistical Monitoring of Multiple Profiles Simultaneously Using Gaussian Processes*

2.1. Overview

Profile monitoring is the application of control charts to monitor the stability of a process over time when the process can be characterized by a functional relationship between a response variable and one or more explanatory variables. Most of the research in profile monitoring has been focused on monitoring univariate profiles, while multivariate profile data are widely observed in practice. In this chapter, a monitoring approach based on a multivariate Gaussian process (MGP) model is proposed to monitor multivariate profiles simultaneously. In this regard, using a non-separable covariance function, a MGP model is fitted to represent the baseline in-control multivariate profile. Then, the stability of the process is tracked by monitoring a distance measure between the new observations of the multivariate profile and the baseline in-control model. A key advantage of this method is that it considers correlations both within profiles and between profiles. We also introduce, as a benchmark, a univariate Gaussian process based profile monitoring scheme modified for multivariate profiles. The performance of the proposed approaches is investigated and compared through numerical studies and a real-world case study. The analysis confirms the effectiveness of the MGP based monitoring scheme for multivariate profiles.

* This chapter is based on the paper: **Jahani, S.**, Kontar, R., Veeramani, D. and Zhou, S., 2018. Statistical monitoring of multiple profiles simultaneously using Gaussian processes. *Quality and Reliability Engineering International*, 34(8), pp.1510-1529.

2.2. Introduction

Remaining useful life (RUL) estimation and failure prediction play an important role in system reliability analysis and maintenance decision making. Consequently, RUL prediction methods have long been investigated. The approaches of prognosis can be put into three main categories: mechanistic model-based methods, artificial intelligent methods, and data-driven statistical methods (Jardine *et al*., 2006). The mechanistic methods employ the models based on the first principles to describe the evolution of the weakness, e.g., a crack in a structure, and then predict the occurrence of the failure, e.g., structural failure (Kozin and Bogdanoff, 1989). The mechanistic methods are very effective for systems where the physics behind the failure mechanism is known clearly. However, for complex engineering systems, comprehensive mechanistic methods often become intractable. The artificial intelligent methods are built upon the experiences of the experts in the field to establish a set of heuristic rules for the failure prediction (Siddique *et al*., 2003). Although those methods are relatively easy to use, the model building or model training is often time-consuming and costly. Recently, the rapid development of information and sensor technologies have led to the fast development of data-driven statistical methods for RUL prognosis. In such methods, a statistical model is established based on the historical failure event data and system degradation signals, also referred to condition monitoring signals in some applications, to describe and to predict the uncertainties in the failure occurrence. The data-driven statistical methods enjoy the broad applicability and statistical rigor. Therefore, we shall focus on this type of prognostic methods in this chapter.

Advances in sensor and information technology have made measurement of many process variables easily accessible and enabled unprecedented opportunities for process condition monitoring and control. Statistical process control (SPC) has provided a variety of methods and tools to monitor and control a process. Among various SPC techniques, profile monitoring has drawn significant attention in recent years (Noorossana et al., 2011, Jensen and Birch, 2009, Williams et al., 2007, Zhang et al., 2014, Woodall, 2007). In this context, the process characteristic under consideration can be represented by a functional relationship between the response variable and one or more explanatory variables. This functional relationship is typically referred to as a “profile” and “profile monitoring” generally refers to methods used to detect changes in the profile structure due to assignable causes and to accurately identify their sources.

In many engineering processes that are monitored with multiple sensors, the process condition is characterized by two or more profiles, and the response variables of interest are correlated. For instance, consider the force balance calibration in wind tunnel experiments at NASA Langley Research Center (Parker et al., 2001). In this example, three orthogonal force components representing the response variables and three orthogonal torque components as the explanatory variables are measured simultaneously. Another example is the ice making process of an ice machine. For an ice machine, it is known that the performance of the ice making process can be characterized through different temperature signals. Figure 2.1 shows the behavior of four different temperature signals in an ice machine during three consecutive ice making cycles. As seen in Figure 2.1, in each of the panels, different cycles have some similarities as well as some differences. The similarities between the cycles in each panel reflect inherent process characteristics under a specific operational condition, while the differences are due to natural random disturbances. Also, it can be seen that these four different signals demonstrate a correlated behavior with the same cycle mostly because all of them are collected from the same physical system. Such correlation may be due to interactions among the signals or due to the fact that all the signals are impacted by the same latent factor, such as the ambient temperature. While the signals in (a), (b) and (d) of Figure 2.1 exhibit the same or opposite trends and are clearly correlated, the signal in (c) is a bit different and seems to be constant in most of the range. However, by using a formal statistical hypothesis test (such as Pearson's samples correlation coefficient test), one can confirm the existence of correlation between the signal in (c) and other signals of Figure 2.1. For a process having multiple signal profiles, it is highly desired that these profiles be monitored simultaneously in order to quickly detect process condition changes.

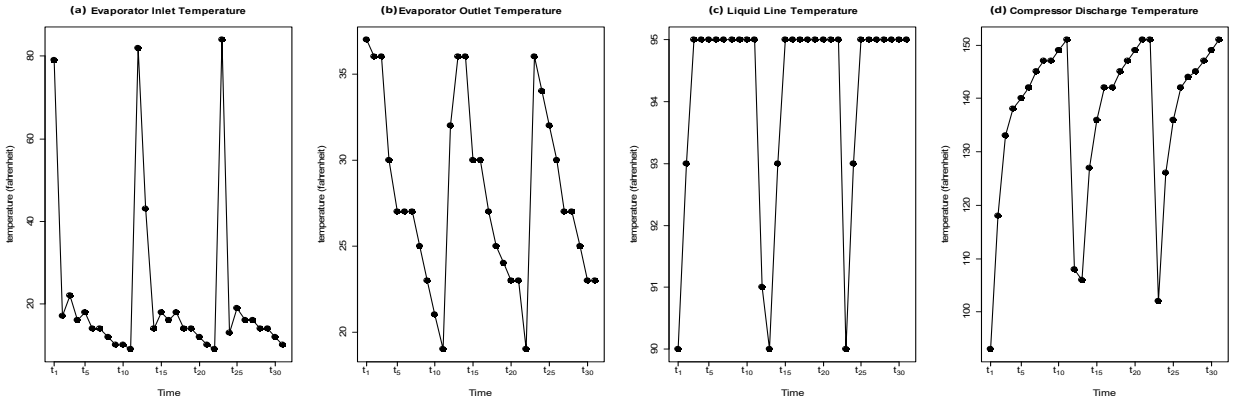

Figure 2.1. Temperature signal profiles for three consecutive ice making cycles

SPC methods, including profile monitoring methods, typically consist of two phases, phase I and phase II. In phase I, a set of process data is gathered and analyzed to see if reliable control limits can be established for future observations. In this phase, any unusual patterns in the data lead to adjustment of the process and the search for some assignable causes. Once all of the assignable causes and corresponding data have been eliminated from the data set, we are left with data associated with a stable operating condition which is called the in-control (IC) data set. Using the IC data set, IC process parameters which are representative of the actual process performance are estimated. In phase II, the process is monitored to detect any change in the process using the parameters estimated in phase I. The performance of a phase II monitoring scheme is typically measured in terms of the average run length (ARL) which is the average number of samples taken from the process until the chart signals a change. For a specific monitoring procedure, the IC ARL is often set to a given level. Then, when the process is out of control (OC), the monitoring procedure with a small ARL is considered to have good performance in detecting the specific change in the process. The ARL when the process is in-control is referred to as ARL_0 whereas the ARL when the process is out of control is referred to as ARL_1.

The existing profile monitoring methods can be broadly classified into two categories: parametric methods and non-parametric methods. Many parametric approaches have been proposed in the research literature for profile monitoring using linear regression models. In most of these approaches, the stability of the linear regression model is tracked by monitoring the regression coefficients using the Hotelling's T^2 control chart. For instance, Stover and Brill (Stover and Brill, 1998) and Kang and Albin (Kang and Albin, 2000) proposed T^2 control charts based on successive vectors of the least squares estimators of the Y-intercept and slope. However, in many real-world applications, linear regression models are often insufficient to represent the shape of the profiles. In such situations, a non-linear regression model may be better suited to model each profile. For a non-linear regression model, one can monitor the stability of the profile structure by monitoring the coefficients of the regression model as discussed by Williams et al. (Williams et al., 2007).

In practice, it might be difficult to assume any form of parametric relationship for the observed profiles. This issue might be due to difficulty in determining the correct parametric form of the relationship or because of the fact that the function is inherently non-parametric, i.e., it does not

have any finite parametric representation (Noorossana et al., 2011). For instance, vertical density profiles (VDPs) data set has been extensively used in the literature (Walker and Wright, 2002, Williams et al., 2007, Chang and Yadama, 2010). Considering the VDPS data set, Chang and Yadama (Chang and Yadama, 2010) proposed a method to identify the mean shifts and shape changes in non-parametric profiles. In their work, a discrete wavelet transformation is applied to separate the noise from the profile contours, and B-splines are used to generate critical points to define the shape of profiles. Applying principal component analysis (PCA), Shiau et al. (Shiau et al., 2009) used charts of principal component scores of profiles in monitoring both phase I and phase II. Chicken et al. (Chicken et al., 2009) proposed a threshold based method for determining the difference between the known wavelet coefficients in phase I and the coefficients of the newly observed profiles. All the above-mentioned approaches focus on single variable profile monitoring. One challenge with these methods is how to select the right basis and the right number of basis functions in the non-parametric representation.

Gaussian process (GP) models provide an interesting alternative for non-parametric profile modeling and monitoring and offer several advantages. First, GP models are non-parametric and do not assume any underlying relationship or rigid structure between the inputs and the outputs (Rasmussen and Williams, 2006). Moreover, GP models provide a unique view on prediction errors and give a powerful tool for uncertainty quantification which can be considered as an advantage over the wavelet and PCA methods. Also, GP models can provide a robust estimate of outputs over inputs in the case where there is insufficient sampling data. These features make GP a useful tool for profile monitoring. For instance, a GP model was used by Colosimo et al. (Colosimo et al., 2014) to model and monitor cylindrical machined surfaces generated by turning operations. Similarly, Cicorella et al. (Cicorella et al., 2013) proposed using a GP approach to model and monitor complex machined shapes. In these methods, a template profile is used to establish a GP model, and then the newly observed profiles are compared with the model outputs. Zhang et al. (Zhang et al., 2014) proposed using a GP model to describe the within-profile autocorrelation (WPA) in a linear profile monitoring problem. They proposed two Shewart-type multivariate control charts to monitor the parameters of the GP corresponding to the linear trend and the WPA separately.

In the above-mentioned GP based non-parametric approaches, only single variable profile is considered and the problem of simultaneously monitoring multivariate profiles is not addressed.

In a study by Zou et al. (Zou et al., 2012) a multivariate linear profile monitoring approach is developed. They proposed to apply a variable-selection-based multivariate control scheme to monitor multiple linear profiles. One restriction of their method is that it is not applicable to general nonlinear profiles. Paynabar et al. (Paynabar et al., 2013) proposed a method for analyzing multichannel nonlinear profiles using an uncorrelated multilinear principal component analysis in order to characterize the process variation and perform fault detection and fault diagnosis. Although the method proposed in their paper can effectively analyze the case of multichannel homogenous profile data, it cannot be used for the case of multi-sensor heterogeneous profile data where various sensors measure different variables. The case of monitoring multivariate nonlinear profiles was also examined in a study by Chou at al. (Chou et al., 2014). In their proposed approach, different profiles are first fitted by B-splines, and then the deviations of the observed profile from the fitted profile are fed into a multivariate EWMA (MEWMA) control scheme for the purpose of process monitoring. Moreover in a comprehensive study by Wu et al. (Wu et al., 2015), the performance of different population covariance matrix estimators for the MEWMA control charts has been investigated and interesting results have been reported. One limitation of these approaches based on the MEWMA chart is that they also do not consider the heterogeneity in the data. Recently, Li et al. (Li et al., 2017) proposed to fit a multivariate Gaussian Process (MGP) model for multivariate profiles of the IC process in phase I, and then established the in-control region of the parameters of the MGP. In phase II, an MGP model for the newly observed profiles is fitted and the fitted model parameters are monitored. The MGP model enjoys the flexibility and desirable analytical properties of the GP along with the ability to capture the correlation among multiple variable profiles. These advantages make MGP an attractive option for the multivariate profile monitoring problem. However, the approach in Li et al. (Li et al., 2017) has some limitations. First, one needs to fit a new MGP model for every incoming multi-profile sample which makes it difficult to monitor the profiles in phase II in real time, since fitting an MGP model takes a considerable amount of time due to complexity in its likelihood function. Second, it is known that the parameter fitting of GP is, in general, a non-convex optimization problem and the solution could easily get stuck at a local optimum. This means that the distribution of the fitted parameters of the MGP is very hard to characterize, which will lead to inefficiency in monitoring the coefficients of the process for the profile monitoring problem.

In this study, we propose a new multivariate profile monitoring chart using the MGP approach. In our approach, using kernel convolution, a non-separable covariance matrix is developed and the MGP model is fitted to establish the baseline in-control structure of the multivariate profile. In phase II, unlike Li et al.'s approach (Li et al., 2017), our MGP chart is based on monitoring the distance between the new and the baseline in-control profile values. This method offers several advantages. First, it does not require fitting of a new MGP model and estimation of parameters for every incoming sample in phase II monitoring. The proposed method can not only significantly reduce the computational load in phase II, but also deal with the issues caused by the uncertainties in parameter fitting in MGP. Furthermore, the flexible non-separable covariance matrix we adopted for the MGP model can effectively address between-profile-correlation (BPC) and within-profile autocorrelation (WPA), the two main challenges in multivariate profile monitoring problems.

The remainder of this chapter is structured as follows. Section 2.3 provides the mathematical formulation of the multivariate profile monitoring problem. In section 2.4, the methodology for monitoring multivariate profiles is introduced. In addition to the MGP based method, we also introduce a method for monitoring multivariate profiles using separate GP based univariate charts for comparison purposes. Section 2.5 presents a numerical study where the performance of the proposed approach is investigated under different scenarios. In section 2.6, the application of the proposed methods on a real-life case study is demonstrated. We also compare the performance of the proposed method with the method proposed in Li et al. (Li et al., 2017). Finally, our concluding remarks are presented in section 2.7.

2.3. Problem Description

In this study, we focus on monitoring general multivariate profiles. In practice, each sample of such multivariate profiles is measured at some specific time points which are referred to as design points in the GP literature. To be more specific, let us assume we have an IC data set of n independent samples of k different profiles, and denote $\boldsymbol{y}_i^{(m)}$ as the m^{th} sample of the ith profile variable, where $m = 1, 2, \dots, n$ and $i = 1,2, \dots, k$. Further, we assume there are p_i different design points namely $x_{i,j}$ $(j = 1,2, \dots, p_i)$ for the i^{th} profile variable. Thus, we have $\boldsymbol{y}_i^{(m)} =$

$\left[y_i^{(m)}(x_{i,1}), y_i^{(m)}(x_{i,2}), \ldots, y_i^{(m)}(x_{i,p_i})\right]^T$. It is assumed that when the process is in statistical control, the underlying model for each profile i is as follows:

$$y_i^{(m)}(x_{i,j}) = g_i(x_{i,j}) + \varepsilon_i^{(m)}(x_{i,j}) \quad (2.1)$$

where g_i is the true underlying function of profile i and $\varepsilon_i^{(m)}$ is the intrinsic noise at the design point $x_{i,j}$. There is no restriction on the form of function g_i and it can be either linear or non-linear. For the intrinsic noise $\varepsilon_i^{(m)}(x_{i,j})$ within each profile, we allow the possibility that $Corr(\varepsilon_i^{(m)}(x_{i,j}), \varepsilon_i^{(m)}(x_{i,j'})) > 0$.

The number of design points for each profile i (p_i) is taken to be equal and the explanatory variables $x_{i,j}$ are assumed to be fixed from sample to sample. This is typically referred to as common fixed design in the non-parametric regression context. However, this assumption is not required for the GP-based and MGP-based profile monitoring methods. It is assumed merely for convenience and for comparison with the legacy method that needs this assumption.

Here, we consider the two phases of a profile monitoring problem. In phase I, we assume that we have a set of IC profiles data from which the IC process parameters can be estimated. Once the IC model is established as a baseline, in phase II, we want to detect any change in the structure of the profiles. The proposed methodology to model and monitor the multivariate profiles described in eq. (1) is discussed in the next section.

2.4. Description of method for monitoring of multivariate profiles

A simple method for monitoring multiple profiles simultaneously is to monitor each profile individually and use a simple rule to determine whether the process is out of control. For example, the process can be considered to be out of control if one of the profiles indicates an out of control situation. In order to compare with this simple method, we will introduce a monitoring scheme based on univariate GP in Section 2.4.1. The MGP based monitoring scheme will be described in Section 2.4.2. The comparison study later shows that the MGP based method performs better because the cross correlation between different profiles is considered in MGP.

2.4.1. Univariate Gaussian Process (GP) Chart

First, we focus on establishing a GP-based univariate profile monitoring scheme for profile i. A GP model of profile i requires a set of training data containing one observation for each design point of profile i; while in phase I analysis, we usually have a set of in-control samples for each profile. Since one GP model can be estimated from one observation of a profile i, we need a way to take advantage of the available multiple in-control observations of profile i while estimating the GP model for profile i. In this regard, our approach is based on fitting a GP regression model for each individual in-control observation of profile ($\boldsymbol{y}_i^{(m)}$) and pooling all n different GP models into one representative model.

A GP is, in fact, a collection of random variables with a joint Gaussian distribution (Rasmussen and Williams, 2006). Thus, having p_i observations from sample m of profile i, we can consider them as a sample of a p_i-variate Gaussian distribution. A GP model for sample m of profile i is completely specified by its mean function $\mu_i^{(m)}(x_{i,j})$ and covariance function $\mathcal{K}_i^{(m)}(x_{i,j}, x_{i,j'})$. Thus, the GP regression model for sample m of profile i can be expressed as follows:

$$y_i^{(m)}(x_{i,j}) = f_i^{(m)}(x_{i,j}) + \varepsilon_i^{(m)}(x_{i,j})$$
$$f_i^{(m)}(x_{i,j}) \sim GP\left(\mu_i^{(m)}(x_{i,j}), \mathcal{K}_i^{(m)}(x_{i,j}, x_{i,j'})\right), \quad \varepsilon_i^{(m)} \sim N(0, \sigma^2) \tag{2.2}$$

In this model, $\varepsilon_i^{(m)}$ represents the measurement noise, the mean function $\mu_i^{(m)}(x_{i,j})$ is usually taken to be zero, and the model is parameterized by defining a positive definite covariance function. In this study, as in most other practical applications, the covariance function is chosen to be a Gaussian kernel where $\mathcal{K}_i^{(m)}(x_{i,j}, x_{i,j'}) = \rho_{i,m}^2 exp\left\{-\lambda_{i,m}(x_{i,j} - x_{i,j'})^2\right\}$ (Zhang et al., 2014, Colosimo et al., 2014, Cicorella et al., 2013, Rasmussen and Williams, 2006). Here $\rho_{i,m}^2$ is defined as the maximum allowable covariance and $\lambda_{i,m}$ is the shape parameter for sample m of profile i. Considering the Gaussian covariance function, the covariance matrix $\boldsymbol{\Sigma}_i^{(m)}$ for the observations of profile i can be constructed. Moreover, having estimated the hyper-parameters of the covariance function through maximizing a log-likelihood function, the prediction for each design point j of profile i $\left(\hat{y}_i^{(m)}(x_{i,j})\right)$can be calculated considering the following distribution:

$$\hat{y}_i^{(m)}(x_{i,j})|\boldsymbol{y}_i^{(m)} \sim \mathcal{N}\left(\boldsymbol{\eta}_{i,m}^T(x_{i,j})\left(\boldsymbol{\Sigma}_i^{(m)}\right)^{-1}\boldsymbol{y}_i^{(m)}, \Sigma_i^{(m)}(x_{i,j},x_{i,j}) - \boldsymbol{\eta}_{i,m}^T(x_{i,j})\left(\boldsymbol{\Sigma}_i^{(m)}\right)^{-1}\boldsymbol{\eta}_{i,m}(x_{i,j})\right) \tag{2.3}$$

where, $\boldsymbol{\eta}_{i,m}(x_{i,j}) = \left[\Sigma_i^{(m)}(x_{i,j},x_{\mathrm{i},1}), \Sigma_i^{(m)}(x_{i,j},x_{\mathrm{i},2}), \ldots, \Sigma_i^{(m)}(x_{i,j},x_{i,\mathrm{p}_i})\right]^T$ and $\Sigma_i^{(m)}(x_{i,j},x_{i,j}) = \mathcal{K}_i^{(m)}(x_{i,j},x_{i,j}) + \sigma^2$. More details about the development of a Gaussian process regression model can be found in Rasmussen and Williams (Rasmussen and Williams, 2006).

Using the above method, we can fit a GP model for each observation m of profile i. As mentioned above, the GP model gives us the covariance matrix $\left(\boldsymbol{\Sigma}_i^{(m)}\right)$ as well as the vector of predictions ($\widehat{\boldsymbol{y}}_i^{(m)}$) in design points for each sample m of profile i. As the next step, we need to estimate the IC profile i by pooling all fitted GP models. In this regard, for each profile i, the final vector of predicted values in its design points ($\widehat{\boldsymbol{y}}_i^*$) can be estimated by averaging over their multiple counterparts as follows:

$$\widehat{\boldsymbol{y}}_i^* = \frac{1}{n}\sum_{m=1}^{n}\widehat{\boldsymbol{y}}_i^{(m)} = \boldsymbol{A}_i\sum_{m=1}^{n}\widehat{\boldsymbol{y}}_i^{(m)} \tag{2.4}$$

where $\boldsymbol{A}_i = \frac{1}{n}\boldsymbol{I}_{p_i\times p_i}$ is a linear transform from the individual samples of profile i to the vector of final predictions and $\boldsymbol{I}_{p_i\times p_i}$ is the identity matrix with dimensions $p_i \times p_i$. For this vector of predictions, the following properties can be derived:

$$\mathbb{E}(\widehat{\boldsymbol{y}}_i^*) = \mathbb{E}\left(\boldsymbol{A}_i\sum_{m=1}^{n}\widehat{\boldsymbol{y}}_i^{(m)}\right) = \boldsymbol{A}_i\,\mathbb{E}\left(\sum_{m=1}^{n}\widehat{\boldsymbol{y}}_i^{(m)}\right) = \boldsymbol{A}_i\sum_{m=1}^{n}\widehat{\boldsymbol{y}}_i^{(m)} \tag{2.5}$$

$$\boldsymbol{\Sigma}_i^* = \mathrm{var}(\widehat{\boldsymbol{y}}_i^*) = \boldsymbol{A}_i\mathrm{var}\left(\sum_{m=1}^{n}\widehat{\boldsymbol{y}}_i^{(m)}\right)\boldsymbol{A}_i^T = \boldsymbol{A}_i\left(\sum_{m=1}^{n}\boldsymbol{\Sigma}_i^{(m)}\right)\boldsymbol{A}_i^T \tag{2.6}$$

Regarding the above two properties, we can estimate the IC vector of predicted values ($\widehat{\boldsymbol{y}}_i^*$) as well as the covariance matrix ($\boldsymbol{\Sigma}_i^*$) of profile i. Moreover, it is guaranteed that using the above linear transform, the resulting covariance matrix is positive definite.

Having estimated the required process parameters of each profile i using the GP regression model, a monitoring scheme is required for the incoming profiles in phase II analysis. Moreover, we can only establish separate univariate charts since the GP approach can only model the

univariate profiles separately. In this regard, the following charting statistic is proposed for each new sample r of profile i.

$$T^2_{GP_{i,r}} = \left(\boldsymbol{y}_i^{(r)} - \widehat{\boldsymbol{y}}_i^*\right)^T (\boldsymbol{\Sigma}_i^*)^{-1}\left(\boldsymbol{y}_i^{(r)} - \widehat{\boldsymbol{y}}_i^*\right) \tag{2.7}$$

where $\boldsymbol{y}_i^{(r)} = \left[y_i^{(r)}(x_{i,1}), y_i^{(r)}(x_{i,2}), \dots, y_i^{(r)}(x_{i,p_i})\right]^T$ is the vector containing the new observations of profile i, $\widehat{\boldsymbol{y}}_i^*$ is the vector of estimated predicted values of profile i and $\boldsymbol{\Sigma}_i^*$ is its estimated covariance matrix. This individual chart triggers an OC signal if $T^2_{GP_{i,r}} > L_{GP_i}$, where $L_{GP_i} > 0$ is the control limit chosen to satisfy

$$\Pr\left(T^2_{GP_{i,r}} > L_{GP_i}\right) = \alpha_i.$$

The value α_i is called the false alarm rate. If the observations of profiles are independent from each other, then $ARL_{0_i} = \frac{1}{\alpha_i}$. Thus, by selecting an appropriate value of α_i, we can achieve a specific ARL_{0_i} value for the individual GP chart i. For a given value of α_i, the control limit (i.e., L_{GP_i} here) is often determined through simulation. A general simulation procedure can be found in Qiu et al. (Qiu et al., 2010) and is also described in the following section where we determine the control limit for the MGP based monitoring scheme. In the above section, we have described how to establish a univariate GP chart for a single variable profile. If there are multiple variable profiles in the process, we can establish multiple univariate GP charts accordingly. However, because we are using multiple charts as a system to monitor the process, the overall false alarm rate of the system, denoted as α, will be different from each individual false alarm rate α_i. If the profile variables are independent from each other, the relationship between α and α_is could be simple as described in Montgomery (Montgomery, 2009):

$$\alpha = 1 - \prod_{i=1}^{k}(1 - \alpha_i) \tag{2.8}$$

Here, once we select a value of α, we can use the above equation and assume all α_is are the same to compute the α_i value. However, if the profile variables are not independent, the relationship between α and α_is could be complex and hard to identify. In this case we can use the above equation as an approximation. This is actually one weakness of using multiple univariate charts to monitor multivariate profiles. In the next section, we introduce an MGP based method for monitoring multivariate profiles simultaneously.

2.4.2. Multivariate Gaussian Process Chart

A MGP model is developed using mechanisms that can simultaneously predict different outputs considering their dependencies. The covariance matrix of a MGP model is defined by a function which considers both BPC and WPA and can be either separable or non-separable. In a separable structure, the same set of parameters is estimated for all of the variables and the correlations between different outputs are forced. However, in a non-separable structure, different outputs have different correlations which allow the model to infer the commonalities and differences between different outputs and provide more flexible predictions. Thus, the non-separable covariance matrices, in which different outputs have shared and independent features, lead to more flexibility in defining the covariance structure over the separable ones. In this study, a MGP model based on the non-separable covariance structure is proposed to model and monitor the multivariate profiles.

A MGP model, similar to the GP model, can be applied in the case that there is only one sample of each profile. However, as mentioned earlier, there are n samples of different profiles in phase I from which the IC process parameters need to be estimated. Therefore, here we need an approach to take advantage of all the IC profiles in phase I to accurately estimate one representative MGP model. In this regard, the proposed approach is based on fitting the MGP model for each in-control sample m of different profiles $\left(\boldsymbol{y}^{(m)} = \left[\boldsymbol{y}_1^{(m)^T}, \boldsymbol{y}_2^{(m)^T}, \dots, \boldsymbol{y}_I^{(m)^T}\right]^T\right)$ and then pooling all of them into one final model.

One common way to construct a non-separable MGP model is based on the kernel convolution (Higdon, 2002) which is the alternative way of constructing a GP model. To be more specific, a GP model can also be constructed by convolving the GP random variables with an arbitrary kernel. Defining $s \in \mathcal{R}^D$ as the spatial region over which the design points are considered, $f_i^{(m)}(s)$ in eq. (2.2) can be constructed through convolving a smoothing kernel $\mathcal{K}_i^{(m)}(s)$ with a continuous Gaussian white noise process $z_i^{(m)}(s)$. The resulting white noise process $f_i^{(m)}(s)$ can be defined as $cov\left(z_i^{(m)}(s), z_i^{(m)}(s')\right) = \tau_{ss'}$ where τ is the Dirac Delta function.

$$f_i^{(m)}(s) = \int_{R^D} \mathcal{K}_i^{(m)}(s-u) z_i^{(m)}(u) du \tag{2.9}$$

The resulting covariance function for $f_i^{(m)}(s)$ can be derived as follows:

$$cov\left(f_i^{(m)}(s), f_i^{(m)}(s')\right) = \int_{R^D} \mathcal{K}_i^{(m)}(s-u)\mathcal{K}_i^{(m)}(s'-u)du \tag{2.10}$$

Therefore, considering the same procedure and a set of k outputs, the general decomposition of the MGP model for the profile i of sample m can be written as follows:

$$y_i^{(m)}(s) = f_i^{(m)}(s) + \varepsilon_i^{(m)}(s) \qquad i = 1,2,\dots,k\,, \quad m = 1,2,\dots,n \tag{2.11}$$

where $f_i^{(m)}(s)$ is the process constructed through kernel convolution and $\varepsilon_i^{(m)}(s)$ is the noise term. The final objective of a non-separable MGP model is to derive processes $\left\{f_i^{(m)}(s)\right\}_{i=1}^{k}$ for each sample m that are dependent upon some common latent processes $\left\{z_u^{(m)}(s)\right\}_{u=1}^{U}$. Here, in the multivariate profile monitoring setting, we consider the case where each profile $y_i^{(m)}(s)$ is constructed by the sum of three stationary Gaussian processes. The first process is the convolution of a smoothing kernel with a unique latent function $z_i^{(m)}(s)$, the second process originates from the convolution of the output and a common latent function $z_0^{(m)}(s)$, and the third one is the measurement noise $\varepsilon_i^{(m)}(s)$. Thus, for each profile i of sample m, we have:

$$y_i^{(m)}(s) = \mathcal{K}_{ii}^{(m)}(s) * z_i^{(m)}(s) + \mathcal{K}_{0i}^{(m)}(s) * z_0^{(m)}(s) + \varepsilon_i^{(m)}(s) \qquad i = 1,2,\dots,k\,, \quad m = 1,2,\dots,n \tag{2.12}$$

where $*$ defines the kernel convolution and $\mathcal{K}_{ui}$ is the kernel connecting the latent function $z_u^{(m)}$ $(u = 0, i)$ to the output $y_i^{(m)}$. Regarding the above formulation, we have successfully considered the independent features of each output in sample m by convolving over unique latent functions, as well as the shared features among all outputs through the common dependency on $z_0^{(m)}(s)$. Thus, this structure provides enough flexibility for the multivariate profile monitoring procedure to extract the shared information among different profiles. Figure 2.2 demonstrates the MGP convolution structure described above.

As the next step, we need to choose a kernel function, and then the MGP model would be fully parametrized through its hyper-parameters. Here, the Gaussian kernel is utilized to model the structure in the MGP. The Gaussian kernels do not require many parameters to be estimated which makes them a perfect choice for the scenario in which there is scarcity of data (Xia et al., 2008). Also, their ability to model different spatial features and achieve reasonable performance in

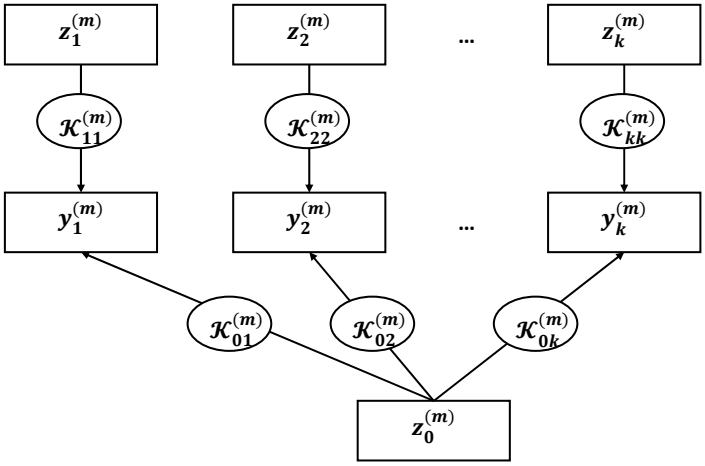

Figure 2.2. MGP convolution structure

different applications has made them a common choice in the literature (Colosimo et al., 2014, Kontar et al., 2017, Zhang et al., 2014). Thus, considering eq. (2.11), the Gaussian kernel used in this study is as follows:

$$\mathcal{K}_{ui}(s) = \frac{\rho_{ui}\sqrt{|L_{ui}|}}{\sqrt[4]{\pi^D}} exp\left(-\frac{1}{2}(s-\mu_{ui})^T L_{ui}(s-\mu_{ui})\right) \tag{2.13}$$

where $s, \mu \epsilon R^D$ and L_{ui} is a $D \times D$ positive definite matrix. Following the kernel convolution discussed in Ver Hoef and Barry (Ver Hoef and Barry, 1998) and Kontar et al. (Kontar et al., 2017), the auto and cross covariance functions considering the kernel in eq. (2.13) can be derived as follows:

$$\begin{aligned}
\Sigma_{ii}^{(m)}(s,s') &= cov_{ii}^{(m)}(s,s') \\
&= \rho_{ii,m}^2 exp\left(-\frac{1}{4}\times\frac{d^2}{L_{ii,m}^2}\right) + \rho_{0i,m}^2 exp\left(-\frac{1}{4}\times\frac{d^2}{L_{0i,m}^2}\right) + \sigma_{i,m}^2\delta_{ss'} \\
\Sigma_{ij}^{(m)}(s,s') &= cov_{ij}^{(m)}(s,s') \\
&= \rho_{0i,m}\rho_{0j,m}\sqrt{\frac{2\left|L_{0i,m}L_{0j,m}\right|}{L_{0i,m}^2 + L_{0j,m}^2}} exp\left(-\frac{1}{2}\times\frac{d^2}{L_{0i,m}^2 + L_{0j,m}^2}\right) \\
&\quad j,i = 1,2,\dots,k \quad and \quad m = 1,2,\dots,n
\end{aligned} \tag{2.14}$$

where $d = s - s'$, $\delta(.)$ is the Kronecker delta function and $\sigma_{i,m}^2$ is the variance of $\varepsilon_i^{(m)}(s)$ corresponding to the noise component of the ith profile in sample m. The detailed derivation of

eq. (2.14) can be found in Appendix A.1. The covariance matrix of the joint Gaussian process of all k profiles in sample m can be constructed as follows:

$$\boldsymbol{\Sigma}^{(m)} = \begin{bmatrix} \boldsymbol{\Sigma}_{11}^{(m)} & \cdots & \boldsymbol{\Sigma}_{1k}^{(m)} \\ \vdots & \ddots & \vdots \\ \boldsymbol{\Sigma}_{k1}^{(m)} & \cdots & \boldsymbol{\Sigma}_{kk}^{(m)} \end{bmatrix} \tag{2.15}$$

The reliability of the MGP model depends upon the correct estimation of its hyper-parameters. Considering $\theta = \{\rho, L, \sigma\}$ as the set of hyper-parameters in the above covariance matrix, the log likelihood function can be expressed as follows:

$$l\left(\theta \middle| \boldsymbol{y}^{(m)}\right) = -\frac{1}{2}\left(\boldsymbol{y}^{(m)}\right)^T\left(\boldsymbol{\Sigma}^{(m)}\right)^{-1}\boldsymbol{y}^{(m)} - \frac{1}{2}\log\left|\boldsymbol{\Sigma}^{(m)}\right| - \frac{\sum_{i=1}^{k} p_i}{2}\log\left(2\pi\right) \tag{2.16}$$

Maximizing the above equation to get θ^*, the predictive distribution for the design point j of ith profile in sample m can be expressed as follows:

$$\begin{aligned} \hat{y}_i^{(m)}\left(x_{i,j}\right)\left|\boldsymbol{y}^{(m)} \sim \mathcal{N}\right.\Big(&\boldsymbol{\eta}_{i,m}^T\left(x_{i,j}\right)\left(\boldsymbol{\Sigma}^{(m)}\right)^{-1}\boldsymbol{y}^{(m)}, \Sigma_{ii}^{(m)}\left(x_{i,j}, x_{i,j}\right) \\ &- \boldsymbol{\eta}_{i,m}^T\left(x_{i,j}\right)\left(\boldsymbol{\Sigma}^{(m)}\right)^{-1}\boldsymbol{\eta}_{i,m}\left(x_{i,j}\right)\Big) \end{aligned} \tag{2.17}$$

where $\boldsymbol{y}^{(m)} = \left[\boldsymbol{y}_1^{(m)^T}, \boldsymbol{y}_2^{(m)^T}, \ldots, \boldsymbol{y}_k^{(m)^T}\right]^T$, $\boldsymbol{\eta}_{i,m}\left(x_{i,j}\right) = \left[\boldsymbol{\eta}_{i1}^T\left(x_{i,j}\right), \ldots, \boldsymbol{\eta}_{ik}^T\left(x_{i,j}\right)\right]^T$ and $\boldsymbol{\eta}_{ii'}\left(x_{i,j}\right) = \left[\Sigma_{ii'}^{(m)}\left(x_{i,j}, x_{i',1}\right), \Sigma_{ii'}^{(m)}\left(x_{i,j}, x_{i',2}\right), \ldots, \Sigma_{ii'}^{(m)}\left(x_{i,j}, x_{i',\mathrm{p}_{i'}}\right)\right]^T$. It should be noted that the number of parameters to be estimated from the log-likelihood function is $5k$ and it increases linearly with the number of variables. In many practical cases, the number of variables that needs to be monitored simultaneously is relatively small. Therefore, the problem we are dealing with is generally not highly complex. Also, one should note that according to Rasmussen and Williams (Rasmussen and Williams, 2006) and many others, the predictions based on GP are robust to its parameters' estimate because of the Bayesian interpretation. In other words, even if the estimates of the Gaussian process parameters are sub-optimal, the prediction of the GP will be stable and relatively accurate. More details about the kernel convolution and development of a MGP model can be find at Higdon (Higdon, 2002), Ver Hoef and Barry (Ver Hoef and Barry, 1998) and Kontar et al. (Kontar et al., 2017).

The main advantage of the non-separable MGP structure as derived above is that it models the behavior of each profile considering its unique features along with the features that are shared

among all the profiles. This learning structure is essential in multivariate profile monitoring where different profiles have commonalities as well as unique behaviors.

The above procedure can be applied on every sample m of the set of IC samples in phase I. Then, we need to pool all of the developed MGP models to estimate one representative MGP model of the IC process. In this regard, like the GP approach, the final vector of predicted values ($\widehat{\boldsymbol{y}}^*$) can be estimated by averaging over its multiple counterparts as follows:

$$\widehat{\boldsymbol{y}}^* = \frac{1}{n}\sum_{m=1}^{n}\widehat{\boldsymbol{y}}^{(m)} = \boldsymbol{B}\sum_{m=1}^{n}\widehat{\boldsymbol{y}}^{(m)} \tag{2.18}$$

where $= \frac{1}{n}\boldsymbol{I}_{P\times P}$, $P = \sum_{i=1}^{k} p_i$ and $\boldsymbol{I}_{P\times P}$ represents the identity matrix with dimension $P \times P$. Here $\boldsymbol{B}$ is a linear transform from the individual samples to the vector of final predictions. For this vector of predictions, the following properties can be derived:

$$\mathbb{E}(\widehat{\boldsymbol{y}}^*) = \mathbb{E}\left(\boldsymbol{B}\sum_{m=1}^{n}\widehat{\boldsymbol{y}}^{(m)}\right) = \boldsymbol{B}\,\mathbb{E}\left(\sum_{m=1}^{n}\widehat{\boldsymbol{y}}^{(m)}\right) = \boldsymbol{B}\sum_{m=1}^{n}\widehat{\boldsymbol{y}}^{(m)} \tag{2.19}$$

$$\boldsymbol{\Sigma}^* = \mathrm{var}(\widehat{\boldsymbol{y}}^*) = \boldsymbol{B}\mathrm{var}\left(\sum_{m=1}^{n}\widehat{\boldsymbol{y}}^{(m)}\right)\boldsymbol{B}^T = \boldsymbol{B}\left(\sum_{m=1}^{n}\boldsymbol{\Sigma}^{(m)}\right)\boldsymbol{B}^T \tag{2.20}$$

Regarding the above two properties, we can estimate the IC vector of predicted values ($\widehat{\boldsymbol{y}}^*$) along with the positive definite covariance matrix ($\boldsymbol{\Sigma}^*$) of the MGP.

The IC process parameters in phase I can be estimated using the above procedure. Next, a procedure is required to monitor the stability of the incoming profiles in phase II. In this regard, we propose using the following charting statistic for each new sample r of the process.

$$T^2_{MGP_r} = \left(\boldsymbol{y}^{(r)} - \widehat{\boldsymbol{y}}^*\right)^T \boldsymbol{\Sigma}^{*-1}\left(\boldsymbol{y}^{(r)} - \widehat{\boldsymbol{y}}^*\right) \tag{2.21}$$

where $\boldsymbol{y}^{(r)} = \left[\boldsymbol{y}_1^{(r)^T}, \boldsymbol{y}_2^{(r)^T}, \dots, \boldsymbol{y}_k^{(r)^T}\right]^T$ is the vector containing the new observations of all profiles, $\widehat{\boldsymbol{y}}^* = \left[\widehat{\boldsymbol{y}}_1^{*T}, \widehat{\boldsymbol{y}}_2^{*T}, \dots, \widehat{\boldsymbol{y}}_k^{*T}\right]^T$ is the vector of estimated MGP predictions for all of the profiles and $\boldsymbol{\Sigma}^*$ is the estimation of the MGP covariance matrix. The above chart triggers an OC signal if

$$T^2_{MGP_r} > L_{MGP}$$

where the control limit (L_{MGP}) should be chosen to achieve a specified overall ARL_0 for the whole process.

In the SPC literature, it is conventionally assumed that the IC distribution of the process measurements is known. Thus, the control limit can be searched using simulation based on this distribution. However, the IC distribution is often unknown in practice and instead there is a large IC data set. In this situation, the control limit can be searched using a resampling algorithm. In this regard, in each run of the simulation, one can resample with replacement from the IC data set until the control chart signals an OC condition. Then, the ARL_0 value can be computed based on multiple runs of this simulation. The control limit is set iteratively to finally get a nominal value for the ARL_0. In this study, 10,000 simulation runs are considered to compute the ARL values.

The design and implementation of the MGP chart can be summarized in the following steps.

Step 1. Fit an MGP regression model for every sample m of IC observations using the procedure discussed in this section. The MGP model gives the vector of estimated predicted values as well as the estimated covariance matrix for each sample m.

Step 2. Estimate the IC process by averaging the vectors of estimated predicted values of IC samples obtained in step 1. Using this method, the IC vector of predicted values along with the covariance matrix of the final MGP model can be estimated as described in eq. (2.19) and eq. (2.20).

Step 3. Monitor the process by monitoring the $T^2_{MGP_r}$ statistic described in eq. (2.21) for every new sample r of the process. The incoming samples are in-control if their corresponding $T^2_{MGP_r}$ statistics are less than a prespecified control limit L_{MGP}.

The MGP chart proposed here offers a key advantage. Specifically, it is established based on the large covariance matrix which captures the cross-correlations between different profiles in each sample along with the correlation within each profile. This feature is crucially important in most applications where different sensors monitor a common underlying process and the measurements are made in consecutive time intervals.

2.5. Numerical Study

In this section, the performance of the multivariate profile monitoring procedures proposed above will be investigated. First, we start with the scenario that two signals are monitored simultaneously where the intrinsic noise in eq. (2.1) is assumed to be independent and identically distributed. Then, the existence of the autocorrelation in the noise in the two-profile case will be examined. We will

also consider the situation where we are monitoring more than two profile variables. Moreover, the case of shift in between profile correlation will be investigated.

For the sake of completeness, in the simulation study, we will compare the performance of the proposed MGP chart with the conventional T^2 chart as shown in Mestek et al. (Mestek et al., 1994) for monitoring each univariate non-parametric profile. For monitoring each new sample r of the profile i we have:

$$T_{i,r}^2 = \left(\boldsymbol{y}_i^{(r)} - \bar{\boldsymbol{y}}_i\right)^T \boldsymbol{S}_i^{-1} \left(\boldsymbol{y}_i^{(r)} - \bar{\boldsymbol{y}}_i\right) \tag{2.22}$$

where $\boldsymbol{y}_i^{(r)}$ is a vector containing the response values of rth new sample of profile i and $\bar{\boldsymbol{y}}_i = \left[\bar{y}_i(x_{i,1}), \bar{y}_i(x_{i,2}), \dots, \bar{y}_i(x_{i,p_i})\right]^T$ is a vector of in-control response averages over the n IC samples of profile i in its design points. Moreover, $\boldsymbol{S}_i$ is the pooled sample covariance matrix of profile i. This individual T^2 control chart triggers an OC signal for sample r if

$$T_{i,r}^2 > L_i$$

where $L_i > 0$ is the control limit chosen to achieve a specific ARL_{0_i} value for the individual T^2 control chart i. Here, as with the GP control chart, the control limit of each individual T^2 chart should be chosen to achieve a specified overall ARL_0 value for the system. It is worth mentioning that this chart typically requires a large number of IC observations in order to give an accurate estimate of the covariance matrix. Moreover, it should be noted that using the conventional T^2 chart has two limitations. First, the number of IC samples (n) should be more than the number of design points p_i; otherwise, the sample covariance matrix of profile i would be singular. Also, it requires fixed design points to construct the covariance matrix and monitor the incoming profiles.

In Section 2.5.5, we will also consider an "aggregated" T^2 chart based on stacking all variables of each observation as follows:

$$T_r^2 = \left(\boldsymbol{y}^{(r)} - \bar{\boldsymbol{y}}\right)^T \boldsymbol{S}^{-1} \left(\boldsymbol{y}^{(r)} - \bar{\boldsymbol{y}}\right) \tag{2.23}$$

where $\bar{\boldsymbol{y}} = [\bar{\boldsymbol{y}}_1^T, \bar{\boldsymbol{y}}_2^T, \dots, \bar{\boldsymbol{y}}_k^T]^T$. Here, $\boldsymbol{S}$ is the pooled sample covariance matrix of all the profiles. The control limit for this chart can also be chosen to achieve a specific ARL_0 value using the procedure discussed previously.

It should be noted that the IC ARL is set to 370 in the simulation study and all the ARL values are reported based on the average of 10,000 simulations. Also, as indicated in the previous sections, both GP and MGP charts have enough flexibility to observe different design points for different

profiles; however, the T^2 charts can only be used for the case of fixed design points. Thus, the design points are assumed to be fixed and same in different profiles of a sample ($p_i = p$) in order to be able to compare the performance of the different profile monitoring schemes.

2.5.1. Two-variable profile monitoring

This section investigates the performance of the proposed profile monitoring schemes for two-variable profiles. To illustrate the performance of different charts, our simulations cover two models: a trigonometric model and a quadratic model. The simulation study is based on the two phases of SPC as mentioned earlier. In each model setting, n in-control profiles are generated in phase I. Then, using the procedure for each chart, the IC process parameters are estimated and the corresponding chart is established to monitor the in-coming profiles in phase II. For each model, three values of n are considered. This includes one sparse case with the least possible number of IC samples allowed by the T^2 chart, another case with moderate number of IC samples, and a dense case with large number of IC samples. For each model, three types of OC situations are considered. The first OC model investigates the performance of the proposed charts in the situation where a mean shift in the process has occurred. The second OC model deals with the shift in the noise of the process. In the third OC model, it is assumed that there is a mean shift in a segment of the process.

First, in the trigonometric model setting, we assume that the underlying process is characterized by the following two signals:

$$\begin{aligned} y_1^{(m)}(x_{1,j}) &= 5 + 2\cos(x_{1,j}) + \varepsilon_1^{(m)}(x_{1,j}) \qquad m = 1,2,\dots,n \\ y_2^{(m)}(x_{2,j}) &= -5 + 2\sin(x_{2,j}) + \varepsilon_2^{(m)}(x_{2,j}) \qquad m = 1,2,\dots,n \end{aligned} \tag{2.24}$$

where $\sigma_1 = \sigma_2 = 0.5$. In this model it is assumed that 30 design points are equally distributed over $[0,2\pi]$. Table 2.1 presents the OC ARL of three charts in the case of mean shift, noise shift and segment shift in this model for different number of IC observations (n). For the segment shift, it is considered that a mean shift occurred in the middle segment of each profile, as displayed in figure 2.3.

Results from table 2.1 show that in the sparse setting with $n = 31$ IC samples, the MGP chart outperforms both the GP and T^2 charts in different shifts in the mean of the process. Moreover, considering mean shift, the T^2 chart's performance is worse than the GP chart in this setting. As

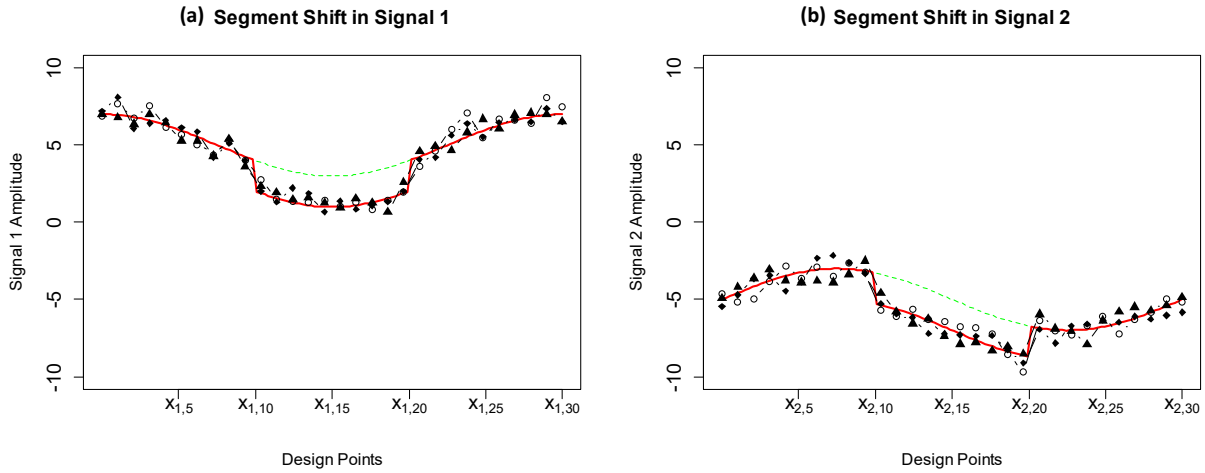

Figure 2.3. Segment shift in the trigonometric model

mentioned earlier, the T^2 chart requires a high number of IC samples in phase I in order to accurately estimate the covariance matrix; therefore, we would expect these results. Table 2.1 also shows the trend in the performance of these charts in different mean shift situations with increase in the number of IC samples (n). The results show that, generally, an increase in the number of IC samples (n) leads to an improvement in the performance of the charts in terms of ARL_1 in different shifts in the mean of process. Specifically, the performance of the T^2 chart considerably improves with the increase in the number of IC samples to the extent that in the case of $n = 100$ IC samples, it performs better than the other charts in all of the mean shift situations.

From table 2.1, it can be seen that when there is a shift in the noise of the process, the MGP chart consistently performs better than the GP and T^2 charts. Moreover, it can be seen that the GP chart's performance is relatively better than the T^2 chart. This is, in fact, due to the power of GP based models in uncertainty quantification and capturing the cross-correlation between the two profiles. In this OC situation, as it can be seen from table 2.1, increasing n improves the performance of all charts; nevertheless, the MGP chart outperforms other charts in different cases with high number of IC samples. Further, when only a segment of the profiles has shifted, the MGP chart outperforms the GP and T^2 charts in different amounts of shift. Here also, although increasing n improves the performance of the charts, the MGP chart's performance is relatively better than the others.

Table 2.1. ARL_1 comparison of the three charts in the trigonometric model

		n=31			n=50			n=100		
	Shift	GP	MGP	T^2	GP	MGP	T^2	GP	MGP	T^2
Mean	0.1	341.3	278.3	355.6	244.8	234.5	318.5	242.6	230.6	109.6
	0.2	184.1	117.1	302.0	117.6	87.2	144.2	115.5	80.1	67.9
	0.3	69.0	33.1	217.2	41.7	23.6	48.8	39.7	21.1	13.0
	0.4	20.2	8.4	138.2	13.1	6.0	15.2	15.7	6.0	5.0
	0.5	6.1	2.6	84.5	4.2	2.1	5.5	4.1	2.0	2.0
Noise	0.01	215.9	178.1	271.0	184.0	156.5	189.0	172.7	147.4	175.6
	0.02	133.0	93.5	191.7	120.0	89.5	185.9	107.1	87.2	146.9
	0.03	78.2	51.2	188.5	64.3	48.7	149.9	64.1	45.2	98.9
	0.04	49.4	31.6	157.7	42.0	30.1	112.9	41.0	30.8	67.2
	0.05	32.8	19.9	130.1	27.6	18.7	86.2	25.3	17.8	48.2
Segment	0.1	392.8	346.7	358.4	319.3	314.1	340.6	305.6	299.5	315.8
	0.2	320.9	266.4	296.7	231.6	219.3	267.6	229.7	205.0	222.3
	0.3	186.0	137.0	197.5	146.9	116.7	193.4	142.3	114.2	122.7
	0.4	121.0	80.5	214.6	85.4	58.2	84.1	84.3	54.6	61.5
	0.5	65.0	34.8	176.6	45.1	24.8	41.2	42.6	24.7	29.5

Next, we consider a quadratic setting in which the underlying process is characterized with two signals as follow.

$$\begin{aligned} y_1^{(m)}(x_{1,j}) &= 1 + 5x_{1,j} + x_{1,j}^2 + \varepsilon_1^{(m)}(x_{1,j}) \quad && m = 1,2,\dots,n \\ y_2^{(m)}(x_{2,j}) &= 2x_{2,j}^2 + \varepsilon_2^{(m)}(x_{2,j}) && m = 1,2,\dots,n \end{aligned} \tag{2.25}$$

where $\sigma_1 = \sigma_2 = 1$. The measurements are made in 10 design points equally over $[0,10]$. The OC ARL of three charts in the case of mean shift, noise shift and segment shift in this model for different number of IC observations (n) are summarized in table 2.2. Regarding the segment shift, here also, it is assumed that a mean shift occurred in the middle segment of each profile.

In the quadratic model, also, the MGP chart outperforms the other charts in the sparse setting when dealing with the mean shift in the process. Moreover, in this setting, the GP chart's performance is better than that of the T^2 chart. As expected, increasing the number of IC samples (n) in phase I improves the performance of the charts, to the extent that the T^2 chart outperforms the other charts in a dense setting with $n = 50$ IC samples in different mean shift situations.

Table 2.2, furthermore, confirms the superiority of the GP based charts in detecting the noise shift in different settings with different number of IC samples. Especially, it can be seen that the MGP chart which considers the cross-correlation structure of two profiles performs relatively better than the GP chart. Regarding segment shift, the similar trend as the trigonometric model can be seen where the MGP chart outperforms the other charts.

Table 2.2. ARL_1 comparison of the three charts in the quadratic model

		n=11			n=30			n=50		
	Shift	GP	MGP	T^2	GP	MGP	T^2	GP	MGP	T^2
Mean	0.6	122.0	81.9	339.9	119.3	80.1	208.5	120.1	80.3	51.1
	0.7	81.7	45.4	334.1	79.8	45.3	154.9	77.3	44.5	31.7
	0.8	53.9	29.9	318.9	52.7	29.6	89.3	51.6	28.0	19.7
	0.9	35.9	18.2	303.8	35.3	17.7	58.9	35.1	16.8	12.5
	1	22.7	10.6	283.0	21.9	10.3	23.3	20.9	10.2	8.1
Noise	0.02	265.4	242.6	263.6	248.5	235.0	259.1	248.7	233.5	240.6
	0.04	178.9	156.6	222.1	169.5	154.7	209.0	168.6	129.2	206.4
	0.06	128.0	109.1	179.7	122.9	107.7	162.0	121.4	104.5	133.7
	0.08	95.0	76.1	145.1	91.4	75.6	125.1	91.9	75.4	102.9
	0.1	70.7	56.4	122.7	70.3	54.8	116.8	70.7	54.8	78.4
Segment	0.6	182.3	143.0	422.9	112.9	109.3	386.9	94.6	90.6	276.9
	0.7	148.1	105.2	390.3	128.6	85.7	278.1	61.9	55.4	213.3
	0.8	114.7	77.8	344.4	64.1	34.2	222.2	39.3	32.8	170.7
	0.9	86.5	54.2	299.2	47.6	23.6	176.1	25.0	19.5	126.1
	1	67.1	38.7	261.8	35.6	16.6	132.9	16.3	11.8	90.1

Next, the effect of the number of design points on the performance of the three monitoring procedures is investigated. In this regard, for each model, the setting with large number of IC samples is considered. For this setting, we increase the number of design points in both trigonometric and quadratic models. In order to obtain a fair comparison, we focus on the OC model with shift in the mean and noise of the process. Table 2.3 and table 2.4 show the results of this analysis for the trigonometric and the quadratic models.

The results from table 2.3 and table 2.4 show that increasing the number of design points improves the performance of the GP and MGP charts. As mentioned earlier, the covariance matrix in the GP and MGP charts is calculated based on the radial basis kernel functions. Thus, increasing

the number of design points decreases the distance between the points which leads them to learn better from each other, while large number of design points merely increases the dimensionality for the T^2 chart which results in the loss of efficiency for this chart.

Table 2.3. The effect of number of design points in the trigonometric model

Trigonometric model with n=100 IC samples							
		30 design points			50 design points		
	Shift	GP	MGP	T^2	GP	MGP	T^2
Mean	0.1	242.6	230.6	109.6	230.7	225.1	278.5
	0.2	115.5	80.1	67.9	106.4	76.7	112
	0.3	39.7	21.1	13.0	32.1	16.8	32.1
	0.4	15.7	6.0	5.0	8.2	3.8	8.2
	0.5	4.1	2.0	2.0	2.5	1.5	2.7
Noise	0.01	172.7	147.4	171.6	165.8	146.8	238.5
	0.02	107.1	87.2	146.9	87.1	66.3	155.6
	0.03	64.1	45.2	98.9	47.0	33.4	102.4
	0.04	41.0	30.8	67.2	27.6	18.3	67.1
	0.05	25.3	17.8	48.2	17.0	10.7	47.5

Table 2.4. The effect of number of design points in the quadratic model

		Quadratic model with n=50 IC samples					
		10 design points			30 design points		
	Shift	GP	MGP	T^2	GP	MGP	T^2
Mean	0.6	120.1	80.3	51.1	63.2	30.9	31.0
	0.7	83.3	47.5	31.7	36.1	15.5	17.5
	0.8	56.6	28.0	19.7	19.7	7.9	10.8
	0.9	35.6	16.8	12.5	11.2	4.3	6.5
	1	22.9	10.2	8.1	6.2	2.5	4.2
Noise	0.02	248.7	233.5	240.6	208.3	169	262.2
	0.04	168.6	129.2	206.4	121.3	88.8	198.9
	0.06	121.4	104.5	133.7	72.4	49.2	147.2
	0.08	91.9	75.4	102.9	46.1	30.5	113.0
	0.1	70.7	54.8	78.4	30.5	18.7	88.7

2.5.2. Two-variable profile monitoring with autocorrelation

In this section, we investigate the performance of the proposed profile monitoring schemes in the presence of autocorrelation. In this regard, our simulation is based on the two model settings introduced in the previous section. The main difference here is that the noise term in eq. (2.1) within each profile is not iid anymore and the successive noise terms are correlated. Specifically, we consider the case where the current noise term depends on its previous lagged noise term. Thus, the following process is assumed for the structure of the noise term:

$$\varepsilon_i^{(m)}(x_{i,j}) + \phi\varepsilon_i^{(m)}(x_{i,j-1}) \tag{2.26}$$

As for the trigonometric model, the two profiles are defined using the eq. (2.24) with 30 equally spaced design points over $[0,2\pi]$. Moreover, it is assumed that $\phi = 0.5$ defines the coefficient of autocorrelation in eq. (2.26). Again, using the same logic in the previous section, n IC samples of two-variable profiles with autocorrelation are generated in phase I. Then, the IC parameters are estimated and the monitoring is performed according to the procedure for each chart. Table 2.5 gives the ARL_1 values for the specified OC models of three charts in the trigonometric model under the sparse and dense settings.

Table 2.5. ARL_1 comparison of the three charts in the trigonometric model with autocorrelation

		n=31			n=100		
	Shift	GP	MGP	T^2	GP	MGP	T^2
Mean	0.1	289.9	279.7	358.1	277.0	265.4	278.8
	0.2	150.5	123.7	329.8	143.1	112.1	149.5
	0.3	63.7	38.3	274.7	32.4	30.9	70.6
	0.4	23.5	11.4	220.9	21.1	9.4	30.7
	0.5	8.6	4.0	172.1	8.1	3.2	13.2
Noise	0.01	210.7	204.0	299.4	201.3	192.3	245.9
	0.02	127.8	116.7	246.9	113.7	101.4	165.8
	0.03	81.3	64.8	202.5	81.4	60.0	109.9
	0.04	54.3	40.6	171.9	51.7	37.0	75.1
	0.05	36.6	26.1	144.5	36.7	23.4	53.8
Segment	0.1	294.8	284.3	347.1	281.3	253.0	314.4
	0.2	155.0	152.5	277.1	137.9	128.4	240.8
	0.3	86.7	82.5	190.9	81.9	71.4	162.1
	0.4	35.5	29.1	115.7	34.9	29.6	103.4
	0.5	16.7	12.2	65.2	17.7	12.6	59.4

Results from table 2.5 show that in the sparse setting with $n = 31$ IC samples, the MGP chart performs better than the other charts in the presence of autocorrelation. Also, the GP chart's performance is better than the T^2 chart in terms of ARL_1. This, in fact, originates from the nature of the Gaussian process models that can capture the correlations within each profile. Although increasing the number of IC samples generally leads to improvement of the charts, even with $n = 100$, the MGP chart performs relatively better than the other charts. Moreover, these results show that, in the presence of autocorrelation, the GP chart performs relatively better than the T^2 chart in the dense setting with $n = 100$ IC samples.

Table 2.6. ARL_1 comparison of the three charts in the quadratic model with autocorrelation

		n=11			n=50		
	Shift	GP	MGP	T^2	GP	MGP	T^2
Mean	0.6	80.4	65.2	509.7	70.8	34.9	113.0
	0.7	54.7	41.3	481.5	42.9	19.5	81.2
	0.8	36.7	25.4	462.7	27.0	10.8	57.5
	0.9	24.7	16.3	431.2	16.3	6.2	40.6
	1	16.7	10.7	389.9	9.9	3.9	28.0
Noise	0.02	240.2	224.3	303.1	209.5	188.5	257.6
	0.04	173.4	151.6	247.1	125.9	99.9	191.8
	0.06	125.3	108.2	205.9	81.4	60.8	146.3
	0.08	96.4	77.4	165.6	53.7	39.2	109.8
	0.1	72.3	55.3	140.0	36.3	25.0	82.7
Segment	0.6	160.2	158.1	406.4	95.3	88.0	161.0
	0.7	120.7	120.2	395.7	67.5	57.4	129.7
	0.8	94.7	93.8	389.9	46.9	38.0	98.5
	0.9	71.9	68.2	399.5	31.1	24.3	75.6
	1	55.5	48.6	391.1	20.8	15.7	54.8

Next, the performance of the proposed charts in the presence of autocorrelation is investigated for the quadratic model. In this regard, the functions in eq. (2.25) are considered and it is assumed that the design points are equally distributed over $[0,10]$. Here also, $\phi = 0.5$ is considered as the IC parameter. The results of simulation for this model are given in table 2.6.

The results in table 2.6 show the similar trend in the performance of the three charts as with the trigonometric model. Here again, in the sparse setting, the MGP chart has a superior performance

in terms of ARL_1 compared to the other charts. Moreover, as expected, the GP chart performs better in the sparse setting than the T^2 chart. Also, in the dense setting with $n = 50$ IC samples, the MGP chart's performance is relatively better than that of the other two charts.

2.5.3 Monitoring profiles with more than two-variables

In this section, we investigate the performance of the proposed charts in the scenario of more than two-variable profiles. In this regard, we consider the cases where the underlying process is defined through three or four variables. First, let us consider that the following three functions characterize the underlying process under consideration:

$$\begin{aligned} y_1^{(m)}(x_{1,j}) &= 5 + 2\cos(x_{1,j}) + \varepsilon_1^{(m)}(x_{1,j}) \quad m = 1,2,\dots,n \\ y_2^{(m)}(x_{2,j}) &= -5 + 2\sin(x_{2,j}) + \varepsilon_2^{(m)}(x_{2,j}) \quad m = 1,2,\dots,n \\ y_3^{(m)}(x_{3,j}) &= 2e^{-0.2x_{3,j}}\cos(x_{3,j}) + \varepsilon_3^{(m)}(x_{3,j}) \quad m = 1,2,\dots,n \end{aligned} \tag{2.27}$$

where $\sigma_1 = \sigma_2 = \sigma_3 = 0.5$ are iid noises and the measurements are made in 30 equally spaced design points over $[0,2\pi]$. Following the general procedure in this study, $n = 50$ IC samples of the above three-variable profiles are generated and the IC parameters are estimated. In phase II, the performance of the three proposed charts are compared in terms of ARL_1. Next, we consider a case with four-variable profiles where the following function is added to the set of functions defined in eq. (2.27).

$$y_4^{(m)}(x_{4,j}) = 10 + 2e^{-0.2x_{4,j}}\sin(x_{4,j}) + \varepsilon_4^{(m)}(x_{4,j}) \quad m = 1,2,\dots,n \tag{2.28}$$

For the two scenarios explained here, different OC situations including shifts in the mean, noise and the segment containing 10 design points in the middle of each profile is considered. The results for these shifts are summarized in table 2.7.

The results in table 2.7 show that in the case of monitoring more than two variables, the performance of the MGP chart is significantly better than that of the GP and T^2 charts. First, it can be seen that when monitoring both three signals and four signals, the MGP chart consistently outperforms the other two charts in different OC shifts. Moreover, it can be seen that increasing the number of signals further enhances the MGP chart where with the same amount of shift in the four signal case, the ARL_1 for the MGP chart is less than its corresponding value for the three signal case. However, looking at the results for the GP and T^2 charts, it can be concluded that the

inverse relationship holds and increasing the number of signals leads to a decrease in their performance.

Table 2.7. ARL_1 performance of monitoring with three signals and four signals

		Three Signals			Four Signals		
	Shift	GP	MGP	T^2	GP	MGP	T^2
Mean	0.1	243.1	224.0	269.1	277.3	206.3	301.6
	0.2	118.9	68.1	158.0	136.4	56.9	139.5
	0.3	40.3	14.2	74.4	49.1	10.2	49.2
	0.4	11.8	3.4	29.2	13.9	2.5	13.5
	0.5	3.7	1.4	11.3	4.1	1.2	4.3
Noise	0.01	175.1	143.7	238.2	190.1	132.5	276.9
	0.02	99.8	69.1	170.3	111.6	58.4	196.0
	0.03	59.8	34.5	123.2	67.8	29.0	151.4
	0.04	37.7	19.6	91.1	41.9	15.1	113.0
	0.05	24.3	12.0	69.6	27.0	9.1	87.3
Segment	0.1	286.5	285.0	307.6	333.1	287.8	363.9
	0.2	217.2	180.9	232.4	260.5	165.6	298.1
	0.3	134.9	85.9	149.9	165.4	68.8	208.0
	0.4	71.5	34.6	92.5	91.7	25.6	142.4
	0.5	35.5	13.2	52.6	44.2	8.8	87.9

2.5.4 Two-variable profile monitoring with covariance shift

In this section, we investigate the performance of profile monitoring schemes in the case where there is a shift in the between-profile correlation of IC profiles. In this regard, in the trigonometric model setting, we generate the initial IC samples from a multivariate Gaussian process with known IC parameters as stated in eq. (2.14) with 30 equally spaced design points over $[0,2\pi]$. Specifically, it is assumed that the vector of IC parameters is $\{\rho_{11}, L_{11}, \rho_{22}, L_{22}, \rho_{01}, L_{01}, \rho_{02}, L_{02}, \sigma_1, \sigma_2\} = \{2,\ 1, 2, 1, 4, 1.5, 4, 1.5, 0.5, 0.5\}$. Next, using the same logic as in previous sections, n IC samples of two-variable profile are generated in phase I. Then, using the proposed methods, the estimated IC model is built to monitor the new incoming samples. Moreover, in order to define the required OC condition, we change the corresponding cross-correlation parameters (ρ_{01}) of the covariance function. Table 2.8 gives the ARL_1 values of the OC model for the three charts.

Results from the above table show that MGP chart always performs better than the other charts where there is a shift in between-profile correlation. This is mostly because of the non-separable covariance function of the MGP method that explicitly considers the cross-correlation between different profiles of a sample.

Table 2.8. ARL_1 performance in covariance shift

	n=31			n=50			n=100		
Shift	GP	MGP	T^2	GP	MGP	T^2	GP	MGP	T^2
0.2	390.5	288.5	360.7	379.5	279.0	333.1	313.2	268.8	324.6
0.4	232.6	190.3	344.5	229.9	186.7	278.2	192.5	179.9	270.6
0.6	112.1	104.6	318.8	113.3	101.2	233.7	106.0	88.4	209.4
0.8	57.2	45.3	273.5	60.8	45.1	164.3	55.0	40.6	134.4
1	32.3	20.5	231.6	32.4	20.8	98.7	29.9	18.8	68.3

2.5.5 Comparison of the MGP chart with the "aggregated" T^2 chart

This section aims at comparing the performance of the MGP chart with the T^2 chart as proposed in eq. (2.23). In this regard, two-variable profiles in both trigonometric and quadratic model settings are considered. The same logic as discussed in section 2.5.1 is also used here to generate the IC samples. Considering the cases of moderate and large number of IC samples, the estimated IC models are built in order to monitor the new incoming samples. The OC ARL of two charts in the case of mean shift, noise shift and segment shift are summarized in table 2.9.

The results from table 2.9 show that the MGP chart outperforms the T^2 chart described in eq. (2.23) in different OC conditions. The only exception is the case of mean shift when the number of IC samples is large. It should be noted that the MGP method can capture the cross-correlation among different profile variables through the shared kernel parameters. Such parameters are estimated based on the maximum likelihood method. On the other hand, the T^2 chart captures the cross-correlation by simply pooling all the observations. The T^2 often requires a large number of IC samples in phase I in order to accurately estimate the covariance matrix. Therefore, in the case of mean shift when there is a large number of IC samples, the T^2 chart performs slightly better than the MGP chart.

Table 2.9. ARL_1 comparison of the MGP and T^2 charts in the trigonometric and quadratic model settings

	Trigonometric Model					Quadratic Model				
		n=61		n=100			n=30		n=50	
	Shift	MGP	T^2	MGP	T^2	Shift	MGP	T^2	MGP	T^2
Mean	0.1	285.9	357.6	230.6	224.0	0.6	88.1	118.6	80.3	61.7
	0.2	114.0	229.8	80.1	80.3	0.7	44.2	83.2	44.5	37.2
	0.3	31.5	198.4	21.1	25.9	0.8	29.7	57.6	28.0	23.2
	0.4	7.9	189.3	6.0	9.0	0.9	16.4	40.0	16.8	14.1
	0.5	2.5	185.0	2.0	3.8	1	11.6	27.5	10.2	8.8
Noise	0.01	284.3	381.0	147.4	248.1	0.02	245.4	284.5	233.5	273.9
	0.02	113.4	390.8	87.2	182.2	0.04	162.3	221.6	129.2	196.9
	0.03	31.5	397.5	45.2	130.8	0.06	111.5	183.2	104.5	146.9
	0.04	7.8	401.0	30.8	99.3	0.08	77.6	144.7	75.4	109.7
	0.05	2.5	379.0	17.8	76.0	0.1	55.8	114.0	54.8	83.6
Segment	0.1	380.0	366.3	299.5	330.7	0.6	90.0	344.9	90.6	173.6
	0.2	276.7	287.1	205.0	241.5	0.7	60.6	334.2	55.4	132.5
	0.3	158.6	254.5	114.2	148.9	0.8	43.2	310.9	32.8	99.5
	0.4	79.9	232.7	54.6	80.6	0.9	30.0	287.3	19.5	70.9
	0.5	35.3	215.0	24.7	41.9	1	21.6	265.9	11.8	50.2

2.6. Application to a Real-World Case Study

In this section, the application of the proposed profile monitoring procedures on a real-world case study of an ice machine is demonstrated. In an ice machine, different sensors monitor different aspects of the ice making process. Specifically, the temperature of the liquid refrigerant (evaporator inlet temperature), temperature of the vapor refrigerant (evaporator outlet temperature), the liquid line temperature and compressor discharge temperature are considered to be the main drivers of the performance of the ice making process. These temperature signals for three consecutive working cycles of the ice machine are demonstrated in figure 2.1.

Regarding the ice machine, data are collected every one minute during the machine's operation. Furthermore, the ice making process duration is not fixed from cycle to cycle and depends on some factors including the ambient temperature, the quality of water, etc. However, in order to make a fair comparison between different approaches, a fixed number of design points in different cycles are required. Thus, using an interpolation technique for each individual sample of a four-variable profile, the design points have been fixed at 12 equally spaced time points in the process. Figure

2.4 shows three samples of the temperature signals along with the MGP estimate of the IC profile functions.

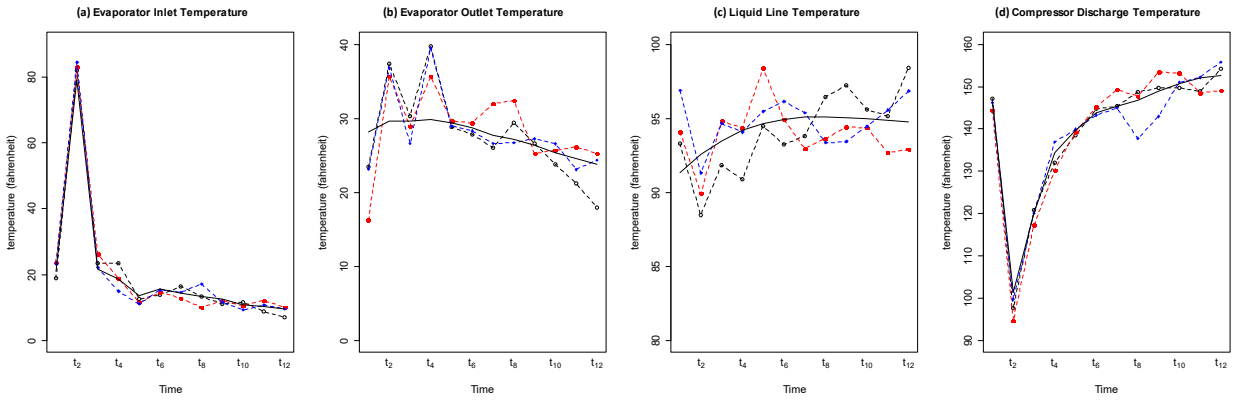

Figure 2.4. Three samples of the temperature signals (dashed lines) and the MGP estimate of the IC profile functions (solid curve).

The ice machine data set contains 148 samples, each with four temperature variables measured in 12 equally spaced design points. The first 20 samples of data set have been considered for the phase I analysis. The IC parameters are then estimated by applying the specific procedures of the proposed charts on the first 20 samples. The resulting MGP estimated IC profiles for the temperature signals are displayed in figure 2.4.

Next, we construct the proposed control charts for phase II profile monitoring by fixing the IC ARL at 200. In order to compare the monitoring procedures, we consider the scenario that a shift in the mean or the middle segment of the profile variables has occurred. The OC simulations are done based on the MGP estimate of the four variables and the results for 10,000 runs are summarized in table 2.10.

Table 2.10. Mean shift and segment shift analysis for case study data set

	Mean shift				Segment shift		
Shift	GP	MGP	T^2	Shift	GP	MGP	T^2
0.5	161.3	152.9	209.5	0.5	187.9	184.7	210.3
1	102.1	94.3	205.0	1.0	147.1	145.1	207.8
1.5	51.3	50.5	201.5	1.5	117.0	106.1	200.7
2	29.0	22.6	195.5	2.0	83.5	70.4	197.4
2.5	16.0	10.0	186.3	2.5	59.0	44.3	193.0

It can be seen from table 2.10 that the MGP chart outperforms the GP and T^2 charts in different mean shift and segment shift situations. This confirms the results we obtained in the simulation study that, for profile monitoring with more than two variables, the MGP chart performance is better than that of the GP and T^2 charts.

Next, we establish a control chart based on monitoring the coefficients of the MGP model as introduced in Li, Y. et al. (Li et al., 2017). Using the 20 initial samples, the coefficients and the Fisher information matrix of the coefficients of MGP model are estimated. We use a T^2 statistic to monitor the coefficients of the MGP model with the Fisher information matrix as the covariance matrix. Again, the ARL_0 is fixed at 200. Table 2.11 demonstrates the OC simulation results in this case.

Table 2.11. ARL_1 performance of monitoring the coefficients of MGP model in case study

	Mean Shift		**Segment Shift**
Shift	Coefficient based MGP chart	Shift	Coefficient based MGP chart
0.5	163.5	0.5	170.8
1	159.8	1	170.2
1.5	154.6	1.5	169.4
2	150.4	2	166.9
2.5	149.9	2.5	165.7

Comparing the results of table 2.11 with table 2.10, one can see that the profile monitoring scheme based on monitoring the coefficients of MGP model is less efficient than the MGP chart proposed in this study. This further confirms the superiority of our proposed MGP monitoring scheme.

In addition to the above comparison, we performed an analysis based on using the first 20 and 104 samples of data to estimate the IC parameters and to find the control limit, respectively. The control limit is set using the procedure discussed in the simulation study section and considering a type I error rate of 0.04. The remaining 44 samples are also used to test the charts discussed in this study as well as the chart based on monitoring the coefficients of the MGP model. The MGP, GP and T^2 charts for samples 105 through 148 are shown in figure 2.5 and figure 2.6. The solid line in each chart represents the control limit of that specific chart.

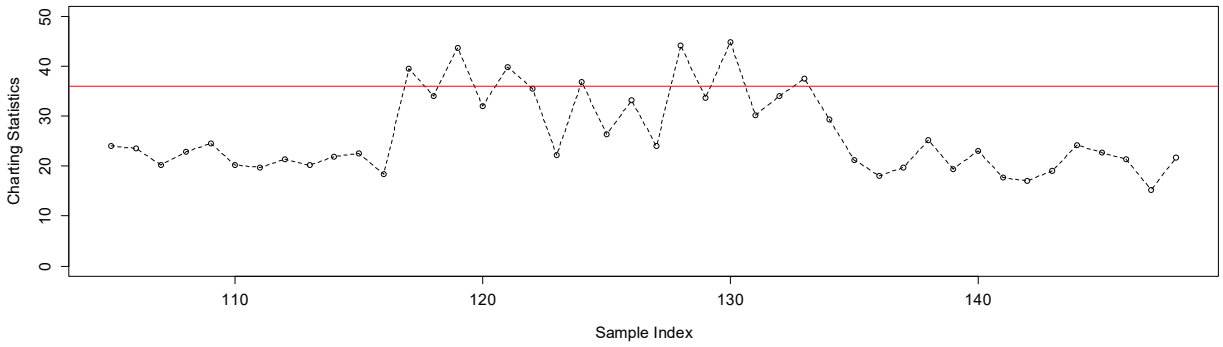

Figure 2.5. MGP chart for the ice machine data set

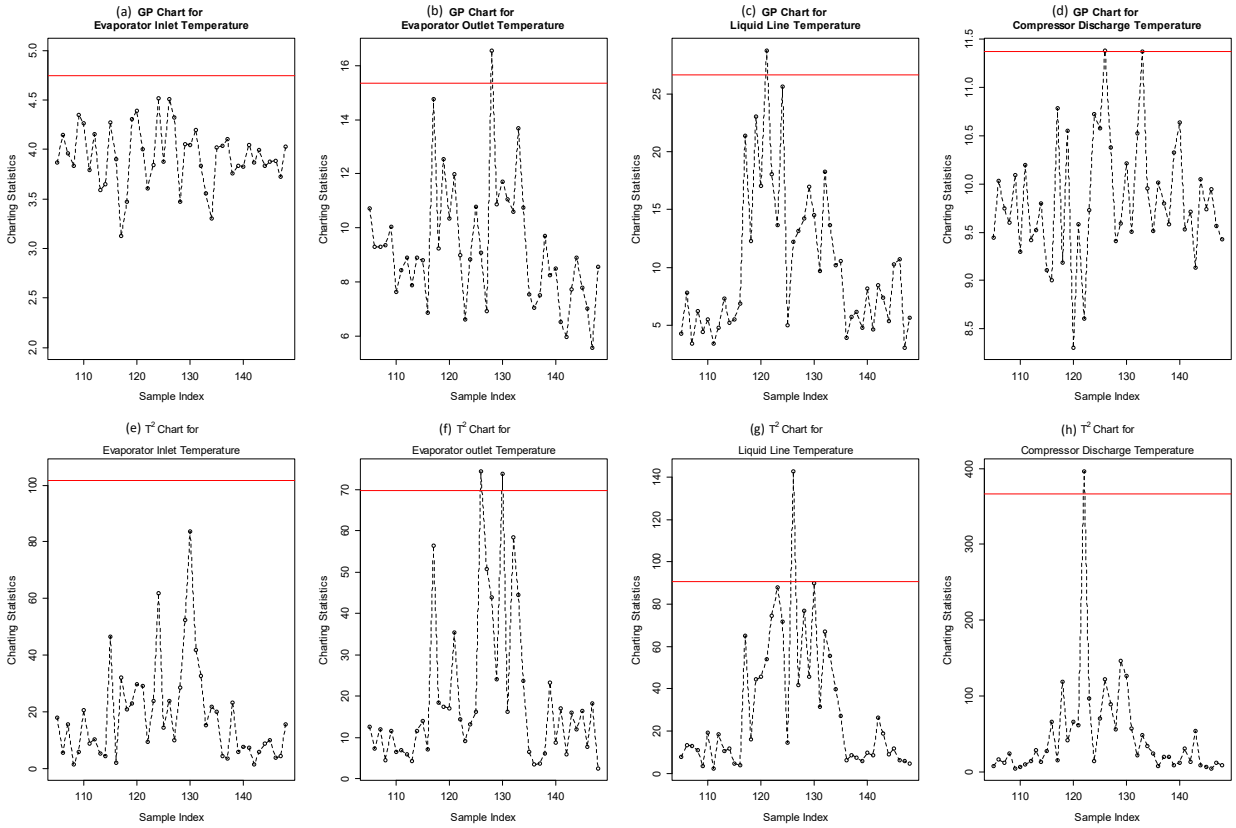

Figure 2.6. Univariate GP and T^2 charts for the ice machine data set

From figure 2.5, it can be seen that the MGP chart first gives an OC signal in the 117th sample. Also, an OC condition is shown in the 119th, 121th, 124th, 128th, 130th and 133th sample. However, regarding the GP chart, it first signals OC in sample 121 where the liquid line temperature chart is out of control. Next, this chart gives OC signals in samples 126, 128 and 133. As for the T^2 chart,

it gives its first OC signal in sample 122 where the compressor discharge temperature chart is out of control. This chart signals out of control condition in samples 126 and 130 as well.

The charting statistics based on monitoring the coefficients of the MGP model for samples 105 through 148 are shown in figure 2.7. As can be seen from figure 2.7, this control chart can only detect an OC condition in sample 110 and remains in-control for the rest of samples. In contrast, the profile monitoring procedures introduced earlier in this study show a change in the ice making process between the 117th and 133th samples.

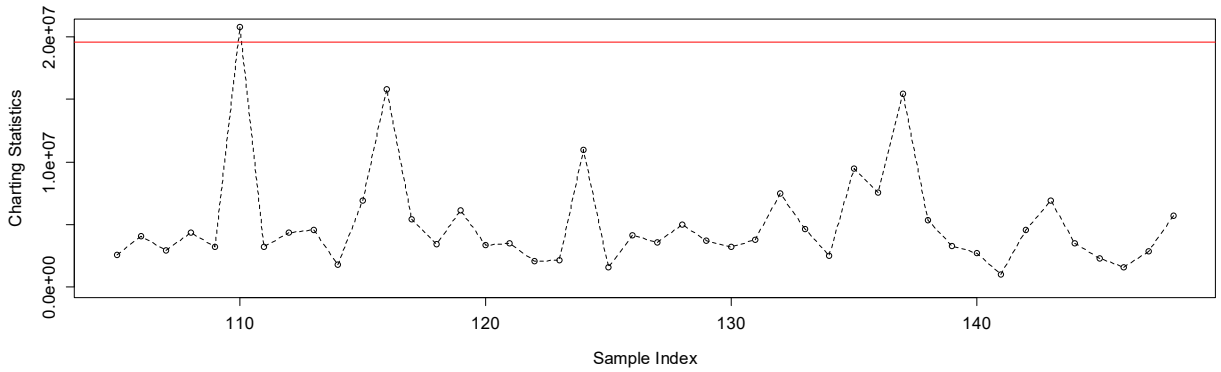

Figure 2.7. Chart of monitoring the coefficients of MGP model for the ice machine data set

The case study analysis shows that the MGP chart proposed in this chapter can detect an OC condition faster and more accurately than the other monitoring schemes discussed here. It can also be concluded that scheme based on monitoring the coefficients of the MGP model is not as efficient as the MGP model proposed here, as it is unable to respond to the changes in the process between the 117th and 133th samples as detected by other charts.

2.7. Conclusion

In this study, modeling and monitoring of multivariate profiles using the MGP model are investigated. Since in most engineering systems different sensors are correlated, it is crucially important to consider this correlation in modeling and monitoring the resulting multivariate profiles. The MGP model enjoys the flexibility and desirable analytical properties of the GP along with the ability to capture the correlation among multiple variables of a profile. Thus, it provides a powerful tool to model different profiles considering the correlations existing both within and between profiles. Along with the MGP based profile monitoring scheme, methods based on

modifying univariate GP and T^2 charts for the case of multivariate profiles are also presented in this chapter.

The MGP chart proposed in this study is based on the non-separable covariance structure which offers high flexibility in modeling and monitoring multivariate profiles. This flexibility typically leads to better performance in term of ARL_1 which is confirmed by the results in our numerical study. The results also show that in the presence of autocorrelation in measured values of a profile, the MGP chart outperforms other charts in different out-of-control situations with different number of in-control samples. An important feature of the MGP model is that it can learn from different dependent profiles. Therefore, increasing the number of profiles potentially enhances the MGP model, while this merely increases the misdetection rate for the univariate charts. This is also confirmed by the analysis in the numerical study section. Finally, the real-world case study further confirms the results from the numerical study and shows the advantages of the MGP based chart for monitoring multivariate profiles in practice.

It should be pointed out that the efficiency of MGP models can be further improved by optimally selecting the design points in the measurement region. In this regard, one can use a space filling algorithm like Latin hypercube or sliced Latin hypercube to select the optimal design points in space. We aim to investigate along this direction in our future research. . Also, it is known that the multivariate profile monitoring charts based on EWMA scheme can catch the OC faster in the case of small shifts (Chou et al., 2014). One potential direction of research for the MGP chart proposed here could be integrating it with an EWMA scheme to enhance its performance in the case of small shifts. Finally, with the advent of stochastic kriging based methods, it would be desirable to develop a chart using this approach and compare its performance with the MGP chart.

2.8. Appendix

2.8.1. Covariance Function

Considering the general decomposition of profile i in eq. (2.12) and the Gaussian Kernel in eq. (2.13), the $cov_{ij}^{(m)}(s,s')$ can be written as follows:

$$\begin{aligned} cov_{ij}^{(m)}(s,s') = & \int_{-\infty}^{+\infty} \frac{\rho_{ii,m}\sqrt{|\boldsymbol{L}_{ii,m}|}}{\sqrt[4]{\pi^D}} exp\left\{-\frac{1}{2}(\boldsymbol{u}+\boldsymbol{d}-\boldsymbol{\mu}_{ii,m})^T \boldsymbol{L}_{ii,m}(\boldsymbol{u}+\boldsymbol{d}-\boldsymbol{\mu}_{ii},m)\right\} \\ & \times \frac{\rho_{ij,m}\sqrt{|\boldsymbol{L}_{ij,m}|}}{\sqrt[4]{\pi^D}} exp\left\{-\frac{1}{2}(\boldsymbol{u}-\boldsymbol{\mu}_{ij,m})^T \boldsymbol{L}_{ij,m}(\boldsymbol{u}-\boldsymbol{\mu}_{ij,m})\right\} d^D\boldsymbol{u} \\ & + \int_{-\infty}^{+\infty} \frac{\rho_{0i,m}\sqrt{|\boldsymbol{L}_{0i,m}|}}{\sqrt[4]{\pi^D}} exp\left\{-\frac{1}{2}(\boldsymbol{u}+\boldsymbol{d}-\boldsymbol{\mu}_{0i,m})^T \boldsymbol{L}_{0i,m}(\boldsymbol{u}+\boldsymbol{d}-\boldsymbol{\mu}_{0i,m})\right\} \\ & \times \frac{\rho_{0j,m}\sqrt{|\boldsymbol{L}_{0j,m}|}}{\sqrt[4]{\pi^D}} exp\left\{-\frac{1}{2}(\boldsymbol{u}-\boldsymbol{\mu}_{0j,m})^T \boldsymbol{L}_{0j,m}(\boldsymbol{u}-\boldsymbol{\mu}_{0j,m})\right\} d^D\boldsymbol{u} \end{aligned} \tag{2.29}$$

Thus, for each integral term we have that

$$\begin{aligned} \int_{-\infty}^{+\infty} & exp\left\{-\frac{1}{2}(\boldsymbol{u}+2\boldsymbol{d}-\boldsymbol{\mu}_{ui,m})^T \boldsymbol{L}_{ui,m}(\boldsymbol{u}+\boldsymbol{d}-\boldsymbol{\mu}_{ui,m})\right\} exp\left\{-\frac{1}{2}(\boldsymbol{u}-\boldsymbol{\mu}_{uj,m})^T \boldsymbol{L}_{uj,m}(\boldsymbol{u}\right. \\ & \left.-\boldsymbol{\mu}_{uj,m})\right\} d^D\boldsymbol{u} = exp\left(-\frac{1}{2}\varphi\right) \exp\left\{-\frac{1}{2}(\boldsymbol{u}-\phi)^T\boldsymbol{\Sigma}(\boldsymbol{u}-\phi)\right\} d^D\boldsymbol{u} \end{aligned} \tag{2.30}$$

Considering $\boldsymbol{\Psi} = \boldsymbol{L}_{ui,m}^{-1} + \boldsymbol{L}_{uj,m}^{-1}$, we have that $\boldsymbol{\Sigma} = \boldsymbol{L}_{ui,m} + \boldsymbol{L}_{uj,m}$, $\phi = \boldsymbol{\Sigma}^{-1}\{\boldsymbol{L}_{uj,m}\boldsymbol{\mu}_{uj,m} + \boldsymbol{L}_{ui,m}(\boldsymbol{d}-\boldsymbol{\mu}_{ui,m})\}$ and $\varphi = \psi^T\boldsymbol{\Psi}\psi$ where $\psi = \boldsymbol{d} - \{\boldsymbol{\mu}_{ui,m} - \boldsymbol{\mu}_{uj,m}\}$. We can derive the following:

$$\frac{(2\pi)^{\frac{D}{2}}}{\sqrt{|\boldsymbol{L}_{ui,m}+\boldsymbol{L}_{uj,m}|}} exp\left\{-\frac{1}{2}(\boldsymbol{d}-\{\boldsymbol{\mu}_{ui,m}-\boldsymbol{\mu}_{uj,m}\})^T\boldsymbol{\Psi}^{-1}(\boldsymbol{d}-\{\boldsymbol{\mu}_{ui,m}-\boldsymbol{\mu}_{uj,m}\})\right\} \tag{2.31}$$

And we have:

$$\frac{\left|\boldsymbol{L}_{ui,m}\right|^{\frac{1}{2}}\left|\boldsymbol{L}_{uj,m}\right|^{\frac{1}{2}}}{\left|\boldsymbol{L}_{ui,m}+\boldsymbol{L}_{uj,m}\right|^{\frac{1}{2}}}=\frac{\left|\boldsymbol{L}_{uj,m}^{-1}\right|^{\frac{1}{2}}\left|\boldsymbol{L}_{uj,m}\right|^{\frac{1}{2}}}{\left|\boldsymbol{L}_{ui,m}^{-1}+\boldsymbol{L}_{uj,m}^{-1}\right|^{\frac{1}{2}}}=\frac{1}{\left|\boldsymbol{L}_{ui,m}^{-1}+\boldsymbol{L}_{uj,m}^{-1}\right|^{\frac{1}{2}}} \tag{2.32}$$

Finally, considering the $L \epsilon R$ and adjusting eq. (2.29) for the measurement noise the covariance functions in eq. (2.14) can be derived.

2.8.2. Nomenclature

$\boldsymbol{y}_i^{(m)}$	mth sample vector of the ith profile variable
$x_{i,j}$	design point j of profile variable i
p_i	number of design points in each profile i
$\varepsilon_i^{(m)}(x_{i,j})$	intrinsic noise of profile i in sample m at design point $x_{i,j}$
$\mu_i^{(m)}$	mean function of profile i in sample m of GP model
$\mathcal{K}_i^{(m)}$	Gaussian kernel of profile i in sample m of GP model
$\boldsymbol{\Sigma}_{\boldsymbol{i}}^{(\boldsymbol{m})}$	covariance matrix of profile i in sample m of GP model
$\widehat{\boldsymbol{y}}_i^{(m)}$	vector of GP prediction for each profile i of sample m
$\widehat{\boldsymbol{y}}_i^{*}$	GP chart estimate of profile i
$\boldsymbol{\Sigma}_i^{*}$	GP chart covariance estimate of profile i
$\boldsymbol{y}^{(m)}$	vector of in-control observations of all profiles in each sample m
$z_i^{(m)}$	Gaussian white noise process of profile i in sample m
τ	Dirac Delta function
$\widehat{\boldsymbol{y}}^{(m)}$	vector of MGP prediction for each sample m
$\boldsymbol{\Sigma}^{(m)}$	MGP estimate of covariance matrix of all k profiles in sample m
$\widehat{\boldsymbol{y}}^{*}$	MGP chart estimate of all profiles
$\boldsymbol{\Sigma}^{*}$	MGP chart covariance estimate of all profiles
$\boldsymbol{S}_i$	Pooled T^2 sample covariance matrix of profile i
$\boldsymbol{S}$	Pooled sample covariance matrix of aggregated T^2
$T_{GP_{i,r}}^2$	GP charting statistic of each new sample r of profile i

$T^2_{MGP_r}$	MGP charting statistic of each new sample r
$T^2_{i,r}$	T^2 charting statistic of each new sample r of profile i
T^2_r	Aggregated T^2 charting statistic of each new sample r
ϕ	coefficient of autocorrelation

Chapter 3

Remaining Useful Life Prediction Based on Degradation Signals Using Monotonic B-splines with Infinite Support*

3.1. Overview

Degradation modeling traditionally relies on monitoring degradation signals to model the underlying degradation process. In this context, failure is typically defined as the point where the degradation signal reaches a pre-specified threshold level. Many models assume that degradation signals are completely observed beyond the failure threshold, while the issue of truncated degradation signals still remains a challenge. Moreover, based on the physics of degradation process, the degradation signal should be inherently monotonic. However, it is almost inevitable that most of the sensor-based degradation signals are subject to noise which can lead to misleading prediction results. In this chapter, a non-parametric approach to modeling and prognosis of degradation signals using B-splines in a mixed effects setting is proposed. In order to deal with the issue of truncated historical degradation signals, our approach is based on augmenting B-spline basis functions with functions of infinite support. Moreover, to model the degradation signal more accurately and

*This chapter is based on the paper: **Jahani, S.**, Kontar, R., Zhou, S. and Veeramani, D., 2019. Remaining useful life prediction based on degradation signals using monotonic B-splines with infinite support. *IISE Transactions*, pp.1-18.

robustly in a noisy setting, necessary and sufficient conditions to ensure monotonic evolution of the modeled signals are derived. Appropriate procedures for online updating of random coefficients of mixed effects model considering derived monotonicity constraints based on degradation data collected from an in-service unit are also presented. The performance of the proposed framework is investigated and benchmarked through analysis based on numerical studies and a case study using real-world data from automotive lead-acid batteries.

3.2. Introduction

Remaining useful life (RUL) estimation is essential in prognostics and health management of a system. RUL can be defined as the remaining life of a component until it is able to function in accordance with its intended purposes. With recent advances in sensor and information technology, growing attention is being paid to RUL prognosis. In general, RUL prognosis models can be categorized into two categories: Model-based prognostics and data-driven prognostics (Vanem, 2018). In model-based prognostics, the RUL prediction of the system is done using physical or mathematical models of the degradation phenomenon. However, in data-driven prognostics, the aim is to transform the data provided by the sensors into relevant models (parametric or non-parametric) of the degradation behavior (Medjaher et al., 2012). In model-based approaches, the prognosis accuracy is highly dependent on the accuracy of the physical model that is used. On the other hand, the independence regarding specific objects in data-driven approaches provides more flexibility which makes them widely used in RUL estimation and degradation modeling (Zhang et al., 2018). This study deals with a data-driven prognostics approach for the estimation of RUL.

Contemporary data-driven prognostics approaches are mostly based on degradation signals. Degradation signals, also known as condition monitoring (CM) signals, are correlated with the physical degradation of the system and can be used to infer the unobservable underlying health status of the system (Kontar et al., 2017). In degradation data analysis, the component under study is considered failed once its degradation level reaches a certain pre-specified level for the first time (first hitting time). Specifically, most data driven prognostics approaches first start by establishing an initial population-level statistical model for describing the evolution of the degradation signals in the offline stage that provides the prior information. Then, the prediction of signal evolution

for a new in-service unit is performed based on both prior information and the newly collected degradation data from the in-service unit to obtain the posterior information.

Most of existing data-driven prognostics methods in literature are based on parametric modeling of the degradation signal evolution. Such parametric models typically assume that the degradation signals behave according to a common functional form, referred to as common shape function (Liao and Köttig, 2014). The most commonly used approach in parametric modeling is based on using mixed effects models that contain a fixed effects part representing the average behavior of the population and a random effects part representing the individual units, characteristics. Lu and Meeker (1993) were among the first who proposed the use of a mixed effects model to characterize the degradation path of a population of units. Based on the general model of Lu and Meeker (1993) and general assumptions summarized by Wang (2000), several mixed effects models have been proposed for RUL estimation (Gebraeel et al., 2005, 2009; Rizopoulos et al., 2014).

Apart from the methods based on the mixed effects models, two other widely-used parametric approaches are Wiener processes and Gamma processes. Wiener processes are typically used for degradation modelling where the degradation process may vary bi-directionally over time. Tseng and Peng (2004) proposed to model the cumulative degradation path of a product,s quality characteristic using Wiener processes. Modeling degradation processes using the Wiener process has some limitations. Firstly, the Wiener processes have the Markov property which means that the evolution of the degradation process at each stage is independent of its past behavior. Also, the Wiener processes are based on the assumption that the mean degradation path is linear. On the other hand, the Gamma process is appropriate for modeling degradation processes that are monotonic and evolving in only one direction (Si et al., 2011; Sun et al., 2018). One limitation of using Gamma processes is that, similar to Wiener processes, they also assume that the degradation process has the independent increment property. Furthermore, the noise in the Gamma process should have a Gamma distribution with a special parameter structure (Son et al., 2016).

The parametric models are typically derived from the underlying physics of the degradation process or empirical evaluation of the degradation signals. However, in many applications it may be difficult to identify the underlying physics and the signal may not follow any functional form (Zhang et al., 2018). Moreover, imposing a parametric form always comes with one caveat that if the specified form is far from the truth the prognostics results are misleading (Kontar et al.,

2018). One approach to overcome the challenges of parametric models is to consider non-parametric degradation models in which the functional form is learned from the degradation data. Zhou et al. (2011) used functional principal component analysis (FPCA) to non-parametrically model the degradation process using the historical data and a set of principal component scores. Moreover, an empirical Bayes approach is used in their paper to update the principal component scores of the degradation model in real-time for online monitoring of the components operating in the field. One major weakness of modeling the degradation signals using the FPCA approach is inaccurate estimation of the mean and covariance function under high noise level (Kontar et al., 2018; Zhou et al., 2012). Besides that, in a recent attempt towards non-parametric prognosis of degradation signals, Kontar et al. (2018) proposed using the multivariate Gaussian convolution processes (MGCP) to model the evolution of individual components taking into account the heterogeneity in data. Although their method can effectively model the evolution of degradation signals, it suffers from the issue of scalability, specifically when number of signals is large.

Despite the recent work on non-parametric methods, both the FPCA and MGCP require that data are densely observed over the whole domain of the experiment, i.e., degradation signals have the same support. As mentioned previously, failure is defined as the moment when the degradation signal reaches a certain pre-specified threshold level. In some engineering practices, it is possible to continue observing the degradation signal after it crosses the failure threshold as the failure does not necessarily imply component replacement (Shiau and Lin, 1999; Wang and Xu, 2010). However, in most cases, the system is shut down or replaced immediately once the degradation signal crosses the failure threshold. This means that no further observations can be made once the unit has failed. Such signals are referred to as truncated degradation signals (Gebraeel et al., 2005; Virkler et al., 1979). Unfortunately, truncation results in wrong estimation of the remaining useful life for the MGCP and FPCA, since we are not able to observe the complete evolution of the historical signals over the whole domain of the experiment. This is intuitively understandable, as prediction for a Gaussian Process (GP) falls back to the mean when predicting far away from observation points (Rasmussen, 2004). Therefore, the prediction may never hit the threshold level in the case of truncation. One exception to this issue is a study by Zhou et al. (2012) where they applied FPCA on the transformed degradation signals. However, their approach cannot guarantee the monotonicity of the CM signal evolution, as the FPCA assumes that the signals indeed follow a

GP, which is non-monotone. Also, the transformation approach requires a relatively large number of training units in the historical database.

In this study, we propose a non-parametric approach to modeling and prognosis of degradation signals using B-spline basis functions in a mixed effects setting. Specifically, our approach is motivated by supplementing the basis with functions of infinite support as proposed in Schumaker (2007) and Corlay (2016). This framework offers numerous advantages. First, B-spline is inherently a non-parametric data-driven approach in which we are allowing the data to speak for themselves. Moreover, by augmenting the basis functions with infinite support we let the B-spline to cover the whole possible range of degradation signal evolution thus allowing to extrapolate the evolution of degradation signal beyond the threshold level. Therefore, it allows us to deal with the issue of truncated signals as mentioned earlier in this study. Furthermore, it is well-known that the B-splines can be derived as polynomials with a certain degree depending on the degree of generating B-spline basis functions. This feature, further, allows us to control the evolution of the degradation signals by imposing appropriate constraints to ensure monotonicity in the resulting polynomial functions. This, in fact, helps with correct modeling and prognosis of the degradation signal when we are observing noisy data. Finally, it should be mentioned that as opposed to MGCP approach developed in Kontar et al. (2018), the number of parameters that needs to be estimated in the log-likelihood function is fixed and depends only on the degree and number of basis functions. This, indeed, offers a huge advantage over the multivariate Gaussian process based approaches that typically suffer from the scalability issues.

The remainder of this chapter is structured as follows. Section 2 reviews degradation signal modeling and conventional Bayesian updating. Moreover, the concept of B-splines with infinite support is described in this section. In section 3, we derive necessary and sufficient conditions to guarantee monotonic evolution of degradation signals in a mixed effects model based on B-splines of infinite support. Moreover, appropriate procedures to conduct online updating based on the collected data from the new in-service unit considering the derived monotonicity constraints are discussed in this section. Section 4 presents numerical studies where the performance of the proposed approach is investigated under different scenarios. In section 5, the application of the proposed method in a real-world case study is demonstrated. Finally, our concluding remarks are presented in section 6.

3.3. Degradation signal modeling and prognosis

3.3.1. Review of B-spline based mixed effects modeling for degradation signals and online updating

The mixed effects model has been widely used in degradation signal modeling and RUL estimation in literature due to its flexible model structure (Gebraeel et al., 2005). The main advantage of the mixed effects model is that it allows each unit to have its own parameters and degradation progression path. The degradation path of the *i*th unit at each time point t in the mixed effects model is typically defined as:

$$y_i(t) = x_i(t) + \varepsilon_i(t) = \boldsymbol{z}^T(t)\,\boldsymbol{\theta}_i + \varepsilon_i(t), \tag{3.1}$$

where $x_i(t)$ is the true but unobservable value of the degradation signal, $\varepsilon_i(t)$ is the measurement error which is assumed to be independent and normally distributed $N(0, \sigma^2)$, $\boldsymbol{z}^T(t)$ is a pre-specified time-dependent regression function and $\boldsymbol{\theta}_i = \left[\theta_{i,1}, \ldots, \theta_{i,d}\right]^T$ is the vector of random coefficients for unit i. The random coefficients in (3.1) allow the units to have distinct but similar degradation paths, and it is assumed that $\boldsymbol{\theta}_i$ follows a multivariate normal distribution $N(\boldsymbol{\mu}, \boldsymbol{\Sigma})$.

In cases where the behavior of degradation signals is evident, we may consider the polynomials of appropriate order or other certain specific nonlinear functions of time (e.g., log(t)) as the regression function $\boldsymbol{z}^T(t)$. However, in most of the cases, it happens that identifying a model that best defines the evolution of degradation signals is difficult if not impossible. In this situation, one can use B-spline basis functions of an appropriate degree as a non-parametric regression approach to define $\boldsymbol{z}^T(t)$ in Eq. (3.1). The value of B-spline basis functions of degree n defined over a set of non-decreasing knot values at time t $\left(\mathbf{b}_n^T(t)\right)$ can be obtained recursively as a function of lower degree basis functions. It is worth mentioning that by properly increasing the number of knots or degree (n), B-splines can approximate arbitrary continuous functions to any given precision (De Boor et al., 1978).

The B-spline based mixed effects model for modeling the degradation path of the *i*th unit at time t can be defined as follows:

$$y_i(t) = \boldsymbol{b}_n^T(t)\,\boldsymbol{\theta}_i + \varepsilon_i(t), \tag{3.2}$$

where $\boldsymbol{b}_n(t) = \left[b_{1,n}(t), \ldots, b_{d,n}(t)\right]^T$ is the vector of B-spline basis functions evaluated at time t over a set of non-decreasing knot values. In order to use the mixed effects model in (3.2), first we need to estimate the parameters of the model such as $\boldsymbol{\mu}, \boldsymbol{\Sigma}$ and σ^2 in the offline stage based on the historical dataset of degradation signals. Then, in the online stage, the estimated model is used as a prior and the Bayesian updating is performed to estimate the model parameters for the new in-service unit based on the degradation data collected from the new unit.

At the current time point t_h, when the prediction is to be made, assume there are s_i values of the degradation signal available from the in-service unit i, i.e. $\boldsymbol{y}_i(\boldsymbol{t}_{i,1:h}) = [\boldsymbol{y}_i(t_{i,1}), \boldsymbol{y}_i(t_{i,2}), ..., \boldsymbol{y}_i(t_{i,s_i})]^T$ and $\boldsymbol{t}_{i,1:h} = [t_{i,1}, t_{i,2}, ..., t_{i,s_i}]^T$ where $t_{i,s_i} \leq t_h$. Therefore, the posterior distribution of the random coefficients based on the newly collected data from the ith in-service unit up to time t_h, can be computed as $p(\boldsymbol{\theta}_i|\boldsymbol{y}_i(\boldsymbol{t}_{1:h})) \propto p(\boldsymbol{y}_i\left(\boldsymbol{t}_{i,1:h}\right)|\boldsymbol{\theta}_i)\pi(\boldsymbol{\theta}_i)$ where $p(\boldsymbol{y}_i\left(\boldsymbol{t}_{i,1:h}\right)|\boldsymbol{\theta}_i)$ represents the likelihood of the observation data and $\pi(\boldsymbol{\theta}_i)$ refers to the prior distribution estimated in the offline stage. Assuming normally distributed $\boldsymbol{\theta}_i$ and ε_i, the posterior is also normally distributed $p\left(\boldsymbol{\theta}_i\middle|\boldsymbol{y}_i\left(\boldsymbol{t}_{i,1:h}\right)\right) \sim N(\hat{\boldsymbol{\mu}}_{i,h}, \hat{\boldsymbol{\Sigma}}_{i,h})$ where $\hat{\boldsymbol{\mu}}_{i,h}$ and $\hat{\boldsymbol{\Sigma}}_{i,h}$ represent the mean and covariance matrix of the posterior. This, in fact, derives from the conjugate property of the normal distribution. Considering the prior parameter estimates as $\boldsymbol{\mu}_0$ and $\boldsymbol{\Sigma}_0$, the closed form expression for the posterior mean and covariance matrix is as follows:

$$\begin{aligned}\hat{\boldsymbol{\mu}}_{i,h} &= \hat{\boldsymbol{\Sigma}}_{i,h}\left[\frac{\boldsymbol{b}_n^T\left(\boldsymbol{t}_{i,1:h}\right)\boldsymbol{y}_i\left(\boldsymbol{t}_{i,1:h}\right)}{\sigma^2} + \boldsymbol{\Sigma}_0^{-1}\boldsymbol{\mu}_0\right],\\ \hat{\boldsymbol{\Sigma}}_{i,h} &= \left[\boldsymbol{\Sigma}_0^{-1} + \left[\frac{\boldsymbol{b}_n^T\left(\boldsymbol{t}_{i,1:h}\right)\boldsymbol{b}_n\left(\boldsymbol{t}_{i,1:h}\right)}{\sigma^2}\right]^{-1}\right],\end{aligned} \tag{3.3}$$

where $\boldsymbol{b}_n\left(\boldsymbol{t}_{i,1:h}\right) = \left[\boldsymbol{b}_n\left(\boldsymbol{t}_{i,1}\right), \boldsymbol{b}_n\left(\boldsymbol{t}_{i,2}\right), \ldots, \boldsymbol{b}_n\left(\boldsymbol{t}_{i,h}\right)\right]^T$ and $\boldsymbol{\mu}_0, \boldsymbol{\Sigma}_0$ and σ^2 can be replaced by their estimates $\hat{\boldsymbol{\mu}}_0, \hat{\boldsymbol{\Sigma}}_0$ and $\hat{\sigma}^2$ from the offline stage. With the updated mean and covariance matrix, the degradation values of the new in-service unit can be predicted for future time $t > t_h$. This procedure considers both the prior information coming from the average behavior of the population and specific behavior of the in-service unit up to time t_h.

It should be mentioned that the B-spline basis functions are always limited to the range of observed data points and vanish outside this range based on their definition. As a result, modeling the evolution of the degradation signals always depends on the specific range of the historical data over which the B-spline basis functions are defined. However, it often happens that the support

range of degradation signals in our historical dataset is limited. In this case, when modeling the evolution of a specific unit, we reach to a state at which we are required to extrapolate outside the range of B-splines. The next subsection introduces infinite support B-splines as a solution to deal with this issue.

3.3.2. B-splines of infinite support

The classical B-spline basis functions have compact support and can only model data limited to this specific support range. This subsection reviews the extension of classical B-spline to include the basis functions with infinite support as proposed in Schumaker (2007).

Let k be a nonnegative integer and $\Gamma = \{\gamma_0 \leq \gamma_1 \leq ... \leq \gamma_{k-1}\}$ be a sorted collection of k knots, where if $k = 0$ then $\Gamma = \emptyset$. Then the B-spline basis function of degree 0 associated with the knots Γ is defined as follows:

$$\begin{cases} b_{0,0}(t) := I_{(-\infty, inf(\Gamma))}(t), \quad b_{k,0} := I_{[sup(\Gamma), +\infty)}(t), \\ b_{j,0}(t) := I_{[\gamma_{j-1}, \gamma_j)}(t), \qquad 1 \leq j \leq k-1, \end{cases} \tag{3.4}$$

where $I_{(\cdot)}$ denotes the indicator function. The B-spline basis functions with higher degree $1 \leq n \leq k$ can be defined using the induction formula given in appendix 3.8.1. The collection of functions $\left(b_{j,n}\right)_{0 \leq j < k+n+1}$ for $0 \leq n \leq k$ are called the B-spline basis functions of degree n. Appendix 3.8.1 also gives the induction formula for the B-spline basis functions of degree n where $n \geq k$. Figure 3.1 shows the B-spline basis functions with infinite supports of different degrees defined over $[-4, 4]$ with 6 equally spaced knot values placed at $\Gamma = \{-2.5, -1.5, -0.5, 0.5, 1.5, 2.5\}$. The classical B-spline basis functions in this case are limited to the range between $\gamma_0 = -2.5$ and $\gamma_5 = 2.5$. However, the basis functions with infinite support can extrapolate beyond this range as demonstrated in Figure 3.1.

One important property of B-spline basis functions is that their derivatives can be decomposed onto B-spline basis functions of lower degree. Therefore, with the same notation as above, the

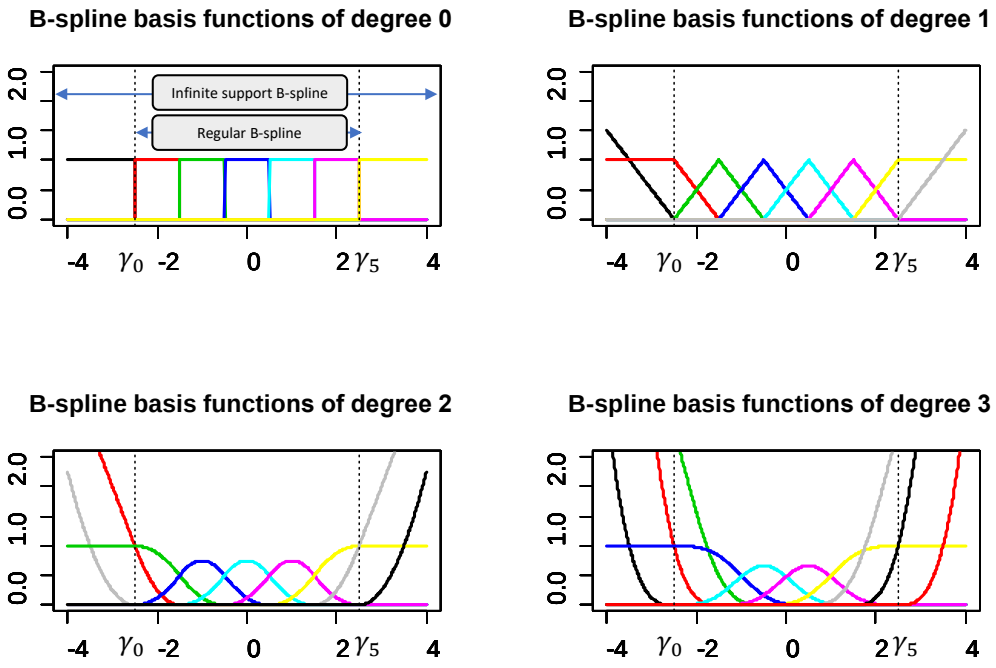

Figure 3.1: B-spline basis functions of infinite support with degrees 0, 1, 2 and 3.

differentiation of B-splines basis functions (for $0 < n \leq k$) is as follows:

$$\left(b_{j,n}\right)' = \begin{cases} -\frac{n}{C_0} b_{j,n-1} & 0 \leq j < min(n,k), \\ -\frac{n}{\gamma_n - \gamma_0} b_{n,n-1} & \text{for } j = n, \\ \frac{n}{\gamma_{j-1} - \gamma_{j-n-1}} b_{j-1,n-1} - \frac{n}{\gamma_j - \gamma_{j-n}} b_{j,n-1} & n+1 \leq j < k, \\ \frac{n}{\gamma_{k-1} - \gamma_{k-n-1}} b_{k-1,n-1} & \text{for } j = k, \\ \frac{n}{C_1} b_{j-1,n-1} & max(n,k)+1 \leq j < k+n+1, \end{cases} \tag{3.5}$$

where for the constants C_0 and C_1, we use the guideline proposed in Corlay (2016). In this study, we take $C_0 = C_1 = \frac{\gamma_{k-1} - \gamma_0}{k-1}$ if $\gamma_{k-1} > \gamma_0$ and $C_0 = C_1 = 1$ otherwise. By iterating over this decomposition, the mth derivative of B-spline basis function of degree n onto the basis of degree $n - m$ can be obtained. More information about the derivatives of B-splines and algorithms to evaluate and calculate them can be found in Schumaker (2007) and Corlay (2016).

A critical stage in evaluating B-splines is the placement of knot values which can be generally done using bisecting method with O(log(k)) complexity (Tjahjowidodo et al., 2017; Corlay, 2016; Aguilar et al., 2018). However the case of equally spaced knots, which is utilized in this paper, leads to further simplifications where all bounded spline basis functions have the same polynomial

representation up to a parallel shift, and unbounded basis functions are symmetric. These properties can be exploited to save a significant amount of memory and computation. Regarding selecting the number of knots, we would like to also mention that it can be simply done using cross validation or any of the well-established versions of statistical information criteria like Akaike Information Criteria (AIC) or Bayesian Information Criteria (BIC).

In this study, we propose to use a non-parametric mixed effects model based on B-spline basis functions of infinite support as the regression function in (3.2). The advantage of using the infinite support B-spline is that, firstly, it is data-driven and does not assume the data to follow a specific functional form. Moreover, by properly constraining the random coefficients of B-spline basis functions in the mixed effects setting, one can ensure the monotonic degradation path of each unit as suggested by our domain knowledge. The next section discusses the development of such constraints and appropriate procedures for online updating of the infinite support B-spline based mixed effects model.

3.4. Remaining useful life prediction using monotonic B-splines with infinite support

In this section, we first derive the monotonicity conditions for infinite support B-Splines of degree 1 and degree 2 in a mixed effects setting. Then, the necessary and sufficient conditions for monotonic degradation of units in a mixed effects model with degree 3 B-spline basis function of infinite support will be derived. Finally, the appropriate procedures to conduct online updating considering these conditions will be discussed in section 3.4.2.

3.4.1. Monotonicity conditions for B-splines with infinite support

In degradation modeling, practitioners typically use B-splines to model degradation signals because of their flexibility in consistently approximating the evolution of signals based on collected data. However, in cases where we are collecting data from sensors, most often it happens that the sensor data are noisy and as a result, the collected data may contradict the underlying physics. In degradation modeling, for example, the degradation signal should be monotonically changing over time since the underlying health condition is always deteriorating unless some maintenance actions have been performed (Son et al., 2016; Byon et al., 2010; Zhou et al., 2012). In cases

where the noise level of the collected data is high, non-parametric approaches like B-splines may lead to incorrect estimation of the degradation signal. To overcome this potential shortcoming, the ideal degradation modeling approach is the one that allows for flexibility while maintaining the monotonic evolution path of the degradation signal. This section discusses the required conditions for modeling of monotonic degradation signals using B-splines of infinite support in a mixed effects setting.

First, we derive the necessary and sufficient conditions for monotonicity of degree 1 and degree 2 B-splines with infinite support in a mixed effects model. As mentioned in section 3.3.2, the derivatives of B-spline basis functions are explicitly decomposed onto the basis of lower degree. Thus, non-negativity constraints on the first derivative of B-splines with infinite support translates into monotonicity constraints. The B-spline basis functions of degree n $(n \leq k)$ associated with the knots $\Gamma = \{\gamma_0 \leq \gamma_1 \leq \ldots \leq \gamma_{k-1}\}$ and given by the induction formula in appendix 3.8.1 are a collection of non-negative functions. Therefore, non-negativity of coefficients of basis functions in the mixed effects model is a sufficient condition for non-negativity of B-splines with infinite support. For B-spline of degree 0 and degree 1, this also happens to be a necessary condition (Yuan et al., 2017; Beliakov, 2002). Thus, for basis functions of degree 1 and degree 2 which decompose onto degree 0 and degree 1 basis functions, one can obtain the monotonicity condition using Eq. (3.5). The following lemma discusses the monotonicity constraints for degree 1 and degree 2 B-splines with infinite support.

Lemma 1 *Let* $\boldsymbol{\theta}_i = \left[\theta_{i,1}, \ldots, \theta_{i,n+k+1}\right]^T$ *be the coefficients of infinite support basis functions in the mixed effects model of Eq.* (3.2) *for unit* i *at time* t*. Let* $\Gamma = \{\gamma_0 \leq \gamma_1 \leq \ldots \leq \gamma_{k-1}\}$ *where* $k > n$ *be the set of non-decreasing knot values over which the infinite support B-spline is defined. Then, the necessary and sufficient condition for monotonicity of degree 1 and degree 2 B-spline with infinite support can be encoded in terms of the following constraints:*

$$\begin{aligned} \theta_{i,j} &\leq 0, \quad j = 1, \ldots, n, \\ \theta_{i,j} - \theta_{i,j-1} &\geq 0, \quad j = n+2, \ldots, k+1, \\ \theta_{i,j} &\geq 0, \quad j = k+2, \ldots, k+n+1. \end{aligned} \tag{3.6}$$

Proof. The B-spline of degree n with infinite support over the knot vector Γ is defined as follows:

$$Q_i^{(n)}(t) = \boldsymbol{b}_n^T(t)\,\boldsymbol{\theta}_i = \sum_{j=0}^{k+n} \theta_{i,j+1} b_{j,n}(t). \tag{3.7}$$

The first order derivative of B-spline in (3.7) can be calculated using the differentiation of B-spline basis functions given in (3.5) as follows:

$$\begin{aligned}
Q_i'^{(n)}(t) &= \sum_{j=0}^{k+n} \left(\theta_{i,j+1} b_{j,n}(t)\right)' \\
&= \sum_{j=0}^{n-1} \theta_{i,j+1} \left(\frac{-n}{C_0} b_{j,n-1}(t)\right) + \theta_{i,n+1} \left(\frac{-n}{\gamma_n - \gamma_0} b_{n,n-1}(t)\right) \\
&+ \sum_{j=n+1}^{k-1} \theta_{i,j+1} \left(\frac{n}{\gamma_{j-1} - \gamma_{j-n-1}} b_{j-1,n-1}(t) - \frac{n}{\gamma_j - \gamma_{j-n}} b_{j,n-1}(t)\right) \\
&+ \theta_{i,k+1} \left(\frac{n}{\gamma_{k-1} - \gamma_{k-n-1}} b_{k-1,n-1}(t)\right) + \sum_{j=k+1}^{k+n} \theta_{i,j+1} \left(\frac{n}{C_1} b_{j-1,n-1}(t)\right) \\
&= \sum_{j=0}^{n-1} \left(\frac{-n}{C_0} \theta_{i,j+1}\right) b_{j,n-1}(t) + \sum_{j=n+1}^{k} \left(\frac{n}{\gamma_{j-1} - \gamma_{j-n-1}} \left(\theta_{i,j+1} - \theta_{i,j}\right)\right) b_{j-1,n-1}(t) \\
&+ \sum_{j=k+1}^{k+n} \left(\frac{n}{C_1} \theta_{i,j+1}\right) b_{j-1,n-1}(t),
\end{aligned} \tag{3.8}$$

where, in the last equality, we rearrange the terms for basis functions. The monotonicity condition can be derived by imposing a non-negativity constraint on the first order derivative of B-splines with infinite support. The first order derivative of B-splines of degree 1 and degree 2 can be calculated in terms of basis functions of degree 0 and degree 1, respectively, as given in (3.8). For basis functions of degree 0 and degree 1, non-negativity of coefficients is both a necessary and sufficient condition for non-negativity of B-spline. Therefore, imposing non-negativity constraints on coefficients of basis functions in the last equality of Eq. (3.8) for degree 1 and degree 2 B-splines results in the conditions given in (3.6). As for the necessity of these conditions, it should be noted that the basis functions $b_{j-1,n-1}$ and $b_{j,n-1}$ are always non-negative. Moreover for a degree 2 (or 1) B-spline, each point in a knot interval has non-zero values in 3 (or 2) nearby basis functions (Please refer to Figure 3.1). Therefore if the conditions in (6) for the corresponding coefficients is not satisfied, the derivative of B-spline in that interval would be negative and as a result the B-spline function is not monotonically increasing. This happens for degree 2 and 1 B-splines simply because their

derivatives can be written in forms of polynomials of degree 1 and 0. Thus the condition in (3.6) is both necessary and sufficient and the proof is complete. □

Using Lemma 1, monotonicity constraints for degree 1 and degree 2 B-splines with infinite support can be written in form of linear inequality constraints for each unit i as follows:

$$\boldsymbol{a} \leq \boldsymbol{A}\boldsymbol{\theta}_i \leq \boldsymbol{b}, \tag{3.9}$$

where

$$\begin{aligned}
\boldsymbol{A}_{d\times d} &= \begin{bmatrix} \boldsymbol{A}_{11} & \boldsymbol{A}_{12} & \boldsymbol{A}_{13} \\ \boldsymbol{A}_{21} & \boldsymbol{A}_{22} & \boldsymbol{A}_{23} \\ \boldsymbol{A}_{31} & \boldsymbol{A}_{32} & \boldsymbol{A}_{33} \end{bmatrix}, \\
\boldsymbol{A}_{11} &= \boldsymbol{A}_{33} = \boldsymbol{I}_{n\times n}, \\
\boldsymbol{A}_{13} &= \boldsymbol{A}_{31} = \boldsymbol{0}_{n\times n}, \\
\boldsymbol{A}_{21} &= \boldsymbol{A}_{23} = \boldsymbol{0}_{(k-n+1)\times n}, \\
\boldsymbol{A}_{12} &= \boldsymbol{A}_{32} = \boldsymbol{0}_{n\times(k-n+1)}, \\
\boldsymbol{A}_{22} &= \begin{bmatrix} 1 & 0 & 0 & 0 & 0 & \dots & 0 & 0 \\ -1 & 1 & 0 & 0 & 0 & \dots & 0 & 0 \\ 0 & -1 & 1 & 0 & 0 & \dots & 0 & 0 \\ 0 & 0 & -1 & 1 & 0 & \dots & 0 & 0 \\ \vdots & \vdots & \vdots & \vdots & \vdots & \ddots & \vdots & \vdots \\ 0 & 0 & 0 & 0 & 0 & \dots & -1 & 1 \end{bmatrix},
\end{aligned} \tag{3.10}$$

$\boldsymbol{A}_{22}$ is a $(k-n+1)\times(k-n+1)$ matrix and $d = n+k+1$ is the number of basis functions. For $\boldsymbol{a}_{(k+n+1)\times 1}$ we have $\boldsymbol{a} = \left[\boldsymbol{a}_1^T, \boldsymbol{a}_2^T, \boldsymbol{a}_3^T\right]^T$ where $(\boldsymbol{a}_1)_{n\times 1} = [-\infty, \dots, -\infty]^T$, $(\boldsymbol{a}_2)_{(k-n+1)\times 1} = [-\infty, 0, \dots, 0]^T$ and $(\boldsymbol{a}_3)_{n\times 1} = [0, \dots, 0]^T$. Also, for $\boldsymbol{b}_{(k+n+1)\times 1}$ we have $\boldsymbol{b} = \left[\boldsymbol{b}_1^T, \boldsymbol{b}_2^T, \boldsymbol{b}_3^T\right]^T$ where $(\boldsymbol{b}_1)_{n\times 1} = [0, \dots, 0]^T$, $(\boldsymbol{b}_2)_{(k-n+1)\times 1} = [+\infty, \dots, +\infty]^T$ and $(\boldsymbol{b}_3)_{n\times 1} = [+\infty, \dots, +\infty]^T$.

The conditions in (3.9) should always be considered when updating the posterior distribution for the in-service unit in online stage in order to get a monotone degradation path. Unfortunately, sole application of the Bayesian updating procedure reviewed in section 3.3.1 cannot guarantee these conditions in updating the posterior distribution. In subsection 3.4.2, we introduce an approach for updating the posterior distribution of new in-service unit considering the linear inequality

constraints in (3.9) to ensure monotonicity of the resulting modeled degradation signal in a mixed effects models based on degree 1 and degree 2 B-splines with infinite support.

B-splines of degree 2 are typically sufficient for modeling a wide variety of degradation signal evolution paths. Moreover, adding more knot values increases the accuracy of degree 2 B-splines. However, B-splines of degree 3 are also commonly used in literature due to their flexibility and ability to model curvature(Schumaker, 2007; Yuan et al., 2017). Thus, it is of prime importance to develop necessary and sufficient conditions to ensure monotonic evolution of the degradation signal using degree 3 B-splines of infinite support. In practice, B-splines of degree less than 4 are sufficient for modeling different continuous functions and higher degrees of the B-splines typically increases computational complexity and numerical instability (Schumaker, 2007).

For B-splines of degree 3 with infinite support, slightly more complex necessary and sufficient conditions are required. In this regard, we take advantage of the piecewise representation of B-splines. De Boor et al. (1978) and Schumaker (2007) state that for $t \in \left[\gamma_p, \gamma_{p+1}\right]$ where γ_p and γ_{p+1} are two consecutive knot values, the degree 3 B-spline basis function can be expressed as follows:

$$b_{j,3}(t) = \alpha_{0,p,j} + \alpha_{1,p,j}t + \alpha_{2,p,j}t^2 + \alpha_{3,p,j}t^3, \tag{3.11}$$

where $\alpha_{r,p,j}, r = 0, ..., 3$ are coefficients determined only by placement of the knots. Because of the local support property of B-splines, $b_{j,3}(t)$ are nonzero only when $j = p-3, \ldots, p$. Therefore, for B-spline of degree 3 with infinite support and $t \in \left[\gamma_p, \gamma_{p+1}\right]$ we have that:

$$\begin{aligned} Q_i^{(3)}(t) = \boldsymbol{b}_3^T(t)\,\boldsymbol{\theta}_i = \sum_{j=0}^{k+3} \theta_{i,j+1} b_{j,3}(t) = \sum_{j=p-3}^{p} \theta_{i,j+1} \sum_{r=0}^{3} \alpha_{r,p,j} t^r \\ = \sum_{r=0}^{3} \sum_{j=p-3}^{p} \left(\theta_{i,j+1}\alpha_{r,p,j}\right) t^r = \sum_{r=0}^{3} \eta_{r,p} t^r. \end{aligned} \tag{3.12}$$

Equation (3.12) shows that degree 3 B-splines model the degradation signal in each interval $\left[\gamma_p, \gamma_{p+1}\right]$ using polynomials of degree 3. Figure 3.2 illustrates the piecewise polynomial construction of a degradation signal using degree 3 B-spline basis functions with infinite support. Monotonicity condition for a degree 3 B-splines can be obtained by imposing monotonicity on $Q_i^{(3)}$ in each knot interval. The following lemma gives the required conditions for monotonicity of a degree 3 B-spline with infinite support

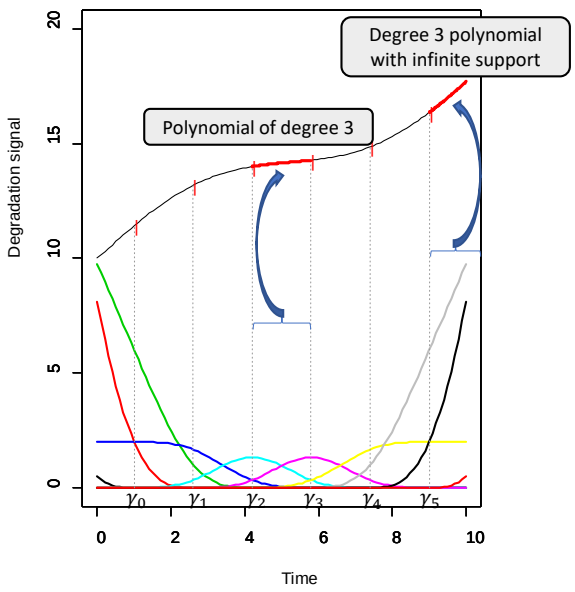

Figure 3.2: Piecewise polynomial construction of degradation signals using degree 3 B-splines with infinite support.

Lemma 2 *Let* $\Gamma = \{\gamma_0 \leq \gamma_1 \leq \ldots \leq \gamma_{k-1}\}$ *where* $k > 3$ *be the set of non-decreasing knot values over which the infinite support B-spline is defined. Let* $\eta_{r,p}, r = 0, ..., 3$ *be the coefficients of derived degree 3 polynomial for* $t \in \left[\gamma_p, \gamma_{p+1}\right]$ *as defined in* (3.12). *Then, the necessary and sufficient conditions for monotonicity of degree 3 B-spline with infinite support can be encoded in terms of the following constraints:*

$$
\begin{aligned}
I\left(3\eta_{3,p}\gamma_{p-1} \leq -\eta_{2,p} \leq 3\eta_{3,p}\gamma_p, \eta_{3,p} \geq 0\right)\left(\eta_{1,p} - \frac{\eta_{2,p}^2}{3\eta_{3,p}}\right) \geq 0, \quad p = 1, \ldots, k-1, \\
\eta_{1,p} + 2\eta_{2,p}\gamma_{p-1} + 3\eta_{3,p}\gamma_{p-1}^2 \geq 0, \quad p = 1, \ldots, k, \\
I\left(3\eta_{3,k}\gamma_{k-1} \leq -\eta_{2,k}, \eta_{3,k} \geq 0\right)\left(\eta_{1,k} - \frac{\eta_{2,k}^2}{3\eta_{3,k}}\right) \geq 0, \\
\eta_{1,k} + 2\eta_{2,k}\gamma_k + 3\eta_{3,k}\gamma_k^2 \geq 0.
\end{aligned}
\tag{3.13}
$$

Proof. In order to obtain necessary and sufficient conditions for monotonicity of $Q_i^{(3)}(t)$, we need to ensure monotonicity in each interval $t \in \left[\gamma_p, \gamma_{p+1}\right]$. In this regard, one needs to just impose monotonicity on a degree 3 polynomial in each interval $t \in \left[\gamma_p, \gamma_{p+1}\right]$ according to Eq. (3.12). The polynomial $Q_i^{(3)}(t) = \sum_{r=0}^{3} \eta_{r,p} t^r$ is monotonically increasing on $t \in \left[\gamma_p, \gamma_{p+1}\right]$ if we force its derivative $Q_i'^{(3)}(t) = \eta_{1,p} + 2\eta_{2,p}t + 3\eta_{3,p}t^2$ to be positive for $t \in \left[\gamma_p, \gamma_{p+1}\right]$. It should be noted

that $Q_i'^{(3)}(t)$ is minimized at $t = -\eta_{2,p}/(3\eta_{3,p})$ and the minimum value is $\eta_{1,p} - \eta_{2,p}^2/(3\eta_{3,p})$ if $\eta_{3,p} > 0$. Thus, the following three conditions ensure monotonicity of degree 3 B-splines with infinite support for $t \in [\gamma_p, \gamma_{p+1}]$.

$$\begin{gathered} I\left(3\eta_{3,p}\gamma_p \le -\eta_{2,p} \le 3\eta_{3,p}\gamma_{p+1}, \eta_{3,p} \ge 0\right)\left(\eta_{1,p} - \frac{\eta_{2,p}^2}{3\eta_{3,p}}\right) \ge 0, \\ Q_i'^{(3)}(\gamma_p) \ge 0, \quad Q_i'^{(3)}(\gamma_{p+1}) \ge 0. \end{gathered} \tag{3.14}$$

In order to obtain necessary and sufficient conditions for monotonicity of $Q_i^{(3)}(t)$, by local support property of B-splines, we only need to ensure monotonicity in each interval of the knot vector. We also need to add one dummy knot value at the end of the knot vector to determine the extent of extrapolation that we are interested in. This knot value is not required to be inside the range of the observed data point as with the regular B-splines. We denote this knot value by γ_k. This results in the conditioned given in (3.13). □

The posterior distribution of the in-service unit should always satisfy the conditions of Lemma 2 in the online stage to obtain monotone evolution of a degradation signal when using degree 3 B-splines of infinite support in a mixed effect model. *The constraints developed in* (3.13) *for online updating of the mixed effects model based on degree 3 B-splines with infinite support are non-linear, unlike the ones derived for the case of degree 1 and degree 2 B-splines with infinite support in* (3.9). Subsection 3.4.2 introduces a procedure to update the posterior distribution of a new in-service unit considering the general form of non-linear inequality constraints derived in Lemma 2 to ensure monotonic evolution of the resulting modeled degradation signal in the mixed effects model based on degree 3 B-splines of infinite support.

3.4.2. Online updating of the mixed effects model based on the B-splines of infinite support with monotonicity constraints

This section discusses appropriate procedures to realize the necessary and sufficient conditions developed previously for online updating of the mixed effects model based on monotonic B-splines of infinite support. Specifically in subsection 3.4.2, we first introduce the constraint Kalman filter (CKF) approach tailored for updating the random coefficients of infinite support basis functions of degree 1 and degree 2 in mixed effects model considering the constraints given in Lemma 1.

The CKF procedure is applicable for updating random coefficients considering linear inequality constraints. However, by Lemma 2, the monotonicity conditions for degree 3 B-splines with infinite support are in the form of nonlinear inequality constraints, and the CKF procedure is not applicable anymore. In order to deal with this issue, our approach to online updating of degree 3 B-splines is based on Monte Carlo (MC) Sampling. The detailed procedure for updating based on the MC sampling approach is discussed in subsection 3.4.2.

Analytical updating procedure based on the constrained Kalman filter for degree 1 and degree 2 B-splines with infinite support

The online Bayesian updating procedure based on collected data from new in-service unit i at time t_h results in a multivariate normal distribution denoted as $p\left(\boldsymbol{\theta}_i \middle| \boldsymbol{y}_i\left(\boldsymbol{t}_{i,1:h}\right)\right) \sim N(\hat{\boldsymbol{\mu}}_{i,h}, \hat{\boldsymbol{\Sigma}}_{i,h})$ for random coefficients of a mixed effects model as discussed in section 3.3.1. In order to get a monotonic degradation signal for the new in-service unit in a mixed effects model based on degree 1 and degree 2 B-splines with infinite support, the posterior distribution should always satisfy the conditions provided by Lemma 1. This, indeed, results in updating the posterior multivariate normal distribution with linear inequality constraint given by Lemma 1. Enforcing the set of constraints given in (3.9) yields the truncated multivariate normal distribution denoetd as $LN\left(\hat{\boldsymbol{\mu}}_{i,h}, \hat{\boldsymbol{\Sigma}}_{i,h}; \boldsymbol{a}, \boldsymbol{b}, \boldsymbol{A}\right)$ with the PDF as follows:

$$p\left(\boldsymbol{\theta}_i \middle| \boldsymbol{y}_i\left(\boldsymbol{t}_{i,1:h}\right); \boldsymbol{\theta}_i \in C_h\right) = \begin{cases} \frac{p\left(\boldsymbol{\theta}_i \middle| \boldsymbol{y}_i\left(\boldsymbol{t}_{i,1:h}\right)\right)}{\int_{C_h} p\left(\boldsymbol{\theta}_i \middle| \boldsymbol{y}_i\left(\boldsymbol{t}_{i,1:h}\right)\right) d\boldsymbol{\theta}_i} = \xi_h^{-1} p\left(\boldsymbol{\theta}_i \middle| \boldsymbol{y}_i\left(\boldsymbol{t}_{i,1:h}\right)\right) & \text{if } \boldsymbol{\theta}_i \in C_h, \\ 0 & \text{otherwise,} \end{cases} \tag{3.15}$$

where ξ_h is a normalizing constant and C_h denotes the constraints, space.

First, in Lemma 3 we discuss transforming the multivariate normal distribution with linear inequality constraints ($\boldsymbol{\theta} \sim LN\left(\boldsymbol{\mu}, \boldsymbol{\Sigma}; \boldsymbol{a}, \boldsymbol{b}, \boldsymbol{A}\right)$) into a simpler form of a truncated multivariate normal distribution with box constraints denoted by $TN(\boldsymbol{\mu}^n, \boldsymbol{\Sigma}^n; \boldsymbol{a}, \boldsymbol{b})$ where $\boldsymbol{\mu}^n$ and $\boldsymbol{\Sigma}^n$ denote the new mean vector and covariance matrix after transformation.

Lemma 3 *Let* $\boldsymbol{\theta} \sim LN\left(\boldsymbol{\mu}, \boldsymbol{\Sigma}; \boldsymbol{a}, \boldsymbol{b}, \boldsymbol{A}\right)$ *and* $\boldsymbol{Z} = \boldsymbol{A\theta}$. *Then* $\boldsymbol{Z} \sim TN(\boldsymbol{A\mu}, \boldsymbol{A\Sigma A}^T; \boldsymbol{a}, \boldsymbol{b})$ *and If* $\boldsymbol{A}^{-1}$ *exists, then* $\boldsymbol{\theta} = \boldsymbol{A}^{-1}\boldsymbol{Z}$.

Proof. We know $\boldsymbol{\theta} \sim LN\left(\boldsymbol{\mu}, \boldsymbol{\Sigma}; \boldsymbol{a}, \boldsymbol{b}, \boldsymbol{A}\right)$ has PDF as follows:

$$C_L^{-1} exp\left\{-\left(\boldsymbol{\theta}-\boldsymbol{\mu}\right)^T \boldsymbol{\Sigma}^{-1}\left(\boldsymbol{\theta}-\boldsymbol{\mu}\right)/2\right\} I_{(\boldsymbol{a}\leq \boldsymbol{A\theta}\leq \boldsymbol{b})}, \tag{3.16}$$

where C_L is the normalizing constant. Let us consider $\boldsymbol{Z} = \boldsymbol{A\theta}$. Then, according to the linear transformation property of multivariate normal distribution, the first part of Eq.(3.16) must change into the PDF of multivariate normal distribution $N\left(\boldsymbol{A\mu}, \boldsymbol{A\Sigma A}^T\right)$ for $\boldsymbol{Z}$. Thus, $\boldsymbol{Z}$ has the PDF as follows:

$$C_T^{-1} exp\left\{-\left(\boldsymbol{Z}-\boldsymbol{A\mu}\right)^T \left(\boldsymbol{A\Sigma A}^T\right)^{-1}\left(\boldsymbol{Z}-\boldsymbol{A\mu}\right)/2\right\} I_{(\boldsymbol{a}\leq \boldsymbol{Z}\leq \boldsymbol{b})}, \tag{3.17}$$

where C_T is the new normalizing constant after transformation. Equation (3.17) shows the PDF of $TN(\boldsymbol{A\mu}, \boldsymbol{A\Sigma A}^T; \boldsymbol{a}, \boldsymbol{b})$. Moreover, following the same steps as above, if $\boldsymbol{A}^{-1}$ exists, then $\boldsymbol{\theta} = \boldsymbol{A}^{-1}\boldsymbol{Z}$, and the proof is complete. □

The monotonicity conditions of degree 1 and degree 2 infinite support B-splines can be analytically imposed using Lemma 3. In this regard, online updating based on the linear inequality constraints of Lemma 1 reduces to a simpler form of box constraints on the coefficients of the mixed effects model. Thus, if we had an approach to update the random coefficients of B-spline basis functions in a box constrained multivariate normal distribution, then we could convert back the updated coefficients according to Lemma 3 into the corresponding linear inequality constrained multivariate normal distribution. Our approach for updating this simpler form of constraints is based on the constrained Kalman filter proposed in Wilhelm et al. (2012) and Son et al. (2016).

The online Bayesian updating procedure discussed in section 3.3.1 eventually gives $\hat{\boldsymbol{\mu}}_{i,h}$ and $\hat{\boldsymbol{\Sigma}}_{i,h}$ where $\hat{\boldsymbol{\mu}}_{i,h} \in \mathbb{R}^d$. The true individual parameter $\boldsymbol{\theta}_i$ for a specific unit is unobservable and should be estimated by the posterior mean $\hat{\boldsymbol{\mu}}_{i,h}$. However applying Lemma 1 and Lemma 3 respectively, suggest that the transformed vector of random coefficients should satisfy a specific set of box constraints. Thus, the posterior distribution of this new transformed vector of random coefficients should be truncated at certain boundaries. This can be achieved through a PDF truncation step in addition to the Bayesian updating step.

To be more specific, suppose that we transform the truncated posterior multivariate normal distribution with linear inequality constraints of Lemma 1 for unit i at time t_h $\left(LN\left(\hat{\boldsymbol{\mu}}_{i,h}, \hat{\boldsymbol{\Sigma}}_{i,h}; \boldsymbol{a}, \boldsymbol{b}, \boldsymbol{A}\right)\right)$ into the new simpler truncated multivariate normal distribution with box constraints denoted by $TN\left(\hat{\boldsymbol{\mu}}^n_{i,h}, \hat{\boldsymbol{\Sigma}}^n_{i,h}; \boldsymbol{a}, \boldsymbol{b}\right)$ using Lemma 3 where $\hat{\boldsymbol{\mu}}^n_{i,h} = \boldsymbol{A}\hat{\boldsymbol{\mu}}_{i,h}$ and $\hat{\boldsymbol{\Sigma}}^n_{i,h} = \boldsymbol{A}\hat{\boldsymbol{\Sigma}}_{i,h}\boldsymbol{A}^T$ and $\boldsymbol{A}, \boldsymbol{a}$ and $\boldsymbol{b}$ are

as given in (3.9). Moreover, we assume that $\boldsymbol{Z}_i = \boldsymbol{A}\boldsymbol{\theta}_i$ is the new vector of coefficients for unit i after transformation. The PDF for $TN\left(\hat{\boldsymbol{\mu}}_{i,h}^{n}, \hat{\boldsymbol{\Sigma}}_{i,h}^{n}; \boldsymbol{a}, \boldsymbol{b}\right)$ can be defined as follows:

$$f_T\left(\boldsymbol{Z}_i \middle| \boldsymbol{y}_i\left(\boldsymbol{t}_{i,1:h}\right); \boldsymbol{a}, \boldsymbol{b}\right) = \frac{f\left(\boldsymbol{Z}_i \middle| \boldsymbol{y}_i\left(\boldsymbol{t}_{i,1:h}\right)\right)}{F\left(\boldsymbol{b} \middle| \boldsymbol{y}_i\left(\boldsymbol{t}_{i,1:h}\right)\right) - F\left(\boldsymbol{a} \middle| \boldsymbol{y}_i\left(\boldsymbol{t}_{i,1:h}\right)\right)}, \quad \text{for } a_j \leq z_{ij} \leq b_j, \tag{3.18}$$

where $f_T\left(\boldsymbol{Z}_i \middle| \boldsymbol{y}_i\left(\boldsymbol{t}_{i,1:h}\right); \boldsymbol{a}, \boldsymbol{b}\right) = 0$ elsewhere, $f_T(\cdot)$ indicates the truncated density function of $\boldsymbol{Z}_i$ with box constraints and $f(\cdot)$ and $F(\cdot)$ denotes the probability density and cumulative density functions of multivariate normal distribution. After truncating the density, the mean $\hat{\boldsymbol{\mu}}_{i,h}^{TN} = \left[\hat{\mu}_{i,h,1}^{TN}, \ldots, \hat{\mu}_{i,h,d}^{TN}\right]^T$ and the covariance matrix $\widehat{Cov}_{i,h}^{TN}\left[z_{i,j}, z_{i,l}\right]$ for $j, l \in \{1, \ldots, d\}$ can be readily computed, as shown in appendix 3.8.2 where $TN\left(\hat{\boldsymbol{\mu}}_{i,h}^{n}, \hat{\boldsymbol{\Sigma}}_{i,h}^{n}; \boldsymbol{a}, \boldsymbol{b}\right) \approx N\left(\hat{\boldsymbol{\mu}}_{i,h}^{TN}, \hat{\boldsymbol{\Sigma}}_{i,h}^{TN}\right)$ due to preserving the reproducibility of conditional PDFs (Simon, 2006; Straka et al., 2012). The detailed procedure to obtain the truncated mean vector $\left(\hat{\boldsymbol{\mu}}_{i,h}^{TN}\right)$ and covariance matrix $\left(\hat{\boldsymbol{\Sigma}}_{i,h}^{TN}\right)$ is given in appendix 3.8.2 for the sake of completeness.

Applying the constrained Kalman filter approach, we can update the posterior distribution of transformed coefficients according to the set of box constraints given by Lemma 3. Finally, we need to transform back the updated mean vector and covariance matrix into the mean vector and covariance matrix of the originally truncated posterior distribution using Lemma 3. Figure 3.3 summarizes the overall procedure for online updating considering the monotonicity constraints for the mixed effects model based on degree 1 and degree 2 B-splines with infinite support using CKF.

General updating procedure based on Monte Carlo sampling for degree 3 B-spline with infinite support

The monotonicity conditions of degree 3 B-splines are in the form of non-linear inequality constraints as derived in Lemma 2. Therefore, the analytical procedure presented in the previous subsection is no longer applicable. In order to conduct online updating in this situation, we propose to use a more general approach based on the MC sampling. To be more specific, suppose that the unconstrained updating of mixed effects parameters based on the Bayesian procedure of section 3.3.1 results in the posterior distribution $p\left(\boldsymbol{\theta}_i \middle| \boldsymbol{y}_i\left(\boldsymbol{t}_{i,1:h}\right)\right) \sim N(\hat{\boldsymbol{\mu}}_{i,h}, \hat{\boldsymbol{\Sigma}}_{i,h})$ for unit i at time t_h. In order to model a monotonic degradation signal using degree 3 B-splines with infinite support, the random coefficients of mixed effects model should constantly satisfy the conditions derived by Lemma 2. The aim is to estimate the posterior distribution of random coefficients subject to

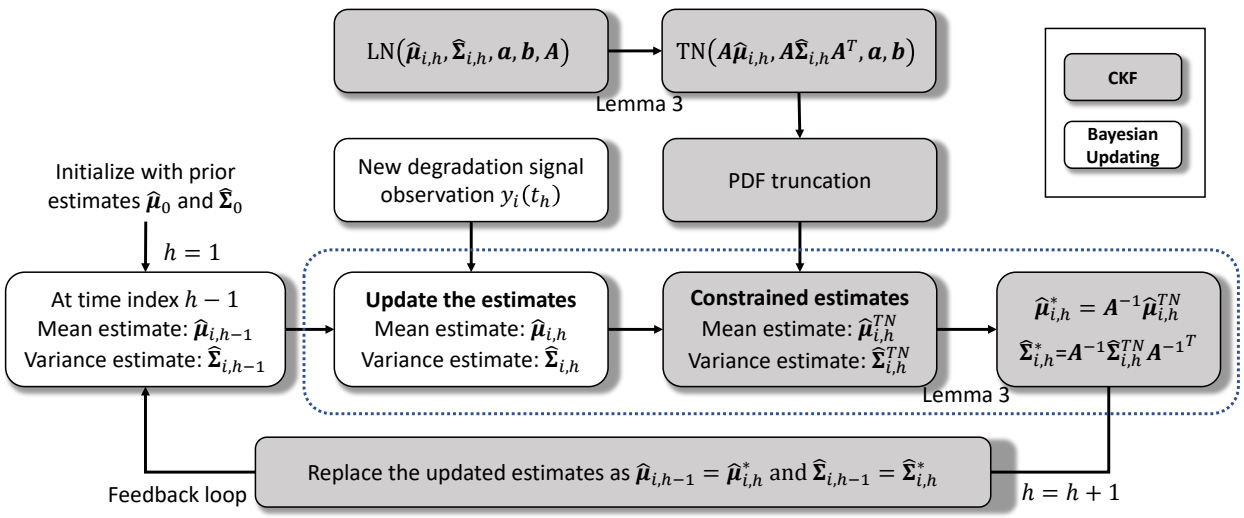

Figure 3.3: Summary of CKF procedure for online updating

constraints in (3.13), i.e., $p\left(\boldsymbol{\theta}_i \middle| \boldsymbol{y}_i\left(\boldsymbol{t}_{i,1:h}\right); \boldsymbol{\theta}_i \in C_h\right) \sim TN\left(\hat{\boldsymbol{\mu}}_{i,h}, \hat{\boldsymbol{\Sigma}}_{i,h}; \boldsymbol{\theta}_i \in C_h\right)$ where C_h denotes the constraints, space. The PDF of $TN\left(\hat{\boldsymbol{\mu}}_{i,h}, \hat{\boldsymbol{\Sigma}}_{i,h}; \boldsymbol{\theta}_i \in C_h\right)$ can be expressed similar to (3.15). Equation (3.15) presents a closed form description of the PDF of random variable $\boldsymbol{\theta}_i$ with respect to constraints in (3.13). Here, due to preserving the reproducibility of the conditional PDFs (Simon, 2006; Straka et al., 2012), the truncated PDF must be approximated by a Gaussian PDF as follows:

$$p\left(\boldsymbol{\theta}_i \middle| \boldsymbol{y}_i\left(\boldsymbol{t}_{i,1:h}\right); \boldsymbol{\theta}_i \in C_h\right) \approx N(\hat{\boldsymbol{\mu}}_{i,h}^{c}, \hat{\boldsymbol{\Sigma}}_{i,h}^{c}). \tag{3.19}$$

It should be noted that the Gaussian approximation of the truncated PDF in (3.19) has nonzero values outside the constrained region. However compared to the original unconstrained distribution, the volume of approximate Gaussian distribution above the constrained region is close to 1. Similar approximations can also be found in Straka et al. (2012) and Simon (2006). The moment of the PDF function in (3.19) can be written as follows:

$$\hat{\boldsymbol{\mu}}_{i,h}^{c} = \int \boldsymbol{\theta}_i p\left(\boldsymbol{\theta}_i \middle| \boldsymbol{y}_i\left(\boldsymbol{t}_{i,1:h}\right); \boldsymbol{\theta}_i \in C_h\right) d\boldsymbol{\theta}_i, \tag{3.20}$$

$$\hat{\boldsymbol{\Sigma}}_{i,h}^{c} = \int \left(\boldsymbol{\theta}_i - \hat{\boldsymbol{\mu}}_{i,h}^{c}\right)\left(\boldsymbol{\theta}_i - \hat{\boldsymbol{\mu}}_{i,h}^{c}\right)^T p\left(\boldsymbol{\theta}_i \middle| \boldsymbol{y}_i\left(\boldsymbol{t}_{i,1:h}\right); \boldsymbol{\theta}_i \in C_h\right) d\boldsymbol{\theta}_i. \tag{3.21}$$

The mean and covariance in (3.20) and (3.21) are difficult to solve analytically except for some special cases like linear inequality constraints (Straka et al., 2012). Here, we use MC sampling technique to approximate the integrals of Equations (3.20) and (3.21). The MC sampling

technique is based on approximating integrals using dense sampling of the truncated PDF. In order to approximate the integrals in (3.20) and (3.21), suppose that N samples $\boldsymbol{\theta}_i^{(r)}, r = 1, 2, \ldots, N$, are drawn from the unconstrained posterior distribution $N(\hat{\boldsymbol{\mu}}_{i,h}, \hat{\boldsymbol{\Sigma}}_{i,h})$. We divide the samples into two groups: the samples satisfying the constraints C_h denoted as $\boldsymbol{\theta}_i^{c,(l)},\ l = 1, 2, \ldots, N^c,\ N^c \leq N$ and the ones not satisfying the constraints. Thus, the mean and covariance matrix of the truncated PDF in (3.19) can be approximated as follows:

$$\hat{\boldsymbol{\mu}}_{i,h}^c \approx \frac{1}{N^c} \sum_{l=1}^{N^c} \boldsymbol{\theta}_i^{c,(l)}, \tag{3.22}$$

$$\hat{\boldsymbol{\Sigma}}_{i,h}^c \approx \frac{1}{N^c - 1} \sum_{l=1}^{N^c} \left(\boldsymbol{\theta}_i^{c,(l)} - \hat{\boldsymbol{\mu}}_{i,h}^c\right) \left(\boldsymbol{\theta}_i^{c,(l)} - \hat{\boldsymbol{\mu}}_{i,h}^c\right)^T. \tag{3.23}$$

Therefore, in order to find the approximate mean and covariance matrix of the truncated posterior PDF in (3.19), we need to simulate a large number of samples from $N(\hat{\boldsymbol{\mu}}_{i,h}, \hat{\boldsymbol{\Sigma}}_{i,h})$ and form the pool of samples satisfying the required constraints given in (3.13). Then the mean and covariance matrix of posterior distribution considering the constraints in (3.13) can be approximated using Equations (3.22) and (3.23). Figure 3.4 illustrates the online updating procedure considering the monotonicity constraints using MC sampling for a mixed effects model based on infinite support B-splines of degree 3 when we get a new observation from the in-service unit.

3.5. Numerical Study

In this section, the performance of the proposed mixed effects model framework will be investigated. Specifically, we first discuss the general procedure to simulate the degradation signals and evaluate the performance of different methods. Then, using the simulated signals, we demonstrate the advantages of our proposed method compared with some existing methods in the literature.

To motivate the application of the proposed approach, we consider an illustrative example. Let us assume we have signals generated from a true underlying function with noise. Specially we assume that the signals are generated from $R_y(t) = \omega_y t^{1.5} + \epsilon$, where $y = 1, 2, \ldots, 15$, $t \in [0, 10]$ and $\omega_y \sim N(1, 0.25^2)$. The observations are made at 30 evenly spaced points and the measurement noise is set to $\sigma_\varepsilon = 5$. Moreover, it is assumed that all the signals in the historical dataset are truncated after a specific observation time. Figure 3.5 demonstrates the signals generated in such

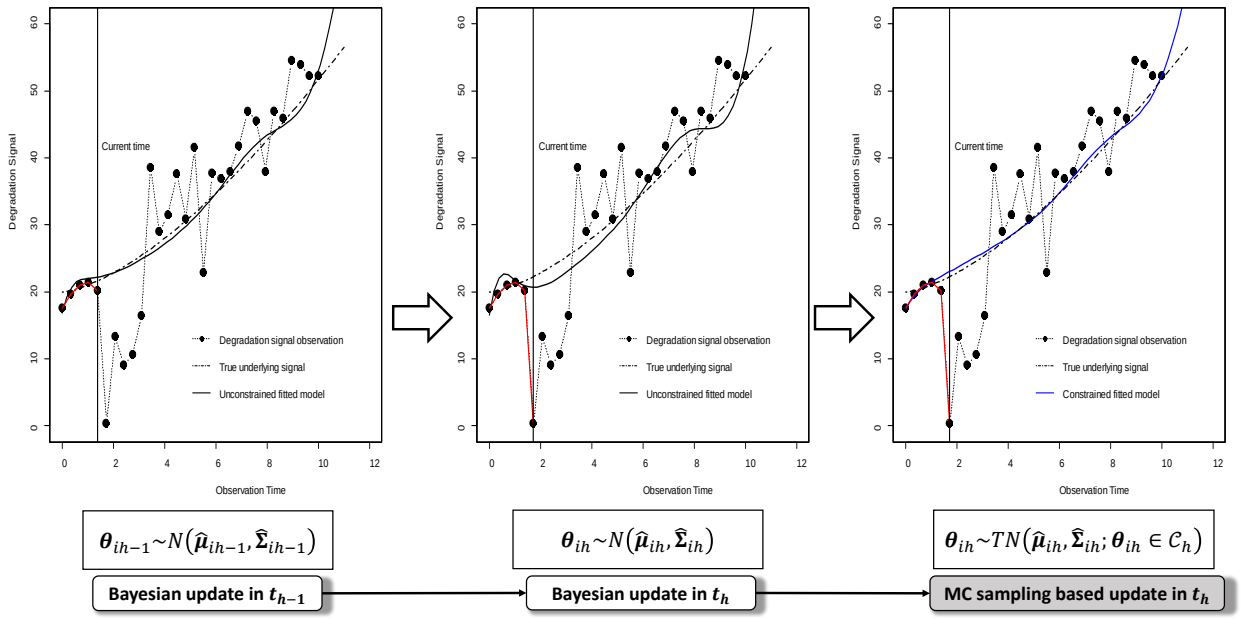

Figure 3.4: Online updating for the in-service unit using B-splines of degree 3 with infinite support.

a setting where it is assumed that all the historical signals are observed until time point $t = 8$. The failure threshold for this specific example is set to TH=30.

As shown in Figure 3.5, the failure time of all units is not observed. Therefore, if the new in-service unit fails after $t = 8$, then we need to extrapolate to find its failure time. Considering these truncated historical signals, we can fit a mixed effects model to predict the remaining useful life for the new in-service unit. In this regard, we consider the case where the mixed effects model is used both with regular degree 3 basis functions and degree 3 basis functions with infinite support. It is assumed that we have partial observations for the new in-service unit and the aim is to predict its failure time. Figure 3.6 demonstrates the prognosis results for the new in-service unit.

From Figure 3.6, it can be clearly observed that the prediction results based on the regular B-spline are misleading. The main reason is that the regular B-spline, as with most of the non-parametric approaches, is limited to the range of historical observations which prevents it from extrapolating beyond this range. However, for the infinite support B-spline, there is no such limitation and the method can extrapolate and predict beyond the range. This extrapolation results in accurate estimation of the failure time in this method as can be seen from Figure 3.6. However, it should be mentioned that the extrapolation result of the proposed framework is indeed more

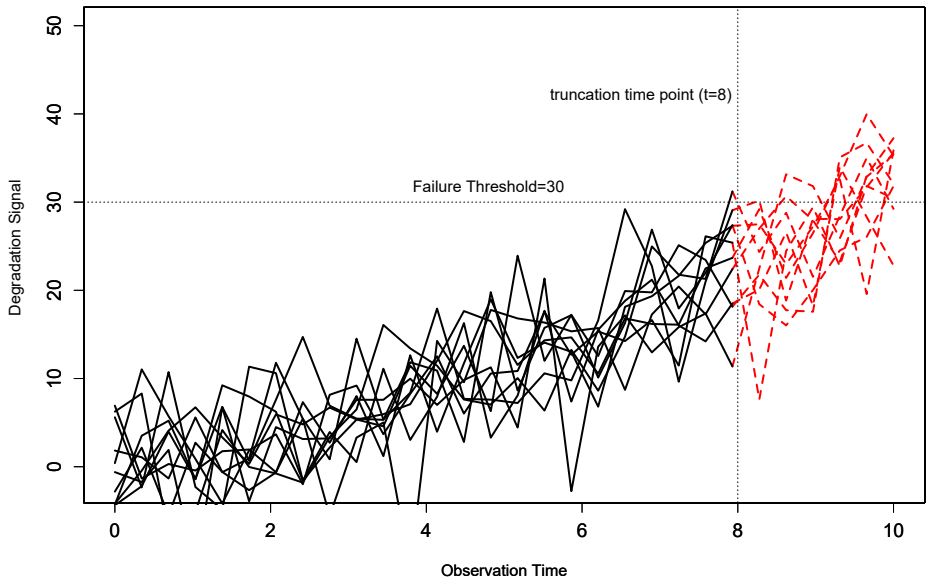

Figure 3.5: Truncated historical observations with noise.

accurate when the truncation point is closer to the failure time and the signal trend is similar after and before the truncation point.

Further, insight regarding the importance of monotonicity of the proposed approach can also be gained from Figure 3.6. As can be seen, the regular B-spline based approach with no constraints on the evolution of the degradation signals results in a signal which is not monotonically increasing. This contradicts the underlying domain knowledge that the degradation signal cannot decrease over time. This phenomenon, in practice, happens as a result of high level of noise in sensor data observations. Therefore, the most suitable approach is the one that allows for certain flexibility along with the ability to impose the domain knowledge. Imposing the appropriate monotonicity constraint in the infinite support B-spline approach can account for the high level of noise and adjust the prediction which, in turn, results in more accurate prediction of the failure time. This feature is well demonstrated in the evolution path of the in-service unit based on the two model settings in Figure 3.6.

Regarding the numerical study, we simulate the degradation signals from five different model settings. In each model setting, we report the prediction accuracy of different methods for partially observed in-service signal at varying time points t^*. Specifically, we report the prediction accuracy

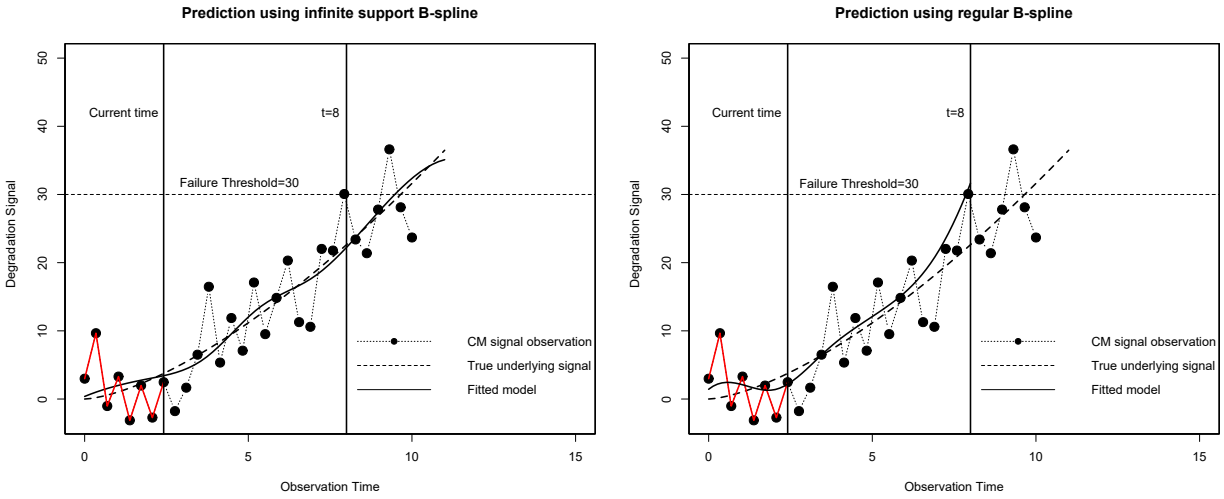

Figure 3.6: Prognostics using infinite support B-splines vs. regular B-splines.

for different percentiles of observed in-service signal (i.e., 40%, 60% and 80%). Our procedure to compare different methods is based on simulating Y=15 degradation signals from a specific model setting and then randomly selecting one of them as the in-service unit r, and the rest as the historical dataset. This procedure is repeated for 1000 times and each time we report the absolute error (AE) as our criterion for comparing different methods. The absolute error between the true failure time T_r and the estimated failure time $\hat{T}_r(t^*)$ can be described as follows:

$$AE\ (t^*) = \left|\hat{T}_r\ (t^*) - T_r\right|, \tag{3.24}$$

where as mentioned before a unit fails when its degradation signal passes the failure threshold.

The performance of different approaches are compared using a series of boxplots highlighting the distribution of AE through 1000 simulation runs. Specifically, we compare the performance of the proposed degree 3 infinite support B-spline with monotonicty constraint approach with four other methods proposed in the literature. The first one is the parametric mixed-effects model using an exponential function denoted by ME-Exp introduced by Gebraeel et al. (2005). The second method is the nonparametric FPCA approach proposed by Zhou et al. (2011). The third approach is the mixed-effects model using general polynomial function proposed by Son et al. (2013) and Rizopoulos (2011) denoted as ME-Poly. The appropriate degree of polynomial is determined using the Akaike information criteria (AIC). For this approach we also consider the case where the degree of polynomial is always fixed at 3 to have a measure of comparision with our proposed

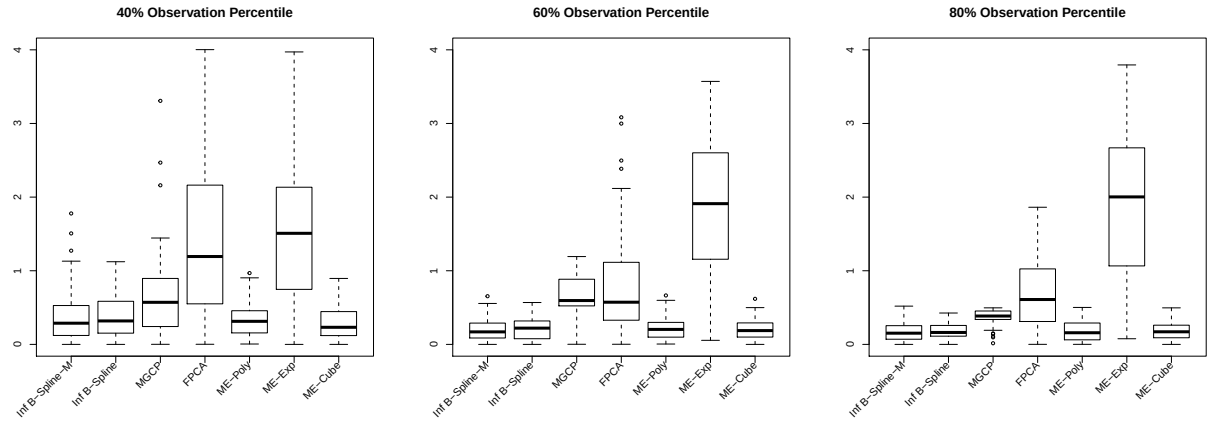

Figure 3.7: Prediction accuracy results of model setting I.

framework with degree 3 B-splines. We denote this approach as ME-Cube. Finally, we compare the performance of our approach with the MGCP approach of Kontar et al. (2018). In addition to the proposed framework with monotonicity constraints, we also consider the performance of infinite support B-spline without the monotonicity constraints to make the numerical study more complete. We denote the former as Inf B-spline-M, while the latter is denoted as Inf B-spline in our model settings.

In this study, we consider five model settings to compare the performance of different approaches. In model setting I, we highlight the importance of monotonicity in degradation modeling. Specifically in model setting I, we adopt the quadratic function defined in Kontar et al. (2018). In this regard, we consider the setting where the outputs for the Y curves are generated from the $R_y(t) = \omega_{1,y}^I t^2 + \epsilon$, where $y = 1, 2, \ldots, Y$, $t \in [0, 10]$ and $\omega_{1,y} \sim N(1, 0.25^2)$. Moreover it is assumed that the observations are made at 30 evenly spaced points, the measurement noise standard deviation is set to $\sigma_\varepsilon = 0.5$ and the failure threshold is set at TH=40. In order to benchmark the result with the correctly specified parametric form, we use the quadratic function in the polynomial mixed effects model (ME-Poly). The results are demonstrated in Figure 3.7.

From Figure 3.7, we can see that the performance of the proposed non-parametric approach based on the B-Splines of infinite support is comparable to that of the correctly specified parametric model in ME-Poly approach. Specifically, in the earlier stage when only 40% of the in-service unit signal is available, the variance of prediction error for the proposed method is a little bit higher than the ME-Poly approach which is based on the true parametric function. This happens because

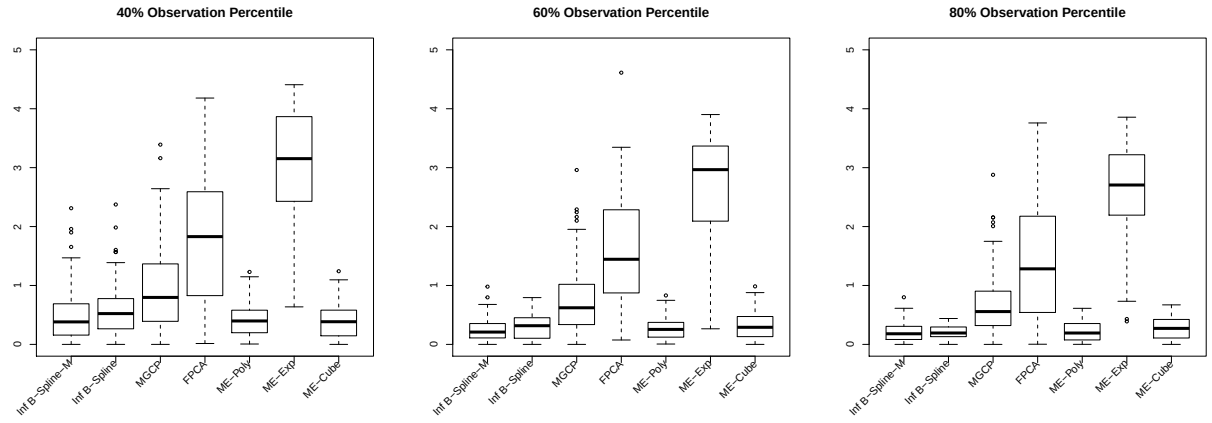

Figure 3.8: Prediction accuracy results of model setting II.

the ME-Poly approach which is based on the true parametric form, can inherently capture the trend even with a small number of observations. However, our proposed method requires more observations to capture the true underlying trend and its prediction accuracy improves as it gets more data. Moreover, we can see that by increasing the order of polynomial of mixed effect model in ME-Cube approach we get similar performance as in ME-Poly.

From the results in Figure 3.7, we can gain insight regarding the importance of the monotonicity constraint considered in our approach. The degradation signals generated in model setting I are inherently monotone and imposing monotonicity through our proposed framework increases the accuracy of its predictions. However, other non-parametric approaches considered in this study cannot guarantee monotonicity. This is, in fact, the main reason that their prediction errors are higher than that of our proposed method. It should also be mentioned that an important issue with MGCP approach is scalability as mentioned in Kontar et al. (2018). This issue becomes more prominent as we increase the number of signals in the historical dataset which leads the optimization of log-likelihood to converge to local optima. This, in turn, results in inferior result for the MGCP approach.

In order to further highlight the importance of extrapolation in our proposed approach, we conduct a numerical study with doubly truncated signals. Specifically, in model settings II, we adopt the signals introduced in model setting I with one modification. In model setting II, we assume that in addition to the failure threshold, all the signals in the offline stage are truncated after time $t = 7$. The prediction accuracy results of this model setting are given in Figure 3.8.

As can be seen from Figure 3.8, the performance of the infinite support B-spline approach proposed in this study is comparable to the ME-Poly approach which is based on the correctly specified parametric approach. As mentioned earlier, in this model setting, no historical observations are available after time $t = 7$. However, this does not significantly affect the performance of the ME-Poly approach as it is inherently based on the correctly specified parametric form. This, in fact, happens because even if the signals in the historical dataset are truncated after time $t = 7$, this approach can learn the true behavior of degradation signals based on the initial observations. Regarding the infinite support based B-spline approach, however, the evolution of the in-service degradation signal is extrapolated based on the behavior of the historical degradation signals until time $t = 7$. As can be seen from Figure 3.8, the performance of this extrapolation is comparable to that of the true parametric form in different observation percentiles. However, as for the other non-parametric approaches, the predictions outside the range of historical data converge to an overall mean function which result in wrong estimation of the failure time. This can be seen from the result of numerical study in Figure 3.8.

In order to further investigate the performance of our approach, we conduct three more numerical studies. Specifically, in model setting III, we focus on a nonlinear signal function adapted from Kontar et al. (2018). The output for Y curves are generated from $R_y(t) = 1.5t + \omega_{1,y}^{III} \sin(t) + \omega_{2,y}^{III}$, where $y = 1, 2, \ldots, Y$ and $t \in [0, 10]$. For the yth output, $\omega_{1,y}^{III} \sim U(0.8, 1.2)$ and $\omega_{2,y}^{III} \sim U(0, 7)$. It is assumed that there are 35 evenly spaced observations per signal. The measurement noise standard deviation is set to $\sigma_\varepsilon = 0.01$ and the failure threshold is set at TH=14. In model setting IV, we randomly sample 10 observations from each signal to further evaluate the robustness of our approach when sparse data are available. Moreover, model setting V investigates the performance of the proposed method when the noise level is high. Specifically, we set the measurement noise standard deviation to $\sigma_\varepsilon = 0.05$. Figure 3.9 demonstrates the results of model setting III.

From Figure 3.9, we can see that in different observation percentiles, the median and variance of the prediction errors of the proposed method are less than those of the other parametric and non-parametric approaches proposed in the literature. Moreover, it can be seen that the variance and median of prediction errors decreases with increase in the observation percentiles. In fact, as more data from the in-service unit becomes available in the online stage, the accuracy of different methods gets better. We can also get an interesting insight by comparing the results of

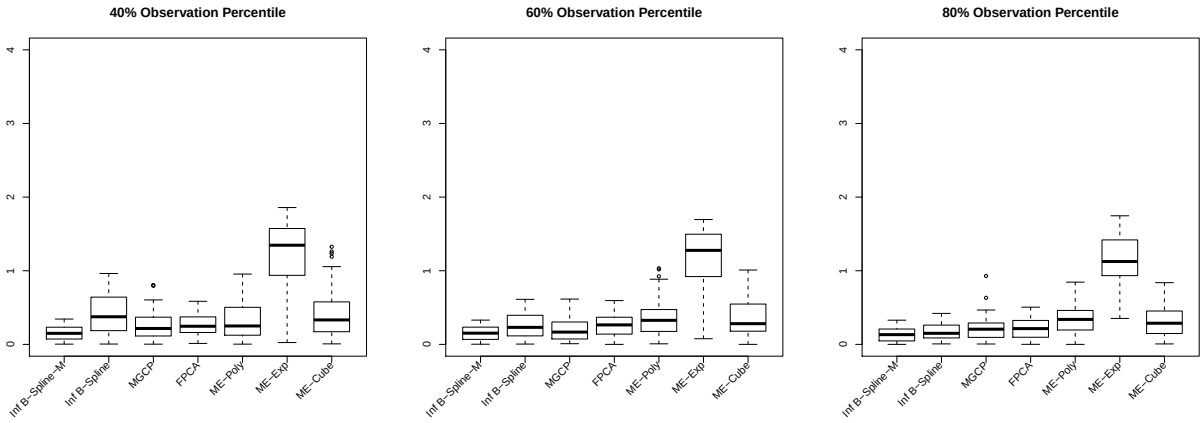

Figure 3.9: Prediction accuracy results of model setting III.

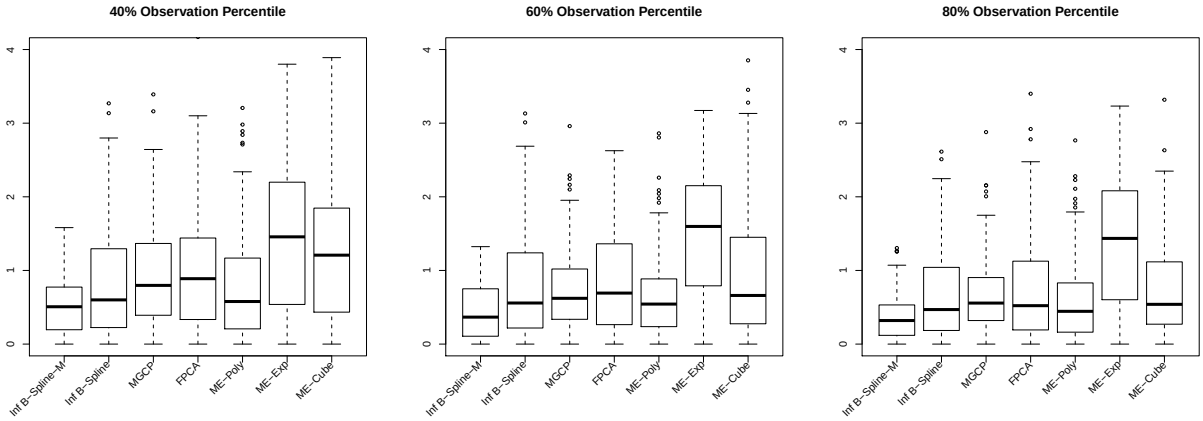

Figure 3.10: Prediction accuracy results of model setting IV.

the parametric and non-parametric approaches. As can be seen from Figure 3.9, the prediction based on the parametric approaches of ME-Poly, ME-Exp and ME-Cube leads to worse results than that of the non-parametric approaches in different observation percentiles. This signals the prominent hazard of defining a wrong parametric model in predicting the RUL. On the other hand, the non-parametric approaches enjoy enough flexibility to adapt with the specific trend of the signal. Moreover comparing the performance of Inf B-Spline-M and Inf B-Spline models, we can see that imposing monotonicity constraints increases the prediction accuracy of the proposed framework for nonlinear signal function forms.

Results from Figure 3.10 further demonstrate the robustness of different approaches to sparsity in observations from the in-service unit. It can be seen that sparsity in observations leads to increase

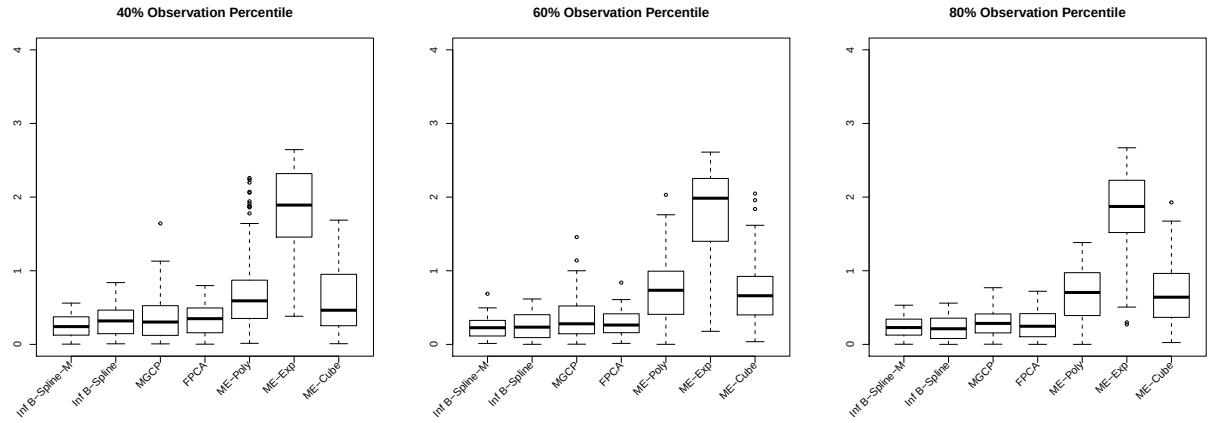

Figure 3.11: Prediction accuracy results of model setting V.

in the prediction errors of different approaches. However, the mean and variance of absolute error of predictions based on our proposed method remains less than those of other approaches. Moreover, Figure 3.11 showcases the impact of increase in the noise of observations. It can be seen that increase in the level of noise increases the prediction error of the different approaches; however, the performance of our proposed approach remains superior to that of other methods.

From the result of numerical study we can see that the importance of monotonicity constraint is, in fact, more notable in the early stage of prediction when the data is rare. This can be observed more vividly comparing the performance of the infinite support B-spline with and without monotonicity constraints in all our model settings. As can be seen from Figures 3.7-3.11, the infinite support B-spline with monotonicity constraint typically performs better than other approaches in the early stage of RUL prediction when we cannot learn the monotonic trend of signal based on available data. This better performance gets clearer, especially, when we have scarcity or higher noise level in our observations as discussed in model settings IV and V. The scarcity, insufficient sampling data and high measurement noise are, indeed, inevitable in most manufacturing systems which makes it crucial for decision making and control policies to have a robust measure of RUL.

3.6. Real-world case study

In this section, application of the proposed prognosis procedure on the real-world data collected from an automotive lead-acid battery aging test is demonstrated. The dataset contains 14 batteries

and each battery fails when its degradation signal reaches a prespecified threshold level. Figure 3.12 demonstrates the degradation signal evolution of batteries from this dataset. The failure threshold is defined as 5.4 and all the units are considered failed once their degradation signal hits the failure threshold which results in truncated signals. Due to confidentiality, the data presented in Figure 3.12 has been slightly modified from the original data, but this modification does not affect our study here.

In order to compare the performance of different methods, we use the leave-one-out cross validation approach. Specifically, we consider that one of the 14 batteries is the in-service unit and the model fitting in offline stage is performed for the remaining 13 ones. Then, the predictions for the in-service battery is performed for different percentiles of its lifespan (i.e., 40%, 60% and 80%). Both degree 3 and degree 2 infinite support B-spline with monotonicity constraint are used in this case study. We denote the former as Inf B-Spline-D2 while the latter is denoted as Inf B-Spline-D3. The whole procedure is repeated 14 times and the AE is calculated each time. Figure 3.13 summarizes the results for the case study.

To the best of authors, knowledge, there is no general physical model for the degradation of

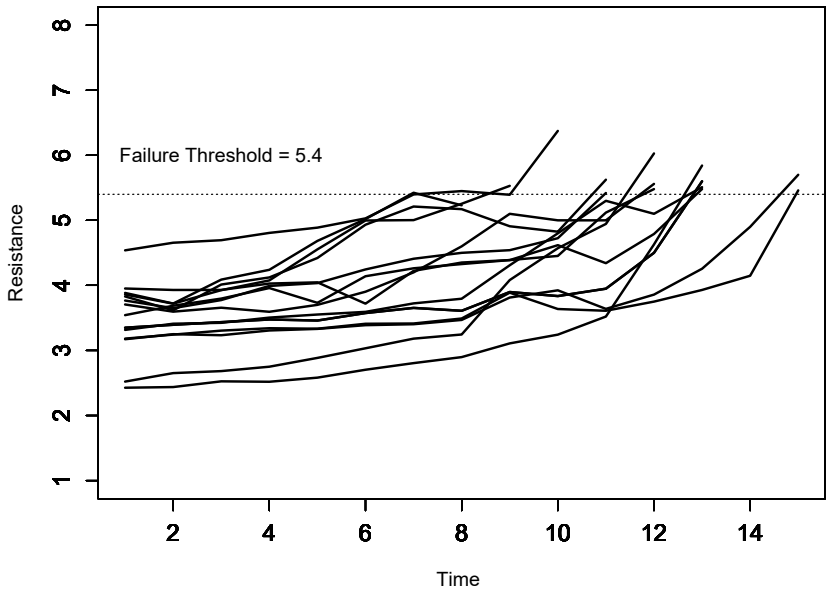

Figure 3.12: Battery resistance data from an accelerated aging test.

lead acid batteries. Therefore, a quadratic degradation path is used for the ME-Poly approach. This further highlights the importance of non-parametric approaches in degradation modeling when there is no general physical model. As can be seen from Figure 3.13, in different percentiles of the observed signal of the in-service unit, our approach based on degree 3 B-splines of infinite support performs relatively better than the other approaches proposed in literature. The main reason for the superior performance of our method is that it can effectively deal with truncated signals using the basis functions of infinite support. This feature combined with the monotonicity constraint on the evolution of the degradation signal guarantee that predictions are not limited to the range of historical data as with other non-parametric approaches. On the contrary, in non-parametric approaches like MGCP, predictions outside the range of historical data converge to an overall mean function which is typically defined as zero. This, indeed, results in wrong estimation of the RUL as the predications may never hit the failure threshold. However, this is not an issue in our approach which is based on B-splines of infinite support. Moreover comparing B-splines models, we can see that the degree 3 B-splines which provide higher flexibility have a better performance in terms of the absolute error compared with the degree 2 B-spline. Thus, the case study further confirms the results of the numerical study that, in the case of truncated degradation signals, the performance of our proposed approach is superior to the methods proposed in the literature.

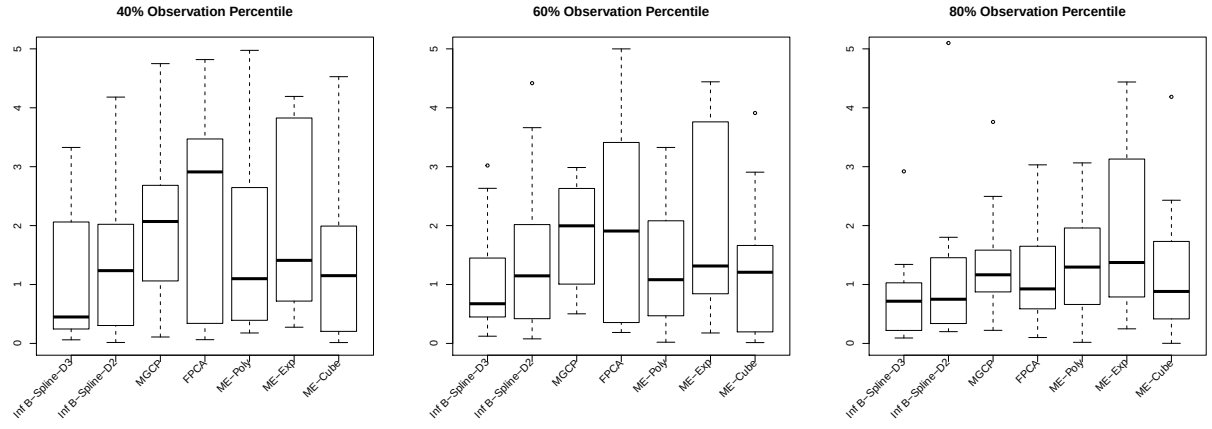

Figure 3.13: Prediction accuracy results for case study.

3.7. Conclusion

In this chapter, a non-parametric approach to modeling and prognosis of degradation signals using B-splines in a mixed effects framework is proposed. Unlike most of non-parametric approaches that rely on a historical sample of complete degradation signals, our approach is suitable for modeling truncated signals. In this regard, our approach is based on the B-splines augmented with basis functions of infinite support. One advantage of using this framework is that it allows us to extrapolate the evolution of the in-service degradation signal beyond the range of truncated degradation signals from our historical dataset.

Moreover, the B-spline setting allows us to encode the inherent monotonic evolution path of degradation signals. In this regard, the necessary and sufficient conditions to guarantee monotonic evolution of degradation signals in a mixed effects model based on B-splines of infinite support are derived. Our approach for updating random coefficients of the proposed mixed effects model with B-splines of degree 1 and degree 2 considering the derived monotonicity constraints is based on transforming the resulted truncated multivariate normal distribution of coefficients into a simpler form of box constrained multivariate normal distribution and updating using the constraint Kalman filter. Regarding the B-splines of degree 3, slightly more complicated necessary and sufficient monotonicity conditions based on polynomial representation of the B-spline basis functions are developed. The derived conditions for updating the mixed effects model in the online stage in this case leads to a truncated multivariate normal distribution with non-linear inequality constraints. In order to estimate the mean and covariance matrix of the resulting truncated PDF, we resort to the Monte Carlo sampling technique. The results of our numerical study along with the real-world case study confirm the advantage of the proposed framework in dealing with truncated signals.

In this study, we have only considered modeling of one degradation signal. However, most of the contemporary real-time monitoring systems tend to collect more than one degradation signal. In such cases, the need for developing more sophisticated degradation modeling approaches arises that can deal with both the issues of monotonicity and truncated degradation signal paths. This can be considered as a potential future research direction that we intend to pursue.

3.8. Appendix

3.8.1. Induction Formula for Infinite Support B-splines

The induction formula for the infinite support B-spline of degree $1 \leq n \leq k$ is as follows:

$$\begin{cases} b_{j,n}(t) := \frac{\gamma_j - t}{C_0} b_{j,n-1}(t), & j = 0, \\ b_{j,n}(t) := b_{j-1,n-1}(t) + \frac{\gamma_j - t}{C_0} b_{j,n-1}(t), & 1 \leq j < min(n,k), \\ b_{j,n}(t) := \begin{cases} b_{j-1,n-1}(t) + \frac{\gamma_j - t}{\gamma_j - \gamma_{j-n}} b_{j,n-1}(t), & if k > n \\ b_{j-1,n-1}(t) + b_{j,n-1}(t), & if k = n \end{cases} & j = min(n,k) \\ b_{j,n}(t) := \frac{t - \gamma_{j-n-1}}{\gamma_{j-1} - \gamma_{j-n-1}} b_{j-1,n-1}(t) + \frac{\gamma_j - t}{\gamma_j - \gamma_{j-n}} b_{j,n-1}(t), & min(n,k) + 1 \leq j < max(n,k), \\ b_{j,n}(t) := \begin{cases} b_{j,n-1}(t) + \frac{t - \gamma_{j-n-1}}{\gamma_{j-1} - \gamma_{j-n-1}} b_{j-1,n-1}(t), & if k > n \\ b_{j-1,n-1}(t) + b_{j,n-1}(t), & if k = n \end{cases} & j = max(n,k) \\ b_{j,n}(t) := \frac{t - \gamma_{j-n-1}}{C_1} b_{j-1,n-1}(t) + b_{j,n-1}(t), & max(n,k) + 1 \leq j < k + n, \\ b_{j,n}(t) := \frac{t - \gamma_{j-n-1}}{C_1} b_{j-1,n-1}(t), & j = k + n \end{cases} \tag{3.25}$$

where the term $\frac{t - \gamma_{j-n-1}}{\gamma_{j-1} - \gamma_{j-n-1}}$ and $\frac{\gamma_j - t}{\gamma_j - \gamma_{j-n}}$ are replaced by 1 and 0 respectively, when their denominators are equal to zero. Regarding the choice of constants C_0 and C_1, we use the guideline proposed in Corlay (2016). In this paper, we take $C_0 = C_1 = \frac{\gamma_{k-1} - \gamma_0}{k-1}$ if $\gamma_{k-1} > \gamma_0$ and $C_0 = C_1 = 1$ otherwise.

The B-spline basis functions of degree $n > k$ associated with knots Γ are defined as follows:

$$\begin{cases} b_{j,n}(t) := \frac{\gamma_j - t}{C_0} b_{j,n-1}(t), & j = 0, \\ b_{j,n}(t) := b_{j-1,n-1}(t) + \frac{\gamma_j - t}{C_0} b_{j,n-1}(t), & 1 \leq j < min(n,k), \\ \left(b_{j,n}\right)_{min(n,k) \leq j < max(n,k)+1} & \text{any basis of } \rho_{max(n,k)-min(n,k)}(\mathbb{R}) = \rho_{n-k}(\mathbb{R}) \\ b_{j,n}(t) := \frac{t - \gamma_{j-n-1}}{C_1} b_{j-1,n-1}(t) + b_{j,n-1}(t), & max(n,k) + 1 \leq j < k + n, \\ b_{j,n}(t) := \frac{t - \gamma_{j-n-1}}{C_1} b_{j-1,n-1}(t), & j = k + n \end{cases} \tag{3.26}$$

3.8.2. Details of Constrained Kalman Filter

Using the moment generating function (MGF), the mean $\hat{\boldsymbol{\mu}}_{ih}^{TN} = \left[\hat{\mu}_{ih,1}^{TN}, \ldots, \hat{\mu}_{ih,d}^{TN}\right]^T$ and the covariance matrix $\widehat{Cov}^{TN}\left[\theta_{i,j}, \theta_{i,l}\right]$ for $j, l \in \{1, \ldots, d\}$ of the $TN\left(\hat{\boldsymbol{\mu}}_{i,h}^{n}, \hat{\boldsymbol{\Sigma}}_{i,h}^{n}; \boldsymbol{a}, \boldsymbol{b}\right)$ with density function given in (3.18) can be computed as follows:

$$\hat{\mu}_{ih,j}^{TN} = \hat{\mu}_{ih,j}^{n} + \psi_j\left(\boldsymbol{a}, \boldsymbol{b}; \hat{\boldsymbol{\Sigma}}_{ih}^{n}\right) = \hat{\mu}_{ih,j}^{n} + \sum_{l=1}^{d} \sigma_{ih,j,l}\left\{\varphi_l\left(a_l\right) - \varphi_l\left(b_l\right)\right\}, \tag{3.27}$$

and

$$\begin{aligned}\widehat{Cov}^{TN}\left[z_{i,j}, z_{i,l}\right] = \sigma_{ih,j,l} &+ \xi_{j,l}\left(\boldsymbol{a}, \boldsymbol{b}; \hat{\boldsymbol{\Sigma}}_{ih}^{n}\right) + \eta_{j,l}\left(\boldsymbol{a}, \boldsymbol{b}; \hat{\boldsymbol{\Sigma}}_{ih}^{n}\right) \\ &- \psi_j\left(\boldsymbol{a}, \boldsymbol{b}; \hat{\boldsymbol{\Sigma}}_{ih}^{n}\right)\psi_l\left(\boldsymbol{a}, \boldsymbol{b}; \hat{\boldsymbol{\Sigma}}_{ih}^{n}\right),\end{aligned} \tag{3.28}$$

where $\sigma_{ih,j,l}$ denotes covariance between the jth and the lth parameters. The $\xi_{j,l}\left(\boldsymbol{a}, \boldsymbol{b}; \hat{\boldsymbol{\Sigma}}_{ih}^{n}\right)$ and $\eta_{j,l}\left(\boldsymbol{a}, \boldsymbol{b}; \hat{\boldsymbol{\Sigma}}_{ih}^{n}\right)$ functions used in (3.27) and (3.28) are respectively defined as follows

$$\xi_{j,l}\left(\boldsymbol{a}, \boldsymbol{b}; \hat{\boldsymbol{\Sigma}}_{ih}^{n}\right) = \sum_{q=1}^{d} \frac{\sigma_{ih,j,q}\sigma_{ih,l,q}\left\{a_q\varphi_q\left(a_q\right) - b_q\varphi_q\left(b_q\right)\right\}}{\sigma_{ih,q,q}}, \tag{3.29}$$

and

$$\begin{aligned}\eta_{j,l}\left(\boldsymbol{a}, \boldsymbol{b}; \hat{\boldsymbol{\Sigma}}_{ih}^{n}\right) = \sum_{q=1}^{d} \sigma_{ih,j,q} \sum_{q \neq o} \Bigg[\Bigg(&\sigma_{ih,l,o} - \frac{\sigma_{ih,q,o}\sigma_{ih,l,q}}{\sigma_{ih,q,q}}\Bigg) \\ &\times\left\{\varphi_{q,o}\left(a_q, a_o\right) + \varphi_{q,o}\left(b_q, b_o\right) - \varphi_{q,o}\left(a_q, b_o\right) - \varphi_{q,o}\left(b_q, a_o\right)\right\}\Bigg]\end{aligned} \tag{3.30}$$

where φ_l and $\varphi_{q,o}$ are univariate and bivariate marginal density functions. The univariate marginal density is $\varphi_l(x) = \int_{\boldsymbol{\Omega}_{-l}} f_T(x, \boldsymbol{Z}_{-l})\, d\boldsymbol{Z}_{-l}$ where $\boldsymbol{Z}_{-l}$ is a $(d-1)$-dimensional vector that excludes $z_{i,l}$ and $\boldsymbol{\Omega}_{-l} = \left\{a_j \leq z_{i,j} \leq b_j : \forall j \neq l, j = 1, \ldots, d\right\}$. The bivariate marginal density is $\varphi_l(x, y) = \int_{\boldsymbol{\Omega}_{-q-o}} f_T\left(x, y, \boldsymbol{Z}_{-q-o}\right)\, d\boldsymbol{Z}_{-q-o}$ where $\boldsymbol{Z}_{-q-o}$ is a $(d-2)$-dimensional vector $\boldsymbol{Z}_{-q-o} = \left[z_{i,1}, \ldots, z_{i,q-1}, z_{i,q+1}, \ldots, z_{i,o-1}, z_{i,o+1}, \ldots, z_{i,d}\right]^T$ that excludes both $z_{i,q}$ and $z_{i,o}$ for $q \neq o$, and $\boldsymbol{\Omega}_{-q-o} = \left\{a_j \leq z_{i,j} \leq b_j : \forall j \neq q \text{and} \forall j \neq o, j = 1, \ldots, d\right\}$ for $q \neq o$.

Chapter 4

Stochastic Prognostics under Multiple Time-varying Environmental Factors*

4.1. Overview

Prediction of the remaining useful life of in-field components, traditionally, relies on condition monitoring signals which are correlated with the physical degradation of the system. Many models assume that condition monitoring signals behave under similar environmental conditions (e.g. pressure, temperature, workload and relative humidity) or these conditions have no effect on degradation process. In this chapter, we propose a Brownian motion process with a stress-dependent drift to model multiple time-varying environmental covariates. A semiparametric regression approach utilizing penalized splines is, further, proposed to model the environmental covariates-drift relationship. The unique feature of our approach is that it does not assume a functional form for the degradation process drift and models multiple environmental covariates' effect on the degradation process. Moreover, the model is combined with in situ degradation measurements of the in-field unit and its environmental conditions to predict the unit's remaining useful life through a Bayesian updating scheme. The performance of the proposed framework is investigated and benchmarked through analysis based on numerical studies and a case study using real-world data of frying oil degradation collected from connected fryers.

*This chapter is based on the paper: Jahani, S., Zhou, S. and Veeramani, D., 2020. Stochastic Prognostics Under Multiple Time-varying Environmental Factors. Under Review at *Reliability Engineering & System Safety*.

4.2. Introduction

Recent advances in sensor technology and wireless communication systems are playing a significant role in what is referred to as the Internet of Things (IoT). Remote condition monitoring of physical assets using sensor data provides unprecedented opportunity for assessing the health and performance of engineering systems. Many statistical models have used sensor data, typically referred to as condition monitoring (CM) signals e.g. internal resistance of automotive battery or vibration signal of a rotating machinery, to predict the remaining useful life (RUL) of in-service units (Kontar et al., 2018; Gebraeel et al., 2009). In such models, a historical database of CM signals is utilized to predict the RUL of an in-service unit through a linkage between the historical data and real-time CM information collected from the in-service units. A unit is typically deemed failed once its CM signal reaches a pre-specified threshold value (Nelson, 2009).

In most of the existing RUL prediction models, it is assumed that the units perform under a fixed operating condition (e.g. pressure, temperature, workload and relative humidity), i.e. the environmental condition has no effect on the failure and degradation process (Kontar et al., 2018, 2017; Son et al., 2016; Liao et al., 2021; Wen et al., 2018; Barri et al., 2020). However, in many cases, the environmental condition varies with time and units may be exposed to different operating conditions. Under such circumstances, the degradation of an operating unit can greatly decelerate or accelerate, and the CM signal may exhibit different evolution rate over time. For products with degradation driven by environmental conditions, information about these variables can be critical for modeling the degradation process. For example, the degradation of the frying oil is primarily driven by a series of physical and chemical reactions as a result of change in temperature, humidity, and other factors affecting oil quality during frying. There are many other examples where degradation is driven by the usage and environmental variables, such as degradation of ball bearings, the loss of color and gloss of an automobile coating, and corrosion in oil transportation pipeline.

Development in technology makes collection and transmission of massive amount of data possible in many systems. Nowadays, it is common to dynamically record product/system usage as well as other environmental condition information like temperature, humidity, and etc. Environmental condition data contains rich information and can be utilized for modeling and predicting product

reliability. Most of the literature that incorporates environmental condition in reliability modeling is based on proportional hazards models. Such models handle the environmental conditions by incorporating them as covariates in the parametric hazard functions. For instance, Jardine et al. (1997) used the hazard model for condition-based maintenance by modeling different attributes of CM signals as covariates. Along this line, Banjevic and Jardine (2006) modeled the operating condition as Markov processes and developed approximations for the failure time distribution. Moreover, Rizopoulos (2011) proposed a joint framework that incorporates a polynomial mixed effects model and the proportional hazards model. This framework was later extended in Zhou et al. (2014) through updating the parameters of the polynomial mixed effects models. Other extensions and applications of the proportional hazards model can be found in Gorjian et al. (2010) and Zhao et al. (2010).

For degradation data analysis, the operating condition and environmental effects are also available in several settings such as accelerated repeated measure degradation tests (Meeker et al., 1998) and accelerated destructive degradation tests (Escobar et al., 2003). Most of these approaches proposed in the literature for modeling the environmental conditions estimate the lifetime of the population rather than that of a single unit operating in the field. However the few approaches that utilize CM signals for RUL estimation are usually based on mixed effects model, gamma processes, Brownian motion process and other Lévy processes. Gebraeel and Pan (2008), for instance, extended the mixed effects model with an exponential function to provide individualized prognosis for an in-service unit with different attributes using a Bayesian approach. Doksum and Hoyland (1993) proposed a stress-dependent drift to account for environmental condition in accelerated life testing experiments. Later, Whitmore and Schenkelberg (1997) proposed a time-scale transformation for accelerated experiments to account for the level of stress under which the CM signals are operated. Lawless and Crowder (2004) modeled CM signals as a gamma process with random effects and covariates. Li et al. (2019) modeled the effect of a single time-varying environmental covariate based on a two-factor state-space model considering signal jumps at condition change points. Pang et al. (2021) proposed a non-linear diffusion process model to characterize the degradation process of a product and then a parametric model is developed to establish the relationship between a single environmental covariate and the model parameters. Similar ideas can be found in Liao and Tseng (2006), Liao and Tian (2013) and Al-Dahidi et al. (2016).

Most of the existing statistical models, including the above-mentioned studies, consider only the effect of a single environmental covariate on the degradation signal. Few studies extended this assumption to incorporate the effects of multiple environmental factors on CM signal modeling. Park and Padgett (2006) and Ye and Chen (2014), for instance, modeled the effect of multiple environmental covariates by assuming a known physics-based model. A limitation of these approaches is the need to specify the correct physical model for the covariate-CM signal relationship. However, there exist numerous practical situations where this parametric form is unknown or difficult to specify. For instance, consider the degradation of ball bearings operated under different loads and speeds where the parametric form of degradation signal as a function of environmental covariates is hard to specify (Bian and Gebraeel, 2013). As another case in point, consider the degradation of frying oil in fast food restaurants. During the frying process a complex series of physical and chemical reactions takes place, resulting in degradation of frying oil. In the field of food science, the physical and chemical changes of oil and its degradation during frying operations have been extensively studied through lab testing and experiments (Choe and Min, 2007; Juárez et al., 2011; Brühl, 2014). Although very useful, most of these studies are qualitative or use a simple quantitative model under a very specific well-controlled lab environment to describe oil degradation. Thus, the results in above studies cannot be directly used to model the oil degradation in a real-life setting, such as in a restaurant environment. An exception is the work by Hong et al. (2015) where they modeled the effect of multiple covariates on degradation process using a non-parametric general path model and considered a parametric model to describe the covariate process. While this approach works well in case all the units are exposed to the same environmental condition, it does not apply to the scenario that the environmental condition covariates are evolving uniquely for each unit. For instance, the case study of this chapter models the degradation of frying oil in different frying pots where the environmental conditions (e.g. temperature, cooking time, humidity, and etc.) are changing uniquely for each pot. An ideal degradation model in this case should be able to take into account this unique evolution of environmental conditions. With the growing usage of IoT-enabled fryers in fast food restaurants, the comprehensive dataset collected from the connected fryers enables us to establish a quantitative data-driven model to consider multiple dynamic factors in the oil degradation model. Little work has been done in degradation data modeling that considers the uniquely evolving environmental covariates. Table 4.1 summarizes the result of literature

survey on prognostics models considering time-varying environmental condition.

Table 4.1: Summary of existing literature on prognostics models considering time-varying environmental condition.

Number of covariates	**Covariate effect model**	**Online updating**	**Parameter estimation procedure**	**Unique evolution of environmental covariates**	**Sources**
Single	Parametric	No	Monte Carlo	No	Jardine et al. (1997); Escobar et al. (2003); Banjevic and Jardine (2006); etc.
Single	Parametric	Yes	MLE	No	Rizopoulos (2011); Zhou et al. (2014); Gebraeel and Pan (2008); Liao and Tian (2013); Pang et al. (2021); Li et al. (2019); Al-Dahidi et al. (2016); etc.
Single	Parametric	No	MLE	No	Lawless and Crowder (2004); etc
Multiple	Parametric	No	MLE	No	Park and Padgett (2006); Ye and Chen (2014); etc
Multiple	Non-parametric	Yes	MLE	No	Hong et al. (2015); Xu et al. (2016)
Multiple	Non-parametric	Yes	EM algorithm with penalized splines	Yes	Current work

The purpose of this study is to develop a degradation modeling framework that does not depend on a specific parametric form and considers the effect of multiple time-varying environmental covariates as well as their unit-to-unit variability. Specifically, we propose a stochastic Brownian motion process with a drift dependent on the environmental conditions to incorporate the

effects of multiple operational covariates. A semi-parametric regression model using penalized splines is considered to model the drift of proposed Brownian motion process. Estimation is then performed through casting the problem into a mixed effects modeling framework. A Expectation-Maximization (EM) procedure is further developed to estimate the parameters of the proposed framework. This framework offers a number of advantages. First, it is semiparametric and does not assume any rigid parametric form on the Brownian motion process drift. The penalized splines that combine a set of spline basis functions with a quadratic penalty on the corresponding coefficients, also, strike a balance between ovefitting and accuracy of covariate-drift relationship. Moreover, the mixed modeling framework proposed offers a natural way for choosing the smoothing parameters. The proposed framework allows for the unique evolution of environmental covariates for each unit. Also, the stochastic model can further be updated through a Bayesian procedure combining the degradation signal observations and environmental conditions to predict the RUL of the in-field unit in real-time.

The remainder of this chapter is organized as follows. Section 4.3 provides a detailed framework of our modeling approach and estimation procedure and presents the RUL prediction using online updating for the in-field units. To illustrate the effectiveness of our proposed approach, extensive numerical study and a case study based on the degradation data of frying oil are conducted in Section 4.4 and Section 4.5. Finally, Section 4.6 concludes the chapter with a short discussion.

4.3. Model Development

In this section, we first introduce the notation and then develop an offline modeling framework using a semi-parametric based Brownian motion process modeling the effect of multiple time varying environmental covariates on the degradation process. Then, an online updating procedure is proposed to combine the degradation data and environmental condition observations of the in-service unit with the developed offline model.

4.3.1. Notation for the data

Here, we introduce some notations for the degradation data model and the environmental covariate information. Suppose the database contains a historical dataset of N units. For the ith

unit, denote the degradation measurements at time $t_{i,j}$ by $X_i(t_{i,j})$, $i = 1, ..., N$, $j = 0, ..., n_i$, and n_i marks the last timepoint where the degradation measurement was taken. The history of degradation signal observations for unit i is denoted as $\boldsymbol{X}_i(\boldsymbol{t}_{i,0:n_i}) = \left[X_i(t_{i,0}), ..., X_i(t_{i,n_i})\right]^t$. Let $\boldsymbol{\omega}_i(\tau) = \left[\omega_{i,1}(\tau), \omega_{i,2}(\tau), ..., \omega_{i,q}(\tau)\right]^t$ be a vector denoting the values of q environmental covariates at time τ for unit i. The value of covariate l for unit i at the time τ is denoted by $\omega_{i,l}(\tau)$. The history of covariate process for unit i is denoted by $\boldsymbol{\Omega}_i(\boldsymbol{t}_{i,n_i}) = \{\boldsymbol{\omega}_i(\tau) : 0 \leq \tau \leq t_{i,n_i}\}$, which records the dynamic covariates information from time 0 to time t_{i,n_i} for unit i. We consider all the observed degradation signals and the corresponding operating condition for each unit i in our historical database as $\mathcal{D}_i$ and all observed data from N units as $\mathcal{D} = \{\mathcal{D}_i\}_{i=1}^N$.

4.3.2. Offline degradation modeling based on the Brownian motion process

Model Structure

The Borwnian motion process has several good properties and is often used to describe the degradation of products (Le Son et al., 2013; Ye and Chen, 2014; Abdel-Hameed, 2014; Riascos-Ochoa et al., 2016). In this study, we model the degradation based on a Brownian motion process as follows:

$$X(t) = x_0 + \int_0^t \Gamma(\boldsymbol{\omega}(\tau))d\tau + \sigma W(t), \tag{4.1}$$

where x_0 is the initial degradation, $\Gamma : \mathbb{R}^q \rightarrow \mathbb{R}$ is the corresponding drift dependent on the level of environmental covariates $\boldsymbol{\omega}(\tau)$ at time τ, and σ is the diffusion parameter. $W(t)$ denotes the standard Brownian motion with the following three properties:

1. $W(0) = 0$, where $W(t) \in (-\infty, +\infty)$.
2. $W(t + \Delta t) - W(t) \sim \mathcal{N}(0, \Delta t)$.
3. $W(t) \sim \mathcal{N}(0, t)$.

We introduce an additive regression model to incorporate operating condition information into the degradation model. In particular, the drift of process for unit i at time t can be modeled as follows:

$$\Gamma(\boldsymbol{\omega}_i(t)) = \beta_0 + \sum_{l=1}^{q} f_l\left(\omega_{i,l}(t); \boldsymbol{\beta}_l\right), \tag{4.2}$$

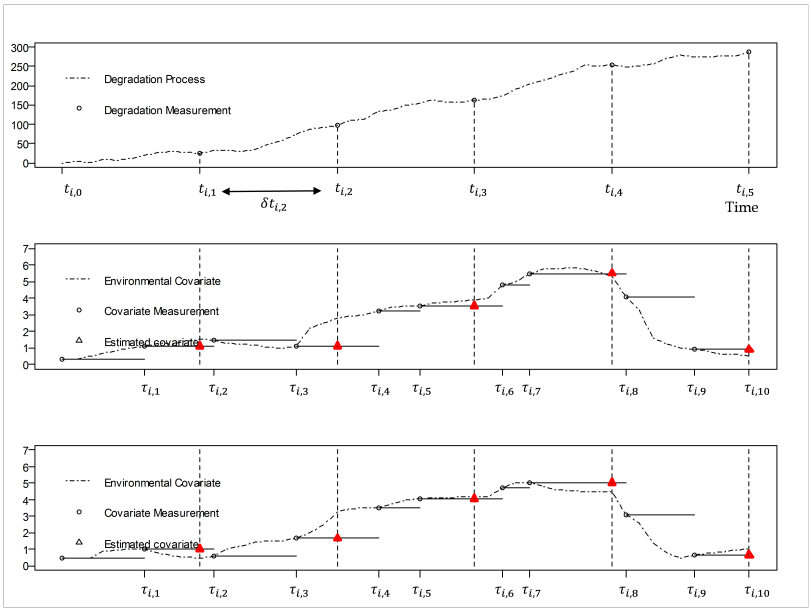

Figure 4.1: Unit degradation in response to time-varying environmental covariates.

where each function $f_l(.)$ models the effect of an environmental covariate. Here β_0 is the intercept and $\boldsymbol{\beta}_l$ denotes the parameter(s) in each function $f_l(.), l \in \{1, ..., q\}$. The coefficient vector of the functions parameters can be denoted as $\boldsymbol{\beta}' = \left[\boldsymbol{\beta}_1^t, ..., \boldsymbol{\beta}_q^t\right]^t$. For each covariate l, the function $f_l(\omega_{i,l}(\tau); \boldsymbol{\beta}_l)$ represents the effect of $\omega_{i,l}(\tau)$ at time τ on the drift of degradation process.

The cumulative damage model considered by equations (4.1) and (4.2) is motivated by the cumulative damage model for the accelerated failure-time model in Nelson (2001). For certain degradation mechanisms (e.g. wear out, crack growth, and decomposition of chemical structures), the assumption of cumulative effects is appropriate. In the motivating example of this article, the environmental variables cause certain chemical reactions which leads to degradation of oil over the time. Thus, the assumption of cumulative effects is appropriate for the application.

Two approaches are typically available to choose the functional form for the effect functions $f_l(.)$. The first approach is based on the models motivated by physical, chemical and engineering knowledge. For example, the Arrhenius relationship (Meeker and Escobar, 2014) is typically used to model the temperature effect on the degradation rate. When there is not enough information on the correct form of $f_l(.)$ from physical/engineering knowledge or when such models do not fit the data well, nonparametric models can be used. For this approach, the functions $f_l(.)$ can be estimated as the linear combination of the spline bases. Considering the B-spline bases to non-parametrically

model each covariate l, we have that:

$$f_l(\omega_{i,l}(\tau);\beta_l) = \sum_{d=1}^{d_l} B^t_{d,l}(\omega_{i,l}(\tau))\beta_{d,l}, \tag{4.3}$$

where $B_{d,l}(\omega_{i,l}(\tau))$ is the value of the corresponding B-spline basis evaluated at $\omega_{i,l}(\tau)$, $\beta_{d,l}$'s are B-spline coefficients and d_l is the number of B-spline bases for each covariate l.

Based on the independent increment property of the Brownian motion process $\Delta X_i(t_{i,j}) = X_i(t_{i,j}) - X_i(t_{i,j-1})$ is independent and identically distributed with a normal distribution $\mathcal{N}\Big(\int_{t_{i,j-1}}^{t_{i,j}} \Gamma(\boldsymbol{\omega}(\tau))d\tau, (\sigma\sqrt{\delta t_{i,j}})^2\Big)$ where σ is the diffusion of the process and $\delta t_{i,j} = t_{i,j} - t_{i,j-1}$. Considering the additive regression model in (4.2), the mean of $\Delta X_i(t_{i,j})$ in each interval $\left[t_{i,j-1}, t_{i,j}\right]$ can be written as follows:

$$\mu_{ij} = \int_{t_{i,j-1}}^{t_{i,j}} \Gamma(\boldsymbol{\omega}_i(\tau))d\tau = \beta_0\delta t_{i,j} + \int_{t_{i,j-1}}^{t_{i,j}} \sum_{l=1}^{q} f_l\left(\omega_{i,l}(\tau);\boldsymbol{\beta}_l\right) d\tau. \tag{4.4}$$

It should be noted that most of the IoT systems record the environmental covariates information in discrete time points. Therefore, a discrete-data version of (4.4) should be estimated for any real life application. Such an estimate can be obtained by replacing (4.4) with $\mu_{ij} = \beta_0\delta t_{i,j} + \sum_{l=1}^{q}\sum_{t_{i,j-1}\le\tau_{i,k}<t_{i,j}} f_l(\omega_{i,l}(\tau_{i,k});\beta_l)(\tau_{i,k+1} - \tau_{i,k})$. Here, $\tau_{i,k}$ are the time points where the environmental covariates were recorded for unit i. Thus, considering B-splines to model $f_l(.)$ as in (4.3), equation (4.4) can be rewritten as follows:

$$\mu_{ij} = \beta_0\delta t_{i,j} + \sum_{l=1}^{q}\sum_{d=1}^{d_l} G^t_{d,l}(t_{i,j})\beta_{d,l}, \tag{4.5}$$

where $G_{d,l}(t_{ij}) = \sum_{t_{i,j-1}\le\tau_{i,k}<t_{i,j}} B_{d,l}(\omega_{i,l}(\tau_{i,k}))(\tau_{i,k+1} - \tau_{i,k})$.

One popular way of modeling the additive regression is through penalized splines, and here we focus on the penalized B-splines or P-splines (Eilers and Marx, 1996). For covariate $l = 1, ..., q$ suppose we choose B-spline of degree m_l and we consider K_l interior knots equally spaced on the input interval. Then, the cumulative effect of each covariate in each time interval can be modeled as $s_l(t_{i,j}) = \boldsymbol{G}^t_l(t_{i,j})\boldsymbol{\beta}_l$ where $\boldsymbol{G}_l(t_{i,j})$ is constructed based on a set of $d_l = K_l + m_l - 1$ basis functions evaluated at $t_{i,j}$ and $\boldsymbol{\beta}_l = \left[\beta_{1,l}, ..., \beta_{d_l,l}\right]^t$ is the corresponding d_l-vector of coefficients.

To avoid overfitting, we augment the bases with a quadratic penalty on the coefficients, typically based on the squared difference of the adjacent coefficients. Such penalty can be written in the form of $P_l = \lambda_l \sum_{d=1}^{d_l-1}(\beta_{d+1,l} - \beta_{d,l})^2$ which has a matrix form as follows:

$$P_l = \lambda_l \boldsymbol{\beta}_l^t \begin{bmatrix} 1 & -1 & 0 & \dots \\ -1 & 2 & -1 & \dots \\ 0 & -1 & 2 & \dots \\ \vdots & \vdots & \vdots & \dots \end{bmatrix} \boldsymbol{\beta}_l = \lambda_l \boldsymbol{\beta}_l^t \boldsymbol{S}_l \boldsymbol{\beta}_l, \tag{4.6}$$

where $\lambda_l \geq 0$ is a smoothing parameter. Increase in the λ_l forces a smoother curve, while $\lambda_l = 0$ implies no penalization. In this study, we focus on the cubic B-splines and set the degree as 3 for all covariates, i.e. $m_1 = ... = m_q = 3$. Regarding the number of knots, for simplicity, we use the same number of interior knots for all q covariates.

Model Estimation

Let $\Psi = \left[\beta_0, \sigma, \boldsymbol{\lambda}^t\right]^t$ denote the parameters corresponding to the parametric component of the model where $\boldsymbol{\lambda} = [\lambda_1, \lambda_2, ..., \lambda_q]^t$. Also, let $\boldsymbol{\beta}' = \left[\boldsymbol{\beta}_1^t, ..., \boldsymbol{\beta}_q^t\right]^t$ denote the coefficients in the non-parametric component corresponding to the B-splines. The penalized log-likelihood estimate of model parameters considering the independent increment property of Brownian motion process can be written as follows:

$$\ell_P(\Psi, \boldsymbol{\beta}') = \sum_{i=1}^{N} \sum_{j=1}^{n_i} \ln\left(p(\Delta X_i(t_{i,j})|\Psi, \boldsymbol{\beta}')\right) - 2^{-1} \sum_{l=1}^{q} \lambda_l \boldsymbol{\beta}_l^t \boldsymbol{S}_l \boldsymbol{\beta}_l, \tag{4.7}$$

where $p(\Delta X_i(t_{i,j})|\Psi, \boldsymbol{\beta}') = \mathcal{N}(\beta_0 \delta t_{i,j} + \boldsymbol{G}^t(t_{i,j})\boldsymbol{\beta}', (\sigma\sqrt{\delta t_{i,j}})^2)$ and $\boldsymbol{G}(t_{i,j}) = \left[G_1^t(t_{i,j}), ..., G_q^t(t_{i,j})\right]^t$. Since the works of Kimeldorf and Wahba (1970), Wahba (1983) and Silverman (1985), it has been recognized that this penalized likelihood estimation can be reformulated as a mixed effects model by considering that the quadratic penalty amounts to assuming a normal random effects distribution. Specifically for $l = 1, ..., q$, let $p(\boldsymbol{\beta}_l|\lambda_l) = \mathcal{N}_{d_l}\left(0, (\lambda_l \boldsymbol{S}_l)^{-1}\right) = c_0 \lambda^{2^{-1}d_l} \exp(-2^{-1}\lambda_l \boldsymbol{\beta}_l^T \boldsymbol{S}_l \boldsymbol{\beta}_l)$ where c_0 is the normalizing constant independent of $\boldsymbol{\beta}_l$ and λ_l. Noting that $\boldsymbol{S}_l$ is of full rank, we then have the marginal log-likelihood as follows:

$$\ell_P(\Psi) = \ln\left(\int \prod_{i=1}^{N}\prod_{j=1}^{n_i} p(\Delta X_i(t_{i,j})|\Psi,\boldsymbol{\beta}')\prod_{l=1}^{q} p(\beta_l|\lambda_l)d\beta_l\right). \tag{4.8}$$

Formulating the additive regression drift as a mixed effects model allows us to exploit the wealth of mixed model methodology for inference. We can utilize an EM algorithm to estimate the model parameters.

The EM algorithm is an iterative method for computing maximum likelihood estimators by alternating between the expectation step, the E-step, and its maximization, the M-step, at every iteration until convergence. We notice here that the coefficients $\boldsymbol{\beta}'$ are actually hidden random variables in our mixed effects framework. The EM algorithm proceeds by computing the expectation of the log-likelihood of the complete data with respect to the posterior $p(\boldsymbol{\beta}'|\mathcal{D};\Psi)$ in the E-step. It is straightforward to show that the posterior distribution of $\boldsymbol{\beta}'$ is multivariate normal $\mathcal{N}_D(\boldsymbol{\beta}'|\boldsymbol{\mu}_{\beta'},\boldsymbol{\Sigma}_{\beta'})$ with :

$$\begin{aligned}
\boldsymbol{\Sigma}_{\beta'} &= \left(\frac{1}{\sigma^2}\sum_{i=1}^{N}\sum_{j=1}^{n_i}\frac{\boldsymbol{G}(t_{i,j})\boldsymbol{G}(t_{i,j})^t}{\delta t_{i,j}} + \boldsymbol{S}_\lambda\right)^{-1},\\
\boldsymbol{\mu}_{\beta'} &= \left(\frac{1}{\sigma^2}\sum_{i=1}^{N}\sum_{j=1}^{n_i}\frac{\boldsymbol{G}(t_{i,j})\boldsymbol{G}(t_{i,j})^t}{\delta t_{i,j}} + \boldsymbol{S}_\lambda\right)^{-1} \times \sum_{i=1}^{N}\sum_{j=1}^{n_i}(\Delta X_i(t_{i,j}) - \beta_0)\boldsymbol{G}(t_{i,j}),
\end{aligned} \tag{4.9}$$

where $\boldsymbol{S}_\lambda$ is a $D \times D$ block diagonal matrix formed by taking the blocks of $\lambda_l \boldsymbol{S}_l$ for $l = 1, ..., q$ and $D = \sum_{l=1}^{q} d_l$. At each iteration ν of the EM algorithm, the expected value of the logarithm of complete likelihood with respect to the posterior $p(\boldsymbol{\beta}'|\mathcal{D};\Psi)$ is as follows:

$$Q^{(\nu)}(\boldsymbol{\Delta X},\boldsymbol{\beta}';\Psi) = E_{p(\boldsymbol{\beta}'|\boldsymbol{\Delta X};\Psi^{(\nu)})}\{\ell_P(\Psi,\boldsymbol{\beta}')\}, \tag{4.10}$$

where $\boldsymbol{\Delta X} = \left\{\left\{\Delta X_i(t_{i,j})\right\}_{j=1}^{n_i}\right\}_{i=1}^{N}$ is the collection of degradation process shift observations from historical data. The E-step corresponds to analytical calculation of the function $Q^{(\nu)}$, considering the model parameters $\Psi^{(\nu)}$ calculated in the previous iteration. The M-step entails maximizing the $Q^{(\nu)}(\boldsymbol{\Delta X},\boldsymbol{\beta}';\Psi)$ with respect to the parameters β_0, σ and λ. In this regard, we get the following formulas to update the parameters β_0, σ and λ:

$$
\begin{aligned}
\beta_0^{(\nu+1)} =& \frac{1}{\sum_{i=1}^{N}\sum_{j=1}^{n_i}\delta t_{i,j}}\sum_{i=1}^{N}\sum_{j=1}^{n_i}(\Delta X_{ij} - \boldsymbol{G}^t(t_{ij})\boldsymbol{\mu}_{\beta'}^{(\nu)}),\\
\sigma^{(\nu+1)} =& \Big(\frac{1}{M}\sum_{i=1}^{N}\sum_{j=1}^{n_i}(\frac{(R_i(t_{ij}) - \boldsymbol{G}^t(t_{ij})\boldsymbol{\mu}_{\beta'}^{(\nu)})^2}{\delta t_{i,j}} + \frac{\boldsymbol{G}^t(t_{ij})\boldsymbol{\Sigma}_{\beta_l}^{(\nu)}\boldsymbol{G}(t_{ij})}{\delta t_{i,j}})\Big)^{1/2},\\
\lambda_p^{(\nu+1)} =& d_l\Big(\boldsymbol{\mu}_{\beta_l}^{(\nu)t}\boldsymbol{S}_l\boldsymbol{\mu}_{\beta_l}^{(\nu)} - \mathrm{tr}(\boldsymbol{S}_l\boldsymbol{\mu}_{\beta_l}^{(\nu)})\Big)^{-1},
\end{aligned}
\tag{4.11}
$$

where $M = \sum_{i=1}^{N} n_i$ and $R_i(t_{i,j}) = \Delta X_i(t_{i,j}) - \beta_0\delta t_{i,j}$ denotes the residual observations from parametric component. Please refer to appendix for a detailed derivation of these updating formulas. Notice that after initializing the parameters to some values ($\beta_0^{(0)}$, $\sigma^{(0)}$, $\boldsymbol{\lambda}^{(0)}$), the algorithm proceeds by iteratively performing the E-step and M-step until some convergence criterion is satisfied. Here, we note that inference for $\boldsymbol{\beta}'$ can be directly obtained since the sufficient statistic for its posterior is computed in the E-step. Using this property, we propose a Bayesian updating scheme for online updating based on the new data available from the in-service unit in the next section.

4.3.3. RUL prediction via online Bayesian updating

The proposed RUL prediction approach requires the simultaneous monitoring of both degradation signal and operating conditions. For in-service unit r at the current time point t_h when the prediction is to be made, assume s_r is the recent value of degradation signal observation, i.e. $\boldsymbol{X}_r(\boldsymbol{t}_{r,0:h}) = [X_r(t_{r,0}), ..., X_r(t_{r,s_r})]^t$ and $\boldsymbol{t}_{r,0:h} = [t_{r,0}, t_{r,1}, ..., t_{r,s_r}]^t$ where $t_{r,s_r} \leq t_h$. Moreover, we consider $\Delta\boldsymbol{X}_r(\boldsymbol{t}_{r,1:h}) = [\Delta X_r(t_{r,1}), ..., \Delta X_r(t_{r,s_r})]^t$ and $\hat{\boldsymbol{R}}_r(\boldsymbol{t}_{r,1:h}) = [\hat{R}_r(t_{r,1}), ..., \hat{R}_r(t_{r,s_r})]^t$ where $\hat{R}_r(t_{r,j}) = \Delta X_r(t_{r,j}) - \hat{\beta}_0\delta t_{r,j}$ as the vector of estimated residual observations for in-service unit r. In addition, let $\boldsymbol{\Omega}_r(\boldsymbol{t}_{r,h}) = \{\boldsymbol{\omega}_r(\tau) : 0 \leq \tau \leq t_{r,s_r}\}$ denote the environmental covariates observations from unit r up to s_r. The posterior distribution of the environmental effect coefficients $\boldsymbol{\beta}'^{(r)}$ based on the newly observed data from the in-service unit up to time s_r, can be computed as $p(\boldsymbol{\beta}'^{(r)}|\hat{\boldsymbol{R}}_r(\boldsymbol{t}_{r,1:h}), \boldsymbol{\Omega}_r(\boldsymbol{t}_{r,h}), \hat{\boldsymbol{\Psi}}) \propto p(\hat{\boldsymbol{R}}_r(\boldsymbol{t}_{r,1:h}), \boldsymbol{\Omega}_r(\boldsymbol{t}_{r,h})|\boldsymbol{\beta}'^{(r)}, \hat{\boldsymbol{\Psi}})\pi(\boldsymbol{\beta}'^{(r)}, \hat{\boldsymbol{\Psi}})$ where $p(\hat{\boldsymbol{R}}_r(\boldsymbol{t}_{r,1:h}), \boldsymbol{\Omega}_r(\boldsymbol{t}_{r,h})|\boldsymbol{\beta}'^{(r)}, \hat{\boldsymbol{\Psi}})$ denotes the likelihood for in-service unit r, which by the property of Brownian motion process is normally distributed, and $\pi(\boldsymbol{\beta}'^{(r)}, \hat{\boldsymbol{\Psi}})$ refers to the prior distribution estimated in the offline stage and in the E-step of EM algorithm. Assuming normally distributed

$\boldsymbol{\beta}'^{(r)}$, and following the conjugate property of multivariate normal distribution, the posterior is also normally distributed $p(\boldsymbol{\beta}'^{(r)}|\hat{\boldsymbol{R}}_r(\boldsymbol{t}_{r,1:h}), \boldsymbol{\Omega}_r(\boldsymbol{t}_{r,h}); \hat{\boldsymbol{\Psi}}) \sim \mathcal{N}(\hat{\boldsymbol{\mu}}_{\beta'_{r,h}}, \hat{\boldsymbol{\Sigma}}_{\beta'_{r,h}})$ where $\hat{\boldsymbol{\mu}}_{\beta'_{r,h}}$ and $\hat{\boldsymbol{\Sigma}}_{\beta'_{r,h}}$ represent the mean and covariance matrix of the posterior. Considering the prior parameter estimates $\boldsymbol{\mu}_{\beta'_0}$ and $\boldsymbol{\Sigma}_{\beta'_0}$, it is straightforward to derive the closed form expression for the posterior mean and covariance matrix as follows:

$$\hat{\boldsymbol{\mu}}_{\beta'_{r,h}} = \hat{\boldsymbol{\Sigma}}_{\beta'_{r,h}} \left[\frac{\boldsymbol{G}^t(\boldsymbol{t}_{r,1:h}) \Delta T^{-1} \hat{R}_r(t_{r,j})}{\sigma^2} + \boldsymbol{\Sigma}^{-1}_{\beta'_0} \boldsymbol{\mu}_{\beta'_0} \right],$$

$$\hat{\boldsymbol{\Sigma}}_{\beta'_{r,h}} = \left[\boldsymbol{\Sigma}^{-1}_{\beta'_0} + \frac{\boldsymbol{G}^t(\boldsymbol{t}_{r,1:h}) \Delta T^{-1} \boldsymbol{G}(\boldsymbol{t}_{r,1:h})'}{\sigma^2} \right]^{-1}, \tag{4.12}$$

where $\boldsymbol{G}^t(\boldsymbol{t}_{r,1:h}) = \left[\boldsymbol{G}(t_{r,1}), ..., \boldsymbol{G}(t_{r,s_r})\right]$, $\Delta T = \text{diag}(\delta t_{r,1}, ..., \delta t_{r,s_r})$. Also $\boldsymbol{\mu}_{\beta'_0}$, $\boldsymbol{\Sigma}_{\beta'_0}$ and σ can be replaced by their estimates $\hat{\boldsymbol{\mu}}_{\beta'_0}$, $\hat{\boldsymbol{\Sigma}}_{\beta'_0}$ and $\hat{\sigma}$ obtained in the previous section from the offline stage. It should be noted that the model updating performed in equation (4.12) involves the inversion of $\boldsymbol{\Sigma}_{\beta'_0}$ which has a computational complexity of $O((q \times d_l)^3)$. We note that $q \times d_l$ is always reasonably small and therefore updating of the parameters does not take much of time.

The RUL of a unit is defined as the remaining time until its degradation level reaches a pre-defined failure threshold D_F. Two assumptions for RUL prediction under time-varying environmental covariates can be considered. The first one assumes that the future environmental covariates are unknown and can be estimated from their most recent observation. Let T_r denote the RUL of unit r, i.e. $T_r = \inf\{t \geq 0 : X_r(t_{r,s_r}) + X_r(t) \geq D_F\}$ where $D_F \geq X_r(t_{r,s_r})$. Then assuming constant stress level $\boldsymbol{\omega}_r(t_{r,s_r})$ after t_{r,s_r} i.e. $\{\boldsymbol{\omega}_r(\tau) = \boldsymbol{\omega}_r(t_{r,s_r}) : t_{r,s_r} \leq \tau\}$, the RUL of unit r conditional on $\hat{\boldsymbol{\Psi}}$ and the updated coefficients $\boldsymbol{\beta}'^{(r)}$ follows an inverse Gaussian (IG) distribution as:

$$P(T_r = t|X_r(t_{r,s_r}), \boldsymbol{\Omega}_r(t_{r,h}), \boldsymbol{\beta}'^{(r)}, \hat{\boldsymbol{\Psi}}) \sim \mathcal{IG}(t; \mu_{\mathcal{IG}}(t_h), \lambda_{\mathcal{IG}}(t_h)), \tag{4.13}$$

where $\mathcal{IG}(t; ., .)$ represents the pdf of an IG distribution, $\mu_{\mathcal{IG}}(t_h) = \frac{D_F - X_r(t_{r,s_r})}{\hat{\beta}_0 + \boldsymbol{B}(\boldsymbol{\omega}_r(t_{r,h}))^t \hat{\boldsymbol{\mu}}_{\beta'_{r,h}}}$ is the mean parameter of IG distribution, and $\lambda_{\mathcal{IG}}(t_h) = \frac{(D_F - X_r(t_{r,s_r}))^2}{\hat{\sigma}^2}$ is the shape parameters of the IG distribution. Here, recall that $\boldsymbol{\omega}_r(t_{r,h})$ is the most recent observation of the environmental conditions for in-service unit r and $\boldsymbol{B}(\boldsymbol{\omega}_r(t_{r,h}))^t = [\boldsymbol{B}_1(\boldsymbol{\omega}_r(t_{r,h})), ..., \boldsymbol{B}_q(\boldsymbol{\omega}_r(t_{r,h}))]^t$ are the B-spline bases.

Typically we have control over the environmental covariates and they can be set according to the specific application. The second assumption, which is used in this study, assumes that the future operating conditions can be set in advance; therefore, the RUL of the component can be predicted based on the profiled environmental covariates. Assume that the stresses in the future after t_{r,s_r} is a time-varying series and denoted as $\mathbf{\Omega}'(t_{r,s_r}) = \{\boldsymbol{\omega}_r(\tau) : s_r \leq \tau\}$. It is quite difficult to obtain an analytical formula of the RUL distribution for a Brownian motion process under varying drift parameters. For this reason, we use a Monte Carlo simulation method to estimate the RUL distribution approximately. The basic idea is to simulate the evolution of the degradation process in the future with the knowledge at time t_{r,s_r}. For simplicity, the time interval for predictions are assumed to be uniform and equal to unit interval 1, namely $t_{r,s_r+j} - t_{r,s_r+j-1} = 1, j = 1, 2, ..., m$. For a simulated degradation path, the m-step prediction of the future state, that is $\boldsymbol{X}_r(t_{r,s_r})$, under varying stress series $\mathbf{\Omega}'(t_{r,s_r})$ is given by the following procedure:

Step 1: Generate a sample $\boldsymbol{\beta}'^{(r)^*}$ from $\mathcal{N}(\hat{\boldsymbol{\mu}}_{\beta'_{r,h}}, \hat{\boldsymbol{\Sigma}}_{\beta'_{r,h}})$;

for $j = 1, 2, ..., m$;

Step 2: Generate a sample $\Delta X_r(t_{r,s_r+j})$ from $\mathcal{N}(\hat{\beta}_0 + \sum_{l=1}^{q} \sum_{t_{r,s_r+j-1} \leq \tau_{r,k} < t_{r,s_r+j}} f_l(\omega_{r,l}(\tau_{r,k}); \beta_l'^{(r)^*})(\tau_{r,k+1} - \tau_{r,k}), \sigma^{*2})$

Step 3: Let $X_r(t_{r,s_r+j}) = X_r(t_{r,s_r+j-1}) + \Delta X_r(t_{r,s_r+j})$.

Repeat Step 1-3 U times (say $U = 1000$), we can obtain U simulated paths to predict the states of $X_r(t)$ after time t_{r,s_r}. To obtain the distribution of the RUL, we can determine when the U samples fail, respectively. As mentioned above, the RUL for a sample can be obtained by the first simulated steps when $\boldsymbol{X}_r(\boldsymbol{t}_{r,s_r+1:s_r+m})$ exceeds D_F. Then, we have U simulated RULs, which are denoted as $\{T_r^1, T_r^2, ..., T_r^U\}$. The mean and confidence interval can be estimated approximately using these simulated RULs. The mean RUL at time t_{r,s_r} is estimated by $\frac{1}{U}\sum_{u=1}^{U} T_r^u$. The approximated $100(1-\alpha)\%$ CI for RUL at time t_{r,s_r} is estimated by $\left[T_r^{(LB)}, T_r^{(UB)}\right]$, where $LB = \lfloor(\alpha/2) \cdot U\rfloor$, $UB = \lfloor(1-(\alpha/2)) \cdot U\rfloor$ and $\lfloor\cdot\rfloor$ means round to the nearest integer and $T_r^{(u)}$ is the u-th ordered statistic of the set of RULs for unit r.

4.4. Numerical Study

In this section we conduct simulations to validate the performance of the proposed modeling approach. Specially, we first discuss the general procedure to generate degradation signals considering the operating conditions and to evaluate the performance of different methods. Then using the simulated signals, we demonstrate the advantage of our proposed framework.

4.4.1. Simulation Setup

We simulate degradation signals from three model settings. In each model setting, we report the RUL prediction accuracy of a partially observed in-service unit at varying time points t^*. Specifically, we report the prediction accuracy for different percentiles of the observed in-service signal (i.e. 35%, 50% and 85%). Our procedure is based on simulating 20 degradation signals from a specific model setting and then randomly selecting one of them as the in-service unit, and treating the rest as our historical dataset. This procedure is repeated 1000 times, and each time we report the absolute error (AE) between the true RUL ($T_r(t)$) and the estimated RUL ($\hat{T}_r(t^*)$ as follows:

$$AE(t^*) = |\hat{T}_r(t^*) - T_r(t)|, \tag{4.14}$$

where, as mentioned before, a unit is deemed failed once its degradation signal passes its failure threshold. Specifically, we compare the performance of our approach with the degradation modeling approach proposed in Liao and Tian (2013) where a Brownian motion process with a parametric stress-dependent drift is defined to model the degradation process.

Let us first assume that we have signals generated from a Brownian motion process with a drift dependent on the effect of one environmental covariate where $\mu_{ij} = \beta_0 \delta t_{i,j} + \alpha_i \sin(\pi \omega_i(t_j))(t_{j+1} - t_j)$, $i \in \{1, ..., 20\}$, $j \in \{1, ..., 20\}$. Specifically, we assume that $\alpha_i \sim U[3, 3.5]$ and we generate ω_i from a uniform distribution $U[0, 1]$. The initial degradation measure is normally distributed as $x_0 \sim \mathcal{N}(20, 1)$, the diffusion is set to $\sigma = 1$ and degradation signal observations are made at equal time intervals $\delta t_{i,j} = 0.5, \forall i, j$. Figure 4.2 demonstrates the signals generated in such a setting.

As shown in Figure 4.2, the generated degradation signals are heterogeneous and do not follow a common functional form. The reason is that unlike the traditional RUL prediction models

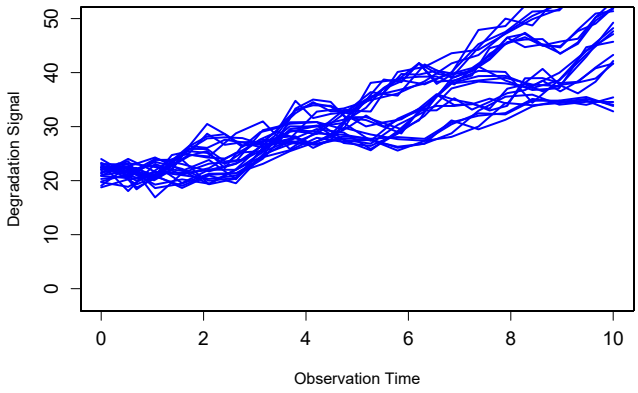

Figure 4.2: Historical signal observations

(Jahani et al., 2020; Kontar et al., 2018, 2017) where the degradation signals are generated from a common function and have similar temporal evolution, here in each degradation signal observation stage, the Brownian motion drift is generated according to a random covariate effect function. Considering these historical signal observations, we can use the framework proposed in this study which utilizes environmental covariate observations to model the degradation process. For the sake of comparison, we can fit the mixed effects model proposed in Jahani et al. (2020) to predict the RUL of a new in-service unit. The model in Jahani et al. (2020) utilizes B-splines to model the temporal evolution of degradation signals and does not consider the effect of environmental covariates. Figure 4.3 demonstrates the prognosis results for the new in-service unit considering the mean of the parameters' posterior and the future environmental conditions as discussed in section 4.3.3.

From Figure 4.3, it can be observed that the prediction results based on B-splines as proposed in Jahani et al. (2020) are misleading. The main reason is that the historical signal data is heterogeneous hence making it difficult, even for a non-parametric approach like B-splines, to converge to the true underlying signal of the in-service unit. However, the model based on the environmental covariate observations can quickly adapt to the trend of the new in-service unit. The reason is that this model is not limited to the temporal evolution of the degradation signal and performs regression on the environmental covariate which controls the degradation process evolution over the time in future.

In order to get insight on the performance of the proposed framework, we perform further

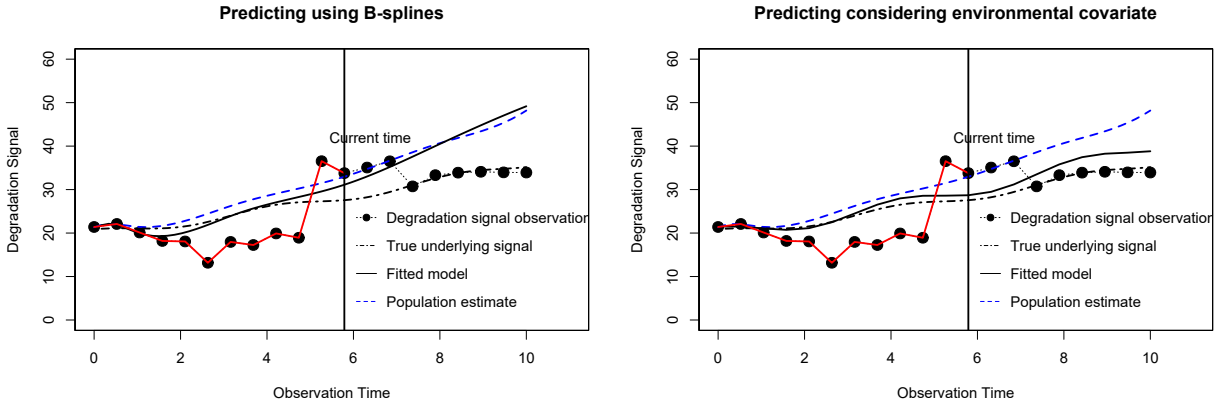

Figure 4.3: Prognostics using B-spline vs. using proposed method considering the environmental covariate.

numerical study. We assume that the initial degradation measure is $x_0 = 0.5$ and the diffusion parameter is set to $\sigma = 1$, which are identical across all units. Moreover, it is assumed that the degradation signal observations are made at equal time intervals $\delta t_{i,j} = 1, \forall i, j$, the environmental covariates are fixed during the time intervals, and the failure threshold is set to $D_F = 350$. We simulate degradation signals dependent on the effect of three environmental covariates from the Brownian motion with the following drift in each interval j of unit i:

$$\mu_{ij} = \beta_0 \delta t_{i,j} + \sum_{l=1}^{3} f_l(\omega_{i,l}(t_j); \beta_l)(t_{j+1} - t_j), \tag{4.15}$$

Specially, for $j \in \{1, ..., 30\}$ and $i \in \{1, ..., 20\}$ a vector of three covariates $(\omega_{i,l}(t), l = 1, 2, 3)$ is generated by simulating $\omega_{i,1}$ from a uniform distribution $U[0, 2]$, $\omega_{i,2} = 0.9\omega_{i,1} + e_1$ where $e_1 \sim U[0, 1]$ and $\omega_{i,3}$ from a uniform distribution $U[0, 1]$. We adopt the linear function of stress as proposed in Liao and Tian (2013) with some modifications to model the stress-drift relationship of $\omega_{i,1}$. Specially, we consider $f_1(\omega_{i,1}) = \alpha_{i,1}\omega_{i,1}$ where $\alpha_{i,1} \sim \mathcal{N}(0.1, 0.25^2)$. The second covariate effect function is designed as $f_2(\omega_{i,2}) = \exp(-\alpha_{i,2}\omega_{i,2})$ where $\alpha_{i,2} \sim \mathcal{N}(2.5, 0.25^2)$. The effect of the third covariate is modeled as $f_3(\omega_{i,3}) = \alpha_{i,3} \sin(\pi\omega_{i,3})$ where $\alpha_{i,3} \sim U[1.2, 2.5]$. It is also considered that $\beta_0 = 20$.

4.4.2. Performance Comparison

We first generate the degradation signals as discussed in section 4.4.1. In model setting I, we initially only consider the effect of the first covariate for degradation modeling using the procedure proposed in section 4.3. Then, we add the effect of the second covariate to the proposed framework and finally we consider the effect of all three covariates in RUL prediction. These three models are denoted as "Additive Regression I", "Additive Regression II", "Additive Regression III", respectively. In each of these three models, we compare the performance of our proposed framework with Liao and Tian (2013)'s approach where the drift is modeled to be linearly dependent on $\omega_{i,1}$ for each unit i denoted as "Linear Drift Model". Figure 4.4 shows the results of numerical study in this model setting.

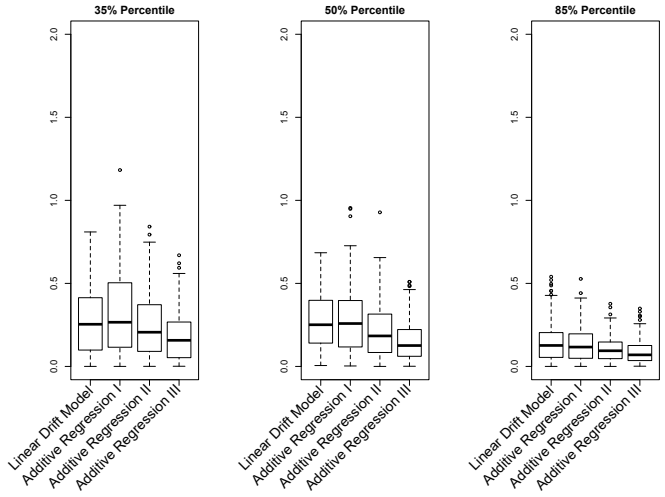

Figure 4.4: Results of model setting I

Figure 4.4 shows the performance of the proposed framework in comparison to the Brownian motion process with parametric linear drift model proposed in Liao and Tian (2013). As can be seen from this figure, with increase in the number of observations from the in-service unit the prediction accuracy generally improves. Moreover, figure 4.4 shows that as we include more covariates in the proposed degradation modeling framework, the prediction accuarcy increases. We would, in fact, expect these results as the originally generated degradation signals are affected by all three environmental covariates. Removing covariates from the degradation modeling framework introduces extra bias in estimating the diffusion term of the Brownian motion process and

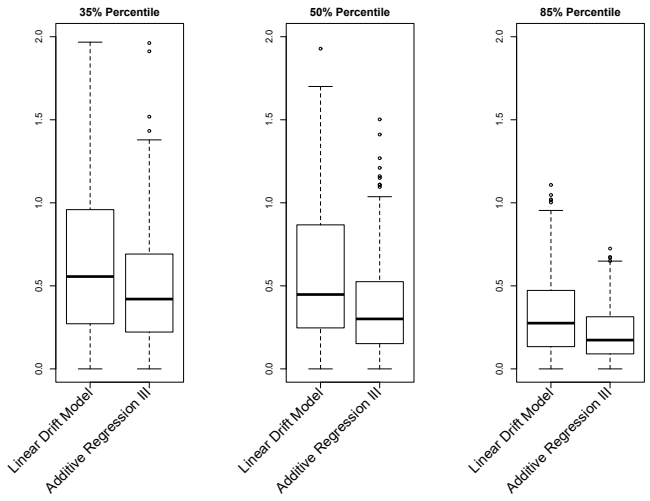

Figure 4.5: Results of model setting II

consequently causes inaccurate RUL prediction.

Figure 4.4 also shows that in the case where we only consider the effect of the first covariate, the nonparametric approach proposed in this study performs relatively similar to the linear drift model based on this covariate. In the earlier stage of RUL prediction when only 35% of in-service unit degradation signal is observed, however, the parametric approach performs relatively better than our non-parametric approach. This is intuitively understandable as the linear drift model is based on the true parametric function and can inherently capture the correct unit specific parameters even with small number of observations from the in-service unit.

In order to further investigate the performance of our approach, we conduct two more numerical studies. Specially in model setting II, we investigate the effect of proposed approach when the noise level is high. In this model setting, we set the diffusion parameter of the Brownian motion process to $\sigma = 5$. Figure 4.5 demonstrates the performance of the parametric model which only considers the effect of one covariate with the proposed procedure with all three covariates. It can be seen that increasing the diffusion generally increases the prediction error of different approaches; however, the proposed framework of this study which considers all three covariates effect remains superior.

In model setting III, we add extra environmental covariates' observations in each time interval i, j. Specially, we assume that in each time interval i, j of degradation shift, we observe environmental covariates in four equally-spaced time intervals. The drift-effect relationship for each covariate l would then be modeled as $\sum_{t_{i,j-1} \leq \tau_{i,k} < t_{i,j}} f_l(\omega_{i,l}(\tau_{i,k}); \beta_l)(\tau_{i,k+1} - \tau_{i,k})$ where $\tau_{i,k+1} - \tau_{i,k} = \frac{1}{4}\ \forall i, j$.

Specially, we compare the performance of our proposed framework with the case where we ignore the extra environmental covariate observations and only consider the observations made at the beginning of each degradation measurement interval. We denote the former model with extra environmental observations modeling as "Additive Regression V" and the latter as "Additive Regression IV" model. Figure 4.6 demonstrates the performance of two models. As can be seen from Figure 4.6, ignoring extra environmental covariates information affecting the degradation process in our modeling, indeed, hurts the RUL prediction accuracy.

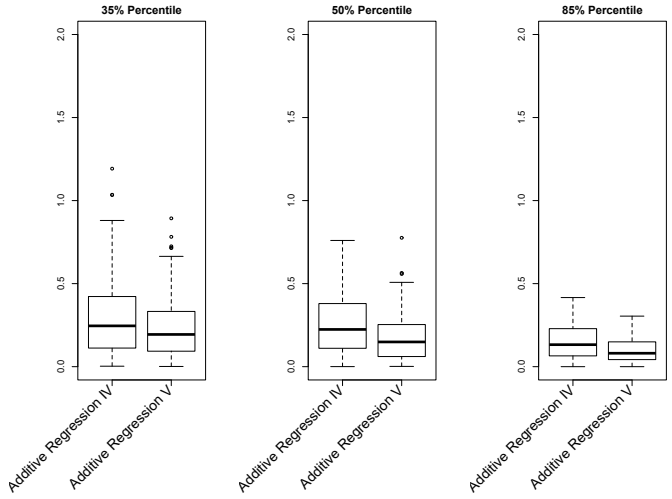

Figure 4.6: Results model setting III

4.5. Case Study

This section applies the proposed framework on a real-world case study of frying oil degradation modeling. During the frying process, typically, a complex series of physical and chemical reactions occur leading to the degradation of oil. The total polar component (TPC) which is a measure of proportion of polar materials in the oil, is the most predominant indicator for oil degradation. TPC can be obtained by measuring the dielectric of the oil. Fortunately, modern fryers are equipped with a sensor that can provide TPC measurements and daily TPC readings from the connected fryers can be collected. Per oil disposal, the frying vat is refilled with fresh oil and the TPC values reset to a lower value. The oil is typically deemed bad once its TPC value hits a pre-specified threshold value. We note that this threshold value is domain specific and depends on the degradation process under

study. Also, this threshold value does not necessarily indicates hard failure and merely suggests that the oil is not healthy any more with TPC above this value. This pre-specified threshold value is considered to be 25 in this study. Figure 4.7 demonstrates the TPC measurements for 12 such oil disposal cycles.

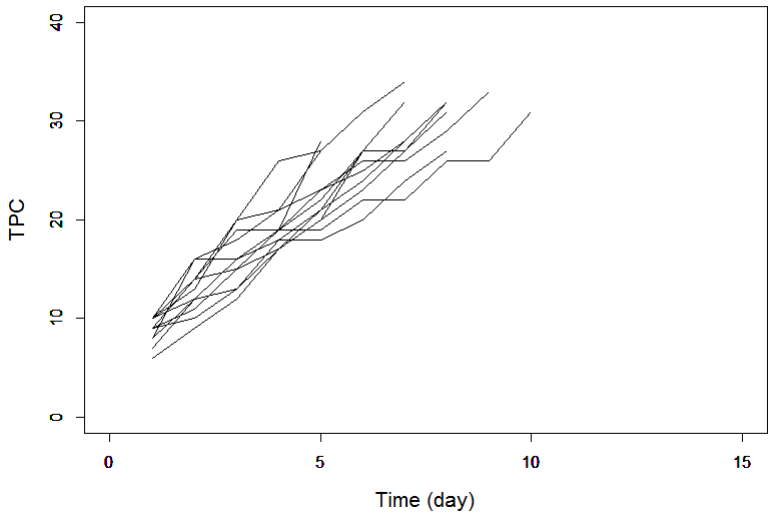

Figure 4.7: Degradation paths of frying oil

Figure 4.7 shows that the degradation rates of frying oil are considerably heterogeneous in different oil disposal cycles. Moreover, the degradation rate of each oil disposal cycle is different in different time intervals. This is, in fact, directly related to the condition that the frying oil was exposed to. Oil temperature is the most significant time-varying covariate contributing to the oil degradation. Beside temperature, other covariates like number of cooks and number of filterings in each time interval influence the corresponding degradation rate. We also checked the degradation data model fit based on the Brownian motion process for the oil degradation data. The results are in figure 4.8. The plot of studentized residuals in figure 4.8 shows that the constant variance assumption holds reasonably well. We can also check the normality assumption using the QQ-plot. The plot shows that the normality assumptions holds well. These graphical check shows that the overall the model assumptions holds reasonably well.

Figure 4.9 shows the plot of estimated functions for the drift-environmental covariates relationship estimated by the procedure introduced in Section 4.3.2. This figure, further, demonstrates that

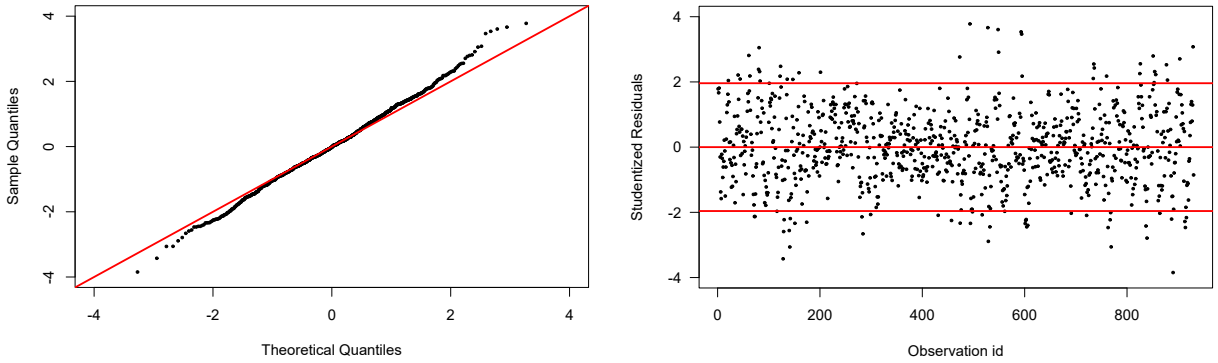

4.7(a) Q-Q plot

4.7(b) Residuals

Figure 4.8: QQ-plot and the studentized residual plots for the residuals of the degradation data.

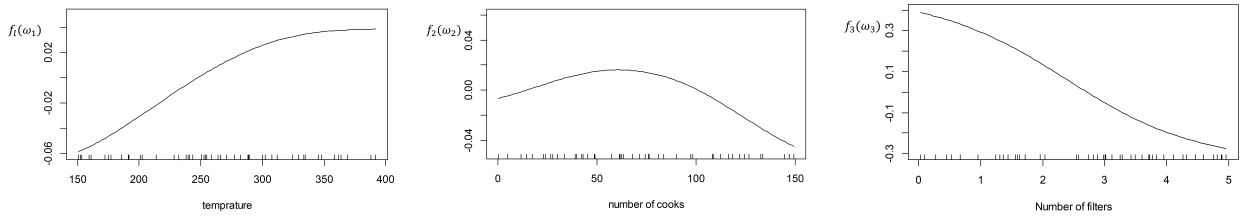

Figure 4.9: Estimated covariate effect functions and the corresponding approximate 95% confidence interval.

there is a strong non-linear relationship between the temperature and the drift of Brownian motion process defining the degradation.

In order to investigate the performance of our proposed method, we pursue the leave-one-out cross validation scheme for the available 117 oil disposal cycles. Specially, we leave one of the available cycles as the testing data and fit the model using all other available data. Then, the prediction for the in-service unit is performed for different percentiles of its lifespan. The whole procedure is repeated 117 times and the AE is calculated each time. Each time, we fit three models similar to numerical study section. The first model considers only the effect of temperature, the second model adds the effect of number of cooks and the third model considers all three covariates. We denote these three models as "Case I", "Case II" and "Case III" respectively. Figure 4.10 summarizes the results for the case study.

As can be seen from Figure 4.10, increasing the number of covariates using the proposed framework increases the RUL prediction accuracy. We would, indeed, expect this result as increasing the

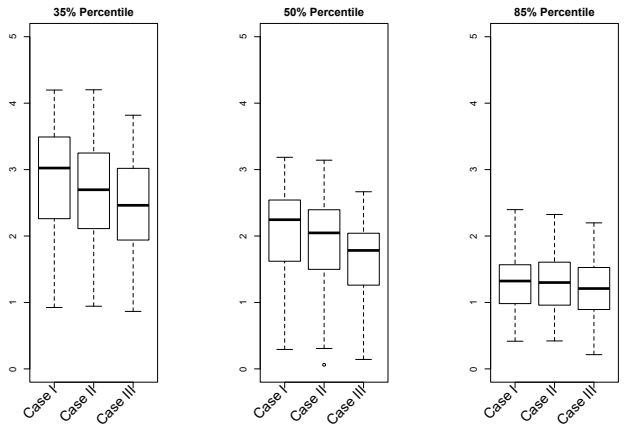

Figure 4.10: Results of case study

number of covariates increases the available information affecting the change in the oil degradation process.

4.6. Conclusion

In this chapter, we proposed a statistical framework for modeling degradation signals using a Brownian motion process with a drift dependent on the time-varying environmental covariates. Specially, our proposed framework considers a semi-parametric regression based on penalized splines to model the environmental covariates-drift relationship. An EM algorithm is further developed to estimate the model parameters. The advantage of the proposed approach is that while it models the effect of multiple time-varying environmental covariates on the degradation process, it does not assume any rigid parametric assumption on the environmental covariate-drift relationship of the Brownian motion process. The penalized splines that combine a set of splines basis functions with a quadratic penalty on the corresponding coefficients, also, strike a balance between ovefitting and accuracy of covariate-drift relationship while not being limited to specifying the exact number and location of knot values. Moreover leveraging the mixed effect modeling framework and EM algorithm, it offers a natural way of choosing the smoothing parameters of penalty term. Combining the offline model estimation with degradation data and environmental covariates observations from the in-service unit, we proposed a Bayesian updating scheme to conduct individualized RUL

prediction. We evaluated the performance of our approach using both simulated and real data of frying oil degradation collected from connected fryers. The numerical study and case study results confirmed that ignoring the extra information available through multiple time varying covariates affecting the degradation process hurts the RUL prediction accuracy.

This study considers a penalty based on the squared difference of the adjacent coefficients which results in smoother functional forms. One can also use the adaptive LASSO penalty or any other appropriate penalty form which provides a natural framework for variable selection for stress-drift relationship. Moreover, the proposed model in this study only considers the additive effect of multiple covariates. However, one can consider interactions among some of the covariates in the degradation modeling framework using a tensor based spline approach. Also, the degradation process developed in this study mainly concerns modeling the evolution of a one-dimensional degradation process. However, one can extend this framework by considering techniques like data fusions to develop a composite health index for degradation modeling and prognostics analysis based on multidimensional degradation process (Liu et al., 2013; Yan et al., 2016; Song and Liu, 2018). We will investigate along this lines and report the results in a future study.

4.7. Appendix

The equation in (4.10) can be further expanded as follows:

$$
\begin{aligned}
Q^{(\nu)}(\boldsymbol{\Delta X}, \boldsymbol{\beta}'; \Psi) = &- \frac{1}{2}\sum_{i=1}^{N}\sum_{j=1}^{n_i} \ln \sigma^2 - \frac{1}{2\sigma^2}\sum_{i=1}^{N}\sum_{j=1}^{n_i} \frac{\left(R_i(t_{ij}) - \boldsymbol{G}^t(t_{ij})\boldsymbol{\mu}_{\beta'}^{(\nu)}\right)^2}{\delta t_{i,j}} \\
&- \frac{1}{2\sigma^2}\sum_{i=1}^{N}\sum_{j=1}^{n_i} \frac{\boldsymbol{G}^t(t_{ij})\boldsymbol{\Sigma}_{\beta'}^{(\nu)}\boldsymbol{G}(t_{ij})}{\delta t_{i,j}} \\
&+ \frac{1}{2}\sum_{l=1}^{q}\left\{ d_l \ln(\lambda_l) - \lambda_l \boldsymbol{\mu}_{\beta_l}^{(\nu)t}\boldsymbol{S}_l\boldsymbol{\mu}_{\beta_l}^{(\nu)} - \lambda_l \operatorname{tr}(\boldsymbol{S}_l\boldsymbol{\Sigma}_{\beta_l}^{(\nu)})\right\} + \text{const},
\end{aligned}
\tag{4.16}
$$

where $\boldsymbol{\mu}_{\beta_l}^{(\nu)}$ and $\boldsymbol{\Sigma}_{\beta_l}^{(\nu)}$ correspond to coefficients posterior of l^{th} covariate and $\boldsymbol{\Sigma}_{\beta_l}^{(\nu)}$ is of dimension $d_l \times d_l$ and denotes the l^{th} diagonal block in $\boldsymbol{\Sigma}_{\beta'}^{(\nu)}$ estimated in iteration ν. Here $\boldsymbol{\mu}_{\beta'}^{(\nu)}$ and $\boldsymbol{\Sigma}_{\beta'}^{(\nu)}$ are computed using the current estimates of $\Psi^{(\nu)}$. The M-step entails maximizing the $Q^{(\nu)}(\boldsymbol{\Delta X}, \boldsymbol{\beta}'; \Psi)$ with respect to the parameters β_0, σ and λ. The derivatives of $Q^{(\nu)}(\boldsymbol{\Delta X}, \boldsymbol{\beta}'; \Psi)$ with respect to these parameters are as follows:

$$
\begin{aligned}
\frac{dQ^{(\nu)}(\boldsymbol{\Delta X}, \boldsymbol{\beta}'; \Psi)}{d\beta_0} =& \frac{1}{\sigma^2}\sum_{i=1}^{N}\sum_{j=1}^{n_i} (\Delta X_i(t_{i,j}) - \beta_0 \delta t_{i,j} - \boldsymbol{G}^t(t_{i,j})\boldsymbol{\mu}_{\beta'}^{(\nu)}), \\
\frac{dQ^{(\nu)}(\boldsymbol{\Delta X}, \boldsymbol{\beta}'; \Psi)}{d\sigma} =& -\sum_{i=1}^{N}\sum_{j=1}^{n_i} \frac{1}{\sigma} + \frac{1}{\sigma^3}\sum_{i=1}^{N}\sum_{j=1}^{n_i} \left(\frac{\left(R_i(t_{i,j}) - \boldsymbol{G}^t(t_{i,j})\boldsymbol{\mu}_{\beta'}^{(\nu)}\right)^2}{\delta t_{i,j}} + \frac{\boldsymbol{G}^t(t_{i,j})\boldsymbol{\Sigma}_{\beta_l}^{(\nu)}\boldsymbol{G}(t_{i,j})}{\delta t_{i,j}}\right), \\
\frac{dQ^{(\nu)}(\boldsymbol{\Delta X}, \boldsymbol{\beta}'; \Psi)}{d\lambda_l} =& \frac{d_l}{\lambda_l} - \boldsymbol{\mu}_{\beta_l}^{(\nu)t}\boldsymbol{S}_l\boldsymbol{\mu}_{\beta_l}^{(\nu)} - \operatorname{tr}(\boldsymbol{S}_l\boldsymbol{\mu}_{\beta_l}^{(\nu)}).
\end{aligned}
\tag{4.17}
$$

Setting these to zero, we get the formulas to update the parameters β_0, σ and λ in equation (4.11).

Chapter 5

Multi-output Gaussian Process Modulated Poisson Processes for Event Prediction*

5.1. Overview

Prediction of events such as part replacement and failure events plays a critical role in reliability engineering. Event stream data are commonly observed in manufacturing and teleservice systems. Designing predictive models for individual units based on such event streams is challenging and an under-explored problem. In this chapter, we propose a non-parametric prognostic framework for individualized event prediction based on the inhomogeneous Poisson processes with a multivariate Gaussian convolution process (MGCP) prior on the intensity functions. The MGCP prior on the intensity functions of the inhomogeneous Poisson processes maps data from similar historical units to the current unit under study which facilitates sharing of information and allows for analysis of flexible event patterns. To facilitate inference, we derive a variational inference scheme for learning and estimation of parameters in the resulting MGCP modulated Poisson process model. Experimental results are shown on both synthetic data as well as real-world data for fleet based event prediction.

*This chapter is based on the paper: **Jahani, S.**, Zhou, S. and Veeramani, D., 2020. Multi-output Gaussian Process Modulated Poisson Processes for Event Prediction. *Under review at IEEE Transactions on Reliability*.

5.2. Introduction

Recent advances in information and communication technology are playing a pivotal role in enabling what is referred to as Internet of Things (IoT). An example of IoT technology is teleservice systems. In a teleservice system, the data collected from a fleet of in-field units are transmitted through the communication network to the data processing center where the aggregated data are analyzed for condition monitoring and prognosis of in-field units. Figure 5.1 illustrates such a teleservice system.

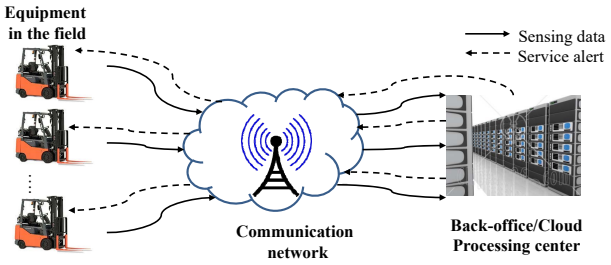

Figure 5.1: The structure of a teleservice system

Through the centralized data repository, the teleservice system has access to historical off-line records of events such as part replacements and failure events from all the units. The teleservice system also receives real-time event information from the in-field units. The availability of such a rich set of historical and real-time data in a teleservice system poses significant intellectual opportunities and challenges. On opportunities, since we have observations from potentially a very large number of similar units, we can compare their event patterns, share the information, and extract some common knowledge to enable accurate prediction at the individual level. On challenges, because the data are collected in the field and not in a controlled environment, the data contains significant variation and heterogeneity due to the large variations in working conditions for different units. This requires the developed analytics methods to be stochastic in nature to account for the variations.

This work focuses on event prediction for individual units using the real-time event information collected from the unit under study as well as other units managed by the teleservice system. The event of interest occurs multiple times for each one of similar units during their lifetime. Figure 5.2 illustrates typical event data of two forklifts collected in a teleservice system from a warehouse. An example of the event, here, could be replacement of a part due to its failure. In the figure,

we can see that the event repeatedly occurs for each forklift. The pattern of occurrence for two forklifts bears some similarity but is distinct. One of the challenges in event prediction is how to extract useful information from data collected from other units to improve the prediction for the unit under study. This setting is known as *multi-task learning*. The premise of this setting is that when multiple datasets from related outputs exist, their integrative analysis can be advantageous compared to learning multiple outputs independently. The goal of multi-task learning is to exploit commonalities between different units in order to improve the prediction and learning capabilities (Yuan et al., 2012; Caruana, 1997). The key feature of multi-task learning is to provide a shared representation between training and testing outputs to allow inductive transfer of knowledge. In this chapter, this inductive transfer of knowledge is achieved through specifying a valid semi definite covariance function that models dependencies of all data points (Conti et al., 2009).

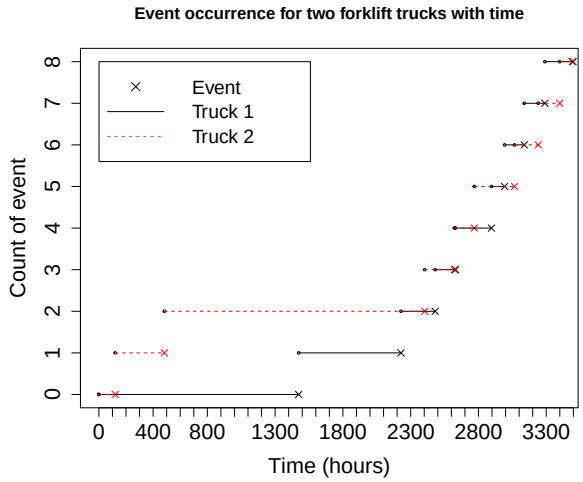

Figure 5.2: Illustration of event data from material handling forklifts.

Events defined over a continuous domain arises in a variety of real-world applications including reliability analysis and event prediction for operational units/machines in connected manufacturing systems (Soleimani et al., 2017), disease prognosis in clinical trials (Jarrett et al., 2019) and events prediction using vital health signals from monitored patients at risk (Lian et al., 2015). One thread of work in such point process data focuses on learning event intensity rates by imposing smoothness on a latent rate function (Adams et al., 2009; Teh and Rao, 2011; Lloyd et al., 2015). Another consists of predicting future events as a direct function of past observations (Pillow et al., 2008; Gunawardana et al., 2011). Taking fleet based event prediction as a motivating example, we

focus on the latter problem: given similar vehicles' history and the events history for the vehicle under-study up to time t^*, how many events will this vehicle have in $[t^*, t^* + L]$? Answering such a question provides a quantitative evaluation of the failure risk, which helps in making efficient maintenance plans and associated allocation of parts and resources.

Extensive research exists on event prediction, specially on failure prediction (Jardine et al., 2006; Si et al., 2011). The main avenue of research for event prediction using event data is focused on the data-driven statistical models. Data-driven statistical models typically estimate the probability of time-to-event distribution through parametric models (such as Weibull distribution) or non-parametric models (Meeker and Escobar, 2014; McPherson et al., 2010). In this context, Cox PH regression has been widely used in clinical survival analysis and reliability engineering to investigate the effect of some covariates on the hazard rate/survival of a patient or a machine (Cox, 1972; Klein and Moeschberger, 2006). Using the previously occurred events as covariates, Cox PH model has been used for event prediction using event stream data (Li et al., 2007; Yuan et al., 2011). The Cox PH model can incorporate several unit-specific factors as covariates in the regression. However, one limitation is that although the value of covariates can be unit specific, the model parameters are fixed and cannot reflect unit-to-unit variation. In other words, if the values of parameters for two units is the same, then the event prediction for these two units using the Cox PH model will always be the same. Also, the Cox PH regression model becomes inapplicable when good covariates are not available.

Another stream of research based on the event data uses frailty models as an extension of the conventional survival regression models, like Cox regression models, by incorporating a random effect term, typically called frailty term, to allow for unit-to-unit variation. Since the frailty term is random and follows a common distribution, the frailty model allows for unit-to-unit variation (Hougaard, 2012; Duchateau and Janssen, 2007; Deep et al., 2019). However, the majority of research on frailty modeling is predominantly focused on investigating the significance of covariates and the frailty term in the fitted model rather than prediction for the individual units. In addition, frailty model is a parametric model that often needs relatively strong assumptions.

A few works have explored the event prediction problem in point processes by learning a functional mapping from history features to the current event intensity rate (Gunawardana et al., 2011; Pillow et al., 2008; Peng et al., 2018). In Gunawardana et al. (2011) the intensity function is

constrained to be piecewise-constant, learned using decision trees and used for events' prediction. This setting is not appropriate for the events observation where the event intensity rate (or average incidence rate) varies smoothly over time. Moreover, this modeling approach does not take into account the variation between individual units. In our proposed approach, we will consider data where the intensity of the event generating process is assumed to vary smoothly over the domain. A popular model for such data is the inhomogeneous Poisson process with a Gaussian Process (GP) prior for the smoothly varying intensity function. This form of point processes are typically known as *Cox processes* in literature (Kingman, 1993; Møller et al., 1998). An example of such modeling approach is the Log Gaussian Cox Process (LGCP) where the log intensity function is driven by a GP prior (Møller et al., 1998). The flexibility of the LGCP comes at the cost of incredibly hard inference challenges due to its doubly stochastic nature and the notorious scalability issues of GP models. Another difficulty is that when available training data for each unit are scarce, then building such predictive models for event occurrence processes is difficult. This happens because industrial equipment nowadays tend to be generally very reliable and not subject to frequent failures. Therefore, we treat each individual event occurrence process as a task and follow a multi-task learning approach to share information from all tasks. This approach is in contrast to the general school of thought where a population level model is constructed (Meeker and Escobar, 2014; Li et al., 2007; Vrignat et al., 2015). Building a population model treats event prediction of different units' similarly. Such a population-level approach lacks the individualization capability where we need event predictions customized to an individual unit's history. The multi-task learning approach we propose here borrows information from the off-line historical event data and makes individualized predictions for a specific unit operating in the field.

Methods for learning GPs from multiple tasks have been proposed (Yu et al., 2005), but they typically involve a shared global mean function and require inference at all observed data points across all the tasks. In the context of Cox processes, the inference of such multi-task models become even more challenging as it is doubly stochastic in nature and involves multiple correlated tasks (Diggle et al., 2013; Flaxman et al., 2015; Leininger et al., 2017). More details on double-stochasticity or double-interactability of Cox processes are given later in this study. One approximation method, variational Bayes, is often applied in such models leading to improvement in the scalablity. However, the inference in such predictive models lacks individualization capability.

In this study we propose a multi-task modeling approach enabling inference at individual level while sharing information from the historical offline data set.

The main objective of this study is to provide a framework for analysis of event occurrence probability of individual units under study. One challenge is that the available training data for each unit is typically sparse. Here, we propose a multivariate Gaussian convolution process (MGCP) modulated Poisson process model which facilities sharing of information from all units through a shared latent function. The proposed framework borrows commonalities from different units and makes it possible to do inference and prediction at individual level. As mentioned before, a difficulty with building such a predictive model is that the inference is doubly-stochastic in nature and it scales poorly with the number of tasks and data points. Borrowing from the framework of the *inducing variables* or *pseudo inputs* in the GP literature (Snelson and Ghahramani, 2006; Titsias, 2009), we propose a variational inference framework to simultaneously estimate parameters in the resulting MGCP-Poisson Process (MGCP-PP) model. This facilitates the scalability and safeguards against model overfitting. Finally the advantageous feature of the proposed model is demonstrated through numerical studies and a case study with real-world data from forklift trucks' events.

The remainder of this chapter is organized as follows: In section 2, we provide an overview of the Cox processes. In section 3, we describe the problem formulation and inference scheme. In section 4 and section 5, we report the results of numerical studies and a real-world case study based on event data from a fleet of forklift trucks. Finally, our concluding remarks are given in section 6.

5.3. Gaussian Process Modulated Poisson Process

Assume data have been collected from N units and let $I = \{1, 2, \ldots, N\}$ denote the set of all units. For unit $i \in I$, its associated data is $\mathcal{D}_i = \{t_i^{(p)}\}_{p=1}^{P_i}$ where $t_i^{(p)}$ is the time that event p occurred for unit i. Formally a Cox process –a particular type of inhomogeneous Poisson process– is defined via a stochastic intensity function $\lambda_i(t) : \mathcal{X} \to \mathbb{R}^+$ for unit $i \in I$. For a domain $\mathcal{X} = \mathbb{R}$ where $\mathbb{R}$ is the real coordinate space, the number of points, $N(\mathcal{T})$, found in a subregion $\mathcal{T} \subset \mathcal{X}$ of unit i is Poisson distributed with parameter $\lambda^i = \int_{\mathcal{T}} \lambda_i(t)dt$ and for disjoint subsets $\mathcal{T}_m$ of $\mathcal{X}$, the counts $N(\mathcal{T}_m)$ are independent. This independence is due to the completely independent nature of points in a Poisson process (Kingman, 1993). If we restrict our consideration to some bounded region $\mathcal{T}$,

the probability density of a set of P_i observed points, $\mathcal{D}_i$, conditioned on the rate function $\lambda_i(t)$ is

$$p(\mathcal{D}_i|\lambda_i) = \exp\left\{-\int_{\mathcal{T}} \lambda_i(u)du\right\} \prod_{p=1}^{P_i} \lambda_i(t_i^{(p)}). \tag{5.1}$$

The likelihood of observed data across all N units is $p(\mathcal{D}|\boldsymbol{\lambda}) = \prod_{i=1}^{N} p(\mathcal{D}_i|\lambda_i)$ where $\mathcal{D} = \{\mathcal{D}_i\}_{i=1}^{N}$ and $\boldsymbol{\lambda} = \{\lambda_i\}_{i=1}^{N}$ is the collection of intensity functions for all units. Using Bayes' rule, the posterior distribution of the rate functions conditioned on the data, $p_d(\boldsymbol{\lambda}|\mathcal{D})$, is:

$$\frac{p_d(\boldsymbol{\lambda}) \prod_{i=1}^{N} \exp\{-\int_{\mathcal{T}} \lambda_i(u)du\} \prod_{p=1}^{P_i} \lambda_i(t_i^{(p)})}{\int p_d(\boldsymbol{\lambda}) \prod_{i=1}^{N} \exp\{-\int_{\mathcal{T}} \lambda_i(u)du\} \prod_{p=1}^{P_i} \lambda_i(t_i^{(p)}) d\boldsymbol{\lambda}}, \tag{5.2}$$

which is often described as doubly-stochastic or doubly-intractable because of the nested integral in the denominator. Here we use the subscript d to indicate the probability density function.

To overcome the challenges posed by the doubly-intractable integral, Adams et al. (2009) propose the Sigmoidal Gaussian Cox Process (SGCP). In the proposed SGCP model, a Gaussian process prior (Rasmussen and Williams, 2006) is used to construct an intensity function by passing a random function, $f \sim \mathcal{GP}$, through a sigmoid transformation and scaling it with a maximum intensity λ^*. The intensity function is therefore $\lambda(t) = \lambda^* \sigma\left(f(t)\right)$, where $\sigma(.)$ is the logistic function

$$\sigma(x) = \frac{1}{1 + \exp(-x)}. \tag{5.3}$$

While this model works well in practice in one dimension, in reality it scales poorly with the dimensionality of the domain and the number of datapoints. Moreover, it only considers the event data from the in-field unit and does not incorporate the off-line information from the historical units stored in the data repository. In order to tackle the issue of scalability, Lloyd et al. (2015) propose to use a variational inference scheme. They assumed that the intensity is defined as $\lambda(t) = f^2(t)$ where $f \sim \mathcal{GP}$ is a GP distributed random function. This approach, also, falls short of considering the information that comes from the peer units in making inference and prediction, and only relies on the event data from the in-field unit.

In this study we use a multi-task modeling approach to model the intensity functions of different units. This approach takes advantage of the multi-output GPs to share information between units

from offline historical data and the online in-field unit via a shared latent function. A GP is formally defined as a collection of random variables, any finite number of which have consistent joint Gaussian distributions. For any input point $t \in \mathcal{X} \subset \mathbb{R}$, observations from a random dataset $\boldsymbol{f}(t) = \{f(t_1), f(t_2), ..., f(t_p)\}^T$ are considered as single sample from some multivariate Gaussian distribution. Thus, the GP can be expressed as $f(t) \sim \mathcal{GP}(0, \Sigma(t, t'))$, where $\Sigma(t, t')$ is a positive definite covariance function. An alternative approach for constructing a Gaussian process is to convolve the GP random variables with an arbitrary kernel. Thus, $f(t)$ can be expressed as the convolution between a smoothing kernel $G(t)$ and a latent function $X(t)$ as follows:

$$f(t) = \int_{\mathbb{R}} G(t-u)X(u)du. \tag{5.4}$$

The resulting covariance function for $f(t)$ is then derived as

$$\text{cov}_f(t, t') = \int_{\mathbb{R}} G(t-u) \int_{\mathbb{R}} G(t'-u')\kappa(u, u')du'du \tag{5.5}$$

where $\text{cov}[X(t), X(t')] = \kappa(t, t')$ is the covariance defining the latent function $X(t)$. We note that this construction is general in the sense that $X(t)$ can be any GP random variable (Alvarez and Lawrence, 2009). Therefore, the covariance matrix can be directly parametrized through parameters in the smoothing kernel. In this article we employ Convolution Process (CP) to build covariance functions that model dependencies within and across units. The basic idea is to build multiple GPs where all outputs depends on some common latent processes. The proposed framework can provide each output with both shared and unique features and allows commonalities between different outputs to be automatically inferred. We introduce our multi-task modeling approach which takes advantage of the MGCPs in modeling the intensity of inhomogeneous Poisson processes in the next section. We also introduce a variational inference approach to make inference in the resulting MGCP modulated Poisson processes. The modeling framework introduced in this study makes inference and prediction for the individual in-field unit possible while tackling the sparsity in the observed event data.

5.4. Construction of Multi-output Gaussian Process Modulated Poisson Process

We construct our prior over the individual rate functions using GPs and assume that the resulting Cox process is driven by a latent log intensity function $\log \lambda_i := f_i$ with a GP prior:

$$f_i(t) \sim \mathcal{GP}\left(0, \Sigma_i(t, t')\right). \tag{5.6}$$

To obtain an accurate predictive result, we need to capture relatedness among all N units. Particularly, we use CP as mentioned in section 5.3 to model the latent log intensity functions $f_i(t)$ for each unit $i \in I$. We can consider a shared independent latent function $X(t)$ and N different smoothing kernels $G_i(t) : i = 1, ..., N$. The latent function is assumed a GP with covariance $\text{cov}[X(t), X(t')] = \kappa(t, t')$. We set the kernels as

$$G_i(t) = \frac{a_i \pi^{-\frac{1}{4}}}{\sqrt{|\xi_i|}} \exp(-\frac{1}{2}\frac{t^2}{\xi_i^2}) := \alpha_i \mathcal{N}(t; 0, \xi_i^2), \tag{5.7}$$

to be scaled Gaussian kernels where $\mathcal{N}(t; 0, \xi_i^2)$ is the density function of a zero mean normal distribution with variance ξ_i^2. We also consider $\kappa(t, t')$ to be the squared exponential covariance function (Alvarez and Lawrence, 2009) as follows:

$$\kappa(t, t') = \exp\left[-\frac{1}{2}\frac{(t - t')^2}{\lambda^2}\right] = \sqrt{2\pi\lambda^2}\mathcal{N}(d; 0, \lambda^2) := C\mathcal{N}(d; 0, \lambda^2), \tag{5.8}$$

The GP $f_i(t)$ is then constructed by convolving the shared latent function with the smoothing kernel as follows:

$$f_i(t) = \int_{\mathbb{R}} G_i(t - u)X(u)du. \tag{5.9}$$

This is the underlying principle of MGCP, where the latent functions $X(t)$ is shared across different units through the corresponding kernel $G_i(t)$. Since the model in Eq. (5.9) shares the latent function, a GP, across multiple units and since convolution is a linear operator, all outputs can be expressed as a jointly distributed GP. Figure 5.3 shows an illustration of such a convolution structure. As shown in figure 5.3, the key feature is that information is shared through parameters

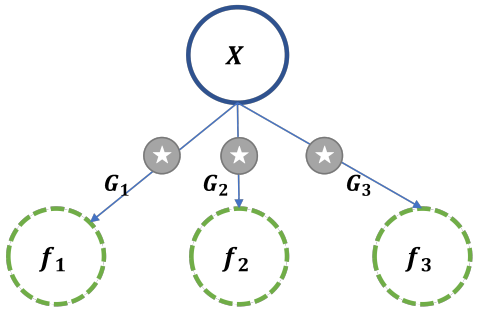

Figure 5.3: A convolution process with one latent functions

encoded in the kernels $G_i(t)$. Outputs then possess both unique and shared features; thus, accounting for heterogeneity in the intensity functions.

Based on equation (5.9), the covariance function between f_i and f_j and the covariance function between f_i and X, can be calculated as follows:

$$\begin{aligned}
\mathrm{cov}_{f_i,f_j}(t,t') &= \int_{\mathbb{R}} G_i(t-u) \int_{\mathbb{R}} G_i(t'-u')\kappa(u,u')du'du = \alpha_i\alpha_j\sqrt{\frac{\lambda^2}{\eta_{i,j}^2}}\exp(-\frac{1}{2}\frac{(t-t')^2}{\eta_{i,j}^2}),\\
\mathrm{cov}_{f_i,X}(t,u) &= \int_{\mathbb{R}} G_i(t-u')\kappa(u,u')du' = \alpha_i\sqrt{\frac{\lambda^2}{\eta_i^2}}\exp(-\frac{1}{2}\frac{(t-u)^2}{\eta_i^2}),
\end{aligned} \tag{5.10}$$

where $\eta_{i,j}^2 = \xi_i^2 + \xi_j^2 + \lambda^2$ and $\eta_i^2 = \xi_i^2 + \lambda^2$. Now denote the underlying latent log intensity rates at the input data points as $\boldsymbol{f} = \{\boldsymbol{f}_1^T, ..., \boldsymbol{f}_N^T\}^T$, where $\boldsymbol{f}_i = \{f_i(t_i^{(1)}), ..., f_i(t_i^{(p_i)})\}^T$. The density function of $\boldsymbol{f}$ can be obtained as $p_d(\boldsymbol{f}) = \mathcal{N}(\boldsymbol{f}; \boldsymbol{0}, \boldsymbol{K}_{f,f})$, where $\boldsymbol{K}_{f,f}$ sized $(\sum_{i=1}^N p_i) \times (\sum_{i=1}^N p_i)$ is the covariance function.

Exact inference in the proposed model entails optimizing the *model evidence* $p(\mathcal{D}) = \mathbb{E}_{p(\boldsymbol{f})}[\, p(\mathcal{D}|\boldsymbol{\lambda} = \exp(\boldsymbol{f}))]$ for which the marginal log-likelihood can be obtained as follows:

$$\log p(\mathcal{D}) = \log \int p\left(\mathcal{D}|\boldsymbol{\lambda} = \exp(\boldsymbol{f})\right) p_d(\boldsymbol{f}) d\boldsymbol{f}, \tag{5.11}$$

where as noted before $p_d(\boldsymbol{f}) = \mathcal{N}(\boldsymbol{f}; \boldsymbol{0}, \boldsymbol{K}_{f,f})$. The likelihood of $\boldsymbol{f}$ in Eq. (5.11) involves inversion of the large matrix $\boldsymbol{K}_{f,f}$ which has a limiting cubic complexity $O\left(\left(\sum_{i=1}^N p_i\right)^3\right)$ and is in general intractable. Moreover, as mentioned in section 5.3, we see that the log-likelihood is doubly-stochastic as it also involves an integration over the latent log intensity functions (see Eq.

(5.1) and Eq. (5.11)). This, in turn, makes the exact inference more challenging. To alleviate the computation burden of matrix inversion, low-rank Gaussian process functions can be constructed by *augmenting* the Gaussian process with a small number of M inducing points or pseudo-inputs from the shared latent function. In next subsection, we introduce a variational inference framework based on the inducing points which tackles the double-stocasticity of Eq. (5.11) by obtaining a lower bound on the model evidence.

5.4.1. Variational Inference

We denote the inducing points by $\mathcal{Z} = \{z_i\}_{i=1}^{M}$ and the value of shared latent function at the inducing points by $\boldsymbol{X} = [X(z_1), ..., X(z_M)]^T$. Since the latent function is GP, any sample $\boldsymbol{X}$ follows a multivariate Gaussian distribution. Therefore, the probability distribution of $\boldsymbol{X}$ can be expressed as $p_d(\boldsymbol{X}|\mathcal{Z}) = \mathcal{N}(\boldsymbol{X}; \mathbf{0}, \boldsymbol{K}_{\boldsymbol{X},\boldsymbol{X}})$, where $\boldsymbol{K}_{\boldsymbol{X},\boldsymbol{X}}$ is constructed by the covariance function in equation (5.8). We now can sample from the conditional prior $p(X(u)|\boldsymbol{X}, \mathcal{Z})$. In equation (5.9) where we construct latent intensity function $f_i(t)$, $X(u)$ can be well approximated by the expectation $\mathbb{E}(X(u)|\boldsymbol{X}, \mathcal{Z})$ as long as the latent function is smooth (Alvarez and Lawrence, 2009). By multivariate Gaussian identities, the probability distribution of $\boldsymbol{f}$ conditional on $\boldsymbol{X}, \mathcal{Z}$ is:

$$p_d(\boldsymbol{f}|\boldsymbol{X}, \mathcal{Z}) = \mathcal{N}(\boldsymbol{f}; \boldsymbol{K}_{\boldsymbol{f},\boldsymbol{X}}\boldsymbol{K}_{\boldsymbol{X},\boldsymbol{X}}^{-\mathbf{1}}\boldsymbol{X}, \boldsymbol{K}_{\boldsymbol{f},\boldsymbol{f}} - \boldsymbol{K}_{\boldsymbol{f},\boldsymbol{X}}\boldsymbol{K}_{\boldsymbol{X},\boldsymbol{X}}^{-\mathbf{1}}\boldsymbol{K}_{\boldsymbol{X},\boldsymbol{f}}), \tag{5.12}$$

where $\boldsymbol{K}_{\boldsymbol{X},\boldsymbol{X}}$ is the covariance matrix between the inducing variables and $\boldsymbol{K}_{\boldsymbol{f},\boldsymbol{X}}$ is the covariance matrix between the latent log intensity values and the inducing variables. Therefore, $p_d(\boldsymbol{f})$ can be approximated by $p_d(\boldsymbol{f}|\mathcal{Z})$, which is given as:

$$p_d(\boldsymbol{f}|\mathcal{Z}) = \int p_d(\boldsymbol{f}|\boldsymbol{X}, \mathcal{Z}) p_d(\boldsymbol{X}|\mathcal{Z}) d\boldsymbol{X}. \tag{5.13}$$

By equation (5.13), the marginal log-likelihood function can be approximated as follows:

$$\begin{aligned} \log p(\mathcal{D}) &= \log \int p\left(\mathcal{D}|\boldsymbol{\lambda} = \exp(\boldsymbol{f})\right) p_d(\boldsymbol{f}) d\boldsymbol{f} \\ &\approx \log \int\int p\left(\mathcal{D}|\boldsymbol{\lambda} = \exp(\boldsymbol{f})\right) p_d(\boldsymbol{f}|\boldsymbol{X}, \mathcal{Z}) p_d(\boldsymbol{X}|\mathcal{Z}) d\boldsymbol{X} d\boldsymbol{f} \end{aligned} \tag{5.14}$$

We next continue by integrating out the inducing variables $\boldsymbol{X}$, using a variational distribution $q_d(\boldsymbol{X}) = \mathcal{N}(\boldsymbol{X}; \boldsymbol{m}, \boldsymbol{S})$ over the inducing points. We then multiply and divide the joint by $q_d(\boldsymbol{X})$ and lower bound using Jensen's inequality to obtain a lower bound on the model evidence:

$$\begin{aligned}\log p(\mathcal{D}) &= \log\left[\int\int p(\mathcal{D}|\boldsymbol{f}) p_d(\boldsymbol{f}|\boldsymbol{X}) p_d(\boldsymbol{X}) \frac{q_d(\boldsymbol{X})}{q_d(\boldsymbol{X})} d\boldsymbol{X} d\boldsymbol{f}\right] \\ &\geq \int\int p_d(\boldsymbol{f}|\boldsymbol{X}) q_d(\boldsymbol{X}) d\boldsymbol{X} \log(p(\mathcal{D}|\boldsymbol{f})) d\boldsymbol{f} + \int\int p_d(\boldsymbol{f}|\boldsymbol{X}) q_d(\boldsymbol{X}) d\boldsymbol{f} \log(\frac{p_d(\boldsymbol{X})}{q_d(\boldsymbol{X})}) d\boldsymbol{X} \\ &= \mathbb{E}_{q_d(\boldsymbol{f})}\left[\log p(\mathcal{D}|\boldsymbol{f})\right] - KL(q_d(\boldsymbol{X}) \parallel p_d(\boldsymbol{X})) \triangleq \mathcal{L}\end{aligned} \tag{5.15}$$

Since $p_d(\boldsymbol{f}|\boldsymbol{X})$ is conjugate to $q_d(\boldsymbol{X})$, we can write down in closed form the resulting integral:

$$\begin{aligned} q_d(\boldsymbol{f}) &= \int p_d(\boldsymbol{f}|\boldsymbol{X}) q_d(\boldsymbol{X}) d\boldsymbol{X} := \mathcal{N}(\boldsymbol{f}; \boldsymbol{\mu}, \boldsymbol{\Sigma}) \\ \boldsymbol{\mu} &= \boldsymbol{K}_{f,X} \boldsymbol{K}_{X,X}^{-1} \boldsymbol{m} \\ \boldsymbol{\Sigma} &= \boldsymbol{K}_{f,f} - \boldsymbol{K}_{f,X} \boldsymbol{K}_{X,X}^{-1} (\boldsymbol{I} - \boldsymbol{S} \boldsymbol{K}_{X,X}^{-1}) \boldsymbol{K}_{X,f}. \end{aligned} \tag{5.16}$$

Here, $KL(q_d(\boldsymbol{X}) \parallel p_d(\boldsymbol{X}))$ is simply the KL-divergence between two Gaussians:

$$KL(q_d(\boldsymbol{X}) \parallel p_d(\boldsymbol{X})) = \frac{1}{2}\left[\mathrm{Tr}(\boldsymbol{K}_{X,X}^{-1}\boldsymbol{S}) - \log\frac{|\boldsymbol{K}_{X,X}|}{|\boldsymbol{S}|} - M + (\vec{0} - \boldsymbol{m})^T \boldsymbol{K}_{X,X}^{-1}(\vec{0} - \boldsymbol{m})\right], \tag{5.17}$$

where Tr(.) is a trace operator. We now take expectation of data log-likelihood under $q_d(\boldsymbol{f})$:

$$\begin{aligned}\mathcal{L} &= \mathbb{E}_{q_d(\boldsymbol{f})}\left[\log p(\mathcal{D}|\boldsymbol{f})\right] - KL(q_d(\boldsymbol{X}) \parallel p_d(\boldsymbol{X})) \\ &= \mathbb{E}_{q_d(\boldsymbol{f})}\left[-\sum_{i=1}^{N}\int_{\mathcal{T}} \exp(f_i(u)) du + \sum_{i=1}^{N}\sum_{p=1}^{P_i} f_i(t_i^{(p)})\right] - KL(q_d(\boldsymbol{X}) \parallel p_d(\boldsymbol{X}))\end{aligned} \tag{5.18}$$

The first term of integration in (5.18) can be analytically calculated as follows:

$$\mathbb{E}_{q_d(\boldsymbol{f})}\left[\sum_{i=1}^{N}\int_{\mathcal{T}} \exp(f_i(u)) du\right] = \sum_{i=1}^{N}\int\int q_d(\boldsymbol{f}) \exp(f_i(u)) d\boldsymbol{f} du = \sum_{i=1}^{N}\int \exp(\mu_i(u) + \frac{1}{2}\sigma_i^2(u)) du \tag{5.19}$$

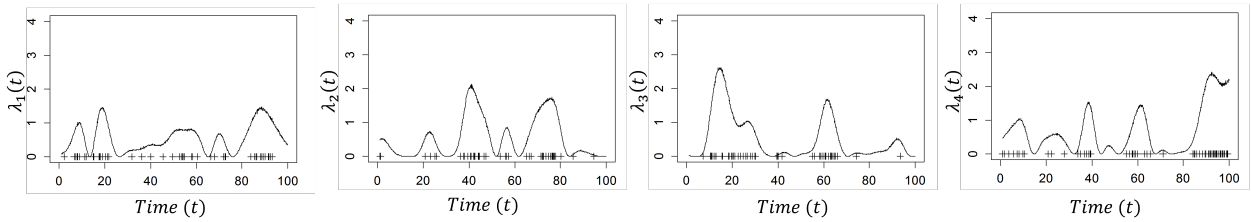

Figure 5.4: A sample of intensity rates generated from MGCP and the sigmoid link function.

where $\mu_i(u) := \boldsymbol{K}_{f_i(u),\boldsymbol{X}}\boldsymbol{K}_{\boldsymbol{X},\boldsymbol{X}}^{-1}\boldsymbol{m}$ and $\sigma_i^2(u) := \boldsymbol{K}_{f_i(u),f_i(u)} - \boldsymbol{K}_{f_i(u),\boldsymbol{X}}\boldsymbol{K}_{\boldsymbol{X},\boldsymbol{X}}^{-1}(\boldsymbol{I} - \boldsymbol{S}\boldsymbol{K}_{\boldsymbol{X},\boldsymbol{X}}^{-1})\boldsymbol{K}_{\boldsymbol{X},f_i(u)}$. The second term in (5.18) can be calculated as follows:

$$\mathbb{E}_{q(\boldsymbol{f})}\left[\sum_{i=1}^{N}\sum_{p=1}^{P_i} f_i(t_i^{(p)})\right] = \sum_{i=1}^{N}\sum_{p=1}^{P_i}\mu_i(t_i^{(p)}) \tag{5.20}$$

where $\mu_i(t_i^{(p)}) = \boldsymbol{K}_{t_i^{(p)},\boldsymbol{X}}\boldsymbol{K}_{\boldsymbol{X},\boldsymbol{X}}^{-1}\boldsymbol{m}$. To perform inference we find the variational parameters $\boldsymbol{m}^*$, $\boldsymbol{S}^*$ and the model parameters $\boldsymbol{\theta}^* = (\{\lambda, \xi_i, \alpha_i\}_{i=1}^N)$ that maximize the $\mathcal{L}$. To optimize these simultaneously, we construct an augmented vector $\boldsymbol{\Theta} = \left[\boldsymbol{\theta}, \boldsymbol{m}^T, vech(\boldsymbol{L})^T\right]$ where $vech(\boldsymbol{L})$ is the vectorization of the lower triangular elements of $\boldsymbol{L}$, such that $\boldsymbol{S} = \boldsymbol{L}\boldsymbol{L}^T$. The $vech(.)$ operator is a linear transformation which converts a matrix into a column vector.

5.4.2. Predictive Distribution

In this section, we derive the predictive distribution for the test unit N based on the optimized $\boldsymbol{\Theta}^*$. Our training data (denoted as $\mathcal{D}$) includes the observations from the offline units $i = 1, 2, ..., N-1$ as well as the partial observations from the online test unit N.

Suppose observations from the test unit N have been collected up to time t^*. We can next derive the predictive distribution for any new input time T of the test unit N. In order to form the predictive distribution we assume our optimised variational distribution $q_d^*(\boldsymbol{X}) = \mathcal{N}(\boldsymbol{X}; \boldsymbol{m}^*, \boldsymbol{S}^*)$ approximates the posterior $p_d(\boldsymbol{X}|\mathcal{D})$. Similar to Equation (5.16), we next compute $q_d^*(\boldsymbol{f}) \approx p_d(\boldsymbol{f}|\mathcal{D})$. We can now derive a lower bound of the (approximate) predictive log-likelihood for unit N in any new input time T:

$$\log p(T|\mathcal{D}, \boldsymbol{\Theta}^*) = \log \mathbb{E}_{p_d(\boldsymbol{f}|\mathcal{D})}[p(T|\boldsymbol{f})] \approx \log \mathbb{E}_{q_d^*(\boldsymbol{f})}[p(T|\boldsymbol{f})] \geq \mathbb{E}_{q_d^*(\boldsymbol{f})}[\log p(T|\boldsymbol{f})] \triangleq \mathcal{L}_p \tag{5.21}$$

The derivation of $\mathcal{L}_p$ follows Equations (5.18)-(5.20). The resulting bound is similar to $\mathcal{L}$ except that $\boldsymbol{m}$, $\boldsymbol{S}$ are replaced with $\boldsymbol{m}^*$ and $\boldsymbol{S}^*$, and there is no KL-divergence term. All the kernel matrices are computed using $\boldsymbol{\Theta}^*$. We use this bound to give results from approximate predictive likelihood when comparing against other approaches.

We can now answer the question posed at the beginning of this study using the derived predictive log-likelihood. The question involves estimating the distribution of event occurrence in $[t^*, t^* + L]$ for the test unit N. This event occurrence probability distribution for unit N depends on the predicted latent log intensity function $\log \lambda_N := f_N(u), u \in [t^*, t^* + L]$. Given the predicted intensity rate $\lambda^{N^*} = \int_{t^*}^{t^*+L} \lambda_N(t)dt$, the event occurrence has Poisson distribution. Given the estimated parameters, we are interested in:

$$p_d(N(t^*) = y) = \frac{e^{-\lambda^{N^*}} \lambda^{N^* y}}{y!}, \; y = 0, 1, 2, ..., \tag{5.22}$$

where y is the number of events. Based on (5.22), the accurate probability of event occurrence depends on the extrapolation of the intensity rate within L for the testing unit N. In the MGCP, the predictive distribution for any new input point T^* is given by:

$$\begin{aligned} p_d(f_N(T^*)|\mathcal{D}) &= \int p_d(f_N(T^*)|\boldsymbol{X}) p_d(\boldsymbol{X}|\mathcal{D}) d\boldsymbol{X} \approx \int p_d(f_N(T^*)|\boldsymbol{X}) q_d(\boldsymbol{X}) d\boldsymbol{X} \\ &= \mathcal{N}\Big(f_N(T^*); \boldsymbol{K}_{f_N(T^*),\boldsymbol{X}} \boldsymbol{K}_{\boldsymbol{X},\boldsymbol{X}}^{-1} \boldsymbol{m}^*, \boldsymbol{K}_{f_N(T^*),f_N(T^*)} - \boldsymbol{K}_{f_N(T^*),\boldsymbol{X}} \boldsymbol{K}_{\boldsymbol{X},\boldsymbol{X}}^{-1} \times \\ &\quad (\boldsymbol{I} - \boldsymbol{S}^* \boldsymbol{K}_{\boldsymbol{X},\boldsymbol{X}}^{-1}) \boldsymbol{K}_{\boldsymbol{X},f_N(T^*)}\Big) \end{aligned} \tag{5.23}$$

where we assumed our optimized variational distribution $q^*(\boldsymbol{X}) = \mathcal{N}(\boldsymbol{X}; \boldsymbol{m}^*, \boldsymbol{S}^*)$ approximates the posterior $p_d(\boldsymbol{X}|\boldsymbol{D})$. We used $\boldsymbol{K}_{f_N(T^*),f_N(T^*)}$ as a notation when the covariance matrix is evaluated at T^*. Consequently, the predictions at the time point T^* for unit N is $\hat{f}_N(T^*) = \boldsymbol{K}_{f_N(T^*),\boldsymbol{X}} \boldsymbol{K}_{\boldsymbol{X},\boldsymbol{X}}^{-1} \boldsymbol{m}^*$.

5.5. Experiments

In this section, the performance of our proposed methodology, denoted as MGCP-PP is investigated. We benchmark the prediction performance of our proposed framework using both synthetic and real-world data. Specifically, we benchmark the performance against Variational Bayes for Point

Processes (VBPP) approach of Lloyd et al. (2015) and the Sigmoidal Gaussian Cox Process (SGCP) of Adams et al. (2009) which are based on considering a univariate Gaussian process prior for the intensity rate. Unlike our proposed approach, the methods discussed in Lloyd et al. (2015) and Adams et al. (2009) do not consider the cross-correlation that exists between different units. Regarding our MGCP-PP model we set the number of pseudo-inputs to $M = 10$. Throughout this section we consider $N = 10$ units and it is assumed that the observations are made in $t \in [0, 100]$.

5.5.1. Data Setting

For the synthetic dataset, we simulate the underlying latent functions $f_i(t), i = 1, ..., 10$, using MGCPs and generate the intensity rates of different units using a sigmoid link function. Then conditioned on this function, we draw training datasets and test datasets (Adams et al., 2009). The number of units generated is $N = 10$ where we pick the Nth unit as the testing unit. This experiment is repeated for $Q = 1000$ times and we report the average prediction performance of the test dataset for each approach. Figure 5.4 visualizes a sample of intensity rates drawn from the defined MGCP model with four outputs passed through a sigmoid link function along with the simulated events based on the method discussed in Adams et al. (2009). We note that here we only have four outputs for the purpose of illustration while the actual simulation study is done using MGCP model with $N = 10$ outputs.

In addition to generating the intensity rates using MGCP and sigmoid link function, we define two parametric functional forms to generate the intensity rates as follows:

1) A sum of an exponential and a Gaussian bump $\lambda_i(x) = a \exp(-\frac{x}{b}) + \exp(-(\frac{x-c}{15})^2)$ where $[a, b, c]^T \sim \mathcal{N}(\boldsymbol{\mu}_1, \boldsymbol{\Sigma}_1)$ with $\boldsymbol{\mu}_1 = [3, 20, 65]^T$ and $\boldsymbol{\Sigma}_1 = \begin{bmatrix} 5e-1 & 4e-4 & -e-5 \\ 4e-4 & 2.5e-1 & 3e-7 \\ e-5 & 3e-7 & 1 \end{bmatrix}$.

2) A sinusoid with increasing frequency: $\lambda_i(x) = a' \sin(b'x^2) \exp(-\frac{x}{c'}) + 1$ where $[a', b', c']^T \sim \mathcal{N}(\boldsymbol{\mu}_2, \boldsymbol{\Sigma}_2)$ with $\boldsymbol{\mu}_2 = [2, 2e-3, 50]^T$ and $\boldsymbol{\Sigma}_2 = \begin{bmatrix} 1 & -e-7 & 2e-4 \\ -e-7 & e-2 & 3e-7 \\ e-5 & 3e-7 & 1 \end{bmatrix}$.

We, also, generate the training and testing data conditioned on these functional forms in the simulation study.

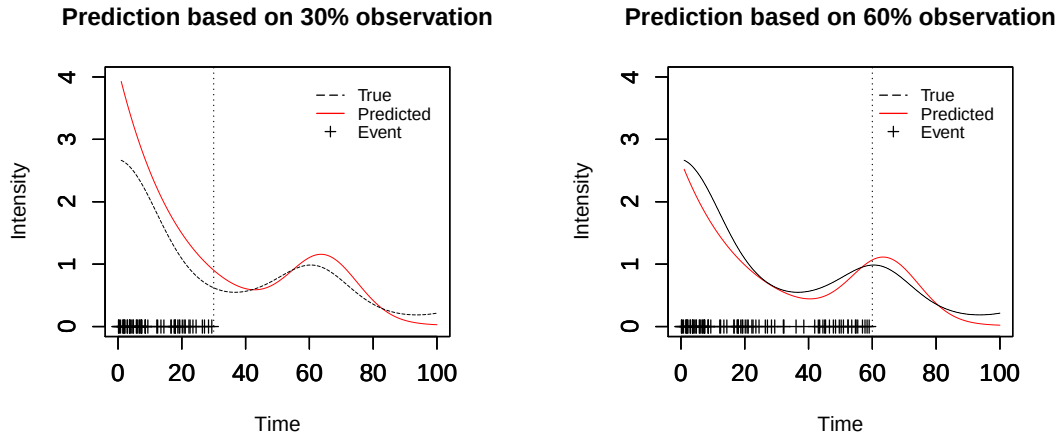

Figure 5.5: Prediction performance for testing unit in different observation percentiles

5.5.2. Results

We compare different approaches in terms of predictive log-likelihood (LL) and root mean squared (RMS) error between the predicted intensity rate and the true intensity rate of the testing unit N. Prediction performance at varying time points t^* for the partially observed unit N is reported. The time instant $t^* = \alpha \times 100$ is defined as the α-observation percentile of the testing unit N. The values of α is specified as 30% and 60% in the simulations. Figure 5.5 illustrates an example of the unit observed up to different percentiles of its life. The intensity rates here are generated using the first parametric functional form explained above. The illustrative example in Figure 5.5 demonstrates the behavior of our method. As can be seen from the figure, our joint modeling framework can provide accurate prediction of the true intensity rate for the testing unit N. It is mainly because of the flexible convolution structure considered for the MGCP approach that makes sharing of information possible among different units. The unique smoothing kernel G_i for each individual allows flexibility in the prediction as it enables each training signal to have its own characteristics. This indeed substantiates the strength of the MGCP. Using the shared latent processes, the model can infer the similarities among all units and predict the intensity rate for the testing unit more accurately by borrowing strength from the training data.

The results in figures 5.6, 5.7 and 5.8 indicates that our MGCP-PP model clearly outperforms the benchmarked models. Based on the figures we can get some important insights. First, as expected, the prediction errors decrease as the lifetime percentile increase for the testing unit N. Thus, the

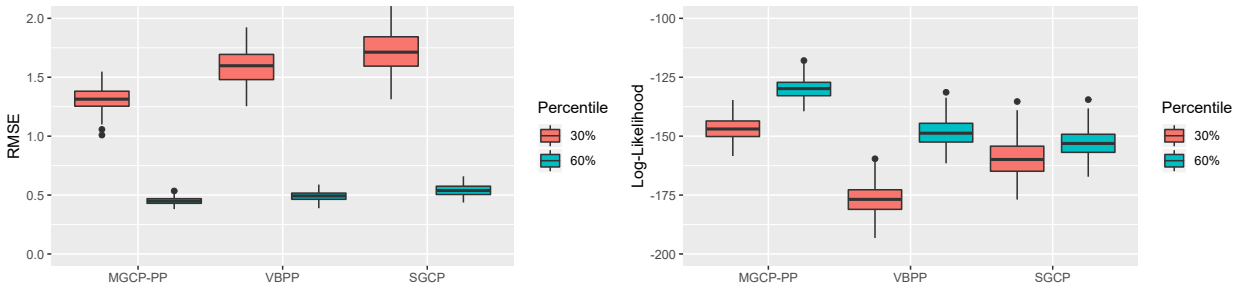

Figure 5.6: Simulation study results with MGCP and the sigmoid link function

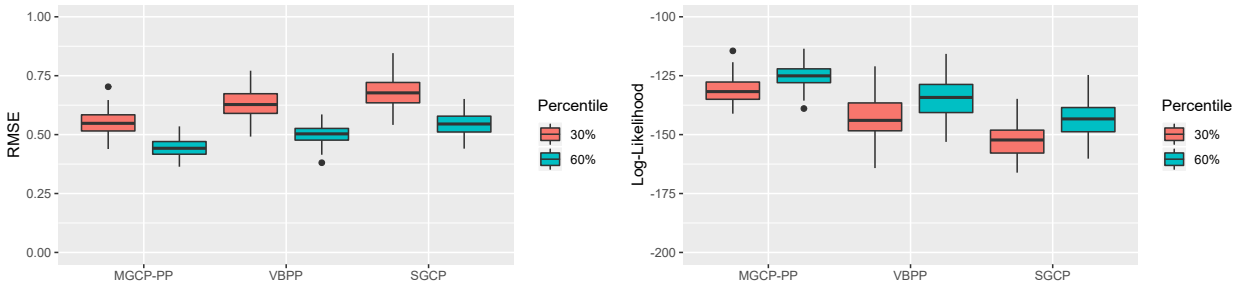

Figure 5.7: Simulation study results with parametric functional form 1

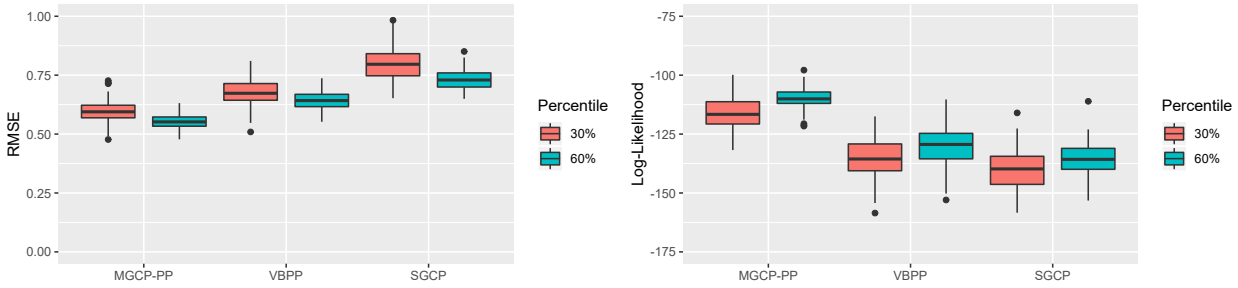

Figure 5.8: Simulation study results with parametric functional form 2

prediction accuracy from the MGCP-PP becomes more accurate as t^* increases and more data are collected from the online monitoring unit. Second, we can observe that in the first simulation study, where the data are generated using MGCP and the sigmoid link function, the SGCP approach gives better predictive performance than the VBPP; however, our MGCP-PP model approach always remains superior as it takes advantage of the pool of historical offline units in making inference for the online unit under consideration. The reason that the SGCP approach performs better than the VBPP here can be attributed to the fact that the SGCP uses the same link function and the generative process which results in well-tuned hyper-parameters. Lastly, one striking feature shown in figures

5.6, 5.7 and 5.8, is that even with a small number of observations (30% observation percentile) from the testing unit we are still able to get accurate prediction results. This is crucially important in many applications, specially when observed data are sparse, as it allows early prediction of an event occurrence such as part replacements.

5.6. Real-world case study

In this section, application of the proposed procedure on the real-world data for fleet based event prediction is demonstrated. The data is collected from material handling forklift trucks and events of interest are part replacements captured in real-time. The event occurs across 20 trucks and the number of events for the trucks lies in the range of 6-23. The actual calendar time is adjusted for each unit, i.e. the starting time is made zero for all the units. Figure 5.2 illustrates the data collected from forklift trucks collected in a teleservice system for warehouse material handling equipment. Please note that the time axis is the lifetime of the forklifts, not the calendar time.

The models MGCP-PP, VBPP, and SGCP are fitted on the case study data. To perform a comprehensive performance evaluation we use a leave-one-out cross-validation approach. First, we exclude one of the 20 units as the testing unit N and the rest are used as the training units. Prediction for testing unit N is then performed at 50% lifetime percentile. The whole procedure is repeated 20 times and the predictive performance of different approaches as a function of prediction window L is illustrated in figure 5.9 .

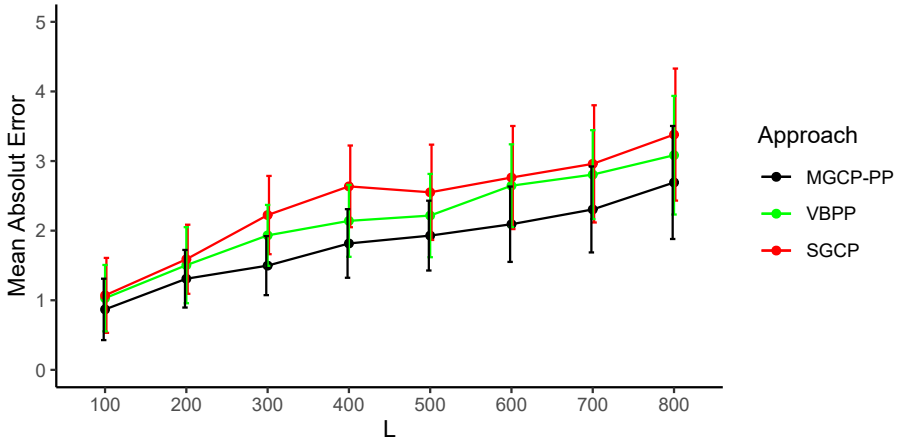

Figure 5.9: MAE of event occurrence in $[t^*, t^* + L]$.

Figure 5.9 shows the Mean Absolute Error (MAE) of the event occurrence counts in $[t^*, t^* + L]$. The MAE of all methods increases monotonically as prediction window length increases. The MGCP-PP approach outperforms the SGCP and VBPP approaches that are based on the univariate Gaussian processes. This indeed highlights the importance of borrowing information from the peer units. Our MGCP-Poisson model that facilitates sharing of information between the testing unit and the training units in the historical datatset clearly extrapolates the intensity rate more accurately which results in better prediction performance.

5.7. Conclusion

In this study, a flexible and efficient non-parametric joint modeling framework for analyzing event data is presented. Specifically, we propose a multivariate Gaussian convolution process modulated Poisson process model that leverages information from all units via a shared latent function. A variational inference framework using inducing variables is further established to jointly estimate parameters from the MGCP-Poisson model accurately. The main advantage of the proposed framework is that it allows accurate individualized prediction for units in the field using the observations from the historical off-line units. The empirical studies highlight the advantageous features of our modeling framework to predict the intensity rates and provide reliable event prediction.

The model presented in this study can be readily extended to incorporate other observation covariates. Moreover, the convolution structure proposed in this study is flexible. Here, we only shared one latent process across all the units. One can modify this structure by adding more independent latent processes for each unit to improve accuracy in modeling heterogeneity across units. Other structures that share a group of latent processes among selected group of units can be also extended from our model structure. Future work will be aimed towards developing these variational structured Poisson process frameworks.

Chapter 6

Deep Reinforcement Learning For Maintenance And Operational Workload Planning

6.1. Overview

Complex systems often consist of multiple components that are required to work together in parallel to satisfy a specific system requirement. Failure of many of these components results from a gradual and irreversible accumulation of damage, a degradation process. Multi-component systems with parallel configuration are typically designed with some level of redundancy to compensate for unexpected failure. In this way, a policy maker can decide on distribution of workload among multiple similar components in the system. However, typically the components that are assigned higher workloads close to their designed capacities experience higher rates of degradation and higher risks of unexpected failure. Another measure that can be taken by a policy maker is to proactively replace a component at a lower cost compared to the corrective maintenance cost. Specially, this chapter develops a deep reinforcement learning based stochastic policy that aims at minimizing replacement and workload assignment costs in a multi component system operating in a finite horizon. Our developed framework considers the individualized degradation evolution of each component in the system in planning for maintenance and workload assignment. A numerical study is also used to evaluate our proposed framework compared to three intuitive benchmark policies.

The results of numerical study and a case study using real-world data of frying machines confirm that significant cost savings can be achieved by adjusting maintenance and workload decisions based on the proposed framework.

6.2. Introduction

Modern complex systems typically consist of multiple components\units, where they need to operate independently and simultaneously in parallel to meet the system requirements. For example, in an automotive paint process with parallel paint booths, multiple cars can be painted simultaneously (Li, 2004) or in an aircraft, multiple engines need to operate simultaneously to produce the sufficient horsepower (Wu and Cui, 2021). Other examples include the single-stage manufacturing work cell which often consists of several identical machines arranged in parallel to simultaneously perform the specific operation to satisfy a high production demand and achieve a smooth production flow (Kaiser and Gebraeel, 2009) or multiple frying machines that need to be available and operate simultaneously to meet the demand of a store. It is noted that in any of the above examples, each paint booth, aircraft engine, manufacturing machine or frying machine is a component in the corresponding system.

In theory, failure of many engineering components usually result from a gradual and irreversible accumulation of damage when performing operation, a process that is often referred to as degradation. In many applications, the only way to observe the physical transitions that occur during degradation is to monitor some manifestation of the process, for example, temperature changes, increased vibration levels, intensity of acoustic emission, etc. These measures are known as degradation signals (Davies, 2012). In this work, we assume that a degradation signal fully captures the underlying degradation state of the components being monitored in the system. A component is considered to have failed once its degradation signal reaches a prespecified failure threshold.

Once a unit fails it needs to undergo corrective maintenance to restore to its original state before it can restart to function properly. The down time cost caused by an unexpected failure is typically significant as it involves additional costs such as lost production and overtime labor. In the automotive industry, for instance, an unexpected failure can result in stopping the assembly line, resulting in very high lost production costs. As the demand for the high reliability systems

increases, it is more imperative to develop efficient maintenance schedules to preventatively replace components.

Moreover, in modern parallel component systems, the operational workload is typically distributed among similar components to avoid overlap of unexpected failures of multiple units. The workload assigned to a component plays a critical role in its expected remaining useful life. In general, components that are assigned higher workloads are bound to fail faster than units operating under mild conditions (Hao et al., 2015). As a result, accounting for components' workload conditions and their effect on components' degradation is very important for planning a cost-effective maintenance schedule.

In recent years, advances in sensor technology and wireless communications are playing a pivotal role in enabling what is referred to as Internet of Things (IoT). Remote condition monitoring of physical assets has enabled an unprecedented opportunity for maintenance planning. The goal of condition monitoring is to leverage data collected from sensors to predict the remaining useful life of the component for a condition based maintenance policy. As a result, the unnecessary maintenance actions and the risk associated with the preventive maintenance reduce which leads to significant cost savings (Alaswad and Xiang, 2017; Yildirim et al., 2016a,b).

Condition based maintenance scheduling has attracted significant attentions in recent years. Research on this topic can be broadly classified into two groups. First group consists of papers that focus merely on maintenance optimization (Yildirim et al., 2016a; Poppe et al., 2018; Zhao et al., 2018; Caballé et al., 2015), while the second group considers the operational decisions in the context of maintenance scheduling (Kaufman and Lewis, 2007; Yildirim et al., 2016b). However, most of these existing maintenance models focus on single-component systems, and are not applicable for complex systems consisting of multiple components, due to various interactions between the components. In general, there are three different types of interactions: economic, structural, and stochastic dependence (Thomas, 1986). Economic dependency is the most common one among these three types of interactions. Systems with the economic decency typically incur a common systme-level cost, often referred to as setup cost, due to mobilizing repair crew, safety provisions, disassembling machines, special transportation, and the downtime loss. These costs are shared by all maintenance activities performed simultaneously. Considerable cost savings can be obtained by jointly maintaining several components instead of separately, especially when the setup cost is

high.

Multi-component maintenance planning problem, which joins the stochastic process regarding the failures of the components with the combinatorial problems regarding the grouping of maintenance activities (Dekker and Scarf, 1998; Van Horenbeek and Pintelon, 2013), is challenging in both modeling and solution techniques, and has remained an open issue in the literature. The problem can quickly end in complex models and explicit analytical expressions for optimal maintenance costs and the corresponding decisions are sometime impossible to obtain. One often has to make special system assumptions (Tian and Liao, 2011; Huynh et al., 2014), impose restrictions on maintenance grouping activities (Ding and Tian, 2012; Van Horenbeek and Pintelon, 2013), and/or resort to simulation tools (Laggoune et al., 2009; Nguyen et al., 2015) so that the decision problem can be formulated with less mathematical difficulty. The difficulty of this problem even exacerbates when optimizing decisions during a specific time horizon.

In this chapter, we study the maintenance and operational workload planning problem for multi-component systems with economic dependence over a finite planning horizon. It is assumed that the components in the system are similar and are working in parallel to satisfy a specific demand. We aim to minimize total maintenance and operational workload costs for all components at each decision period. First, we model the components' degradation with a continuous-time continuous-state stochastic process that captures the effect of workload over time. Moreover, variation in different components are considered in our framework through a random effect modeling the drift of stochastic process. In our degradation-modeling framework, real-time signals are used to update the predictive distribution of the degradation signal using Bayesian techniques at each decision epoch.

Next, we integrate this predictive distribution into our maintenance and operational workload planning problem and formulate it as a Markov decision process (MDP). Moreover, we present a novel Deep Reinforcement Learning (DRL) procedure to smartly decide on the maintenance schedule and to distribute the workload among different components in the system over a finite planning horizon. We note that such an MDP model combines both constrained continuous and binary actions which pose challenges on developing a policy based on DRL. In this regard, we propose a decomposition of the actions embedded in a policy gradient approach based on the advantage actor-critic algorithm.

The rest of this chapter is organized as follows: Section 6.3 presents our predictive degradation modeling framework. Section 6.4 introduces the maintenance and operational workload planning problem. Our MDP formulation of the maintenance and operational planning problem as well as the proposed solution based on DRL are presented in section 6.5. In section 6.6, we present the experimental framework and the results of our numerical studies. Finally, our concluding remarks will be provided in section 6.7.

6.3. Degradation Modeling Framework

In this section, we present a sensor-based degradation modeling framework that is used to characterize the degradation of a component in the system. Within this framework, the evolution of a component's degradation signal is modeled as a stochastic process.

In this study, we model the degradation signal as a continuous-time continuous-state stochastic process. The key underlying assumption here is that the degradation process of each unit depends on the operational workload assigned to them over time. We define $\{X_i(t, \Omega_i(t)) : t \in [0, +\infty)\}$ as the underlying stochastic process of unit i where $\Omega_i(t) = \{\omega_i(s) : s \in [0, t),\ \omega_i(s) \in [0, \omega_{\max}]\}$ is its complete workload information until time t. We note that $\omega_{\max}$ is the upper-bound capacity of component i in the system. Each component i in the system can be assigned a workload up to its capacity. Formally, the degradation signal can be expressed as follows:

$$X_i(t, \Omega_i(t)) = \int_0^t \Gamma_i(\omega_i(s))ds + \int_0^t \nu(\omega_i(s))dW(s), \tag{6.1}$$

where $X_i(t, \Omega_i(t))$ is the amplitude of the degradation signal of component i at time t. $\Gamma_i(\omega_i(t))$ and $\nu_i(\omega_i(t))$ are the functions associated with rate and diffusion of degradation signal, respectively. These functions can be further decomposed as $\Gamma_i(\omega_i(t)) = \beta_i\omega_i(t)$ and $\nu(\omega_i(t)) = [\sigma^2\omega_i(t)]^{1/2}$. β_i denotes the nominal rate of degradation for component i which can be considered to follow a normal distribution $\pi_i(\beta_i) \sim \mathcal{N}(\mu_0, \sigma_0^2)$ to model unit to unit variation. $\{W(t) : t \geq 0\}$ is a standard Brownian motion process that captures the signal noise. In this degradation modeling framework, we make the common assumption that $P(\beta < 0)$ is negligible. Similar assumptions have been widely use in degradation modeling literature; see, for example Bae and Kvam (2006); Hao et al. (2015).

Under this construct, we update the prior distribution $\pi_i(\beta_i)$ in real-time using in situ degradation signals acquired from components operating in the field. The updated (posterior) distribution represents a new predictive distribution of the degradation signal, i.e., a revised distribution on the signal trajectory for each component i of the system. The updating procedure can be performed using a Bayesian framework. Without loss of generality, we assume that condition monitoring and workload adjustment are performed at discrete observation epochs $\{t_j : 1 \leq j \leq k\}$ where t_k is the most recent observation epoch, and the sampling intervals are constant, i.e. $t_1 - t_0 = t_2 - t_1 = ... = t_k - t_{k-1} = \delta t$. Furthermore, let $X_i(t_j, \Omega_i(t_j))$ be the amplitude of the degradation signal of unit i at observation time t_j. We define the signal changes during a sampling interval as $\delta X_i(t_j) = X_i(t_j, \Omega_i(t_j)) - X_i(t_{j-1}, \Omega_i(t_{j-1}))$. Based on the property of Brownian motion process, the signal changes $\delta \boldsymbol{X}_i(t_k) = \{\delta X_i(t_j) : 1 \leq j \leq k\}$ are independent and identically distributed normal random variables. Given β_i and the corresponding workload assignment $\omega_i(t_{j-1})$ during the time interval $[t_{j-1}, t_j]$, we have:

$$\delta X_i(t_j)|\omega_i(t_{j-1}), \beta_i \sim \mathcal{N}\left(\beta_i \omega_i(t_{j-1})\delta t, \sigma^2 \omega_i(t_{j-1})\delta t\right), \tag{6.2}$$

where based on the independent increment property of Brownian motion process, the probability distribution function of signal increments can be expressed as follows:

$$p(\delta \boldsymbol{X}_i(t_k)|\omega_i(t_k), \beta_i) = \prod_{j=1}^{k} \frac{1}{\sqrt{2\pi\sigma^2\delta t}} \exp\left(-\sum_{j=1}^{k} \frac{(\delta X_i(t_j) - \beta_i \omega_i(t_{j-1}))^2}{2\sigma^2 \omega_i(t_{j-1})\delta t}\right). \tag{6.3}$$

Next, considering the degradation signal changes $\delta \boldsymbol{X}_i(t_k)$, workload assignments $\Omega_i(t_k)$ and the above likelihood, the posterior distribution of β_i can be computed using the following proposition.

Proposition 1 *Given the observed signal increments $\delta \boldsymbol{X}_i(t_k)$ and workload assignments $\Omega_i(t_k)$, the posterior distribution of β (denoted as β') at t_k follows a normal distribution with the following parameters:*

$$\mu_0' = \frac{\sigma_0^2 X_i(t_k, \Omega_i(t_k)) + \sigma^2 \mu_0}{\sigma_0^2 \delta t \sum_{j=1}^{k} \omega_i(t_{j-1}) + \sigma^2}, \tag{6.4}$$

$$\sigma_0'^2 = \frac{\sigma_0^2 \sigma^2}{\sigma_0^2 \delta t \sum_{j=1}^{k} \omega_i(t_{j-1}) + \sigma^2}. \tag{6.5}$$

Proof. Given the prior distribution of $\pi(\beta)$, we can obtain its posterior distribution, denoted by

$p(\beta|\delta \boldsymbol{X}_i(t_k), \Omega_i(t_k))$ as follows:

$$
\begin{aligned}
p(\beta_i|\delta \boldsymbol{X}_i(t_k), \Omega_i(t_k)) \propto & p(\delta \boldsymbol{X}_i(t_k)|\Omega_i(t_k), \beta_i)\pi(\beta_i) \\
& \propto \exp\left(\sum_{j=1}^{k} \frac{(\delta X_i(t_j) - \beta_i \omega_i(t_{j-1})\delta t)^2}{2\sigma^2 \omega_i(t_{j-1})\delta t}\right) \exp\left(-\frac{1}{2\sigma_0^2}(\beta_i - \mu_0)^2\right) \\
& \propto \exp\left(-\frac{1}{2\sigma^2}\left[\sum_{j=1}^{k} \frac{\delta X_i(t_j)^2 + \beta_i^2 \omega_i(t_{j-1})^2(\delta t)^2 - 2\delta X_i(t_j)\beta_i \omega_i(t_{j-1})\delta t}{\omega_i(t_{j-1})\delta t}\right]\right) \times \\
& \quad \exp\left(-\frac{1}{2\sigma_0^2}\left[\beta_i^2 + \mu_0^2 - 2\beta_i\mu_0\right]\right) \\
& \propto \exp\left(-\frac{1}{2}\beta_i^2\left[\sum_{j=1}^{k} \frac{\omega_i(t_{j-1})\delta t}{\sigma^2} + \frac{1}{\sigma_0^2}\right] + \frac{1}{2}\beta_i\left[\frac{2\sum_{j=1}^{k} \delta X_i(t_j)}{\sigma^2} + \frac{2\mu_0}{\sigma_0^2}\right]\right) \\
& \propto \exp\left(-\frac{1}{2}\beta_i^2\left[\frac{\sigma_0^2 \delta t \sum_{j=1}^{k} \omega_i(t_{j-1}) + \sigma^2}{\sigma_0^2\sigma^2}\right] + \beta_i\left[\frac{\sigma_0^2 X_i(t_k, \Omega_i(t_k)) + \sigma^2\mu_0}{\sigma_0^2\sigma^2}\right]\right),
\end{aligned}
\tag{6.6}
$$

which follows a normal distribution with the parameters given in the proposition. □

Finally, we note that it is easy to show that the mean of posterior distribution given in proposition 1 is always positive indicating that the signal changes stay non-decreasing. Given the posterior distribution of β, we would like to determine the posterior distribution of degradation signal for each component i. We then define the random variable $X_i(t_k + t, \Omega_i(t_k + t))$ to be the degradation signal value observed at time $t_k + t$, $t > 0$, given degradation signal increments $\delta \boldsymbol{X}_i(t_k)$ and workload assignments $\Omega_i(t_k)$ observed at discrete epochs $\{t_j : 1 \leq j \leq k\}$. We can then determine the predictive distribution of $X_i(t_k + t, \Omega_i(t_k + t))$ as follows.

Proposition 2 *Given the observed signal increments $\delta \boldsymbol{X}_i(t_k)$ and workload assignments $\Omega_i(t_k)$, $X_i(t_k + t, \Omega_i(t_k + t))$ is a normal random variable with mean $\tilde{\mu}(t_k + t)$ and variance $\tilde{\sigma}^2(t_k + t)$, where:*

$$
\tilde{\mu}_i(t_k + t) \triangleq X_i(t_k, \Omega_i(t_k)) + \mu_0' \omega_i(t_k) t, \tag{6.7}
$$

$$
\tilde{\sigma}_i^2(t_k + t) \triangleq \omega_i(t_k)^2 t^2 \sigma_0'^2 + \omega_i(t_k) t \sigma^2, \tag{6.8}
$$

Proof. First, note that using (6.1) we can write $X_i(t_k + t, \Omega_i(t_k + t))$ as:

$$\begin{aligned} X_i(t_k + t, \Omega_i(t_k + t)) =& X_i(t_k, \Omega_i(t_k)) + \int_{t_k}^{t_k+t} \beta' \omega_i(t_k) ds + \int_{t_k}^{t_k+t} \sqrt{\sigma^2 \omega_i(t_k)} dW(s) \\ =& X_i(t_k, \Omega_i(t_k)) + \beta' \omega_i(t_k) t + \sqrt{\sigma^2 \omega_i(t_k)} (W(t_k + t) - W(t_k)). \end{aligned} \tag{6.9}$$

Therefore, given the observed signal increments $\delta \boldsymbol{X}_i(t_k)$ and workload assignments $\Omega_i(t_k)$, $X_i(t_k + t, \Omega_i(t_k + t))$ is a normal random variable with mean $\tilde{\mu}(t_k + t) = X_i(t_k, \Omega_i(t_k)) + E[\beta']\omega_i(t_k)t = X_i(t_k, \Omega_i(t_k)) + \mu_0' \omega_i(t_k)t$ and variance $\tilde{\sigma}^2(t_k + t)\tilde{\mu}(t_k + t) = (\omega_i(t_k)t)^2 var[\beta'] + \sigma^2 \omega_i(t_k) var[W(t_k + t) - W(t_k))] = \omega_i(t_k)^2 t^2 \sigma_0'^2 + \omega_i(t_k) t \sigma^2$. □

This procedure for updating the distribution of degradation signal coefficient (β) can be performed at each observation epoch new sensor information is obtained. In other words, each observation epoch we collect a new signal observation we can recalculate the posterior distribution for β and obtain new estimates of μ_0' and $\sigma_0'^2$ using proposition 1. Then, given these updated parameters, we can update the predictive distribution of the degradation signal for each component i by updating the values of $\tilde{\mu}(t_k + t)$ and $\tilde{\sigma}^2(t_k + t)$ using proposition 2. We note that this updating procedure only requires the last degradation state value and the summation of all assigned workload for each component. Thus, the degradation of each component can be formulated as a Markov decision process (MDP). Next section discusses the MDP formulation of the maintenance and operational planning problem.

6.4. Maintenance and Operational Workload Planning Problem

In this section, we develop a condition monitoring based maintenance and operational workload planning problem. We consider a system with n components working in parallel to satisfy a deterministic demand over a finite planning horizon. Specifically, we discretize a planning horizon of length T into L time intervals each corresponding to a possible workload assignment period. The workload at each time interval can be distributed among multiple similar units working in parallel. The change in the degradation state of each component i ($i = 1, ..., n$) is governed by the degradation framework developed in section 6.3. The components with higher workload tend to degrade faster as outlined in previous section.

Specifically, the inspection are scheduled periodically at times $\delta t, 2\delta t, ..., L\delta t$ to reveal the degradation of each component (δt is predetermined). The detailed degradation information of components between inspections is unavailable. On the l^{th} inspection, we obtain information on the degradation measurements of all components in the system. With some abuse of notation, we denote this information as $\boldsymbol{X}_l = [X_{l1}, X_{l2}, ..., X_{ln}]$ where $X_{li} = X_i(l\delta t, \Omega_i(l\delta t))$. We also denote $\boldsymbol{\eta}_l = [\eta_{l1}, \eta_{l2}, ..., \eta_{ln}]$ as the vector containing the summation of workloads assigned to each component from their last replacement. We note that when the inspection interval is also a decision variable, δt can be optimized by using a grid search approach.

We use $s_l = \{\boldsymbol{X}_l, \boldsymbol{\eta}_l\}$ to denote the overall health state/condition of the system in l^{th} inspection epoch. Based on such conditions, a proactive replacement decision can be made immediately for any component in the system. We denote the proactive maintenance action set of the n-component system with $\boldsymbol{\zeta}_l = [\zeta_{l1}, \zeta_{l2}, ..., \zeta_{ln}]$ where $\zeta_{li} \in \{0, 1\}$. $\zeta_{li} = 1$ indicates that component i should be replaced by a new one with negligible time; and $\zeta_{li} = 0$ indicates that no action is needed. We denote the replacement cost of each component as c_m. To model a form of economic dependence between components in the system and incentivised for opportunistic maintenance, we also consider a setup cost of c_s at any maintenance occasion. For instance, if n components are replaced at the same time, the total savings from executing these n maintenance activities jointly is $c_s(n-1)$.

At each inspection epoch l, we also need to distribute the workload activities among n components in the system to satisfy a fixed demand of D at each time interval. To highlight our main idea, here we assume that the demand is constant and components perform one type of operation. It is worth mentioning that the measurement unit of workload, demand and capacity may be either discrete or continuous, depending on the application areas. For example, in discrete manufacturing processes, the measurement unit can be the number of parts fabricated per hour, while in a continuous system (e.g., the power grid), the measurement unit can be megawatt (MW). We consider a workload cost of c_w for each component in the system. We use $\boldsymbol{\omega}_l = [\omega_{l1}, \omega_{l2}, ..., \omega_{ln}]$ to denote the workload assigned to each component in inspection epoch l. As mentioned in the previous section ω_{li} has an upper-bound capacity of $\omega_{\max}$. If the sum of workload assigned to different components at each time interval is less than the demand, we incur a lost demand cost of λ per unit of unsatisfied demand.

The components fail if their degradation signals pass a pre-specified threshold Λ. If we decide

not to replace a component in the system, we run the risk of sudden failure (within δt time units until the next observation), in such a case we will be forced to perform a failure (reactive) replacement at a cost $c_f > c_m$ for each failed component. Ordering the costs in this manner reflects the fact that reactive replacements may include additional costs such as lost production and overtime labor.

6.5. Deep Reinforcement Learning for Maintenance and Operational Workload Planning Problem

We propose a customized DRL approach for the maintenance and operational workload planning problem depicted in section 6.4. In section 6.5.1, we first discuss the condition monitoring based maintenance and operational workload planning problem as a MDP, based on which in section 6.5.2 we propose a DRL approach that is flexible and efficient at minimizing the maintenance and operational workload costs.

6.5.1. Markov Decision Process for Maintenance and Operational Workload Planning Problem

An MDP is a discrete-time stochastic control process (Puterman, 2014) where at each discrete time step l the agent observes a state s_l and must take an action $a_l \sim \pi(a_l|s_l)$, where π is the agent's policy. On the next step, the environment transitions to the new state $s_{l+1} \sim P(s_{l+1}|s_l, a_l)$ and gives the agent a reward $r_l \sim P(r_l|s_l, a_l, s_{l+1})$. The agent's objective is to find an optimal policy π^* that maximizes the expected discounted return $\mathbb{E}_\pi[\sum_l \gamma^l r_l]$, where $\gamma \in (0, 1]$ is the discount factor.

For the n-component system introduced in the section 6.4, we showed that given the degradation status and the summation of workload assigned to each components at each inspection epoch l the future degradation process does not depend on the degradation history because of the independent increment property of Brownian motion process. Upon each inspection the predictive distribution of degradation signal for each component and the expected reward can be calculated. Therefore the Markov property holds for the system of interest, and the degradation based maintenance and operational workload planning problem can be formulated as an MDP.

We consider $s_l = \{\boldsymbol{X}_l, \boldsymbol{\eta}_l\}$ as the state observed at each decision epoch l. We denote $a_l = \{\boldsymbol{\zeta}_l, \boldsymbol{\omega}_l\}$ as set of actions that can be taken. Upon taking an action a_l, the system transits to a new

state and a reward $r(s_l, a_l, s_{l+1})$ is observed. We note that the observed reward depends on action a_l and both the current state s_l and the next state s_{l+1} that the system transits to as follows:

$$r(s_l, a_l, s_{l+1}) = -\Bigg[\sum_i \zeta_{li} c_m + \text{sgn}\Big(\sum_i \zeta_{li}\Big) c_s + \sum_i \omega_{li} c_w + \max\Big\{0, D - \sum_i \omega_{li}\Big\}\lambda + \sum_i \max\Big\{0, \text{sgn}\Big(X_{(l+1)i} - \Lambda\Big)\Big\} c_f\Bigg]. \tag{6.10}$$

As the state transitions are governed by the environment, we can get an expected values of instant reward by marginalizing on the future state the system will transit to. In this regard, we use the results of proposition 2 developed in section 6.3 to find the expected value as follows:

$$\begin{aligned} r(s_l, a_l) &= \int f(s_{l+1}|s_l, a_l) r(s_l, a_l, s_{l+1}) ds_{l+1} \\ &= -\Bigg[\sum_i \zeta_{li} c_m + \text{sgn}\Big(\sum_i \zeta_{li}\Big) c_s + \sum_i \omega_{li} c_w + \max\Big\{0, D - \sum_i \omega_{li}\Big\}\lambda \\ &\quad + \int \sum_i \max\Big\{0, \text{sgn}\Big(X_{(l+1)i}\Big)\Big\} c_f dF(X_{(l+1)i})\Bigg] \\ &= -\Bigg[\sum_i \zeta_{li} c_m + \text{sgn}\Big(\sum_i \zeta_{li}\Big) c_s + \sum_i \omega_{li} c_w + \max\Big\{0, D - \sum_i \omega_{li}\Big\}\lambda \\ &\quad + \Big(1 - \Phi\Big(\frac{\Lambda - \tilde{\mu}_i((l+1)\delta t)}{\tilde{\sigma}_i((l+1)\delta t)}\Big)\Big) c_f\Bigg], \end{aligned} \tag{6.11}$$

where Φ is the cdf of standard normal distribution. Here we note that a maximization of the reward will lead to a minimization of total cost. The expected instant reward calculated in equation (6.11) will be further utilized in the next section in the proposed DRL procedure.

6.5.2. Deep Reinforcement Learning for Maintenance and Operational Workload Policy Optimization

In this section we propose a DRL approach based on the MDP formulation of the maintenance and operation workload planning problem. Reinforcement Learning (RL) is one of the three fundamental machine learning paradigms, alongside the supervised learning and unsupervised learning (Sutton and Barto, 2018). RL learns to choose optimal actions that maximize rewards or minimize losses for systems that consist of one or more agents interacting with an environment.

The agent chooses actions based on the observed states of the environment, and each action results in an outcome/reward as well as the next state of the environment. As a result, RL is suitable for studying the decision making in MDP problems (Sutton and Barto, 2018).

Most applications of the traditional RL have been limited to domains where the features can be handcrafted or represented in low-dimensional state spaces, e.g., when there is a single component in a system. However, our proposed maintenance and operation workload planning problem involves n components subject to degradation over time. At each inspection epoch, the dimension of maintenance decisions alone is 2^n, which increases exponentially with the number of components. Therefore, directly applying the traditional RL to maintenance and workload planning of n-component systems would be computationally inefficient and challenging.

To overcome the challenge of the traditional RL, we propose a DRL-based approach for the maintenance and operational workload planning problem of n-component systems. The DRL is an integration of the RL and deep learning that provides powerful approximation and representation learning properties, which significantly facilitates the computation speed and is thus suitable for high-dimensional problems. In the literature, the DRL has achieved wide successes in various areas such as the robot control (Bhagat et al., 2019), medical decision making (Tseng et al., 2017), vehicular network scheduling (Atallah et al., 2018) and dialogue system training (Cuayáhuitl, 2017). Various DRL algorithms have been developed recently, among which the policy gradient based algorithms are popular and have achieved significant successes in a variety of applications (Liu et al., 2021; Andriotis and Papakonstantinou, 2019). In this study, the advantage actor-critic algorithm which is a policy gradient based algorithm is selected.

In a policy gradient algorithm a policy can be described as a probability distribution for taking an action a_l given a state s_l parametrized by a p-dimensional vector $\theta \in \mathbb{R}^p$, denoted as $\pi(a_l|s_l;\theta) : \mathcal{S} \rightarrow \mathcal{A}$. At each inspection interval l, a policy distribution $\pi(a_l|s_l;\theta)$ is constructed from the distribution parameters. An action a_l is then sampled from this distribution to interact with the environment, i.e. $a_l \sim \pi(a_l|s_l;\theta)$. Starting from an initial state, an agent follows a policy to interact with the MDP to generate a trajectory of states, actions, and rewards $s_0, a_0, r_0, ..., s_L, a_L, r_L$. The goal of an agent is to maximize the return from a state, defined as the total discounted reward $r_l^\gamma = \sum_{j=1}^{\infty} \gamma^j r(s_{l+j}, a_{l+j})$ where $\gamma \in (0, 1]$ is the discount factor describing how much we favor current reward over those in the future.

To describe how good it is being in state s under the policy π, a state-value function $V^{\pi}(s) = \mathbb{E}_{\pi}[r_0^{\gamma}|s_0 = s]$ is defined as the expected return starting from state s, following the policy π, interacting with environment dynamics, and repeating until the maximum number of episodes is reached. An action-value function $Q^{\pi}(s,a)$, which describes the value of taking a certain action is defined similarly, except it is the expected return starting from state s after taking an action a under policy π. The goal in reinforcement learning is to learn a policy maximizing the expected return from the start distribution

$$\begin{aligned} J(\pi) = &\int_{\mathcal{S}} \rho^{\pi}(s) \int_{\mathcal{A}} \pi(a|s;\theta) r(s,a) da ds \\ = &\mathbb{E}_{s\sim\rho^{\pi}, a\sim\pi}[r(s,a)], \end{aligned} \tag{6.12}$$

where $\rho^{\pi}(s) = \sum_{l=0}^{\infty} \gamma^l p(s_l = s)$ is the unnormalized discounted state visitation frequency in the limit (Sutton et al., 1999).

Policy gradient methods are featured heavily in the state-of-the-art model-free reinforcement learning algorithm (Mnih et al., 2016, 2015; Lillicrap et al., 2015). In these methods, training of the policy is performed by following the gradient of the performance with respect to the parameters $\nabla_{\theta} J(\pi)$. This gradient can be computed from the *Policy Gradient Theorem* by simply changing $r(s,a)$ to $Q^{\pi}(s,a)$ as follows (Sutton et al., 1999):

$$\nabla_{\theta} J(\pi) = \mathbb{E}[Q^{\pi}(s,a) \nabla_{\theta} \log \pi(a|s;\theta)]. \tag{6.13}$$

Estimating the policy gradient is one of the most important issues in reinforcement learning. The action-value function $Q^{\pi}(s,a)$ can be estimated by a variety of sample-based algorithms such as Monte-Carlo (MC) or temporal-difference (TD) learning.

In an Actor-Critic method, an *actor* learns a policy to select actions and a *critic* estimates the value function, and criticizes decisions made by the actor. The actor refers to the part of the agent responsible for the producing the policy, while the critic refers to the part of agent responsible for producing a value function. The gradient estimation technique can have high variance when using only an actor as in (6.13). To solve this problem, actor-critic methods aim to reduce this variance by using an actor and a critic. In this work, we focus on *Advantage Actor-Critic* (A2C) method (Mnih

et al., 2016), which makes update to policy using *advantage function*: $A^{\pi}(s,a) \triangleq Q^{\pi}(s,a) - V^{\pi}(s)$. Replacing the action value function ($Q^{\pi}(s,a)$) with the advantage ($A^{\pi}(s,a)$) reduces the variance in estimating the policy gradient (Mnih et al., 2016; Greensmith et al., 2004). This gives us the following stochastic policy gradient estimates:

$$g = A^{\pi}(s,a)\nabla_{\theta} \log \pi(a|s;\theta), \tag{6.14}$$

where g is the is the policy gradient estimator using the advantage. The advantage function measures how much better than the average it is to take an action a.

Typically, the critic's approximate value of a state $V(s;\theta_v)$ is parametrized by θ_v, where $\theta_v \in \mathbb{R}^d$ and d is the number components of the parameters vector. Both the actor function and the critic function can be updated with the TD learning approach. The actor with policy $\pi(a|s;\theta)$ and the critic with the $V(s;\theta_v)$ are trained simultaneously. In this study, both the actor's policy ($\pi(a|s;\theta)$) and critic's value function ($V(s;\theta_v)$) are replaced with deep neural networks (Mnih et al., 2016, 2015; Lillicrap et al., 2015). Figure 6.1 shows the architecture of the proposed A2C method used in this study.

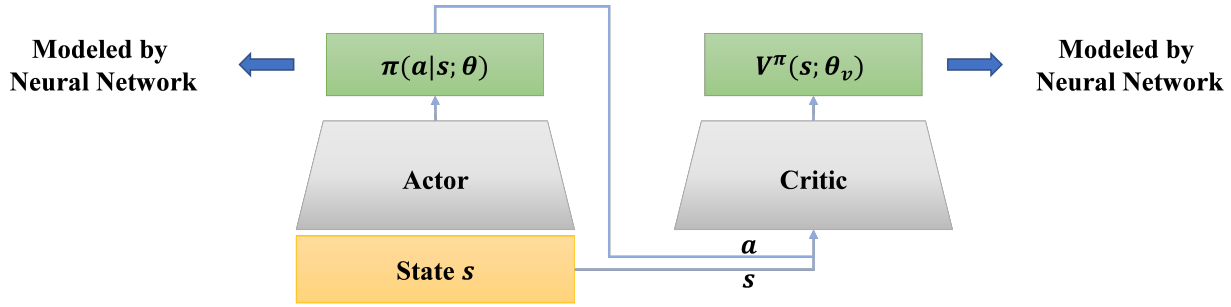

Figure 6.1: Advantage actor-critic architecture.

In the proposed maintenance and operational workload planning problem, the action consists of both binary actions (ζ_l) and continuous actions (ω_l). In the context of problem devised in this study, the binary actions and continuous actions are independent given the observed state s_l, yielding the following decomposition:

$$\begin{aligned}\pi(a_l|s_l;\theta) =& \pi_{\theta_b}(\zeta_l|s_l;\theta)\pi_{\theta_c}(\omega_l|s_l;\theta)\\ =& \prod_i \pi_{\theta_{b_i}}(\zeta_{li}|s_l;\theta)\prod_i \pi_{\theta_{c_i}}(\omega_{li}|s_l;\theta),\end{aligned} \tag{6.15}$$

where $\pi_{\theta_{b_i}}$ is the probability mass function parametrized by θ_{b_i} and $\pi_{\theta_{c_i}}$ is the probability density function parametrized by θ_{c_i}. We propose to model the binary maintenance actions using Bernoulli distributions with parameters θ_{b_i} corresponding to each component i in the system where $\pi_{\theta_{b_i}}(\zeta_{li}|s_l;\theta) = f_{\text{Bernoulli}}\left(\zeta_{li};\theta_{b_i}(s_l;\theta)\right)$, and $f_{\text{Bernoulli}}$ is the probability mass function of Bernoulli distribution. It should be emphasized that the parameters of Bernoulli distributions $\theta_{b_i}(s_l;\theta)$ are modeled by neural networks with parameters θ.

Moreover, we note that the continuous workload assignment actions are bounded in $[0, \omega_{\max}]$ interval. Here, we propose to use a Beta distribution to model these continuous actions. The beta distribution has a support in $[0, 1]$ (as shown in figure 6.2). We use $\pi_{\theta_{c_i}}(\omega_{li}|s_l;\theta) = f_{\text{Beta}}\left(\frac{\omega_{li}}{\omega_{\max}};\alpha_i(s_l;\theta),\beta_i(s_l;\theta)\right)$ to represent the stochastic policy for workload assignment where f_{Beta} is the probability density function of Beta distribution, and $\theta_{c_i} = \{\alpha_i, \beta_i\}$. Since the beta distribution has finite support and no probability density falls outside of the boundary, the Beta distribution is bias-free. The shape parameters $\alpha_i = \alpha_i(s_l;\theta)$, $\beta_i = \beta_i(s_l;\theta)$ are also modeled by neural networks with parameters θ. In this study, we only consider the case where $\alpha_i, \beta_i > 1$, in which the Beta distribution is concave and unimodal.

We borrow from the literature of reinforcement learning (Haarnoja et al., 2018c,a,b) the idea of adding entropy bonus to the objective optimized by the agent, i.e. maximizing $\mathbb{E}_{a\sim\pi}\Big[\sum_l \gamma^l \Big(r(s_l, a_l) + \kappa\mathcal{H}(\pi(a_l|s_l;\theta))\Big)\Big]$. A higher κ encourages the agent to take actions that are more random, which in particular can help with exploration at the beginning of the algorithm. Our action policy distribution in (6.15) has a factorized distribution, therefore we can get a factorized entropy as follows (Chen et al., 2020):

$$\begin{aligned}\mathcal{H}(\pi(a_l|s_l;\theta)) =& \mathcal{H}(\pi_{\theta_b}(\zeta_l|s_l;\theta)) + \mathcal{H}(\pi_{\theta_c}(\omega_l|s_l;\theta))\\ =& \sum_i \mathcal{H}(\pi_{\theta_{b_i}}(\zeta_{li}|s_l;\theta)) + \sum_i \mathcal{H}(\pi_{\theta_{c_i}}(\omega_{li}|s_l;\theta)),\end{aligned} \tag{6.16}$$

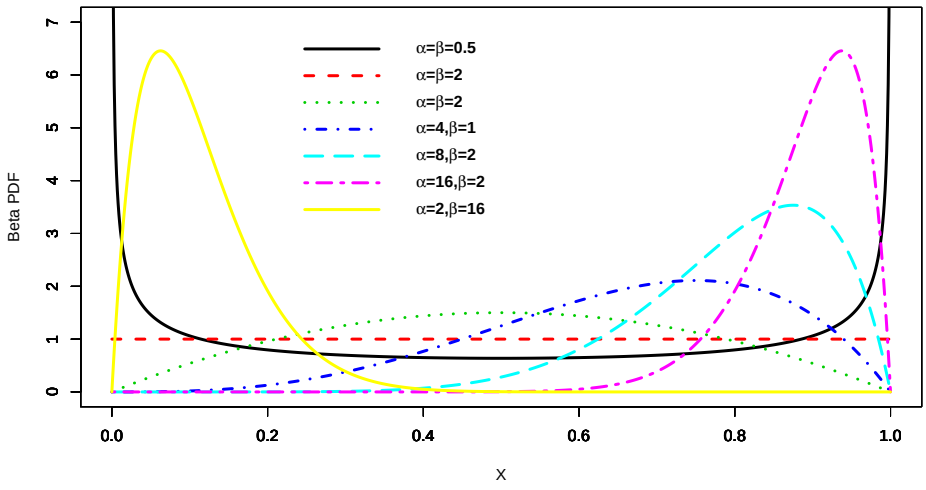

Figure 6.2: Probability density function of Beta distribution with different α and β.

where $\mathcal{H}(\pi_{\theta_{b_i}}(.))$ and $\mathcal{H}(\pi_{\theta_{c_i}}(.))$ are entropies of Bernoulli distribution and Beta distribution respectively. We add the entropy decomposition in (6.16) to the objective function of the agent to encourage for exploration. The final generalized maximum entropy objective is as follow:

$$\mathbb{E}_{a\sim\pi}\Big[\sum_{l}\gamma^{l}\Big(r(s_l,a_l)+\kappa^{b}\Big(\sum_{i}\mathcal{H}(\pi_{\theta_{b_i}}(\zeta_{li}|s_l;\theta))\Big)+\kappa^{c}\Big(\sum_{i}\mathcal{H}(\pi_{\theta_{c_i}}(\omega_{li}|s_l;\theta))\Big)\Big)\Big] \tag{6.17}$$

where hyperparameters κ^b and κ^c encourage exploration for binary and continuous actions, respectively. Note that these two hyper parameters can be tuned using the procedure described in Haarnoja et al. (2018c). The pseudo-code in algorithm 1 depicts the outline of proposed advantage actor-critic algorithm. Here an episode is a trajectory of states, actions, and rewards $s_0, a_0, r_0, ..., s_L, a_L, r_L$ following a policy $\pi(a_l|s_l;\theta)$, $t_{\max}$ is the number of steps used in TD approach to estimate $Q^{\pi}(s,a)$, and $E_{\max}$ is the maximum number of episodes the agent is trained. Next section discusses the performance of the proposed DRL procedure.

6.6. Numerical Study

In this section we investigate the performance of the DRL approach developed in section 6.5 for maintenance and operational workload planning problem. Specifically, we conduct simulation

Algorithm 1: Advantage actor-critic pseudo-code

//Assume parameter vectors θ and θ_v;
initialize step counter $t \leftarrow 1$;
initialize episode counter $E \leftarrow 1$;
repeat
  Reset gradient: $d\theta \leftarrow 0$ and $d\theta_v \leftarrow 0$;
  $t_{start} = t$;
  Get state s_t;
  repeat
    Perform a_t according to policy $\pi(a_t|s_t;\theta)$;
    Receive reward r_t and new state s_{t+1};
    $t \leftarrow t + 1$;
  until $t - t_{start} == t_{\max}$;
  $R = V(s_t;\theta_v)$ //Bootstrap from last state;
  for $l \in \{t-1, ..., t_{start}\}$ **do**
    $R \leftarrow r_l + \gamma R$;
    Accumulate gradient wrt θ: $d\theta \leftarrow d\theta + \nabla_\theta \log \pi(a_l|s_l;\theta)(R - V(s_l;\theta_v)) + \kappa^b \sum_i \partial\mathcal{H}(\pi_{\theta_{b_i}}(\zeta_{li}|s_l;\theta))/\partial\theta + \kappa^c \sum_i \partial\mathcal{H}(\pi_{\theta_{c_i}}(\omega_{li}|s_l;\theta))/\partial\theta$;
    Accumulate gradient wrt θ_v: $d\theta_v \leftarrow d\theta_v + (R - V(s_l;\theta_v))(\partial V(s_l;\theta_v)/\partial\theta_v)$;
  end
  Perform update of θ using $d\theta$ and θ_v using $d\theta_v$;
  $E \leftarrow E + 1$
until $E > E_{\max}$;

studies for a two-component system and a ten-component system in sections 6.6.1 and 6.6.2, respectively.

6.6.1. Two-component System Maintenance and Operational Workload Planning

We first consider a two component system (i.e. $n = 2$) for illustration purposes subject to Brownian motion process as described in section 6.3. The degradation coefficient β is assumed to have a prior normal distribution with $\beta \sim \mathcal{N}(\mu = 0.5, \sigma_0^2 = 0.01)$. The Brownian motion part is assumed to have a variance of 0.01 ($\sigma^2 = 0.01$). The component degradation coefficient are generated according to this prior distribution and they are updated using the Bayesian procedure proposed in section 6.3. The failure threshold is set at $\Lambda = 10$. The two components capacities are fixed at 10 ($\omega_{\max} = 10$). We assume a demand of $D = 10$ units should be satisfied in each inspection time interval. Note that the demand and capacity structure provides some level of redundancy in the components' utilization. Moreover, the cost parameters are set as in Table 6.5.

Table 6.1: Cost parameters setting

Maintenance setup cost	Replacement cost per component	Downtime cost per component per unit time	Workload cost per unit	Lost demand cost per unit
c_s =\$10	c_m =\$5	c_f =\$500	c_{wl} =\$1	λ =\$100

We consider a time horizon of length $T = 100$ unit where inspections are done every one unit of time, i.e. $L = 100$, $\delta t = 1$). We first featurize the input space to 400-dimensional vactors using random Radial Basis Functions (Rahimi et al., 2007) and then pass it to a simple neural network where the final layer is a final output layer generating statistics for the policy distribution. This is effectively a linear combination of state state features: $\phi(s)^T\theta$, where ϕ is the featurizing function and θ (θ_v in case of critic's network) is the weight vector to be learnt. The discount rate is set as $\gamma = 0.95$ and agent is trained for 1000 episodes ($E_{\max} = 1000$).

Under the aforementioned parameters setting, we consider the degradation based maintenance and operational workload planning problem. Three baseline policies are chosen as benchmark methods to illustrate the performance of proposed policy. Specially, in first baseline policy (baseline-a) we do not perform any predictive maintenance and equally distribute the workload among all the components in the system. In the second baseline policy (baseline-b) again we do not perform any predictive maintenance but we allow for the agent to optimize the distribution of workload among multiple components of the system. We note that in the baseline policies (a) and (b), we run all components until failure is observed. Then we correctively replace the failed component with a new one. In the third policy (baseline (c)), we train the agent to optimize for the predictive component replacement but distribute the workload equally among all the components. Finally, we compare these three baseline policies with our proposed policy where the agent learns and optimize the planning of maintenance and operational workload in the two component system. Figure 6.3 depicts the convergence of the different policies. Table 6.2 summarizes the performance of the proposed DRL policy and three baseline policies.

It is observed from table 6.2 that DRL-based solution of the proposed maintenance and operational workload planning problem achieves the lowest mean discounted total cost and thus outperform all the three baseline policies. Meanwhile, among the three policies, the baseline policy

Table 6.2: Mean and standard deviation (in brackets) of discounted total cost in two component system

Policy	baseline-a	baseline-b	baseline-c	proposed
Discounted total cost	21445.48 (42.3)	16648.39 (49.2)	10358.03 (55.5)	8833.011 (62.6)

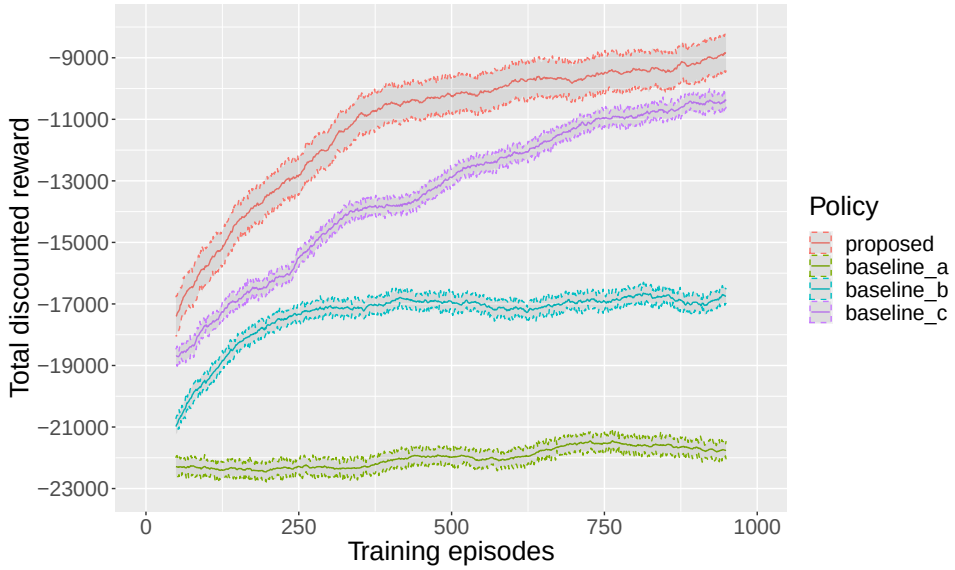

Figure 6.3: Convergence of different policies.

(a) that does not consider any maintenance and simply split the workload among components has the worst performance compared to baseline policy (b) and (c). The reason is that in baseline policy (a), the components are always run to failure and the cost of unexpected failure is higher than replacing the components. Moreover, we can see that the total discounted cost of baseline policy (c) is lower than baseline policy (b) where no maintenance is performed. The reason here can be attributed to the higher cost of unexpected failure as compared to predicatively replacing them considering the failure risk.

6.6.2. Ten-component System Maintenance and Operational Workload Planning

To further illustrate the flexibility and scalability of the proposed DRL based Maintenance and operational workload planning problem, we consider a high dimensional system with 10 components as described in section 6.4. We note that, upon each inspection, we have only $2^{10} = 1024$ different maintenance actions to choose let alone deciding on the optimal level of workload to be distributed among different units. The cost parameters in this section are also chosen from table 6.5. Again,

we consider three baseline policies explained in section 6.6.1 and compare it with the policy based on the proposed DRL. Table 6.3 gives the results of this simulation study. Moreover, the baseline polices (c) that considers predictive replacement performs relatively better than baseline (b) that always runs the risk of unexpected failure.

It can be observed from table 6.3 that the proposed DRL solution for the maintenance and operational workload planning problem outperforms the other three baseline policies. Again baseline policy (a) has the worst performance among all three benchmark policies as it does not consider any corrective maintenance action and the components are run to failure.

In addition to the cost benefit, the proposed model is also computationally efficient in solving the maintenance and operational workload planning problem. For the 10-component system with component-wise degradation and economic dependency, it takes 0.321 h using a computer with a 18 core CPU of 3.0 GHz. However, even if we ignore the optimal adjustment of workload among multiple components of the system and only focus on setting optimal replacement decision under a traditional threshold based maintenance framework (Wang et al., 2015; Li et al., 2009; Zhao et al., 2019), 10 different maintenance threshold need to be set and optimized, which are quite computationally expensive or impractical to implement with a commonly used grid search methodology framework. Furthermore, the computational time over different numbers of components with the same training setting is provided in table 6.4, which demonstrates the overall computational efficiency of the proposed approach for practical system sizes.

6.6.3. Case study

In this section we investigate the performance of the proposed DRL approach for the maintenance and operational workload planning problem based on a real-world data. Specially, we apply the proposed procedure to real-world data of frying oil degradation. During the frying process, typically, a complex series of physical and chemical reactions occur leading to the degradation of

Table 6.3: Mean and standard deviation (in brackets) of discounted total cost in ten component system

Policy	baseline-a	baseline-b	baseline-c	proposed
Discounted total cost	153423.94 (64.1)	103437.25 (65.9)	75986.37 (62.5)	409195 (71.3)

Table 6.4: The computational time over different numbers of components

Number of components	2	4	6	8	10
Computational time (h)	0.126	0.149	0.193	0.277	0.321

oil. Total polar component (TPC) which is a measure of proportion of polar materials in the oil, is the commonly known indicator for oil degradation. This indicator can be obtained by measuring the dielectric of the oil. Modern industrial fryer are equipped with a sensor that can provide daily TPC readings. Per oil disposal, the frying vat is refilled with fresh oil and the TPC reset to a lower value. The oil is typically considered bad once its TPC value reaches a pre-specified threshold value. The higher the TPC of frying oil is, the lower the quality of food produced with it. Thus serving customers the food made in higher TPC value tarnishes the food franchises' reputation. Figure 6.4 demonstrates the TPC measurements during four oil disposal cycles done in four different machines all dedicated to cooking french fries.

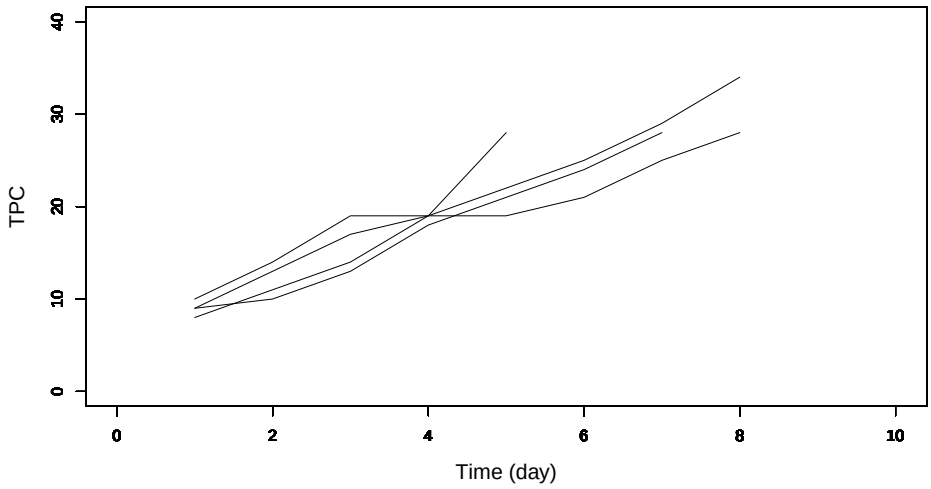

Figure 6.4: Degradation paths of frying oil

We observe from figure 6.4 that the degradation rate of frying oil is considerably heterogeneous in different machines. The main reason underlying the difference in the degradation rates of oil in different vats and in the same vat within different time intervals is attributed to the number of cooks that are done a that specific time interval. The more cook is done in a frying vat, the more frying oil is exposed to the moister content of food which increases the hydrolysis of oils. Following the

Table 6.5: Mean and standard deviation (in brackets) of discounted total cost in case study.

Policy	baseline-a	baseline-b	baseline-c	proposed
Discounted total cost	15438.64 (82.4)	14264.89 (81.9)	13986.38 (79.7)	12724 (93.6)

regulation around deep fat frying (Esfarjani et al., 2019; Choe and Min, 2007; Dobargarnes and Márquez-Ruiz, 1998) we consider a TPC of 25 as the boundary over which the served food is of inferior quality.

We model the degradation of oil as the Brownian motion process in (6.1). We consider 112 oil disposal cycles from similar frying vats where TPC measurements are done daily. The likelihood of TPC increments is as follows:

$$p(\boldsymbol{\Delta X}|\psi,\Omega) = \int \prod_{i=1}^{112} \prod_{j=1}^{n_i} p\left(\delta X_i(t_j)|\omega_i(t_{j-1}),\beta\right) p(\beta) d\beta, \tag{6.18}$$

where $\boldsymbol{\Delta X} = \left\{\{\delta X_i(t)j)\}_{j=1}^{n_i}\right\}_{i=1}^{112}$, $\psi = \{\mu_0, \sigma_0, \sigma\}$, $p(\delta X_i(t_j)|\omega_i(t_{j-1}),\beta) \sim \mathcal{N}(\beta\omega_i(t_{j-1}), \sigma^2\omega(t_{j-1}))$ and $\Omega = \{\Omega_i(t_{n_i})\}_{i=1}^{n}$ is the history of number of cooks done during each oil disposal cycle. The parameter estimation is done using a maximum likelihood approach (Wang, 2010; Wang et al., 2011; Picchini et al., 2010). The degradation coefficient β is estimated to follow a normal distribution with $\beta \sim \mathcal{N}(\mu_0 = 0.043, \sigma_0^2 = 0.00032)$. The Brownian motion part is moreover estimated to have a variance of 0.056 ($\sigma^2 = 0.056$).

We use the threshold value of 25 and the cost parameters in table 6.5. We consider a time horizon of 30 days where degradation measures are observed every day. A fixed demand of 100 cooks must be satisfied in every time interval. We consider three baseline policies introduced in the previous section. Four frying vats are considered each with a capacity of serving 50 cooks every day. Moreover, each inspection of component requires a complete shut down of frying vat and a lengthy cleaning process. To reflect the cost associated with an inspection we consider an inspection cost of \$50 for each component. Table 6.5 shows the result for case study with four frying pots.

It can be observed from table 6.5 that the proposed policy based on DRL procedure outperforms other three benchmark policies that do not optimize for the predictive replacement and/or distribution of workload (cooks) among frying vats. We note that a predictive replacement here

entails cleaning the frying vat and refilling it with fresh oil. Moreover, we consider the case where the inspection interval is a decision variable that needs to be optimized together with maintenance and workload actions. For the optimization, a widely used grid search method is applied on the inspection interval, i.e. the agent is trained over a sequence of discrete inspection intervals, and the inspection interval that results in the lowest discounted total cost is chosen as the optimal inspection interval. Specifically, the discounted total cost over different inspection intervals are calculated and illustrated in figure 6.5.

It is observed from figure 6.5 that the optimal inspection interval is roughly every one and half day based on the considered cost structure. Another observation is that as the inspection interval increases, the variance of calculated discounted total cost increases. The reason is that a periodic inspection policy with a larger inspection interval increases the uncertainty of degradation signal prediction as well as increases the risk of running into unexpected failures, therby increasing the total cost incurred to the system.

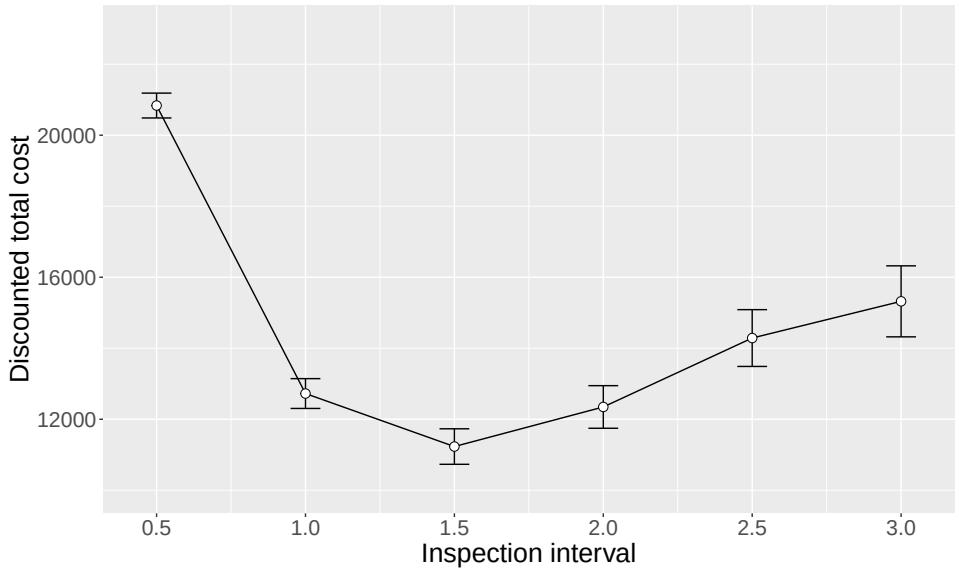

Figure 6.5: Discounted total cost vs. inspection interval

6.7. Conclusion

In this chapter, we proposed a procedure using deep reinforcement learning to solve the maintenance and operational workload planning problem for multi-component systems with economic

dependence over a finite planning horizon. The components in the system are assumed to be similar and to be working in parallel to satisfy a deterministic demand. The goal was to minimize the total cost of the system considering the underlying degradation process governing the health status of all components. We developed an advantage actor-critic algorithm and proposed a decomposition of actions to define the proposed stochastic policy. The workload actions which have an upper-bound limit are modeled using Beta distribution while Bernoulli distribution is considered for predictive maintenance actions. We showed through numerical study and a case study based on real world data that the proposed DRL approach outperforms the simple intuitive policies that are often utilized.

This study only considers economic dependency between components in the system. Future extension of this study can investigate optimal maintenance and workload planning where there is stochastic dependency between components. A well-know model for stochastic dependency between components is the competing risk model where a system fails if any of its components fails. We will investigate along this direction and report the result in a future study.

Chapter 7

Summary and Future Work

7.1. Overview

Prognosis, diagnosis, and decision-making have been highlighted in various applications and the massive data collected by system monitoring technologies can be utilized to effectively accomplish these tasks. The unprecedented data availability realized by the advanced system monitoring technologies, however, would not have a significant utility if appropriate models addressing the issues in prognosis, diagnosis, and decision-making based on such data are absent. The research work presented in this dissertation has focused on establishing a series of new data analytics methods for effective data-driven diagnosis, prognosis, and decision-making addressing various issues in smart and connected systems. The future work can continue to investigate novel data analytics, individualized informatics, metamodeling techniques and data-driven decision-making methodologies to truly realize the competitive advantages that are promised by smart and connected products/systems.

7.2. Summary of Contributions

The contributions of this dissertation can be summarized as follow:

1) *Statistical Monitoring of Multiple Profiles Simultaneously Using Gaussian Processes*

   This study proposes a monitoring approach based on MGP model to monitor multivariate profiles simultaneously. The proposed method uses a non-separable covariance function to construct the MGP model and tracks the stability of the process under study by monitoring a distance measure between the new observations of the multivariate profile and the

baseline in-control model. A key advantage of this method is that it considers correlations both within profiles and between profiles and facilitates sharing of information. The proposed framework is highly flexible and can quickly detect different out-of-control states.

2) *Remaining Useful Life Prediction Based on Degradation Signals Using Monotonic B-splines with Infinite Support*

In this study, a nonparametric approach to modeling and prognosis of CM signals using B-splines in a mixed effects setting is proposed. This study is the first to tackle both truncation and noisy CM signal issues using a non-parametric framework. In order to deal with the issue of truncated historical CM signals, our approach is based on augmenting B-spline basis functions with functions of infinite support. Moreover, to model the CM signal more accurately and robustly in a noisy setting, necessary and sufficient conditions to ensure monotonic evolution of the modeled signals are derived. Appropriate procedures for online updating of random coefficients of mixed effects model considering derived monotonicity constraints based on degradation data collected from an in-service unit are also presented. The performance of the proposed framework is investigated and benchmarked through analysis based on numerical studies and a case study using real-world data from automotive lead-acid batteries.

3) *Nonparametric Condition Based Remaining Useful Life Prediction Incorporating External Factors*

This study proposes a Brownian motion process with a stress dependent drift to model multiple time-varying environmental covariates. A semiparametric regression approach utilizing penalized splines is, further, proposed to model the environmental covariates-drift relationship. The unique feature of the proposed approach is that it does not assume a functional form for the degradation process drift and models multiple environmental covariates' effect on the degradation process. Moreover, the model is combined with in situ degradation measurements of the unit and its environmental conditions to predict the unit's remaining useful life through a Bayesian updating scheme.

4) *Multi-output Gaussian Process Modulated Poisson Processes for Event Prediction*

This study proposes a non-parametric prognostic framework for individualized event prediction based on the inhomogeneous Poisson processes with a MGCP prior on the

intensity functions. The MGCP prior on the intensity functions of the inhomogeneous Poisson processes maps data from similar historical units to the current unit under study which facilitates sharing of information and allows for analysis of flexible event patterns. The unique advantage of this framework is that it models the temporal dependency of each event stream and takes advantage of the cross-correlation that exists among different event streams to give accurate learning and prediction. Moreover, a scalable inference scheme using variational approximation is developed which makes the framework appropriate for high dimensional data.

5) *Deep Reinforcement Learning for Maintenance and Operational Workload Planning*

This study proposes a novel deep reinforcement learning procedure to devise a stochastic control policy for planning both maintenance and operational workload decisions. Unlike previous research, the developed framework considers the individualized degradation evolution of each component in the system in planning for both maintenance and workload assignment and accounts for economic dependency among them. Moreover, in the proposed framework, the effect of workload on component degradation is modeled through a Brownian motion process and unit-to-unit variation is considered using a Bayesian updating technique. The predictive maintenance decisions are modeled using Bernoulli distribution while workload assignments are modeled based on Beta distribution. An advantage actor-critic algorithm is proposed to set the optimal parameters of the stochastic policy distribution. The proposed framework takes into account the uncertainty of components failure and outperforms the commonplace maintenance policies.

7.3. Future Work

Recent innovations across all engineering disciplines have converged to make smart and connected systems technically/economically feasible. In the future, most (if not all) of the systems in various engineering disciplines will eventually become smart and connected systems. The data analytics methodologies proposed in this dissertation can help with achieving effective data-driven diagnosis, prognosis, and decision-making based on the modern smart and connected systems. However, new methodologies are urgently needed for data analytics and decision making to complete this transformation towards smart and connected systems. There are still many issues

that can be further investigated such as novel data analytics, individualized informatics, metamodeling techniques and data-driven decision-making methodologies to truly realize the competitive advantages that are promised by smart and connected products/systems. The potential future research directions are:

1. *Data fusion and individualized modeling and analysis towards smart and connected systems.* Future research can investigate novel data-driven methods to enable effective diagnostic and predictive data analytics by leveraging distributed estimation, multivariate Gaussian convolution processes, functional graphical models, and network modeling tools to establish a unified data analytics framework that scales efficiently to high dimensions and can incorporate functional heterogeneity and diverse data types both quantitative and qualitative.
2. *Data-driven reinforcement learning and Bayesian optimization for optimal management of smart and connected systems*. Effective decision making is crucial for maintaining and operating any engineering and healthcare system. A future research direction can focus on sequential and adaptive sampling methods, sequential Bayesian optimization and developing distributionally robust optimization capabilities to address the challenges of smart and connected systems as well as other engineering systems.
3. *Bayesian deep learning for uncertainty quantification of deep neural networks*. A comprehensive artificial intelligence system established through any smart and connected systems needs to not only perceive the environment with different sensors but also infer the world conditional or causal relations and corresponding uncertainty. The past decade has seen major advances in many perception tasks using deep learning models. For higher level inference, however, probabilistic graphical models and machine learning approaches like Gaussian processes with their Bayesian nature are still more powerful, and flexible, and can effectively quantify uncertainty. Future studies can work on Bayesian deep learning to provide a unified probabilistic framework to tightly integrate deep learning and Bayesian models. This unified framework would be able to process dense high-dimensional data while modeling conditional dependencies and relations and providing a procedure for uncertainty quantification to get the best of both worlds.

4. *Emerging applications in smart and connected manufacturing, healthcare and service systems*. Besides the abovementioned endeavors on the theoretical aspects, one can work on the emerging applications in the smart and connected systems such as IoT-enabled smart manufacturing and healthcare systems, and cloud-enabled remote infrastructure management.

References

Mohamed Abdel-Hameed. *Lévy processes and their applications in reliability and storage*. Springer, 2014.

Ryan Prescott Adams, Iain Murray, and David JC MacKay. Tractable nonparametric bayesian inference in poisson processes with gaussian process intensities. In *Proceedings of the 26th Annual International Conference on Machine Learning*, pages 9–16, 2009.

Enrique Aguilar, Hugo Elizalde, Diego Cárdenas, Oliver Probst, Pier Marzocca, and Ricardo A Ramirez-Mendoza. An adaptive curvature-guided approach for the knot-placement problem in fitted splines. *Journal of Computing and Information Science in Engineering*, 18(4):041013, 2018.

Sameer Al-Dahidi, Francesco Di Maio, Piero Baraldi, and Enrico Zio. Remaining useful life estimation in heterogeneous fleets working under variable operating conditions. *Reliability Engineering & System Safety*, 156:109–124, 2016.

Suzan Alaswad and Yisha Xiang. A review on condition-based maintenance optimization models for stochastically deteriorating system. *Reliability Engineering & System Safety*, 157:54–63, 2017.

Mauricio Alvarez and Neil D Lawrence. Sparse convolved gaussian processes for multi-output regression. In *Advances in neural information processing systems*, pages 57–64, 2009.

CP Andriotis and KG Papakonstantinou. Managing engineering systems with large state and action spaces through deep reinforcement learning. *Reliability Engineering & System Safety*, 191: 106483, 2019.

Ribal F Atallah, Chadi M Assi, and Maurice J Khabbaz. Scheduling the operation of a connected vehicular network using deep reinforcement learning. *IEEE Transactions on Intelligent Transportation Systems*, 20(5):1669–1682, 2018.

Suk Joo Bae and Paul H Kvam. A change-point analysis for modeling incomplete burn-in for light displays. *Iie Transactions*, 38(6):489–498, 2006.

D Banjevic and AKS Jardine. Calculation of reliability function and remaining useful life for a markov failure time process. *IMA journal of management mathematics*, 17(2):115–130, 2006.

Kaveh Barri, Behnam Jahangiri, Omid Davami, William G Buttlar, and Amir H Alavi. Smartphone-based molecular sensing for advanced characterization of asphalt concrete materials. *Measurement*, 151:107212, 2020.

Gleb Beliakov. Monotone approximation of aggregation operators using least squares splines. *International Journal of Uncertainty, Fuzziness and Knowledge-Based Systems*, 10(06):659–676, 2002.

Sarthak Bhagat, Hritwick Banerjee, Zion Tsz Ho Tse, and Hongliang Ren. Deep reinforcement learning for soft, flexible robots: brief review with impending challenges. *Robotics*, 8(1):4, 2019.

Linkan Bian and Nagi Gebraeel. Stochastic methodology for prognostics under continuously varying environmental profiles. *Statistical Analysis and Data Mining: The ASA Data Science Journal*, 6(3):260–270, 2013.

Ludger Brühl. Fatty acid alterations in oils and fats during heating and frying. *European Journal of Lipid Science and Technology*, 116(6):707–715, 2014.

Eunshin Byon, Lewis Ntaimo, and Yu Ding. Optimal maintenance strategies for wind turbine systems under stochastic weather conditions. *IEEE Transactions on Reliability*, 59(2):393–404, 2010.

Nuria C Caballé, Inma T Castro, Carlos J Pérez, and José Manuel Lanza-Gutiérrez. A condition-based maintenance of a dependent degradation-threshold-shock model in a system with multiple degradation processes. *Reliability Engineering & System Safety*, 134:98–109, 2015.

Rich Caruana. Multitask learning. *Machine learning*, 28(1):41–75, 1997.

Shing I Chang and Srikanth Yadama. Statistical process control for monitoring non-linear profiles using wavelet filtering and b-spline approximation. *International Journal of Production Research*, 48(4):1049–1068, 2010.

Zongchen Chen, Kuikui Liu, and Eric Vigoda. Optimal mixing of glauber dynamics: Entropy factorization via high-dimensional expansion. *arXiv preprint arXiv:2011.02075*, 2020.

Eric Chicken, Joseph J Pignatiello Jr, and James R Simpson. Statistical process monitoring of nonlinear profiles using wavelets. *Journal of Quality Technology*, 41(2):198–212, 2009.

E Choe and DB Min. Chemistry of deep-fat frying oils. *Journal of food science*, 72(5):R77–R86, 2007.

Shih-Hsiung Chou, Shing I Chang, and Tzong-Ru Tsai. On monitoring of multiple non-linear profiles. *International Journal of Production Research*, 52(11):3209–3224, 2014.

Paolo Costantino Cicorella, Bianca Maria Colosimo, and Massimo Pacella. Statistical process monitoring of complex shapes via gaussian process modeling. In *Milan, Italy*, pages 1–6, 2013.

Bianca M Colosimo, Paolo Cicorella, Massimo Pacella, and Marzia Blaco. From profile to surface monitoring: Spc for cylindrical surfaces via gaussian processes. *Journal of Quality Technology*, 46(2):95–113, 2014.

Stefano Conti, John Paul Gosling, Jeremy E Oakley, and Anthony O'Hagan. Gaussian process emulation of dynamic computer codes. *Biometrika*, 96(3):663–676, 2009.

Sylvain Corlay. B-spline techniques for volatility modeling. *Journal of Computational Finance*, 19, 2016.

David R Cox. Regression models and life-tables. *Journal of the Royal Statistical Society: Series B (Methodological)*, 34(2):187–202, 1972.

Heriberto Cuayáhuitl. Simpleds: A simple deep reinforcement learning dialogue system. In *Dialogues with social robots*, pages 109–118. Springer, 2017.

Alan Davies. *Handbook of condition monitoring: techniques and methodology*. Springer Science & Business Media, 2012.

Carl De Boor, Carl De Boor, Etats-Unis Mathématicien, Carl De Boor, and Carl De Boor. *A practical guide to splines*, volume 27. Springer-Verlag New York, 1978.

Akash Deep, Dharmaraj Veeramani, and Shiyu Zhou. Event prediction for individual unit based on recurrent event data collected in teleservice systems. *IEEE Transactions on Reliability*, 69 (1):216–227, 2019.

Rommert Dekker and Philip A Scarf. On the impact of optimisation models in maintenance decision making: the state of the art. *Reliability Engineering & System Safety*, 60(2):111–119, 1998.

Peter J Diggle, Paula Moraga, Barry Rowlingson, Benjamin M Taylor, et al. Spatial and spatio-temporal log-gaussian cox processes: extending the geostatistical paradigm. *Statistical Science*, 28(4):542–563, 2013.

Fangfang Ding and Zhigang Tian. Opportunistic maintenance for wind farms considering multi-level imperfect maintenance thresholds. *Renewable Energy*, 45:175–182, 2012.

MC Dobargarnes and Gloria Márquez-Ruiz. Regulation of used frying fats and validity of quick tests for discarding the fats. *Grasas y Aceites*, 49(3-4):331–335, 1998.

KA Doksum and A Hoyland. Models for variable-stress accelerated life testing experiments based on wiener processes and the inverse gaussian distribution. *Theory of Probability & Its Applications*, 37(1):137–139, 1993.

Luc Duchateau and Paul Janssen. *The frailty model*. Springer Science & Business Media, 2007.

Paul HC Eilers and Brian D Marx. Flexible smoothing with b-splines and penalties. *Statistical science*, pages 89–102, 1996.

Luis A Escobar, William Q Meeker, Danny L Kugler, and Laura L Kramer. Accelerated destructive degradation tests: data, models, and analysis. In *Mathematical and statistical methods in reliability*, pages 319–337. World Scientific, 2003.

Fatemeh Esfarjani, Khadijeh Khoshtinat, Aziz Zargaraan, Fatemeh Mohammadi-Nasrabadi, Yeganeh Salmani, Zahra Saghafi, Hedayat Hosseini, and Manochehr Bahmaei. Evaluating the rancidity and quality of discarded oils in fast food restaurants. *Food science & nutrition*, 7 (7):2302–2311, 2019.

Seth Flaxman, Andrew Wilson, Daniel Neill, Hannes Nickisch, and Alex Smola. Fast kronecker inference in gaussian processes with non-gaussian likelihoods. In *International Conference on Machine Learning*, pages 607–616, 2015.

Nagi Gebraeel and Jing Pan. Prognostic degradation models for computing and updating residual life distributions in a time-varying environment. *IEEE Transactions on Reliability*, 57(4):539–550, 2008.

Nagi Gebraeel, Alaa Elwany, and Jing Pan. Residual life predictions in the absence of prior degradation knowledge. *IEEE Transactions on Reliability*, 58(1):106–117, 2009.

Nagi Z Gebraeel, Mark A Lawley, Rong Li, and Jennifer K Ryan. Residual-life distributions from component degradation signals: A bayesian approach. *IiE Transactions*, 37(6):543–557, 2005.

Nima Gorjian, Lin Ma, Murthy Mittinty, Prasad Yarlagadda, and Yong Sun. A review on reliability models with covariates. In *Engineering Asset Lifecycle Management*, pages 385–397. Springer, 2010.

Evan Greensmith, Peter L Bartlett, and Jonathan Baxter. Variance reduction techniques for gradient estimates in reinforcement learning. *Journal of Machine Learning Research*, 5(9), 2004.

Asela Gunawardana, Christopher Meek, and Puyang Xu. A model for temporal dependencies in event streams. In *Advances in neural information processing systems*, pages 1962–1970, 2011.

Tuomas Haarnoja, Kristian Hartikainen, Pieter Abbeel, and Sergey Levine. Latent space policies for hierarchical reinforcement learning. In *International Conference on Machine Learning*, pages 1851–1860. PMLR, 2018a.

Tuomas Haarnoja, Aurick Zhou, Pieter Abbeel, and Sergey Levine. Soft actor-critic: Off-policy maximum entropy deep reinforcement learning with a stochastic actor. In *International Conference on Machine Learning*, pages 1861–1870. PMLR, 2018b.

Tuomas Haarnoja, Aurick Zhou, Kristian Hartikainen, George Tucker, Sehoon Ha, Jie Tan, Vikash Kumar, Henry Zhu, Abhishek Gupta, Pieter Abbeel, et al. Soft actor-critic algorithms and applications. *arXiv preprint arXiv:1812.05905*, 2018c.

Li Hao, Kaibo Liu, Nagi Gebraeel, and Jianjun Shi. Controlling the residual life distribution of parallel unit systems through workload adjustment. *IEEE Transactions on Automation Science and Engineering*, 14(2):1042–1052, 2015.

Dave Higdon. Space and space-time modeling using process convolutions. In *Quantitative methods for current environmental issues*, pages 37–56. Springer, 2002.

Yili Hong, Yuanyuan Duan, William Q Meeker, Deborah L Stanley, and Xiaohong Gu. Statistical methods for degradation data with dynamic covariates information and an application to outdoor weathering data. *Technometrics*, 57(2):180–193, 2015.

Philip Hougaard. *Analysis of multivariate survival data*. Springer Science & Business Media, 2012.

Khac Tuan Huynh, Anne Barros, and Christophe Bérenguer. Multi-level decision-making for the predictive maintenance of k-out-of-n: F deteriorating systems. *IEEE transactions on Reliability*, 64(1):94–117, 2014.

Salman Jahani, Raed Kontar, Shiyu Zhou, and Dharmaraj Veeramani. Remaining useful life prediction based on degradation signals using monotonic b-splines with infinite support. *IISE Transactions*, 52(5):537–554, 2020.

AKS Jardine, D Banjevic, and V Makis. Optimal replacement policy and the structure of software for condition-based maintenance. *Journal of Quality in Maintenance Engineering*, 3(2):109–119, 1997.

Andrew KS Jardine, Daming Lin, and Dragan Banjevic. A review on machinery diagnostics and prognostics implementing condition-based maintenance. *Mechanical systems and signal processing*, 20(7):1483–1510, 2006.

Daniel Jarrett, Jinsung Yoon, and Mihaela van der Schaar. Dynamic prediction in clinical survival analysis using temporal convolutional networks. *IEEE Journal of Biomedical and Health Informatics*, 24(2):424–436, 2019.

Willis A Jensen and Jeffrey B Birch. Profile monitoring via nonlinear mixed models. *Journal of Quality Technology*, 41(1):18–34, 2009.

María Daniela Juárez, Cibele Cristina Osawa, María Elina Acuña, Norma Sammán, and Lireny Aparecida Guaraldo Gonçalves. Degradation in soybean oil, sunflower oil and partially hydrogenated fats after food frying, monitored by conventional and unconventional methods. *Food Control*, 22(12):1920–1927, 2011.

Kevin A Kaiser and Nagi Z Gebraeel. Predictive maintenance management using sensor-based degradation models. *IEEE Transactions on Systems, Man, and Cybernetics-Part A: Systems and Humans*, 39(4):840–849, 2009.

Lan Kang and Susan L Albin. On-line monitoring when the process yields a linear profile. *Journal of quality Technology*, 32(4):418–426, 2000.

David L Kaufman and Mark E Lewis. Machine maintenance with workload considerations. *Naval Research Logistics (NRL)*, 54(7):750–766, 2007.

George S Kimeldorf and Grace Wahba. A correspondence between bayesian estimation on stochastic processes and smoothing by splines. *The Annals of Mathematical Statistics*, 41(2):495–502, 1970.

JF Kingman. Poisson processes. *Oxford Studies in Probability. Oxford: Oxford University Press*, 1993.

John P Klein and Melvin L Moeschberger. *Survival analysis: techniques for censored and truncated data*. Springer Science & Business Media, 2006.

Raed Kontar, Junbo Son, Shiyu Zhou, Chaitanya Sankavaram, Yilu Zhang, and Xinyu Du. Remaining useful life prediction based on the mixed effects model with mixture prior distribution. *IISE Transactions*, 49(7):682–697, 2017a.

Raed Kontar, Shiyu Zhou, and John Horst. Estimation and monitoring of key performance indicators of manufacturing systems using the multi-output gaussian process. *International Journal of Production Research*, 55(8):2304–2319, 2017b.

Raed Kontar, Shiyu Zhou, Chaitanya Sankavaram, Xinyu Du, and Yilu Zhang. Nonparametric modeling and prognosis of condition monitoring signals using multivariate gaussian convolution processes. *Technometrics*, 60(4):484–496, 2018a.

Raed Kontar, Shiyu Zhou, Chaitanya Sankavaram, Xinyu Du, and Yilu Zhang. Nonparametric modeling and prognosis of condition monitoring signals using multivariate gaussian convolution processes. *Technometrics*, 60(4):484–496, 2018b.

Radouane Laggoune, Alaa Chateauneuf, and Djamil Aissani. Opportunistic policy for optimal preventive maintenance of a multi-component system in continuous operating units. *Computers & Chemical Engineering*, 33(9):1499–1510, 2009.

Jerry Lawless and Martin Crowder. Covariates and random effects in a gamma process model with application to degradation and failure. *Lifetime Data Analysis*, 10(3):213–227, 2004.

Khanh Le Son, Mitra Fouladirad, Anne Barros, Eric Levrat, and Benoît Iung. Remaining useful life estimation based on stochastic deterioration models: A comparative study. *Reliability Engineering & System Safety*, 112:165–175, 2013.

Thomas J Leininger, Alan E Gelfand, et al. Bayesian inference and model assessment for spatial point patterns using posterior predictive samples. *Bayesian Analysis*, 12(1):1–30, 2017.

Jingshan Li. Modeling and analysis of manufacturing systems with parallel lines. *IEEE transactions on automatic control*, 49(10):1824–1832, 2004.

Lin Li, Mingyi You, and Jun Ni. Reliability-based dynamic maintenance threshold for failure prevention of continuously monitored degrading systems. *Journal of manufacturing science and engineering*, 131(3), 2009.

Naipeng Li, Nagi Gebraeel, Yaguo Lei, Linkan Bian, and Xiaosheng Si. Remaining useful life prediction of machinery under time-varying operating conditions based on a two-factor state-space model. *Reliability Engineering & System Safety*, 186:88–100, 2019.

Yongxiang Li, Qiang Zhou, Xiaohu Huang, and Li Zeng. Pairwise estimation of multivariate gaussian process models with replicated observations: Application to multivariate profile monitoring. *Technometrics*, 60(1):70–78, 2018.

Zhiguo Li, Shiyu Zhou, Suresh Choubey, and Crispian Sievenpiper. Failure event prediction using the cox proportional hazard model driven by frequent failure signatures. *IIE transactions*, 39(3): 303–315, 2007.

Wenzhao Lian, Ricardo Henao, Vinayak Rao, Joseph Lucas, and Lawrence Carin. A multitask point process predictive model. In *International Conference on Machine Learning*, pages 2030–2038, 2015.

Chen-Mao Liao and Sheng-Tsaing Tseng. Optimal design for step-stress accelerated degradation tests. *IEEE Transactions on Reliability*, 55(1):59–66, 2006.

Guobo Liao, Hongpeng Yin, Min Chen, and Zheng Lin. Remaining useful life prediction for multi-phase deteriorating process based on wiener process. *Reliability Engineering & System Safety*, 207:107361, 2021.

Haitao Liao and Zhigang Tian. A framework for predicting the remaining useful life of a single unit under time-varying operating conditions. *Iie Transactions*, 45(9):964–980, 2013.

Linxia Liao and Felix Köttig. Review of hybrid prognostics approaches for remaining useful life prediction of engineered systems, and an application to battery life prediction. *IEEE Transactions on Reliability*, 63(1):191–207, 2014.

Timothy P Lillicrap, Jonathan J Hunt, Alexander Pritzel, Nicolas Heess, Tom Erez, Yuval Tassa, David Silver, and Daan Wierstra. Continuous control with deep reinforcement learning. *arXiv preprint arXiv:1509.02971*, 2015.

Kaibo Liu, Nagi Z Gebraeel, and Jianjun Shi. A data-level fusion model for developing composite health indices for degradation modeling and prognostic analysis. *IEEE Transactions on Automation Science and Engineering*, 10(3):652–664, 2013.

Weiwei Liu, Linpeng Peng, Junjie Cao, Xiaokuan Fu, Yong Liu, Zaisheng Pan, and Jian Yang. Ensemble bootstrapped deep deterministic policy gradient for vision-based robotic grasping. *IEEE Access*, 9:19916–19925, 2021.

Chris Lloyd, Tom Gunter, Michael Osborne, and Stephen Roberts. Variational inference for gaussian process modulated poisson processes. In *International Conference on Machine Learning*, pages 1814–1822, 2015.

C Joseph Lu and William O Meeker. Using degradation measures to estimate a time-to-failure distribution. *Technometrics*, 35(2):161–174, 1993.

Joe W McPherson, JW McPherson, and Glaser. *Reliability physics and engineering*. Springer, 2010.

Kamal Medjaher, Diego Alejandro Tobon-Mejia, and Noureddine Zerhouni. Remaining useful life estimation of critical components with application to bearings. *IEEE Transactions on Reliability*, 61(2):292–302, 2012.

William Q Meeker and Luis A Escobar. *Statistical methods for reliability data*. John Wiley & Sons, 2014.

William Q Meeker, Luis A Escobar, and C Joseph Lu. Accelerated degradation tests: modeling and analysis. *Technometrics*, 40(2):89–99, 1998.

Oto Mestek, Jiří Pavlík, and Miloslav Suchánek. Multivariate control charts: control charts for calibration curves. *Fresenius' journal of analytical chemistry*, 350(6):344–351, 1994.

Volodymyr Mnih, Koray Kavukcuoglu, David Silver, Andrei A Rusu, Joel Veness, Marc G Bellemare, Alex Graves, Martin Riedmiller, Andreas K Fidjeland, Georg Ostrovski, et al. Human-level control through deep reinforcement learning. *nature*, 518(7540):529–533, 2015.

Volodymyr Mnih, Adria Puigdomenech Badia, Mehdi Mirza, Alex Graves, Timothy Lillicrap, Tim Harley, David Silver, and Koray Kavukcuoglu. Asynchronous methods for deep reinforcement learning. In *International conference on machine learning*, pages 1928–1937. PMLR, 2016.

Jesper Møller, Anne Randi Syversveen, and Rasmus Plenge Waagepetersen. Log gaussian cox processes. *Scandinavian journal of statistics*, 25(3):451–482, 1998.

Douglas C Montgomery. *Statistical quality control*. Wiley Global Education, 2012.

Wayne Nelson. Prediction of field reliability of units, each under differing dynamic stresses, from accelerated test data. *Handbook of Statistics*, 20:611–621, 2001.

Wayne B Nelson. *Accelerated testing: statistical models, test plans, and data analysis*, volume 344. John Wiley & Sons, 2009.

Kim-Anh Nguyen, Phuc Do, and Antoine Grall. Multi-level predictive maintenance for multi-component systems. *Reliability engineering & system safety*, 144:83–94, 2015.

Rassoul Noorossana, Abbas Saghaei, and Amirhossein Amiri. *Statistical analysis of profile monitoring*, volume 865. John Wiley & Sons, 2011.

Zhenan Pang, Xiaosheng Si, Changhua Hu, Dangbo Du, and Hong Pei. A bayesian inference for remaining useful life estimation by fusing accelerated degradation data and condition monitoring data. *Reliability Engineering & System Safety*, 208:107341, 2021.

Chanseok Park and William J Padgett. Stochastic degradation models with several accelerating variables. *IEEE Transactions on Reliability*, 55(2):379–390, 2006.

P Parker, M Morton, N Draper, and W Line. A single-vector force calibration method featuring the modern design of experiments. In *39th Aerospace sciences meeting and exhibit*, page 170, 2001.

Kamran Paynabar, Jionghua Jin, and Massimo Pacella. Monitoring and diagnosis of multichannel nonlinear profile variations using uncorrelated multilinear principal component analysis. *Iie transactions*, 45(11):1235–1247, 2013.

Min Peng, Qianqian Xie, Hua Wang, Yanchun Zhang, and Gang Tian. Bayesian sparse topical coding. *IEEE Transactions on Knowledge and Data Engineering*, 31(6):1080–1093, 2018.

Umberto Picchini, ANDREA DE GAETANO, and Susanne Ditlevsen. Stochastic differential mixed-effects models. *Scandinavian Journal of statistics*, 37(1):67–90, 2010.

Jonathan W Pillow, Jonathon Shlens, Liam Paninski, Alexander Sher, Alan M Litke, EJ Chichilnisky, and Eero P Simoncelli. Spatio-temporal correlations and visual signalling in a complete neuronal population. *Nature*, 454(7207):995–999, 2008.

Joeri Poppe, Robert N Boute, and Marc R Lambrecht. A hybrid condition-based maintenance policy for continuously monitored components with two degradation thresholds. *European Journal of Operational Research*, 268(2):515–532, 2018.

Martin L Puterman. *Markov decision processes: discrete stochastic dynamic programming*. John Wiley & Sons, 2014.

Peihua Qiu, Changliang Zou, and Zhaojun Wang. Nonparametric profile monitoring by mixed effects modeling. *Technometrics*, 52(3):265–277, 2010.

Ali Rahimi, Benjamin Recht, et al. Random features for large-scale kernel machines. In *NIPS*, volume 3, page 5. Citeseer, 2007.

Carl Edward Rasmussen. *Gaussian Processes in Machine Learning*, pages 63–71. Springer Berlin Heidelberg, Berlin, Heidelberg, 2004. ISBN 978-3-540-28650-9. doi: 10.1007/978-3-540-28650-9_4. URL https://doi.org/10.1007/978-3-540-28650-9_4.

C.E. Rasmussen and C.K.I. Williams. *Gaussian Processes for Machine Learning*. Adaptive computation and machine learning. MIT Press, 2006.

J Riascos-Ochoa, M Sánchez-Silva, and Georgia-Ann Klutke. Modeling and reliability analysis of systems subject to multiple sources of degradation based on lévy processes. *Probabilistic Engineering Mechanics*, 45:164–176, 2016.

Dimitris Rizopoulos. Dynamic predictions and prospective accuracy in joint models for longitudinal and time-to-event data. *Biometrics*, 67(3):819–829, 2011.

Dimitris Rizopoulos, Laura A Hatfield, Bradley P Carlin, and Johanna JM Takkenberg. Combining dynamic predictions from joint models for longitudinal and time-to-event data using bayesian model averaging. *Journal of the American Statistical Association*, 109(508):1385–1397, 2014.

Larry Schumaker. *Spline functions: basic theory*. Cambridge University Press, 2007.

Jyh-Jen Horng Shiau, Hsiang-Ling Huang, Shuo-Hui Lin, and Ming-Ye Tsai. Monitoring nonlinear profiles with random effects by nonparametric regression. *Communications in Statistics—Theory and Methods*, 38(10):1664–1679, 2009.

Jyh-Jeu Horng Shiau and Hsin-Hua Lin. Analyzing accelerated degradation data by nonparametric regression. *IEEE Transactions on reliability*, 48(2):149–158, 1999.

Xiao-Sheng Si, Wenbin Wang, Chang-Hua Hu, and Dong-Hua Zhou. Remaining useful life estimation–a review on the statistical data driven approaches. *European journal of operational research*, 213(1):1–14, 2011.

Bernhard W Silverman. Some aspects of the spline smoothing approach to non-parametric regression curve fitting. *Journal of the Royal Statistical Society: Series B (Methodological)*, 47(1): 1–21, 1985.

Dan Simon. *Optimal state estimation: Kalman, H infinity, and nonlinear approaches*. John Wiley & Sons, 2006.

Edward Snelson and Zoubin Ghahramani. Sparse gaussian processes using pseudo-inputs. In *Advances in neural information processing systems*, pages 1257–1264, 2006.

Hossein Soleimani, James Hensman, and Suchi Saria. Scalable joint models for reliable uncertainty-aware event prediction. *IEEE transactions on pattern analysis and machine intelligence*, 40(8): 1948–1963, 2017.

Junbo Son, Qiang Zhou, Shiyu Zhou, Xiaofeng Mao, and Mutasim Salman. Evaluation and comparison of mixed effects model based prognosis for hard failure. *IEEE Transactions on Reliability*, 62(2):379–394, 2013.

Junbo Son, Shiyu Zhou, Chaitanya Sankavaram, Xinyu Du, and Yilu Zhang. Remaining useful life prediction based on noisy condition monitoring signals using constrained kalman filter. *Reliability Engineering & System Safety*, 152:38–50, 2016.

Changyue Song and Kaibo Liu. Statistical degradation modeling and prognostics of multiple sensor signals via data fusion: A composite health index approach. *IISE Transactions*, 50(10):853–867, 2018.

Frederick S Stover and Robert V Brill. Statistical quality control applied to ion chromatography calibrations. *Journal of Chromatography A*, 804(1-2):37–43, 1998.

Ondřej Straka, Jindřich Duník, and Miroslav Šimandl. Truncation nonlinear filters for state estimation with nonlinear inequality constraints. *Automatica*, 48(2):273–286, 2012.

Bo Sun, Meichen Yan, Qiang Feng, Yu Li, Yi Ren, Kun Zhou, and Weifang Zhang. Gamma degradation process and accelerated model combined reliability analysis method for rubber o-rings. *IEEE Access*, 2018.

Richard S Sutton and Andrew G Barto. *Reinforcement learning: An introduction*. MIT press, 2018.

Richard S Sutton, David A McAllester, Satinder P Singh, Yishay Mansour, et al. Policy gradient methods for reinforcement learning with function approximation. In *NIPs*, volume 99, pages 1057–1063. Citeseer, 1999.

Yee W Teh and Vinayak Rao. Gaussian process modulated renewal processes. In *Advances in Neural Information Processing Systems*, pages 2474–2482, 2011.

LC Thomas. A survey of maintenance and replacement models for maintainability and reliability of multi-item systems. *Reliability Engineering*, 16(4):297–309, 1986.

Zhigang Tian and Haitao Liao. Condition based maintenance optimization for multi-component systems using proportional hazards model. *Reliability Engineering & System Safety*, 96(5): 581–589, 2011.

Michalis Titsias. Variational learning of inducing variables in sparse gaussian processes. In *Artificial Intelligence and Statistics*, pages 567–574, 2009.

Tegoeh Tjahjowidodo et al. A direct method to solve optimal knots of b-spline curves: An application for non-uniform b-spline curves fitting. *PloS one*, 12(3):e0173857, 2017.

Huan-Hsin Tseng, Yi Luo, Sunan Cui, Jen-Tzung Chien, Randall K Ten Haken, and Issam El Naqa. Deep reinforcement learning for automated radiation adaptation in lung cancer. *Medical physics*, 44(12):6690–6705, 2017.

Sheng-Tsaing Tseng and Chien-Yu Peng. Optimal burn-in policy by using an integrated wiener process. *IIE Transactions*, 36(12):1161–1170, 2004.

Adriaan Van Horenbeek and Liliane Pintelon. A dynamic predictive maintenance policy for complex multi-component systems. *Reliability Engineering & System Safety*, 120:39–50, 2013.

E Vanem. Statistical methods for condition monitoring systems. *International Journal of Condition Monitoring*, 8(1):9–23, 2018.

Jay M Ver Hoef and Ronald Paul Barry. Constructing and fitting models for cokriging and multivariable spatial prediction. *Journal of Statistical Planning and Inference*, 69(2):275–294, 1998.

Dennis Andrew Virkler, Brnm Hillberry, and PK Goel. The statistical nature of fatigue crack propagation. *Journal of Engineering Materials and Technology*, 101(2):148–153, 1979.

Pascal Vrignat, Manuel Avila, Florent Duculty, and Frédéric Kratz. Failure event prediction using hidden markov model approaches. *IEEE Transactions on Reliability*, 64(3):1038–1048, 2015.

Grace Wahba. Bayesian "confidence intervals" for the cross-validated smoothing spline. *Journal of the Royal Statistical Society: Series B (Methodological)*, 45(1):133–150, 1983.

Esteban Walker and S Paul Wright. Comparing curves using additive models. *Journal of Quality Technology*, 34(1):118–129, 2002.

W-bin Wang. A model to determine the optimal critical level and the monitoring intervals in condition-based maintenance. *International Journal of Production Research*, 38(6):1425–1436, 2000.

Wenbin Wang, Matthew Carr, Wenjia Xu, and Khairy Kobbacy. A model for residual life prediction based on brownian motion with an adaptive drift. *Microelectronics Reliability*, 51(2):285–293, 2011.

Xiao Wang. Wiener processes with random effects for degradation data. *Journal of Multivariate Analysis*, 101(2):340–351, 2010.

Xiao Wang and Dihua Xu. An inverse gaussian process model for degradation data. *Technometrics*, 52(2):188–197, 2010.

Yuxin Wen, Jianguo Wu, Devashish Das, and Tzu-Liang Bill Tseng. Degradation modeling and rul prediction using wiener process subject to multiple change points and unit heterogeneity. *Reliability Engineering & System Safety*, 176:113–124, 2018.

GA Whitmore and Fred Schenkelberg. Modelling accelerated degradation data using wiener diffusion with a time scale transformation. *Lifetime data analysis*, 3(1):27–45, 1997.

Stefan Wilhelm et al. Moments calculation for the doubly truncated multivariate normal density. *arXiv preprint arXiv:1206.5387*, 2012.

James D Williams, William H Woodall, and Jeffrey B Birch. Statistical monitoring of nonlinear product and process quality profiles. *Quality and Reliability Engineering International*, 23(8): 925–941, 2007.

William H Woodall. Current research on profile monitoring. *Production*, 17(3):420–425, 2007.

Bei Wu and Lirong Cui. On reliability analysis of a load-sharing k-out-of-n: G system with interacting markov subsystems. *International Journal of Production Research*, pages 1–15, 2021.

Xiaosong Wu, Rui Miao, Zefeng Li, Jie Ren, Jie Zhang, Zhibin Jiang, and Xuening Chu. Process monitoring research with various estimator-based mewma control charts. *International Journal of production research*, 53(14):4337–4350, 2015.

Haifeng Xia, Yu Ding, and Jyhwen Wang. Gaussian process method for form error assessment using coordinate measurements. *Iie Transactions*, 40(10):931–946, 2008.

Zhibing Xu, Yili Hong, and Ran Jin. Nonlinear general path models for degradation data with dynamic covariates. *Applied Stochastic Models in Business and Industry*, 32(2):153–167, 2016.

Hao Yan, Kaibo Liu, Xi Zhang, and Jianjun Shi. Multiple sensor data fusion for degradation modeling and prognostics under multiple operational conditions. *IEEE Transactions on Reliability*, 65(3):1416–1426, 2016.

Zhi-Sheng Ye and Nan Chen. The inverse gaussian process as a degradation model. *Technometrics*, 56(3):302–311, 2014.

Murat Yildirim, Xu Andy Sun, and Nagi Z Gebraeel. Sensor-driven condition-based generator maintenance scheduling—part i: Maintenance problem. *IEEE Transactions on Power Systems*, 31(6):4253–4262, 2016a.

Murat Yildirim, Xu Andy Sun, and Nagi Z Gebraeel. Sensor-driven condition-based generator maintenance scheduling—part ii: incorporating operations. *IEEE Transactions on Power Systems*, 31(6):4263–4271, 2016b.

Kai Yu, Volker Tresp, and Anton Schwaighofer. Learning gaussian processes from multiple tasks. In *Proceedings of the 22nd international conference on Machine learning*, pages 1012–1019, 2005.

Xiao-Tong Yuan, Xiaobai Liu, and Shuicheng Yan. Visual classification with multitask joint sparse representation. *IEEE Transactions on Image Processing*, 21(10):4349–4360, 2012.

Yuan Yuan, Shiyu Zhou, Crispian Sievenpiper, Kamal Mannar, and Yibin Zheng. Event log modeling and analysis for system failure prediction. *IIE Transactions*, 43(9):647–660, 2011.

Yuan Yuan, Nan Chen, and Shiyu Zhou. Modeling regression quantile process using monotone b-splines. *Technometrics*, 59(3):338–350, 2017.

Yang Zhang, Zhen He, Chi Zhang, and William H Woodall. Control charts for monitoring linear profiles with within-profile correlation using gaussian process models. *Quality and Reliability Engineering International*, 30(4):487–501, 2014.

Zhengxin Zhang, Xiaosheng Si, Changhua Hu, and Yaguo Lei. Degradation data analysis and remaining useful life estimation: A review on wiener-process-based methods. *European Journal of Operational Research*, 2018.

Hongshan Zhao, Fanhao Xu, Botong Liang, Jianping Zhang, and Peng Song. A condition-based opportunistic maintenance strategy for multi-component system. *Structural Health Monitoring*, 18(1):270–283, 2019.

Xiujie Zhao, Shuguang He, Zhen He, and Min Xie. Optimal condition-based maintenance policy with delay for systems subject to competing failures under continuous monitoring. *Computers & Industrial Engineering*, 124:535–544, 2018.

Xuejing Zhao, Mitra Fouladirad, Christophe Bérenguer, and Laurent Bordes. Condition-based inspection/replacement policies for non-monotone deteriorating systems with environmental covariates. *Reliability Engineering & System Safety*, 95(8):921–934, 2010.

Qiang Zhou, Junbo Son, Shiyu Zhou, Xiaofeng Mao, and Mutasim Salman. Remaining useful life prediction of individual units subject to hard failure. *IIE Transactions*, 46(10):1017–1030, 2014.

Rensheng Zhou, Nagi Gebraeel, and Nicoleta Serban. Degradation modeling and monitoring of truncated degradation signals. *IIE Transactions*, 44(9):793–803, 2012.

Rensheng R Zhou, Nicoleta Serban, and Nagi Gebraeel. Degradation modeling applied to residual lifetime prediction using functional data analysis. *The Annals of Applied Statistics*, pages 1586–1610, 2011.

Changliang Zou, Xianghui Ning, and Fugee Tsung. Lasso-based multivariate linear profile monitoring. *Annals of Operations Research*, 192(1):3–19, 2012.